UNIVERSITÀ DEGLI STUDI DI PARMA

DIPARTIMENTO DI INGEGNERIA INDUSTRIALE

(I)-43100 PARMA, VIALE G.P.USBERTI 181A/7
TEL.: +39 0521 905701 - FAX.: +39 0521 905705

DOTTORATO DI RICERCA IN INGEGNERIA INDUSTRIALE
XXI CICLO

DEFINITION OF AN OBJECT ORIENTED LIBRARY FOR THE DYNAMIC SIMULATION OF ADVANCED ENERGY SYSTEMS: METHODOLOGIES, TOOLS AND APPLICATION TO COMBINED ICE-ORC POWER PLANTS

IACOPO VAJA

DISSERTAZIONE PRESENTATA PER IL CONSEGUIMENTO DEL TITOLO DI DOTTORE DI RICERCA
GENNAIO 2009

UNIVERSITÀ DEGLI STUDI DI PARMA

DIPARTIMENTO DI INGEGNERIA INDUSTRIALE

(I)-43100 PARMA, VIALE G.P.USBERTI 181A/7
TEL.: +39 0521 905701 - FAX.: +39 0521 905705

DOTTORATO DI RICERCA IN INGEGNERIA INDUSTRIALE
XXI CICLO

DEFINITION OF AN OBJECT ORIENTED LIBRARY FOR THE DYNAMIC SIMULATION OF ADVANCED ENERGY SYSTEMS: METHODOLOGIES, TOOLS AND APPLICATION TO COMBINED ICE-ORC POWER PLANTS

IACOPO VAJA

COORDINATORE:
PROF.ING. MARCO SPIGA

SUPERVISORE:
PROF.ING. AGOSTINO GAMBAROTTA

DISSERTAZIONE PRESENTATA PER IL CONSEGUIMENTO DEL TITOLO DI DOTTORE DI RICERCA
GENNAIO 2009

CONTENT

CHAPTER ONE

CHAPTER TWO

CHAPTER THREE

CHAPTER FOUR

CHAPTER FIVE

CHAPTER SIX

LIST OF FIGURES

CHAPTER TWO

CHAPTER THREE

CHAPTER FOUR

CHAPTER FIVE

LIST OF TABLES

CHAPTER TWO

CHAPTER THREE

CHAPTER FOUR

CHAPTER FIVE

CHAPTER
ONE

INTRODUCTION

The present Thesis covers part of the work that has been carried out during the three year Ph.D. course in Industrial Engineering at the University of Parma.

Scope of the work is developing theoretical methodologies and a full library of dynamic models that can represent the components that usually appear in energy conversion systems. The proposed library should endorse the possibility to create any desire arrangement of the studied systems, to overcome the lack of testing facilities in order to create full virtual machines capable of representing the main phenomena that occur in the real systems to get a full and deep understanding on the way they operate and respond to transients and off design operating condition.

In Chapter Two an overview and classification of modeling techniques, suitable for energy systems analysis, is presented. Among the different classification criteria introduced, it is crucial to define whether state variables can be used for the considered component. This option leads to very different ways of developing the model: if the component modeled displays some "storage" capabilities (i.e. it is assumed to be able to store mass, energy, momentum, or moment of momentum) it is intended as a "state determined" system and state variables are defined through the introduction of cardinal physical laws in differential form. From a mathematical viewpoint this implies integrating in time (time is the only domain considered within this work) ordinary differential equations (ODE) expressed in term of the state variables, whose evolution hence will not depend only on the system inputs but on its complete "history", that starts with the initialization at simulation time t=0. If the storage capabilities of the model are neglected it will be defined as "not state determined" and only algebraic equations (AE) will be introduced. Often the equations used in this case are derived from steady state performance data, gathered either from experimental investigations or by more complex model tools, thus simplifying the description of their transient behaviour as a continuous progression of steady state operating conditions. This modelling approach is known as "quasi-steady".

The models that will be created should be *proper* (i.e. models that achieve the accuracy required by the application with minimal complexity) scalable and flexible. The approach is followed is typical of object-oriented modeling and each realized component refers to a physical part (or a physical phenomena) of the system. Particular attention is also paid to causality, i.e. every model should be created in such a way to properly represent the cause-effect correlation between inputs and outputs.

Another issue faced is the modeling environment to be chosen. After assessing some of the most widely known softwares that looked suitable for the scope, the choice has fallen on the

Matlab®/Simulink® package. Simulink® is appreciated for modelling, simulation and analysis of dynamic systems by use of standard or customized blocks that allow great flexibility in model designing and are suitable for control purposes. Matlab® is exploited for its graphical and result analysis capabilities and the possibility to write specific functions which can be called during simulation. The potentialities in matrix calculation of the Matlab® language are also often exploited.

In Chapter Three the complete library of components is presented. According to what seen previously the components created have been split in the two main sub-libraries depending if dealing with "state determined" or "not state determined" components. A full complete system model should comprise a proper alternation of components coming from the two libraries to guarantee a better numerical solvability of the system of equations generated and to avoid algebraic loops.

The two realized libraries have been enclosed in the Simulink® library root from where the realized custom blocks can be choosen, analogously to the way the standard blocks are employed. This option not only allows easy access to the developed block in creating any new lay-out, but turns useful since the models picked up from the library, if improved or modified, extend the changes to any Simulink® lay-out where they are employed.

For each component a detailed description of the inputs, outputs and state variables (if present) is provided. The realized Simulink® models are also shown along with the specific dialog windows realized to introduce model parameters. Nearly all the models are based on *s-functions*, which allows executing the compiled Matlab® code while Simulink® is performing the simulation of a system.

The sub-library 'state determined components' will contain the following components:

- thermal solar collectors;
- single phase heat exchangers;
- heat exchangers with phase change;
- drums;
- constant pressure combustion chambers;
- rotating shafts dynamics;
- General fluid Receivers;
- ICE intercoolers.

Among these particular emphasis is given on the models of heat exchangers. This component has been characterized through the adoption of finite volume approach where a set of differential equations, expressing the energy balances in the axial nodes, is introduced and solved numerically adopting a forward finite difference method. Peculiarity of the proposed procedure is the degree of accuracy that may be tuned by the user defining the precision of the component discretization. The approach has also been applied to model an heat exchanger with phase change (evaporator or condenser) where also mass balances are considered in the component control volumes.

The 'not state determined' library contains the following models:

- compressors;
- turbines;
- pumps;
- valves;

- heat exchangers with no thermal dynamics;
- in cylinder combustion processes (in ICE).

As seen the library features all the “flow control devices’ that may appear in a fluid system, such as turbines, compressors, pumps and valves. Among the elements introduced, a special one in the “ICE in-cylinder processes”. The component is based on characteristic maps that allow to know the state of gases trapped inside an ICE cylinder at the end of expansion stroke. This model will turn useful in realizing a full dynamic model of an ICE. The maps are not based on experimental data, as common practice, but are obtained by means of a specifically developed computer code that resolves the chemical equations that refer to species dissociation at chemical equilibrium. Even though it is just an approximation of the real combustion process, the procedure has been believed to be a useful way to gather information of the engine combustion processes when no (or limited) experimental data are available.

In Chapter Four examples of applications of the realized models for fluid components are provided, with reference to power systems widely diffused and of known and proven design. The scope is to display the ease of creating new full models from the base component blocks, and the way to properly couple and link them together.

Besides a simple example of a cogenerative micro gas turbine system, deeper insight is provided to the models of an organic Rankine power cycle and an alternative stationary internal combustion engine used for cogeneration purposes. These models will be employed for further analysis in Chapter Five.

Results of simulations are presented for all the full models described under transient operating conditions inducted by some changes in the main model inputs.

All the presented models have been introduced in a further Simulink® sub-library (‘complete power systems’). To be noted that the example presented are not exhaustive of the capabilities of the presented set of computer models discussed in Chapter Three, but new systems can be easily created depending on the research needs.

Chapter Five show the way the developed models are intended for system design purposes. It is author’s belief that a full validated computer model for the dynamic simulation of energy systems can constitute a proper tool aimed at developing, assessing and optimizing new system design configurations, developed to increase energy conversion efficiency and reducing primary energy consumption.

In this case a combined ICE-ORC system (intended for stationary applications) is proposed as solution to improve the second principle efficiency of the engine generating unit. Many configurations are proposed and discussed through a comprehensive energy and exergy analysis of the system, in order to highlight the theoretical benefits in terms of energy conversion efficiency that can be achieved in some cases.

To prove the feasibility of the design and to deeply assess the mutual interactions that exist between the two prime engines, a complete dynamic model of the system has been proposed and some results, under transient operational conditions are reported.

The dynamic model of the full system therefore constitute a virtual test bench for development and enhancement of the new proposed energy conversion unit, relieving the energy system researcher from the costly and demanding real testing that, at least in the first stages of development, can thus be substituted by the simulation model.

CHAPTER
TWO

OVERVIEW ON MODELING OF THERMO-FLUID SYSTEMS

The present Chapter provides an insight on the modelling approaches considered proper in the field of energy conversion systems. After providing a broad and general classification of the modelling techniques and approaches, with reference to the main peculiarities that may characterize the model of a physical component, an overview is provided also on some commercial software that have been considered as base environments for the development of the dynamic models that will be considered in this Work. The analysis on the commercial software indeed is not exhaustive and the market proposes many other tools that probably are as powerful as the one chosen or more. The analysis has been limited to the software considered to apply for the scope and all these software have been carefully evaluated and also tried prior to make the decision.

The one that turned out to be more appropriate is Matlab®/Simulink®. This software features an its own language that may allows all the flexibility in typing customized codes where all the physical or empirical equations that describe the components under analysis can be properly described, but also the immediateness of an icon based environment, that is the Simulink® package, where the built in code sources can be embedded into block icons through proper functions called *s-functions*, and solved in the time domain.

Nomenclature

c	Velocity [m/s]
e	Specific energy [kJ/kg]
m	Mass [kg]
$\dot{m}$	Mass flow rate [kg/s]
$\overline{n}$	Unit normal vector
p	Pressure [Pa]
$\overline{r}$	Position vector
s	Specific entropy [kJ/kg K]
t	Time [s]
u	Specific internal energy [kJ/kg]
v	Specific volume [m^3/kg]
A	Area [m^2]
F	Force [N]
M	Momentum [kg m/s]

R	Specific gas constant [kJ/kg K]
T	Temperature [K]
V	Volume [m^3]
W	Work [kJ]

Greek symbols

ρ	Density [kg/ m^3]
Φ	Generic system property

Abbreviations and subscripts

cs	Control surface
cv	Control volume
in	Inlet
out	Outlet

2.1 Modeling approach for fluid systems

In modeling fluid system usually the modular system dynamic approach is applied which leads to consider the whole system as the result of interconnecting several components. The mathematical model of the whole plant therefore can be carried out by identifying the relevant components and sub-systems and properly connecting them by means of signals that can be either a mechanical energy coupling or a working fluid stream. The model therefore is modular in structure, and the used approach allows for realizing a “component based” model, where each main component of the system is mathematically modelled and integrated with the other to simulate the plant behaviour in steady and transient operating conditions1.

This approach is typical of object-oriented methodologies and each model strictly defines an object of the physical system. Indeed defining the boundary of the main system and of the many components that constitute the system itself is crucial for the effectiveness of the analysis and sometimes it is not an obvious process. It may also happen that models that do not really correspond to physical objects have to be introduced in order describe phenomena that do not belong to just one components but whose dynamics characterizes a wider set of components; this is the case for example when all rotating inertia of the masses linked to a shaft are lumped together in order to determine the actual rotating velocity.

In general, regardless the type of model considered, in an object oriented modelling approach each model can be characterized by a set of input variables (vector $\overline{U}$), a vector of output signals ($\overline{Y}$), a vector of information signals ($\overline{I}$) (that may be associated to external control actions as the variation of the position of a valve or of the geometry of a VGT turbine) and a vector of state variables ($\overline{X}$). Each of these vectors may undergo changes during simulation time hence the dependency upon time displayed in Fig. 2.2.1.

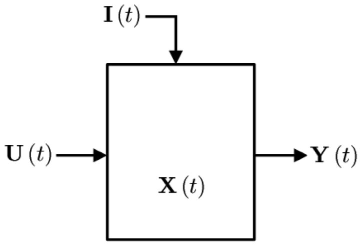

Fig. 2.2.1. General representation of a component in an object-oriented modelling approach.

Three main general approaches may be adopted in dealing with modelling:

- *Analysis*: determines the output $\overline{Y}$ given the input variables $\overline{U}$ and the set of state variables $\overline{X}$ at an initial instant and the system;
- *Synthesis*: determines the system if the input variables are known and output variables are imposed;
- *Identification*: when a model of the system is defined for a known set of input variables and given the outputs (that may for example be gathered by experiments).

The activity within this Work is focused mainly in the *analysis* of the components and the systems studied. The lack of experimental data did not allow to proceed to a proper *identification* of the models therefore the work was mainly focused on building up models based on rigorous mathematical equations through which determine the values of the outputs with respect to time providing a prediction on behaviour of the real component, hence the *analysis*.

Usually, when the analysis of a system is being carried out, according to an input/system/output approach, once the inputs have been defined the output are immediately determined hence a classification of only input signals is pertinent 2, as shown in Fig. 2.2.

In general it can be assumed to be an input of a system every agency that may cause the system modelled to respond. A general classification thus divides the inputs in two main types: initial energy storage and external driving. Whereas initial energy storage always refers to the state of the system at initial time of simulation, external driving inputs are classified according to how they vary with time, the first broad classification being into deterministic or random variation.

All real word inputs have some component of randomness or unpredictability thus deterministic inputs are always a simplification of reality, although they may be adequate for many purposes.

In general therefore common modelling application consider deterministic set of inputs as mathematical idealization of the actual set of inputs that the real object being studied might encounter. Deterministic models in general are those whose complete time history is explicitly given either by mathematical formulas or by tables of data. They are further divided in transient, periodic or “almost periodic”.

A transient input can have any desired shape but exists only for a certain time interval, being constant before and after the interval where it experiences the variation. These are adopted to study the response at sudden variation of significant inputs in models of a system which is usually considered to operate at stationary conditions.

Periodic input models repeat a certain waveform over the entire spam of time considered for simulation. This kind of input signals are proper for the representation of the operation of many periodic processes, as those that occur within an alternative engine operating at constant speed and fixed load.

Almost periodic input signals are continuous functions which are completely predictable but do not exhibit strict periodicity. They are of scarce interest for the analysis of energy systems.

On the other hand random inputs, in the most general form, could be an exact representation of the real world variables and are usually adopted when experimental data are used to run a mathematical model. This is the case for example of validation or identification processes. Random inputs in fact have time histories that cannot be determined mathematically before they occur and they have to be characterized either statistically or through the collection of empirical experimental data.

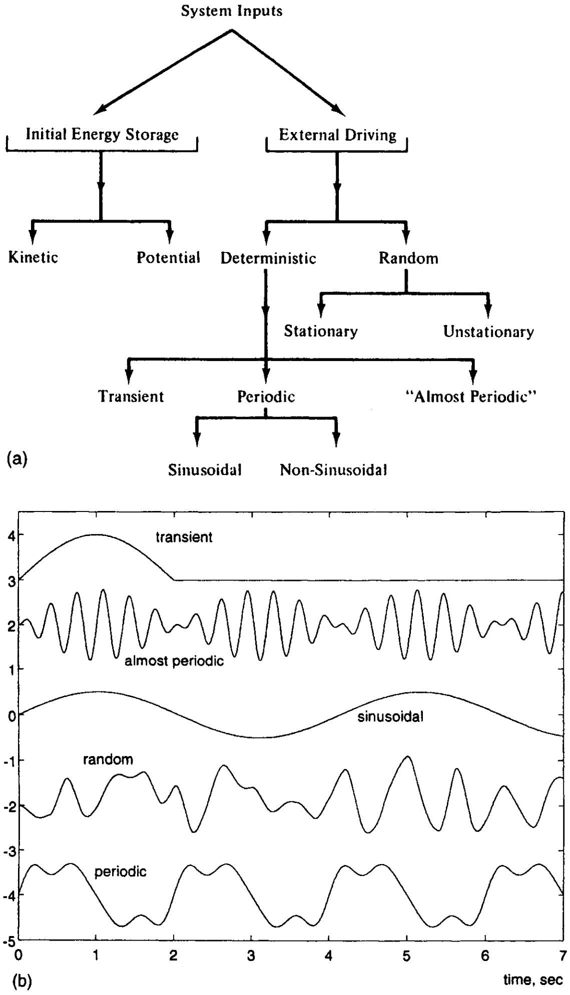

Fig. 2.2. Classification of model inputs.

2.2 Classification of models

There is not in literature a unique classification of the models that may be used for fluid system analysis. Here is provided the summary of some classifications criteria widely adopted, but may not be exhaustive.

In Tab. 2.1 some of the typical characteristics of a mathematical simulations model are reported hence determining different types of models that in turns are associated to different modelling techniques. Below are further discussed these characteristics.

Characteristic	**Modelling technique**
Existence of state parameters	State determined
	Not state determined
Time dependence	Stationary
	Dynamic
Geometry	3D, 2D, 1D, 0D
Type of mathematical correlations adopted	Black Box
	White Box

Tab. 2.1. Possible classification for models of fluid systems.

Existence of state parameters

The existence of a set of a state variables is a first and very discriminating difference among models. If a state vector exists a *state determined* model will be created otherwise a *not state determined* model is considered.

State determined models are usually characterized by the existence of a set of differential equations (expressed in terms of time derivatives of the state variables) and possibly a set of algebraic equations (that bound the other variables of the system to the state variables). The existence of time derivatives of the state variables allows to determine the value of the output variables as a function of the input variables and once known the value of state variables at an initial instant.

The component is therefore mathematically modeled by means of a system of differential equations (written in terms of the state variables) and algebraic equations (which links the other variables of the system to the state variables). In a general form this system of equation, in vector form, can be written as follows:

$$\begin{cases} \dot{\bar{X}}(t) = f(\bar{X}(t),\bar{U}(t)) & \text{State Equation} \\ \bar{Y}(t) = g(\bar{X}(t),\bar{U}(t)) & \text{Output Equation} \end{cases} \tag{2.1}$$

In general *f* and *g* functions can be nonlinear but in many applications of interest within the field of this Work they may be considered as linear functions and their coefficients can be called *static functions*

3, because whenever arguments $\bar{X}$ or $\bar{U}$ are known then the functions may be evaluated, that is the expressions for $\dot{\bar{X}}$ and $\bar{Y}$ are known.

In many applications the *f* and *g* functions as well as their coefficients do not change with time. In this case the system is stationary, and in the linear case the system is called *constant coefficient linear system*. More generally, the functions and their coefficients vary with time of simulation and in this case the system can be accounted for as *time-variable linear systems*. In such systems, one cannot evaluate the functions given only the values of $\bar{X}$ and $\bar{U}$ but the time must be also known.

In a state determined time-variable linear system therefore the values of output parameters at time *t* depend not only on the instantaneous values of input parameters, but also on the state of the system at that time instant, expressed by the State Equation. The state of the system at time *t* depends on the input values and on the time derivative of the state vector (Output Equation), which represent the dynamic behaviour of the system.

The State Equation has to be integrated in time in order to solve the state equation to give the output vector:

$$\bar{X}(t) = \bar{X}_0 + \int_{t_0}^{t} f\left(\bar{U}(t), \bar{X}(t)\right) dt \tag{2.2}$$

Eq.(2.2) shows how the values of the output vectors depend on the initial state of the system $\bar{X}_0$ and on the “history” of the system, i.e., its evolution through time, mathematically represented by the time integral of the State Equation.

Equation (2.2) poses problem of numerical integration when a *state determined* model is considered; in principle it is easy to compute how the system changes in a short interval of time Δt, using the concept of derivative directly. For example, if x is one of the state variables included in the state vector $\bar{X}$, the following can be written:

$$x\left(t_0 + \Delta t\right) = x\left(t_0\right) + \dot{x}\left(t_0\right) \Delta t \tag{2.3}$$

This equation can be easily recognized as an arrangement of the definition of derivative:

$$\dot{x} = \frac{dx}{dt} = \lim_{\Delta t \to 0} \left[\frac{x\left(t_0 + \Delta t\right) - x\left(t_0\right)}{\Delta t} \right] \tag{2.4}$$

in which Δt is small but finite. Since $\dot{x}(t_0)$ depends on the initial state and the inputs at the same instant which are known, one can use Eq. (2.3) to find the state at $t_0 + \Delta t$. This is also called *Euler’s formula* for integrating equations and it may be applied to all the state equations at $t = t_0$. It can be reapplied at $t = t_0 + \Delta t$ since the inputs are known at any time and after applying Eq. (2.3) at t_0, the state at $t_0 + \Delta t$ is then known. The equation may therefore be applied recursively to march the solution in time. This process can be readily adapted to automatic digital computation but it should be bore in mind that the result of such integration is correct only for $\Delta t \to 0$. As Δt is very small usually the approximation committed is very small and the result accurate, but it takes more steps and more evaluations of the functions to cover the time span of interest. A new issue then arises concerned with choosing the appropriate value of Δt that allows for generating a suitable solution in term of accuracy and number of iterations involved.

If no state variables are defined for the component under study a *not state determined* model is created and the output vector $\bar{Y}(t)$ at time t only depends on the value of the input vector $\bar{U}(t)$ at the same time instant, according to a purely algebraic equation in the form:

$$\bar{Y}(t) = h\left(\bar{U}(t)\right) \tag{2.5}$$

and in this case the dynamic behaviour of the component is neglected since no differential equations are introduced.

With reference to thermo-fluid systems it is possible to consider *state determined* models as those referring to physical systems where a mass energy or momentum storage is possible and hence conservation equations will be applied in differential form.

However, in the analysis of fluid systems a simple and immediate representation can be obtained by dividing the system input and output variables in two categories:

- Level Variables: in general they are differential variables provided by the fundamental equations that indicate the amount of thermodynamic extensive or intensive properties stored inside a component. They are an expression of the state variables in *state determined* systems;
- Flow Variables: they usually relate to fluxes of extensive properties through boundary surfaces or components and can be considered as outputs of *not state determined* systems.

Examples of level variables may be mass (either total mass or mass of individual components in a mixture), internal energy, or kinetic energy; flow variables may be mass flow rate or enthalpy flow rate.

Likewise, when modeling any physical system there are two main classes of objects that must be considered 4:

- Reservoirs: these components are characterized by one or more states that represent the "stored" amount of level variables;
- Flow Control Devices: they determine the amount of properties that flow through the component itself, typically as a result of differences between reservoir levels.

Reservoirs receive flow variables as inputs and their outputs are level variables. Conversely, flow control devices receive level variables and determine the flows associated. Fig. 2.3 briefly summarizes the concept. In general, every complex fluid system can be divided into elementary components. The number of these "lumps" can be evaluated in relation with the level of detail required. Since the presence of level variables is strictly connected with the order of the differential equations describing the model, a high number of reservoirs increases the model order and therefore its capability of representing fast dynamics of the system. However this is not always a convenient feature, because a differential equations set of elevated order usually generates numerical issues related to model stability. Moreover, if the reservoirs have different characteristic frequencies, stiffness problems will arise 5. For these reasons, a meaningful MVM (Mean Value Model) will contain only the minimum number of reservoirs that allows to account for the relevant dynamics of the system to be modelled, where *Mean Value Model* is usually intended a modelling approach based on dividing the system into several interconnected components and properly modeling the input/output time behaviour of each elementary component.

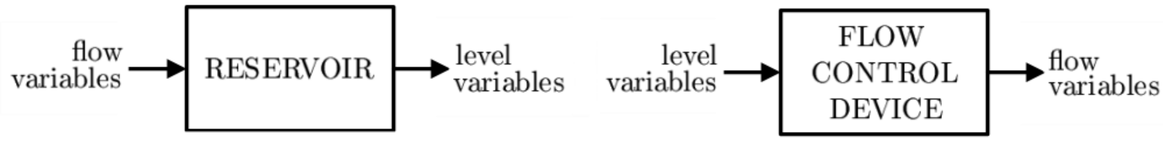

Fig. 2.3. Classification of system components and variables.

It is to be said that the definition of Mean value Models, while broadly used in literature, is sometimes used in different senses. The most general definition is that provided above and Mean Value Models are those where the general behaviour of a component is averaged upon some variable. For example considering just one thermodynamic state for a gas reservoir means recurring to a MVM where the real distribution of thermodynamic properties is neglected and just an average condition is considered. This definition is equivalent to that of 0D models (se below). The diction “Mean Value Model” is however often employed in internal combustion engines modeling meaning that the model considers only the lowest frequency phenomena that occur in the engine components neglecting the high frequencies. In this case the properties are averaged over several engine cycles: This is the case for example of assuming constant properties in the engine manifolds when the engine is running steady state since all the variations linked to the valves opening and closing are neglected.

Another issue characteristic of MVM is causality, a concept related to how the components forming the overall system are connected within the model 5.

In general, when two or more elementary blocks are assembled, it is necessary to respect the cause and effect priorities between the input and output signals of each block, otherwise the model will be affected by numerical problems called algebraic loops, under which the integration techniques fail to control the solution error or to converge.

The proposed classification criterion becomes useful in this context. The diagram resulting from the connection of reservoirs and flow control devices is named cause and effect diagram because it makes the relations between the components and the variables visible, allowing to immediately identify the driving and driven variables.

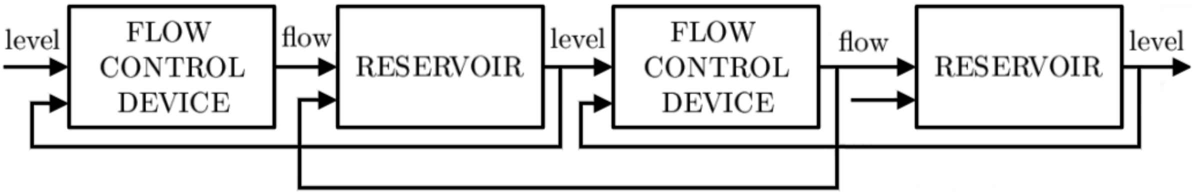

Fig. 2.4. Example of connection between *state determined* and *not state determined* components (reservoir and flow control devices).

Time dependence and geometry of the system

When referring to a physical *state determined* system the most general representation of a state variable considers its variation in space according to a three dimensional representation. The generic state variable Φ therefore may be expressed as function of a position vector $\vec{r} = (r_1; r_2; r_3)$ (the expression of $\vec{r}$ depends on the reference system chosen for the study e.g. Cartesian, spherical. etc.).

Also, being the analysis oriented to the study of the dynamic response, each system property at any given location will be a function time t. Therefore, the generic property Φ will be a function of four independent scalar variables **7**:

$$\Phi = \Phi\left(\vec{r},t\right) = \Phi\left(r_1,r_2,r_3,t\right) \tag{2.6}$$

From a macroscopic viewpoint, as it is usual in various fields of engineering, the matter is considered as a continuum, thus any property of a system varies continuously over space. Considering the relations between the properties and the geometry of the system, it is possible to distinguish between:

- 3D Models: when the parameters appearing in the system equations are functions of all the geometric coordinates of the reference system, namely:

$$\frac{\partial \Phi}{\partial r_1} \neq 0, \quad \frac{\partial \Phi}{\partial r_2} \neq 0, \quad \frac{\partial \Phi}{\partial r_3} \neq 0 \tag{2.7}$$

- 2D Models: when the parameters appearing in the system equations are functions of two geometric coordinates, for example:

$$\frac{\partial \Phi}{\partial r_1} \neq 0, \quad \frac{\partial \Phi}{\partial r_2} \neq 0, \quad \frac{\partial \Phi}{\partial r_3} = 0 \tag{2.8}$$

- 1D Models: when the parameters appearing in the system equations are functions of only one geometric coordinate:

$$\frac{\partial \Phi}{\partial r_1} \neq 0, \quad \frac{\partial \Phi}{\partial r_2} = 0, \quad \frac{\partial \Phi}{\partial r_3} = 0 \tag{2.9}$$

- 0D Models: when the parameters appearing in the system equations do not depend on the geometry of the system:

$$\frac{\partial \Phi}{\partial r_1} = 0, \quad \frac{\partial \Phi}{\partial r_2} = 0, \quad \frac{\partial \Phi}{\partial r_3} = 0 \tag{2.10}$$

In the last case the system properties are assumed to be uniformly distributed in the control volume.

It is immediately clear that the complexity of the fundamental equations is strictly related to the number of dimensions considered for the problem. Since the fundamental equations have been analytically solved only in a restricted number of cases, often with strong simplifications, a very important step in the construction of a model is to correctly determine the minimum number of dimensions that are meaningful for the analysis.

Another useful distinction can be made considering the dependence of the system properties on the time variable:

- Dynamic models: when the parameters appearing in the system equations are time functions (*state determined*):

$$\frac{\partial \Phi}{\partial t} \neq 0 \tag{2.11}$$

- Steady-State models: when the system parameters are not time dependent (*not state determined*):

$$\frac{\partial \Phi}{\partial t} = 0 \tag{2.12}$$

With reference to the time dependency a further category of models can be identified that is quasi-steady models.

In this case the behaviour in time of the actual system is represented as a sequence of steady conditions which can be identified by experimental parameters. When assessing experimental data that characterize a physical component these data are gathered once the component is at steady state conditions. These data may be aggregated together in the so called *characteristics curves*. When a model is based on experimental characteristics its behaviour at varying input is reduced to a sequence of steady state values. This representation of the time response is not strictly rigorous but may be utilized when the dynamic phenomena of the component represented as quasi-steady is much faster than the main dynamics of the other *state determined* components enclosed within the system. This approach leads to simple and fast models but their predictive capability is limited by the range of the data available and the specific setup considered.

In general all the parameters relevant to the study of fluid systems are dependent on time. However, certain kinds of analysis do not necessarily require this information, which can be neglected to simplify the model equations.

Another important criterion is related to the number of dimensions considered for the analysis. For example, to solve many practical applications it is necessary to give up the continuous medium scheme and deal instead with a discretized, or lumped, approach. Therefore the following two categories can be distinguished:

- Distributed-parameter models: the dependent variables are functions of more than one independent variable, yielding to partial differential equations; in this case the system is modelled as a “continuous” distribution of matter and energy.
- Lumped-parameter models: the dependent variables are functions of only one independent variable (often on time), allowing the fundamental equation to be written in the form of

nonlinear ordinary differential equations; in this case energy and matter are concentrated in discrete “lumps”

In general, most of the practical applications in system dynamics deal with lumped-parameter models. The reasons for this approach have to be found in the wide availability of techniques and mathematical tools that can be used to solve nonlinear ordinary differential equations. By applying suitable discretization techniques, it is possible to represent most of the meaningful dynamics of the systems with satisfying accuracy and limited computation effort. Indeed it should bore in mind that discretization techniques adopted for the creation of lumped models and to integrate the ordinary differential equation provide approximate numerical solutions, not analytical solutions, that therefore always contain errors and that solve only special cases, with specific numerical values of the parameters 2.

Although the distinction between lumped and distributed-parameter models can be made with reference to any of the independent variables ($r1$; $r2$; $r3$ or t), engineering applications commonly consider as lumped-parameter models only those that have no spatially dependent variables and are represented by ordinary differential equations. However, a further distinction can be made regarding how the time dependence is considered:

- Time-based models: the model is continuous with respect to time;
- Event-based models: the model parameters are not defined or not relevant at any time, but only in certain discrete instances.

Event-based models are required when the system behaviour associated with the signals sampling, or the delay caused by the timing relations of the components becomes important for the analysis. These models are also used for applications related to control design and implementation, since existing production controllers operate with discrete sampling times.

For example, in internal combustion engines the phenomena related to the flows into and out of the components (such as manifolds, valves, turbochargers etc.) are typically continuous, thus a time-based model would be suitable for the analysis. On the contrary, phenomena related to in-cylinder processes, like the indicated work per cycle or the flows through the intake and exhaust valves, are typically discontinuous due to the nature of the system. This behaviour introduces delays and timing relations for which an event-based approach is more appropriate.

Typically, the in-cylinder processes are studied with crank angle based models, where the crank angle replaces time t as the independent variable. An assumption commonly made is that the engine speed does not significantly change during one engine cycle. By consequence these models, although being defined in the crank angle domain, are formulated on the basis of constant sampling times.

On the other hand all of the most common components involved in energy conversion systems can be represented according to a time based modelling approach, especially if these components refer to power systems based on dynamical radial or axial machines (as turbines compressors and pumps) which by definition have no periodical behaviour.

Type of mathematical correlations adopted

Another significant distinction between models is concerned to the nature of the correlations adopted within the model in order to calculate the output or state variables (Eqs.(2.1) and (2.5)). Black box models are based either on empirical correlations or on data gathered from other models (often more complex). In black box models therefore the understanding and application of the physical correlations that characterise the phenomena is limited. A typical example of black box model is a model of a compressor or turbine based on characteristic maps. In these cases the fluid dynamic phenomena that control the flow within the component are ignored and the model is based on the data gather experimentally, thus the input/output correlation is merely empirical.

When a white box approach is used the correlations between the variables are derived from the conservation equations instead, hence the phenomena occurring are fully described in a rigorous physical way. White box models can be further divided in:

- thermodynamic models, based upon the conservation of energy and mass, on the state equation and on the equation describing the transformation. For this reason the variables usually considered are thermodynamic variables (i.e. pressure, temperature, specific volume etc…);
- fluid dynamic models: when also the cinematic variables (as for example velocity) are considered to describe the flow conditions within the system and the energy and mass conservation equation are no longer sufficient to describe the flow conditions and hence the momentum (or moment of momentum) equation must be also considered. These models are usually more complex than thermodynamic and require higher computational times.

In engineering practice it is not common to design models that are purely black-box or white-box, since most of the fluid systems can be described to a fairly large extent by applying the fundamental equations. With this procedure, grey-box models are obtained.

Grey-box models are developed from the fundamental conservation principles, hence the model structure is known. However, the system of differential and algebraic equations obtained will contain a certain number of unknown parameters, which can be estimated in a way similar to black-box models. This approach leads usually to relatively simple models which can grant a certain level of generalization at the same time. Since the equations are derived from the basic principles, the calibration process is focused only on the determination of few parameters starting from experimental data.

In the description of both white box or grey box thermodynamic models the following state variables might have to be calculated:

$$p,\ T,\ \rho,\ \overline{c}\ ,\ z$$

The knowledge of all these five parameters requires that five independent equation to be introduced and solved. These equations may be physical laws (mass conservation equation, energy conservation equation, momentum conservation equation) or equations describing characteristics of fluid or of the transformation occurring to the fluid within the fluid system (fluid equation of state, equation describing the process).

A brief description of these equations is provided below, with reference to a finite control volume *cv* of fluid with control surface *cs* fixed in space according to Euler’s approach [8].

To be noted that, of the mentioned equations, the momentum conservation equation is in vectorial form and in fact is employed when fluid dynamic problem arise hence the fluid velocity vector $\overline{c}$ has to be calculated.

Mass conservation equation

In its general form the equation states that the mass variation of the system equals the mass flow through the surface:

$$\int_{cv} \frac{\partial \rho}{\partial t} dV = -\oint_{cs} \rho \bar{c} \times \bar{n} dA \tag{2.13}$$

where in this case *ρ* is the local instantaneous mass density of the fluid crossing the elementary area *dA*. Since the unit vector *n*, normal to *dA*, is considered positive if oriented outward the control volume, the right hand side of equation (2.13) must be multiplied by a negative unit.

In steady state condition the net flow through the control surface is zero, hence the previous equation becomes:

$$-\oint_{cs} \rho \bar{c} \times \bar{n} dA = 0 = \int_{cv} \frac{\partial \rho}{\partial t} dV \tag{2.14}$$

Energy conservation equation

The energy conservation equation is the expression of the first law of thermodynamics for open or closed systems (systems capable of exchanging mass and/or energy).

The general form of energy conservation equation for open systems states that rate of change of the total energy of the system is equal to the difference between the rate of energy flowing into the system and the rate of energy flowing out of the system:

$$\Phi + \Pi = \int_{cv} \frac{\partial (e_t \rho)}{\partial t} dV + \oint_{cs} \rho e_t \bar{c} \times \bar{n} dA \tag{2.15}$$

where the total energy per unit mass e_t comprises the thermodynamic internal energy *u*, as well as the kinetic and potential energy. The latter includes all the forms of potential energy associated to conservative fields, such as gravitational or electrical; for fluid systems usually only the gravitational term is considered, hence *u* is given by:

$$e_t = u + \frac{c^2}{2} + gz \tag{2.16}$$

The terms *Φ* and *Π* in Eq. (2.15) represent instead the thermal flow and mechanical flow through the control surface respectively.

Momentum equation

The momentum equation, unlike the others, is not the result of a conservation principle but rather the application of Newton's second law of motion to an open thermodynamic system. Since the interest is in obtaining integral equations, the law is applied to the finite control volume *cv*. The outcome is a vector relation stating that the rate of change of the system momentum is equal to difference between the incoming and the outgoing rate of momentum flow and the sum of the external forces acting on the system:

$$\sum \overline{F} = \frac{\partial}{\partial t} \int_{cv} \rho \overline{c} dV + \oint_{cs} \rho \left(\overline{c} \times \overline{n} dA \right) \overline{c} \tag{2.17}$$

The term $\sum \overline{F}$ is the resultant of external forces applied to the fluid system, hence both body forces (proportional to mass) and surface forces (proportional to overall surface).

Moment of momentum

In dynamics useful information is often obtained by employing Newton's law of motion in the form where it applies to the moments of the forces; this is the case of turbomachinery analysis. For a system, the sum of the moments of external forces is equal to the time rate of change of moment of momentum. Applying the definition to a control volume the following vectorial expression for the moment of momentum can be derived:

$$\sum \overline{F} \times \overline{r} = \frac{\partial}{\partial t} \int_{cv} \left(\rho \overline{c} \times \overline{r} \right) dV + \oint_{cs} \rho \left(\overline{c} \times \overline{n} dA \right) \overline{c} \times \overline{r} \tag{2.18}$$

which states that the algebraic sum of moments is equal to the time rate of change of moment of momentum within the control volume plus the excess of outgoing flux of moment of momentum over the corresponding incoming flux.

State equation

The state equation is a *constitutive relation* that, differently to the conservation equations, whose validity is completely general, usually is strictly related to the fluid considered and involves its specific and intensive properties (or *field properties*), in the following form:

$$f\left(p,\rho,T \right) = 0 \tag{2.19}$$

Equation (2.19) assumes same simplified forms in special cases.

For perfect gases the state equations becomes:

$$\frac{p}{\rho} = RT \tag{2.20}$$

where R is the universal gas constant.

For the applications of interest within the present Work liquids may be considered perfectly uncompressible, hence the state equation assumes the form:

$$\rho = const. \tag{2.21}$$

More complicated is usually the definition of the state equation for vapours. The correlations that bound together the fluid properties are derived experimentally and provided in the form of tables or diagram as no theoretical correlation of general validity can be provided in this case.

Some fluid systems considered in this Work will involve liquid vapour phase changes hence the need to introduce the state equation for fluids in this very particular field.

The problem has been tackled by recurring to fluid properties databases where correlations between state parameters for fluids at saturation conditions or for superheated vapours and subccoled liquids are provided through correlations which validity is limited to a very strict field of state parameters and whose nature is purely empirical.

These databases of experimental data constitutes however, in fact, the state equations in those regions where the fluid can neither be considered a perfect gas or an ideal incompressible fluid.

Equation describing the process

This last set of equations mathematically expresses the way the fluid system undergoes a process, as in the following cases:

- isobaric: $p=const$
- isochor: $v=const$
- isothermal: $T=const$
- isoentropic: $s=const$
- etc.

For perfect gases under the hypothesis of reversibility, the general polytropic equation can be defined:

$$pv^m = const. \tag{2.22}$$

Particularly, since a general real transformation involving a gas (as for example a compression or expansion) cannot be defined mathematically but usually only thermodynamic conditions at the beginning (*state 1*) and end (*state 2*) of simulation are known, the exponent m can be calculated being the only unknown in the following equation:

$$p_1 v_1^{\ m} = p_2 v_2^{\ m} \tag{2.23}$$

In many applications the exponent m calculated according to Eq. (2.23) provides a reasonable enough representation of the real process.

It should also be noted that the exponent m of the general Eq. (2.22) assumes some notable values for the most significative transformations that the perfect gas can undergo:

- $m=1$ for isothermal processes;
- $m=0$ for isobaric processes;
- $m=\infty$ for isochor processes;
- $m=k=c_p/c_v$ for adiabatic-reversible (hence isoentropic) processes.

2.3 Survey of available codes for fluid systems modeling.

Prior to starting the work of accurate modelling of components of energy systems, an analysis has been conducted in order to determine available commercial softwares that might have been employed as tools for the modelling process. Other computer based models within the field of energy conversion system available in the open literature have also been surveyed.

The analysis has brought to identify some software that may appear to be proper for the scope. The softwares considered are Matlab®/Simulink®, AMESim®, Trnsys® Modelica® and GateCycle®. To be noted that the analysis of commercial softwares reported here is neither complete nor exhaustive but is limited to those packages that have been reckoned to apply for the Work. These softwares have been utilized in these years of activity in order to gather a deeper understanding of their characteristics and a brief description is provided herein.

Some of these software like GateCycle® and Trnsys®, while appropriate for some applications turned out to be improper for the scope of the work, as further discussed.

AMESim®, Modelica® and Matlab®/Simulink® feature some common characteristics that would make them all suitable for the development of custom dynamic components in the field of energy systems, for control purposes and for optimization procedures.

The existence of other models already built in the Matlab® environment, and the higher confidence with the Matlab® language and its embedded function for implementation of proper model routines, has at the end brought to the choice of this language for the development of the models described within this Work even though AMESim® and Modelica® can be assumed as a valid alternative to be further assessed in future developments of the Work.

2.3.1 Matlab®/Simulink®

Matlab® is a high-performance language for technical computing; the name Matlab® stands for matrix laboratory. The Matlab® language is a high-level matrix/array language with control flow statements, functions, data structures, input/output, and object-oriented programming features.

Matlab®/Simulink® is a general purpose software package for dynamic systems which is well known among the control community as it offers excellent performance qualities for designing regulation algorithms and this makes it an ideal candidate when it is required that both the process and control engineers can work with the same software package.

Matlab® integrates computation, visualization, and programming in an easy-to-use environment where problems and solutions are expressed in familiar mathematical notation. Typical uses include:

- math and computation;
- algorithm development;
- data acquisition;
- modeling, simulation, and prototyping;
- data analysis, exploration, and visualization;
- scientific and engineering graphics;

- application development, including graphical user interface building.

Matlab® is an interactive system whose basic data element is an array and this allows to solve many technical computing problems, especially those with matrix and vector formulations. Matlab® also has an extensive collection of precompiled computational algorithms ranging from elementary functions, like sum, sine, cosine, and complex arithmetic, to more sophisticated functions like matrix inverse, matrix eigenvalues, Bessel functions, and fast Fourier transforms, Newton-Raphson procedures to solve non linear systems and others.

One of the key features of Matlab® is also its graphical capabilities thank to extensive facilities for displaying vectors and matrices as graphs, as well as annotating and printing these graphs. It includes high-level functions for two-dimensional and three-dimensional data visualization, image processing, animation, and presentation graphics. It also includes low-level functions that allow you to fully customize the appearance of graphics as well as to build complete graphical user interfaces of the Matlab® applications.

Also Matlab® has useful external interfaces that allows to write and run C and Fortran® programs that interact with Matlab®. It includes facilities for calling routines from Matlab® (dynamic linking), calling Matlab® as a computational engine, and for reading and writing MAT-files

The mathematichal capabilities of Matlab® are enhanced with Simulink® that is an icon based environment for modeling, simulating, and analyzing dynamic systems. It supports linear and nonlinear systems, modeled in continuous time, sampled time, or a hybrid of the two. Systems can also be multirate, i.e., have different parts that are sampled or updated at different rates.

Simulink® includes a comprehensive block library of sinks, sources, linear and nonlinear components, and connectors. Its capabilities can be further improved by using *S-function*, which allows executing specific function written in C++®, Ada®, Fortran® or the Matlab® language while Simulink® is performing the simulation of a system, thus determining an equation based modeling approach. This peculiarity allows creating customized blocks with high degree of mathematical complexity, which would not be achieved when using only Simulink® custom blocks.

For modeling, Simulink® provides a graphical user interface (GUI) for building models as block diagrams, using click-and-drag mouse operations. Models are hierarchical, so it is possible to build models using both top-down and bottom-up approaches and it is possible to have view of the system at a high level, then double-click blocks to go down through the levels to see increasing levels of model detail.

This approach provides insight into how a model is organized and how its parts interact. When a model is defined, it can be simulated using a choice of integration methods, either from the Simulink® menus or by entering commands in the Matlab® Command Window. Using scopes and other display blocks, one can see the simulation results while the simulation is running. The simulation results can be put in the Matlab® workspace for postprocessing and visualization. Model analysis tools include linearization and trimming tools, which can be accessed from the Matlab® command line, plus the many tools in Matlab® and its application toolboxes. And because Matlab® and Simulink® are integrated, one can simulate, analyze, and revise models in either environment at any point.

Application of the Matlab® language code and its integration with the Simulink® enviromnet and examples of hierarchical and complex dynamic Simulink® models will be provided in the next Chapters where some of the capabilities of the software will be applied in order to create the desired models of components considered in the analysis of energy systems.

2.3.2 Trnsys®

Trnsys® is a simulation program primarily used in the fields of renewable energy engineering and building simulation for passive as well as active solar design. Trnsys® is a commercial software package developed at the University of Wisconsin. One of its original applications was to perform dynamic simulation of the behaviour of a solar hot water system for a typical meteorological year so that the long-term cost savings of such a system could be ascertained. Trnsys® is a transient systems simulation program with a modular structure. It recognizes a system description language in which the user specifies the components that constitute the system and the manner in which they are connected.

The DLL-based architecture allows users and third-party developers to easily add custom component models, using all common programming languages (C, C++, Pascal®, Fortran®, etc.). In addition, Trnsys® can be easily connected to many other applications, for pre- or postprocessing or through interactive calls during the simulation (e.g. Microsoft Excel®, Matlab®, Comis®, etc.).

The Trnsys® library includes many of the components commonly found in thermal and electrical energy systems, as well as component routines to handle input of weather data or other time-dependent forcing functions and output of simulation results. The modular nature of Trnsys® gives the program high flexibility, and facilitates the addition to the program of mathematical models not included in the standard Trnsys® library. Trnsys® in fact offers the possibility to the user to include own components written in Fortran® and translated with the Compaq Visual Fortran® compiler 6.6 or the Intel Visual Fortran® compiler.

Trnsys® is devoted to analyses of systems whose behaviour is dependent on the passage of time, in the scale of hours days or multiples. Main applications of the software include: solar systems (solar thermal and photovoltaic systems), low energy buildings and HVAC systems, renewable energy systems, cogeneration, fuel cells.

It is often used to assess new energy concepts, from simple solar domestic hot water systems to the design and simulation of buildings and their equipment, including control strategies, occupant behavior, alternative energy systems.

The simulation engine is programmed in Fortran and is called by an executable program, TRNExe, which also implements the online plotter which is used to visualize the time pattern of the signals of interest.

The Trnsys® package includes:

- The Simulation Studio: a graphical front-end that houses all aspects of the Trnsys® simulation procedure;
- TRNEdit: a specialized solution for turning the simulation into a stand alone, distributable application;
- TRNBuild: a graphical input program for describing multizone buildings;
- FORTRAN source code for all components used by Trnsys® (except Type 56 – Multizone Building Model).

A Trnsys® project is typically setup by connecting components graphically in the Simulation Studio. Each Type of component is described by a mathematical model in the Trnsys® simulation engine and has a set of matching Proforma's in the Simulation Studio: the proforma has a black-box description of a component: inputs, outputs, parameters, etc. The Simulation Studio generates a text input file for the Trnsys® simulation engine: that input file is referred to as the deck file.

The simulation engine is programmed in Fortran and the source is distributed and accessible. The engine is compiled into a Windows Dynamic Link Library (DLL), TRNDll. The Trnsys® kernel reads all the information on the simulation (which components are used and how they are connected) in the Trnsys® input file, known as the deck file (*.dck). It also opens additional input files (e.g. weather data) and creates output files.

The simulation engine is called by an executable program, TRNExe, which also implements the online plotter, a very useful tool that allows to view output variables during a simulation.

The Trnsys® type 56 also turns to be really useful in order to assess the thermal and cooling loads of a building of known features and despite the implementation is not always intuitive it comes out to be extremely useful because of the capability to be easily coupled to energy conversion system and the steams of hot/cold fluids can be passed from the block representing the heating/cooling devices to the building.

The Trnsys® software package has been used within few application in the field of energy systems [10-12]. It has been found that the software turns to be quite flexible and feasible for overall evaluations of energy networks and consequent economic analyses of different practical solutions to be analyzed, especially in the long time range (i.e. one year of simulation).

Fig. 2.5 for example reports the Trnsys® Simulation Studio interface of a system where a residential building has been modelled recurring to the type 56 component and different lay-outs have been considered for serving the heating/cooling demands. In the reported example a ground source heat pump system based on geothermal loops is considered for both heating and cooling purposes.

The model indeed produced some overall representation in the year behaviour of the complete system but the features of the components do not allow a deep insight of the characteristics of the different energy conversion systems, as the heat pump in this case.

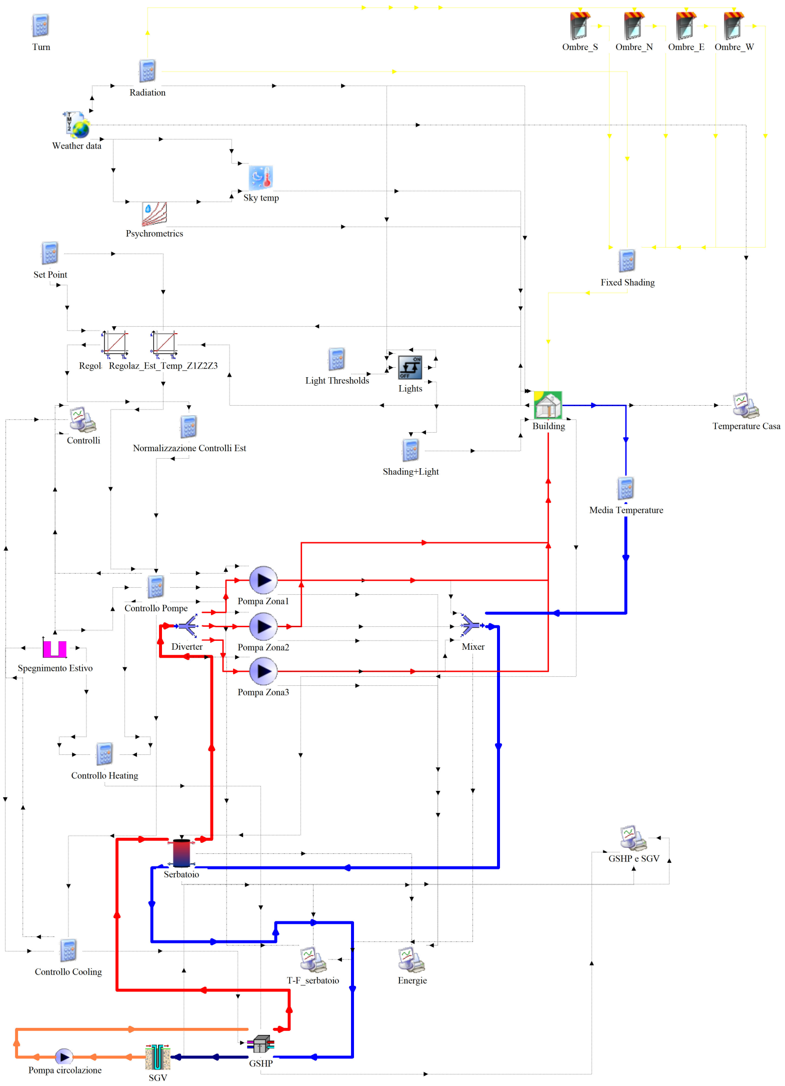

Fig. 2.5.Trnsys® model of a ground source heat pump heating/cooling system [12]**.**

Despite its extreme flexibility Trnsys® displays some limits with some components of the standard libraries. A simple topic as a cogeneration plant applied to the tertiary sector placed some difficulties because of limitations in the maximum allowed size of the engine units [10]. Also the mathematical model upon which some models are created, if proper for an overall representation of the performance of the component on montly-yearly based periods, seems quite poor. Taking again as example the model of cogenerator, it is simply based on a generic characteristic curve that describes the mechanical power generated with respect to the actual fuel consumption. The model proposed is based upon the Willans line method, approach that has been also followed by the research group for overall analysis of the yearly performances of a cogenerator applied to the University of Parma campus through a simple *m-code* script [13,14]. The model therefore is purely algebraic black-box and do not allow any understanding of the possible interaction of the engine with other componensts or does not take into account of dependency in the performances from external factors as air inlet temperature, it also does not allow to assess dynamic responses.

Another aspect to be considered is that Trnsys® standard libraries are more focused on HVAC systems for building applications rather than for power generating systems, which are the focus of the present work.

Trnsys®, while being a good tool for assessing the long term overall energy fluxes that involve heating and cooling applications to building systems, does not however appear to be the proper tool when it comes to component design and also the libraries available are not indicated for power systems design, which is the main topic of interest for the present work.

2.3.3 AMESim®

AMESim® stands for Advanced Modeling Environment for performing Simulations of engineering systems.

Main features and applications of the programme are:

- analyze the functional performance of intelligent systems from the early development stage onwards;
- optimize the complex interaction between mechanical, hydraulic, pneumatic, thermal and electric/electronic systems before prototype testing;
- pro-actively engineer a design’s critical functions and improve overall product performance and quality;
- avoid design flaws, explore innovative designs and accelerate product development.

The software has the typical feature of an icon based program and engineering systems can be built by adding symbols or icons to a drawing area. AMESim® therefore enables users to build complex multi-domain system models through an interactive graphical interface. The resulting sketch is easily understandable and offers a logic representation of the system model under investigation. When the sketch is complete, a simulation of the system proceeds in the following stages:

- mathematical descriptions of components are associated with the icons;
- the features of the components are set;
- a simulation run is initiated;
- graphs are plotted to interpret the system behaviour.

Particularly, the modeling of a system is done in four steps:

- *sketch* mode: in which the different components are linked;
- *submodel* mode: in which the physical submodel associated to each component are chosen;
- *parameter* mode: in which the parameters for each submodel are chosen;
- *run* mode: in which the simulation is started.

In doing so AMESim® refers to the set of equations defining the dynamic behaviour of the engineering system and its implementation as computer code that is the model of the system. The model is built up from equations and corresponding code is referred to as submodels. Once all the procedure for creating the model of a physical system is completed, AMESim® through the use of a proper compiler, produces the executable file of the system and produces a .exe file to run the simulation.

Two compilers may be used with AMESim®: Microsoft® Visual C++ and the GCC compiler. GCC is under the GNU general public license.

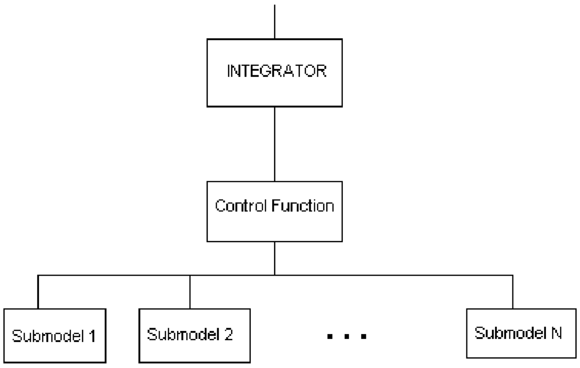

Fig. 2.6. The structure of an AMESim simulation program.

When a simulation using AMESim® is performed, computer code is generated which is specific for the engineering system created. At the core of AMESim® is an integration algorithm, which advances the solution through time. This integration algorithm calls the submodels, which are associated with the components of the system, as shown in Fig. 2.6. These submodels may have been selected by AMESim® automatically or selected manually by the user. In either cases there will be computer code, which implements the mathematical equations on which the submodel is based. The order in which the submodels are called is not normally the same as the order in which the corresponding components were added to the sketch. The submodels are sorted into an order that is more efficient from a computational point of view.

During a simulation some quantities change with time. Typical examples are the pressure in a pipe and the rotary speed of a load. These quantities are called variables. Sometimes in a particular simulation, they are constant but, since in principle they could vary with time, they are still called variables. Other quantities are always fixed during a simulation run. These are called parameters and these quantities normally indicate a size or dimension of a component. Examples are the diameter of a pipe and mass of a body connected to a spring.

AMESim® delivers a 1D simulation platform which addresses multiple domains in an integrated simulation process and accurately predicts the multi-disciplinary performance of intelligent systems. The components of the model are described by analytical models representing the hydraulic, pneumatic, electric or mechanical behavior of the system. Dedicated libraries and application-specific solutions eliminate the need for extensive modeling and deliver simulation capabilities to assess the behavior of specific subsystems in multiple physical domains.

Therefore, to create the system simulation model AMESim, the user can access to a large set of validated libraries of pre-defined components from different physical domains such as fluid, thermal, mechanical, electromechanical, powertrain and many others. The software creates a physics based model of the system, which does not require a full 3D geometry representation. This approach gives AMESim the capability to simulate the behavior of intelligent systems long before detailed CAD geometry becomes available.

Among the many standard libraries provided, the following embody components that may result of interest for the applications considered in the present work:

- Internal Combustion Engine Solutions: this library, developed by French research center IFP, allows users to model and design comprehensive engine systems based on physics-based model components, from air management and combustion up to ECU calibration. These provide a flexible environment for designing and optimizing “virtual” engines and the couplings with subsystems for fuel injection, fuel diversification, thermal management (i.e. for cogeneration purposes), etc. can be studied.
- Thermal Management Solutions: provide dedicated component libraries to build and analyze complete thermal management models in a single environment. The solutions enable the processing of real transient, multi-domain simulations and the handling of heat management scenarios. The Thermal Management Solutions give engineers access to detailed models of sub-systems in vehicle thermal management systems (engine cooling systems, air-conditioning, lubrication system, etc.). This enables them to accurately define and size components, and to study the overall system integration and the interactions between subsystems.
- Fluids Systems Solutions: Using physics-based simulation, the Fluids Systems Solutions enable engineers to design complete fluids hydraulic and pneumatic systems, from the sources (e.g. the fuel tank) to the consumers (e.g. actuators) up to the fluid network.
- Energy Systems: Energy Systems Solutions provide advanced libraries and toolsets to handle specific thermodynamic applications, like aerospace propulsion and pyrotechnics, fuel cells and batteries. The solution come with a set of specific tools and libraries dedicated to thermodynamics, gas mixtures, fluid properties, thermochemistry, and compressible flows.

When custom blocks are required for specific applications AMESet provides a set of tools to extend the standard AMESim® libraries of components. AMESet in fact is designed to assist users in writing standardized, reusable and easily maintainable libraries of component models that are fully compatible with the existing AMESim® models and are automatically usable on each supported platform.

Producing new submodels involves writing code that must be in the correct format to allow AMESim® to call it. AMESim® submodels must be written either in the programming language Fortran 77 or C. A specific tool is also provided in order to help the user compiling and debugging the source code to meet the AMESim® syntax requirements.

To be also noted that AMESim® offers extensive interfaces with third-party software tools for control, real-time simulation, multi-body simulation, process integration and design optimization. Of particular interest for the scope of present Work is the capability of interface AMESim with Matlab scripting language or to Simulink® for control applications.

For example it is possible to use Matlab® for the control of simulation experiments of an AMESim® model. Batch simulations can also be performed from Matlab® where specific scripts can allow producing series simulations of AMESim® model with a set of predefined design parameters. Other possible usage includes more advanced sensitivity analysis, optimization of parameters in the simulation model, etc.

The AMESim® integrators provided can be divided into two types:

- variable step, variable order methods with control of errors;
- fixed step, fixed order methods with no error control.

Fixed step fixed order methods are much less robust and flexible than the variable step variable order methods. The equations governing the model must be explicit in this case. In other words there must be no constraints or implicit state variables.

Common problems that may arise during simulation of engineering systems are stiffness or due to discontinuities. A stiff problem is one in which there is a time constant which is extremely small compared to the simulation time range.

Another common problem is discontinuities. These are points at which there is a switch from a set of one or more governing equation(s) to another completely different set.

AMESim® has developed specific procedures to tackle these problems during the integration of the solving differential equations.

Simple Runge-Kutta algorithms commonly adopted are relatively tolerant of discontinuities and can perform well on some problems but they are very unsuitable for stiff problems. However, many simulations are performed on stiff problems rich in discontinuities using these methods. The standard AMESim® integrator does not give the user a choice of integration algorithm. Instead the characteristics of the equations governing the model are used to select automatically the most appropriate algorithm. If the model contains any implicit variables the differential algebraic equation integration algorithm (DASSL) is used otherwise the ordinary differential equation integration algorithm (LSODA) is used.

AMESim® is therefore a general, multi-purpose icon based software which encloses some very advanced tools as optimization, linearization, customization and proper solution integration that allow great flexibility and significant simulation potentials.

In Fig. 2.7 The AMESim® model of a CI ICE is presented. The model has been created by gathering different components representing the different parts of the real engine (turbocharger, manifolds, combustion chamber, injectors, etc ...) coming from the Authors own developed AMESim® Engine Library (IFP-ENGINE library [17]), which is now part of the AMESim® environment. This engine-dedicated library allows computing a complete virtual engine with a characteristic time-scale of the order of the crank angle. In each component, a 0D/1D model dedicated to the physical phenomena at stake is used, the aim being to perform simulations with particular respect to the dual mode combustion (conventional and HCCI). For this reason the combustion model is one of the most important sub-models and the 0D sub-model developed in the standard IFP-engine library, based on Chmela's model, and has been considered with specific additional developments by the Authors; particularly the standard model was modified in order to take into account both auto-ignition delay and pre-mixed/cold flame combustion. This phenomenological model is a dual mode combustion model, that is to say it is able to represent both HCCI and conventional combustion.

Such a model needs to be calibrated, so its parameters need to be estimated in order to obtain the best behaviour possible of the model when confronted with a wide range of operating conditions. Given the high number of parameters to estimate the calibration procedure is very time consuming and complex. An automatic calibration tool, dedicated to the enhancement of phenomenological modelling of Diesel combustion therefore has been developed capable of dialoguing with the AMESim® based engine model.

This example of application of the AMESim® standard libraries, with custom components where some modifications have been introduced in order to be able to take into proper account of certain phenomena of interest, demonstrates the significant capabilities of the software suggesting therefore that the software might have been an appropriate tool, alternative to Matlab®/Simulink® for the development of the energy systems models proposed within the present work.

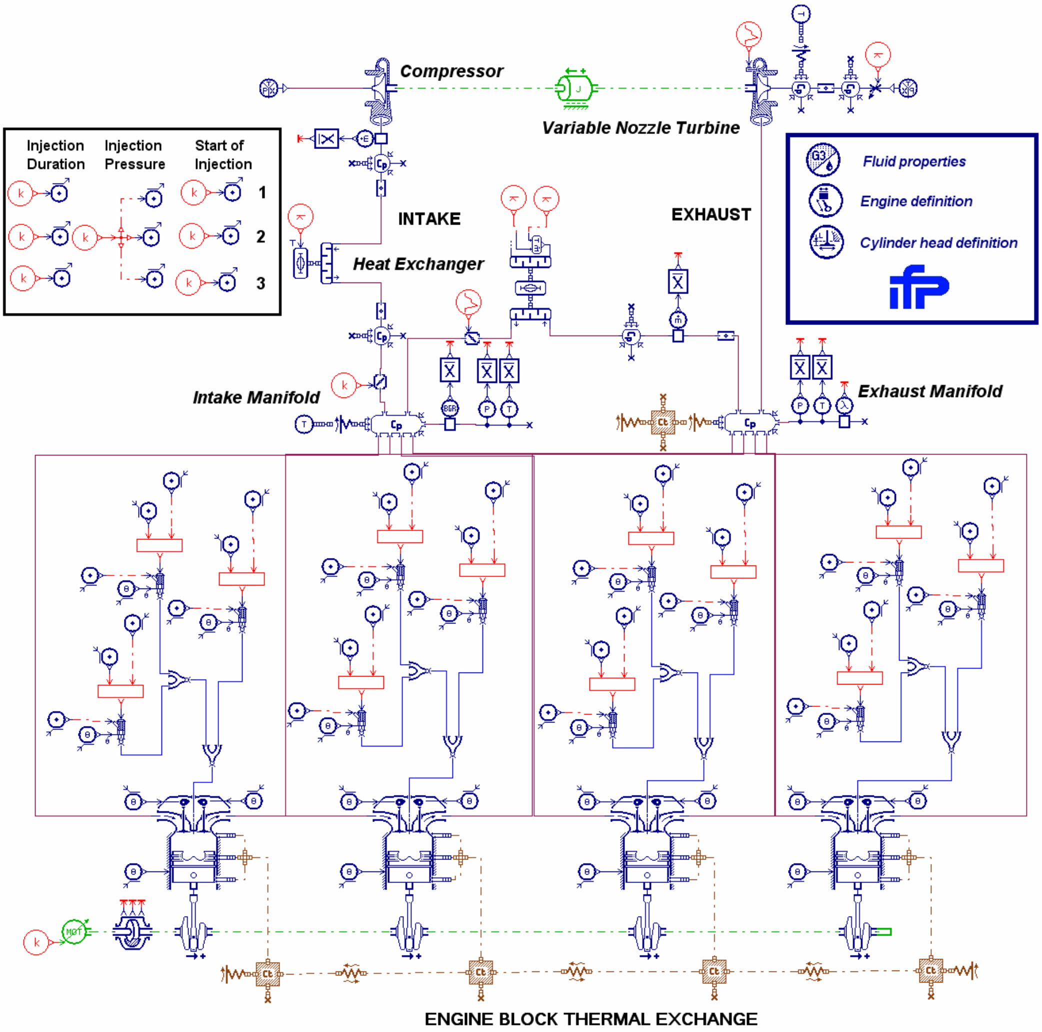

Fig. 2.7. Turbocharged automotive Diesel engine model in AMESim® [17].

2.3.4 Modelica®

Modelica® is an object-oriented modelling language to model large, complex and heterogeneous physical systems. The language is designed for convenient, component- oriented modelling of physical multi-domain systems. A basic design idea of modelling with Modelica® is that it can be utilised in a similar way as an engineer builds a real system: first trying to find standard components like compressor and heat exchanger from manufacturers' catalogues with appropriate specifications and interfaces [15].

Only if a particular subsystem does not exist, a component model would be newly constructed based on standardised interfaces.

The manufacturers' catalogues are represented as a collection of components to be used together in Modelica® by libraries.

The models in Modelica® are mathematically described by differential, algebraic and discrete equations. This means that no particular variable needs to be solved for manually. A Modelica® tool will have enough information to decide that automatically by the causality between components in a complete physical system. Therefore, models in Modelica® do not pre-define the computational causality. This leads to better reusability of the developed models because they contain fewer assumption about the context of their use. The causality between components of a system model is determined by special algorithm. In Modelica® connectors are used to specify the interaction between components.

Therefore, a connector should contain all quantities needed to describe the interaction. The connector variables can be characterised as across and through (resp. flow) variables; the across variables represent the driving force across a component e.g. pressure in a thermohydraulic network, whereas through variables represent the quantities flowing through a component like the flow rate. The through variables sum to zero at a node (resp. connector) and are declared by the prefix flow. So, the application of the sum-to-zero equations of conservation laws results in additional equations determining the overall system equations. They are formulated in all physical domains, e.g. Kirchhoff's law, Newton's law.

As mentioned above the reuse of models is possible as well as a hierarchical structure of models due to the fact that Modelica® is an object-oriented language. The ability of reuse (by inheritance and aggregation), hierarchical decomposition and model exchange enables the handling of complexity in an advantageous way. Furthermore Modelica® supports arrays, the handling of time and state events and the use of external C- and FORTRAN-functions.

For the utilisation of the Modelica® language, a Modelica® translator is needed to transform a Modelica® model into a Differential Algebraic Equation (DAE) system with a fixed causality. Therefore, symbolic transformation algorithms have to be applied to transform the equations into a form which can be integrated with standard methods.

These transformation algorithms and solvers are available in two commercial simulation environments, Dymola® and MathModelica®. Both simulation environments include a graphical user interface (GUI) for model editing and browsing, Modelica® translator, simulation engine and visualisation of results. Dymola, provides some more features like a convenient interfaces to Matlab®/Simulink® and the ability of hardware-in-the-loop simulation.

The free Modelica® language is developed by the non-profit Modelica® Association. The goal of the OpenModelica project is to create complete Modelica® modeling, compilation and simulation environment based on free software distributed in source code form intended for research purposes.

In [16] the results of the development of a Modelica® library for CO2-refrigeration systems based on the free Modelica® library ThermoFluid. The development of the library is carried out in a research project of Airbus Deutschland and the TUHH by the Authors and is focused on the aim to obtain a library for detailed numerical investigations of refrigeration systems with the rediscovered refrigerant carbon dioxide (CO_2). With the developed library components a CO_2 refrigeration cycle has been realized (Fig. 2.8). The developed model can be used for the optimisation of specific heat exchangers, for the evaluating of an optimal system configuration and for the layout and optimisation of the system control.

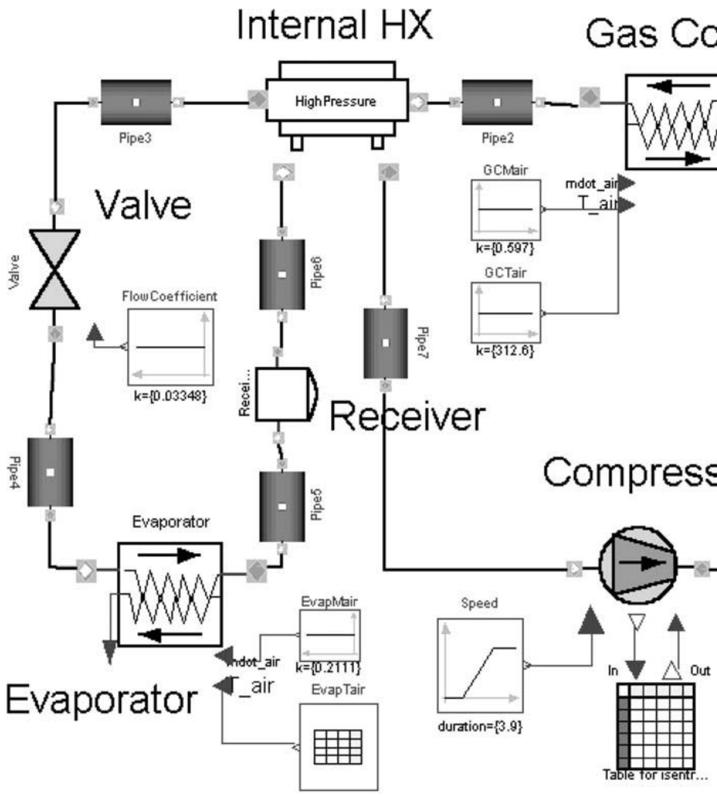

Fig. 2.8. Modelica object diagram of a CO2 cooling cycle.

2.3.5 Gate cycle®

GateCycle® is a commercial heat balance software used to predict design and off-design thermodynamic performances of combined cycles, fossil boiler plants, cogeneration systems, combined heat-and-power plants, advanced gas turbine cycles, and many other energy systems. The software has a graphical interface and a wide library of components and auxiliaries typical of energy power units.

The software first appeared in 1981 and its development is carried on by GE Enter Software, a General electric Power Systems fully owned company. The database therefore features a wide set of GE components.

GateCycle® is specifically designed to perform a large variety of analyses, such as:

- analyzing an overall cycle for a proposed power system or cogeneration station. This analysis produces information on operating performance at all the state points throughout the plant, including overall cycle efficiency and power.
- simulating the performance of existing systems at design and "offdesign" operating conditions.
- predicting the effect of proposed changes or enhancements to existing plants.
- analyzing advanced gas turbine designs, including designs that are fully integrated with the steam/water cycle.
- design new equipment around existing equipment, as in repowered plants or for plant modification.

- mix and match existing compressors and turbines in advanced turbomachinery studies.

The software therefore appears as a tool strongly oriented to advanced analysis of power plants.

To build a model components are selected from the equipment list and dropped on to the model diagram. The process of building a model is typical of an icon based software and includes the dragging and dropping in the working environment of the main components of the plant, properly connecting the i/o ports and providing each component with a set of functional parameters. This last step appears to be one of the most problematic since a wide range of data are required for a correct identification of the component. These data may not always be easily available or accessible, especially when designing "unconventional" units or for pre-feasibility studies when specific data sets of the components are still not available. This requires placing strong hypothesis or even guessing many of the parameters required.

Once everything is properly settled the program proceeds to calculate the steady state operating conditions compatible whit the boundary conditions imposed. Solution of the system is mathematically provided through an iterative process. The model will iterate through all of the equipment icons in the model until all energy and flow streams converge. This is achieved by calculating balance equations at each component while convergence is searched. The degrees of freedom for the software to find the solution are the characteristics dimensions of the components enclosed within the system. The software therefore designs all the main components of the system in such way to satisfy the imposed boundary conditions and required streams and to maximize the actual cycle efficiency. Design (or reference) cases therefore establish the operating characteristics (e.g. steam turbine design efficiency) and physical specifications (heat exchanger size) of key GateCycle equipment icons.

When an off design calculation is required the same optimal geometry calculated for on design conditions is kept and the cycle parameters are calculated for the new set of boundary conditions of streams.

The model therefore produces only a singular equilibrium point of operation for the given configuration of the plant proposed and results contain the state parameters of each component at steady rated conditions. By changing some of the parameters or the configuration new results can be obtained that describe the performances under steady state off design operating conditions. Results are provided in tabular form.

The GateCycle® Graphical User Interface (GUI) enables easy building of any cycle and gives the user an almost unlimited flexibility in modeling and in displaying the calculation results [18]. A GateCycle® model can be created by drawing the desired cycle configuration on the screen using the necessary equipment selected from a graphical menu of icon representations.

After the equipment icons have been positioned on the cycle diagram, the connections between the equipment icons can be drawn. The graphical tools provided with the ProVision interface automatically route the connecting streams on the diagram. Logic is provided in the connection procedures to ensure that all of the ports on each equipment icon are properly connected.

In the example that follows [19] a steam power plant has been considered with a biomass fired boiler. The designed plant is represented through the GateCycle® main operating window in Fig. 2.9. Off design conditions may evaluate changes in the actual fuel composition and changes in the environment temperature and humidity.

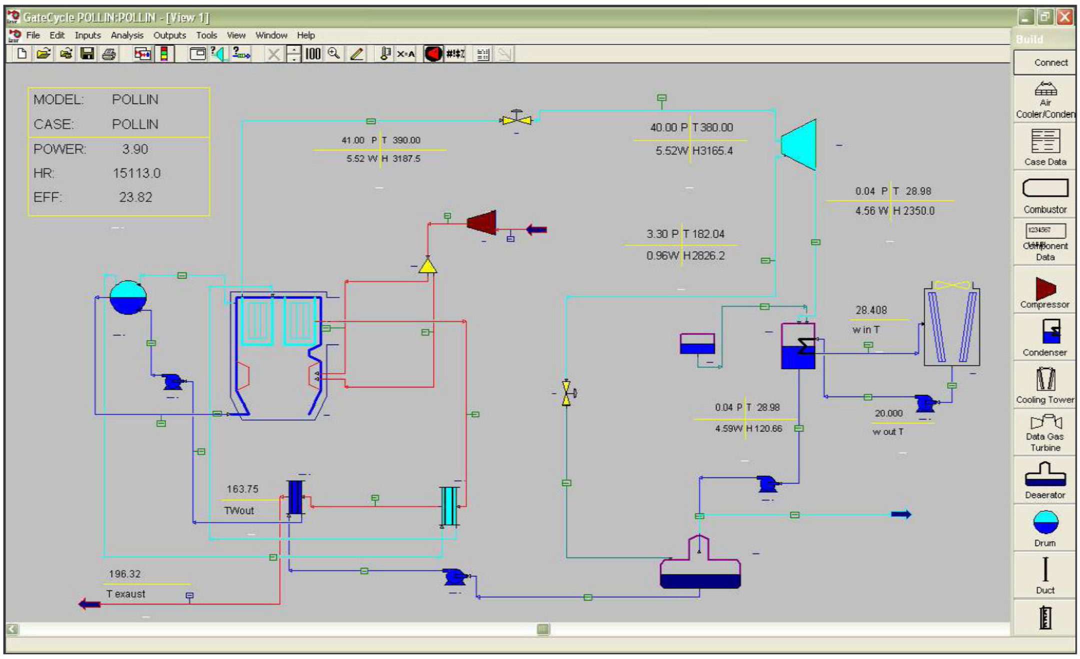

MODEL: POLLIN
CASE: POLLIN
POWER: 3.90
HR: 15113.0
EFF: 23.82

Fig. 2.9. GateCycle® model of a biomass fired steam power unit [19]**.**

Upon execution of the analysis module, the code first reads the connection and equipment icon data from the diagram and database. Next, the GateCycle® code analyzes the connection data to determine the order of calculation for the equipment icons, a procedure known as 'flowsheet decomposition'. This procedure ensures that each equipment icon is included in the calculations and that the order selected will allow the iterative calculations to converge rapidly.

After determining the layout of the plant, the code reads in the system, equipment icon and macro data from the database. It checks for errors in the input values, sets defaults if necessary, and then continues on if no major errors have been found. The code then finds where pressures and flow rates are specified in the system, and checks whether these specifications are consistent throughout the cycle. The GateCycle® code then proceeds to analyze the performance of the system by calling the appropriate equipment model routines one at a time in the order determined by the flowsheet decomposition procedure. After execution of each equipment model, the output data from that equipment icon is passed to all connected equipment icons. One system iteration is completed when all of the equipment models in the cycle have been executed. Macros are called where appropriate, depending on how they have been set up.

At the end of each system iteration, the GateCycle code uses a number of different criteria to determine if the model calculations have converged. First, the calculated output variables from each of the equipment icons must match the values from the previous system iteration within some numerical tolerance. Second, there must be a mass and energy balance around each of the equipment icons in the model and around the system as a whole; this calculation is possible since only steady state operation is possible then nor energy or mass storage has to be accounted for. Finally, the data for every outlet port must equal the data at the connected inlet port within the error tolerance. If there are macros in the model, they must also have converged within their specified tolerance. A typical GateCycle® run will converge within two to forty system iterations, depending upon the complexity of the cycle being modeled, the convergence tolerances selected, the number and complexity of the macros, and the accuracy of the initial values in the database.

The software output is a report which contains the main figures of the system, as Fig. 2.10 for the system of Fig. 2.9. As an additional input/output interface to GateCycle®, the CycleLink add-in is available. This Microsoft® Excel® based tool serves next to the GUI to allow for easy import/export of data between GateCycle® and Excel®. With CycleLink, an engineer can make customized interfaces to his own models. Since CycleLink uses Microsoft® Excel®, the GateCycle® model becomes an integral part of customized Excel sheets, allowing further data analysis, including exergy calculations.

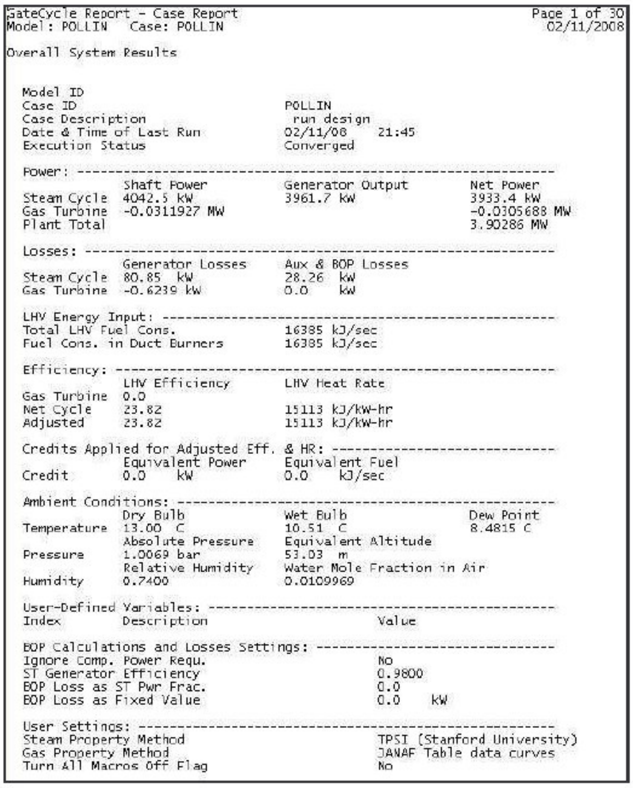

```
GateCycle Report - Case Report                                      Page 1 of 30
Model: POLLIN   Case: POLLIN                                          02/11/2008

Overall System Results


  Model ID
  Case ID                          POLLIN
  Case Description                  run design
  Date & Time of Last Run          02/11/08    21:45
  Execution Status                 Converged

  Power: ---------------------------------------------------------
              Shaft Power          Generator Output     Net Power
  Steam Cycle 4042.5 kW            3961.7 kW            3933.4 kW
  Gas Turbine -0.0311927 MW                             -0.0305688 MW
  Plant Total                                           3.90286 MW

  Losses: --------------------------------------------------------
              Generator Losses     Aux & BOP Losses
  Steam Cycle 80.85  kW            28.26  kW
  Gas Turbine -0.6239 kW           0.0    kW

  LHV Energy Input: ----------------------------------------------
  Total LHV Fuel Cons.             16385 kJ/sec
  Fuel Cons. in Duct Burners       16385 kJ/sec

  Efficiency: ----------------------------------------------------
              LHV Efficiency       LHV Heat Rate
  Gas Turbine 0.0
  Net Cycle   23.82                15113 kJ/kW-hr
  Adjusted    23.82                15113 kJ/kW-hr

  Credits Applied for Adjusted Eff. & HR: ------------------------
              Equivalent Power     Equivalent Fuel
  Credit      0.0    kW            0.0    kJ/sec

  Ambient Conditions: --------------------------------------------
              Dry Bulb             Wet Bulb             Dew Point
  Temperature 13.00  C             10.51  C             8.4815 C
              Absolute Pressure    Equivalent Altitude
  Pressure    1.0069 bar           53.03  m
              Relative Humidity    Water Mole Fraction in Air
  Humidity    0.7400               0.0109969

  User-Defined Variables: ----------------------------------------
  Index       Description                    Value

  BOP Calculations and Losses Settings: --------------------------
  Ignore Comp. Power Requ.                   No
  ST Generator Efficiency                    0.9800
  BOP Loss as ST Pwr Frac.                   0.0
  BOP Loss as Fixed Value                    0.0    kW

  User Settings: -------------------------------------------------
  Steam Property Method                      TPSI (Stanford University)
  Gas Property Method                        JANAF Table data curves
  Turn All Macros Off Flag                   No
```

Fig. 2.10. GateCycle® simulation report.

The calculations produced by the software therefore are provided for a specific operating condition and no transient and dynamical operating conditions can be evaluated.

Scientific literature proposes examples of the GateCycle® software used to design a system at nominal operating conditions and the main parameters of the so designed units and components are employed within softwares that allow for dynamical simulation of the process in order to gather a deeper understanding of the interactions that the designed power generating unit may have with other interconnected units. In [20] for example a Rolls–Royce natural gas powered turbine (RB211T DLE) and its associated economizer is modelled in the simulator GateCycle® in order to study the influence of some variables, such as the air and natural gas temperatures or the water circulation conditions, on the gas turbine and economizer performance. After the model has been completed successfully the interface variables were used as input of the dynamic model of the remaining integrated process, which include a salt recrystallization process where the heat exchange between the cogeneration unit takes place thanks to four plate heat exchangers.

To be noted also that the software also does not allow to define customized components and the application therefore is limited to the field of conventional thermodynamic power units and not to general energy conversion systems. This characteristic, beside the fact that only steady state balance equations can be accounted for in the software, renders this tool unproper for the applications object of this study.

2.3.6 Customized tools for simulation of energy systems

The literature survey of existing non commercial models of interconnectable components of energy system networks has brought to very few examples which has lead to believe that the field still lacks of a complete and exhaustive work.

Mainly the models proposed are developed for very specific applications and often lack in scalability, flexibility or generality, characteristics that have been quite looked for in the present work.

Examples of custom libraries of components for dynamic modelling and analysis of complex energy system can be found in [21-23].

In [21,22] a modular code for the dynamic simulation of a single shaft gas turbine is presented. The code, called CAMEL®, is a modular object-oriented process simulator, for energy conversion system (with specific reference to microturbines) and the modelling method is typical of black-box approaches. Each component of the system under analysis can be assembled in an engineering process scheme where the connections between two elements represent either mechanical power coupling or a working fluid stream.

The code is devoted to energy systems design and is based on original C++ written codes; for each separate component a proper set of first order (linear/non linear) algebraic or differential equations are cast and, as typical for object oriented programming languages, after the proper connectivity to the plant has been imparted to the code, all the proper block equations pertaining to the different blocks are assembled together and solved in matrix form, once assigned proper boundary conditions and parameters. Equations are integrated forward in time according to a fourth-order Runge-Kutta method. The code is used for both steady state off-design and dynamic operating conditions.

The approach followed in the present Work is similar to that assumed for the CAMEL® except for the programming language and for the variety of models proposed in the library of components presented within this Thesis, which goes beyond the elements typical of micro-gas turbine applications. Also, in the present Work, many white-box (or grey-box) models are proposed with proper physical correlations implemented.

In [23] another original code called TRANSEO for the transient and dynamic simulation of micro-gas turbine based systems is presented. The code is a model based software developed in the Simulink® platform, of which exploits the interface and time machine, and comprises a library of proper components, even if the management of some fundamental calculations is demanded outside the Matlab® environment through dynamic-linked libraries.

More particularly the code is structured in such way that at Matlab® level a set of specific thermo-physical functions developed through C MEX files are implemented. At Simulink® level each component model interacts with the C MEX function to get necessary thermo-physical properties through their *C*-

sfunctions; in this respect TRANSEO can be considered a separate code from Matlab®, and it is capable of joining Simulink® features with external simulating resources.

The library features some very advanced components as the heat exchangers, modelled according to finite volume approach, and many blocks have been validated with reference to a commercial recuperated microturbine. From the models realized also some very advance cycles configurations have been proposed and analyzed: externally fired microturbine cycles, closed Brayton cycles for space applications and hybrid microturbine-fuel cell systems.

The library indeed provides some very advanced components and significant modelling techniques are applied in order to generate components applicable to any kind of microturbine based energy conversion system.

Aim and approach of the present work is very similar to that of [23] but the intent is to extend the range of components analyzed beyond a specific field of energy conversion system (like for example microturbines) providing models that can be suitable for a broader range of applications, that may involve conventional and non conventional heat and power generating units. The scope is to help designing, studying and controlling unconventional energy system arrangements that may be of interest for enhancing overall energy efficiency.

One example of that is proposed in Chapter 5, where the developed model of ICE based cogenerator, with implemented the model block of complete combustion analysis, has been coupled to the model of Organic Rankine Cycle unit in order to evaluate this unusual configuration with particular reference to transient and off design operation.

2.4 Aim and overview of the work

Aim of this Thesis is to propose a set of custom models of the main elementary components that can be encountered when analyzing energy conversion systems for power generation. While usually the discussion on dynamic system is concerned on the analysis of existing system, as clarified by Doebelin in 2, a major overall function of engineering is the design of new products and concepts. In this case the latest goal of the design process is to enhance the overall energy efficiency of a power system. One question that may arise is the role played by system dynamics in the framework of energy systems analysis. At the earliest stage when several competing designs are being conceived, system dynamics enters mainly by supplying a point of view that allows a better understanding of the proposed system and that allows for an iterative optimization of the ultimate system design by assessing and eliminating the major criticalities. Being familiar with available components and with their combinations, may make it easier to conceive new arrangements which could accomplish the above mentioned goals.

At the next stage, where the alternative designs have been roughly formulated and must be modelled, the systematic approach of system dynamics to modelling can be very helpful. Once models have been stated they can be analyzed and their performance evaluated with reference to required specifications. In this view the use of the specific detailed dynamic models of peculiar components within energy systems can be seen in the frame of the present work. Specific models of which a good knowledge has been achieved and confirmed by model validation (when possible) or by assessing their time response as ‘reasonable’, can be employed in designing a new system of which no previous knowledge was available and employed to study both steady state operation and off design conditions or specific transient that only reliable models can describe.

The library of components proposed within this Thesis indeed is not exhaustive but refers to specific families of elements that have been considered to be of relevant interest, with the idea of creating a flexible tool that could however be easily extended; the components proposed therefore are merely illustrative and chosen as reference cases, where different modelling techniques have been applied.

Mathematical simulation models are indispensable to engineering system analysis, design, and control development, particularly during preliminary design stages. They enable virtual experiments when physical experimentation is either too expensive, time consuming, infeasible, or even impossible to conduct [24].

It should be noted in fact [25] that, in general, the dynamic performance of a process is not studied at the installation design and engineering phase. This need has only been recognised and included in the planning of important experimental or innovative projects and in nuclear power plants. Introducing dynamic performance at the design stage means specifying and complying with requirements during operational transients. The ability to model and simulate process systems means that computer ‘‘experiments’’ can be carried out with the advantage of eliminating risks and reduce commissioning costs. It also enables ‘‘tests’’ to be run that are physically impossible to perform on the actual installation.

This whole activity also is closely related to the analysis of the regulation and control systems to be implemented [25], as it can be observed from the activity process flow, shown in Fig. 2.11, concerned to a modelling activity specifically aimed to control design. A dynamic model referring to a new plant design, after proving its validity trough comparing its outputs with experimental data (validation) can be employed as test bench to design the control system prior to actually apply it to the test facility and, eventually, to the real plant.

This approach has been followed in [9], where the model of thermo and fluid dynamics of an advanced parabolic through solar collector based power station has been successfully employed as test base for control design. This approach is also typical of the Hardware In the Loop (HIL) simulation approach, used for example to test hardware and software that have to control and manage complex systems, which are introduced in the loop via specific embedded computer models, reducing the test costs. This is the case for example of ICE control unit design that, under certain circumstances, can be first tested with engine emulators based on real time computer models of the engine.

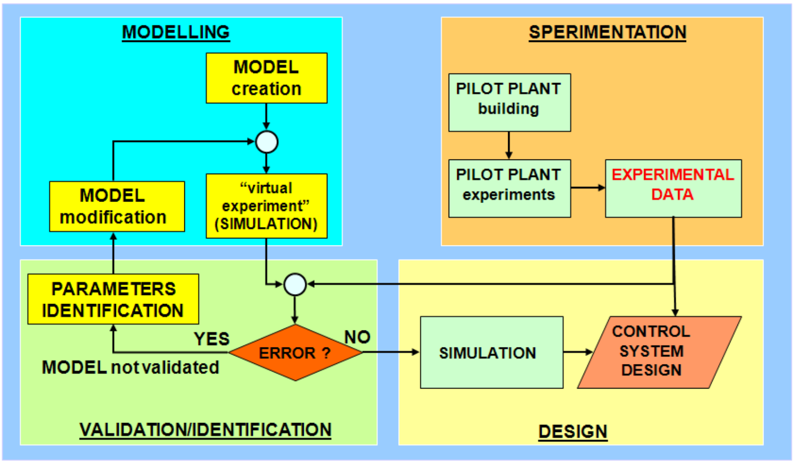

Fig. 2.11: Main steps of a modeling activity aimed to control design.

To be noted that the models presented within this Work, even if are applied only to system design, are still perfectly suitable also to control design purposes, and in the development of these models, their applicability within control design processes have always been considered.

To this extend it should be noted that the software used to create the model (Matlab®/Simulink®) truly incorporates capabilities to analyse and design the regulation and control system, so that both process and control engineers can work with the same software package [25]. In fact control is usually one of the weak points in the software devoted to thermal and fluid devices. This is true to such an extent that there are usually no true controller models available in these simulators. The available commercial software dedicated to dynamic analysis it is not considered to respond satisfactorily to the requirement stated above and this is a field which requires further development before it can reach the objective of application in common industrial practise [25].

The modeling approach followed within this Work is icon-based, where the user can design a program by properly linking together the icons referring to the components of the system, analogously to what seen in [21-23].

The mathematical model of the entire plants (i.e. Micro Gas Turbine systems, Organic Rankine Cycles and others, see Chapter 4) will therefore be carried out by identifying the relevant components and sub-systems and properly connecting them by means of thermodynamics and mechanical links recurring to the model blocks referring to single components presented in Chapter 3. Connections between elements can be either a mechanical energy coupling or a working fluid stream. The model therefore will result modular in structure, and the used approach allows for realizing a “component based” model, where each main component of the system is mathematically modelled –through conservation equations in unsteady form- integrated with the other to simulate the plant behaviour in steady and transient operating conditions [26].

Every component in turn encloses a specific computer code, which may either be compiled recurring to further icons (recurring to the Simulink® libraries of logical elements, thus realizing a graphical executable code) or by properly typing a machine language code.

The blocks created, that are grouped within a proper library, further divided in subfamilies, can be dragged and dropped in the Simulink® simulation environment. Each block features proper time dependant input/output signal ports and is characterized by a dialog window where all the time independent parameters can be uploaded (such as geometric parameters or material properties). Simulink® is then capable of compiling a full system code that comprises all the block codes, that in turn can be executed by its simulation engine in the proper time domain (either continuous or discrete).

This procedure is typical when an object oriented approach is adopted, where every mathematical model introduced correspond to a specific physical object of the real system. Main advantages of such an approach are [21]:

- modularity: the user can define the entire system by correctly assembling components and streams;
- expandability: it is easy to enlarge the component and flow libraries in order to simulate a wider range of plant typologies and configurations.

In fact the study of Large Scale systems requires methodologies that reduce the complexity of the overall problem by reducing it to smaller dimension problems of manageable size. Very frequently it is necessary to deal with systems that can be naturally seen to be composed of modules. The definition of modular structure and decomposition of a system may be a convenient tool to describe, model and simulate complex systems and it is adopted in the study of large dimension processes. Such decompositions however forces to consider interactions between modules as disturbances and make the design process dependent on the specific sequence that is used in design. Modelling and Simulation tools for understanding the problem of *Sequencing of Design* are essential tools for such studies. Procedures for defining the modules and addressing issues of sequencing of the design process are challenging topics [28].

When starting the modeling procedure of a specific Large Scale system it is first necessary to gather a deep understanding on the physical phenomena that occur within the whole system and its components. The second step is to decide the degree of accuracy to describe the process. It is out of doubt that any process can be described starting from the molecular scale but if the scope of the model is to analyze the overall energy streams of a town or a country, the approach might be totally misleading.

Identifying the right level of approximation is not always simple. Within this Work the models created refers to the physical macro-components of power plants, intended as all those components that can be physically identified and that usually affect the main state parameters of the system (since dealing with fluid systems, state parameters are usually pressures, levels, mass flow rates, specific volumes etc). Example of these components are compressor turbines, heat exchangers, combustion chambers, and, in general, all those components where significative energy exchanges take place. In fact energy-based proper modeling techniques are built on the intuitive fundamental premise that in an energetic system the most important components to model accurately are those characterized by the largest magnitudes of energy or power flow [29] (see below for definition of proper models).

Once the components have been identified the second step is concerned with identifying the proper logical inputs and outputs; inputs and outputs of a computer model in fact rarely are the same as the physical inputs and outputs of the real system.

In the example of a simple reservoir a physical input may be the mass flow rate of fluid entering and a physical output may be the fluid leaving the reservoir (Fig. 2.12).

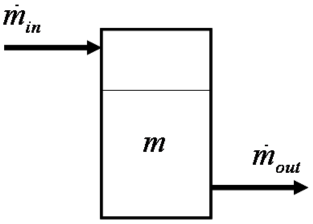

Fig. 2.12: Reservoir with inlet and outlet flow streams.

In a computer model of the same system both the fluid mass flow rates entering and leaving are inputs, while the output might be for example the level of fluid at any instant of time t (Fig. 2.13).

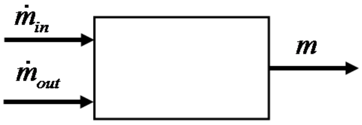

Fig. 2.13. Logical input/output model of a reservoir.

Next step is identifying the equations to be used to represent the physical behaviour of the system: as seen these equations may have empirical nature (like characteristic curves) or may come from the cardinal equations; in this latest case the equations will be differential and dynamics will be introduced.

In the simple example of Fig. 2.13 the equation used to represent the phenomena comes from the mass conservation equation and the time derivative of the state variable, i.e. the mass of liquid within the reservoir, indicates that this component is a *state determined* model:

$$\dot{m}_{in} - \dot{m}_{out} = \frac{dm}{dt} \tag{2.24}$$

As already noted, however, it is usually good modelling practice to alternate *state determined – not state determined* models, according to the scheme of Fig. 2.4, to avoid algebraic loops when the equations of the different components are solved together to give a representation of the whole system.

Another very important issue, when dealing with component models, is their scalability. The aim of this work is not to create a very detailed model of a specific component in order to accurately represent its behaviour, but rather to have a model that can be easily scaled so to represent, if possible, any other component of the same family accepting the approximations that this process may involve.

This capability of models is not very common but on Author's belief very valuable; the techniques adopted to make the models scalable are different depending on the nature of the models themselves.

Within this activity efforts will be focused also on realizing *proper* models. A dynamic system model is proper for a particular application if it achieves the accuracy required by the application with minimal complexity. Because model complexity often—but not always—correlates inversely with simulation speed, which is another key parameter to be considered, a proper model is often defined as one balancing accuracy and speed [29].

Model accuracy is in fact critical for understanding, optimizing, and controlling the dynamics of a given system effectively. Model simplicity, on the other hand, is essential in system identification and optimization. Simpler models are also easier to inspect for physical insights than more complex ones and can lead to lower-order controllers that are easier to implement. Finally, simpler models are often—but not always—faster to simulate, which can be crucial for certain applications such as hardware-in-the-loop simulation or embedded model-reference control. In this view, model accuracy and simplicity are often both crucial for effective system identification, analysis, optimization, and control.

Seeking model accuracy and simplicity simultaneously, however, typically engenders a trade-off: increasing the accuracy of a system model often necessitates increasing the complexity of the model to a level more commensurate with the complexity of the real system. In other words, the requirements of model accuracy and simplicity often compete and must hence be traded off. This competition typically grows as engineering systems become larger, more complex, and more integrated. There is a growing need for system models that mitigate this competition and balance accuracy and simplicity by only capturing the dynamics necessary for their respective applications. To this extent, as said, a dynamic system model can be defined *proper* when it provides the accuracy required for a given application with minimal complexity. Obtaining a proper model, however, is not an easy task. It is not always obvious which phenomena are important for a specific application, i.e., what to include in a model and what to neglect. Literature provides different techniques for creating proper model: some techniques begin with simple models and increment their complexity until they meet their respective accuracy requirements, a process known as *model deduction*. Most techniques, however, begin with excessively complex models and then *reduce* them until they become proper.

Usually the approach that should be followed in the application of proper modelling techniques to energy systems simplify a given model by eliminating less energetic components, while trying to minimize the effect of the elimination on the overall energy flow according to a reduction procedure. In many circumstances, it may also be possible to simplify a given model and thus make it proper not only by reducing or eliminating its various submodels but also by simplifying the interconnections between these submodels. Such *model structure simplification* includes simplifying a model by lumping its coupled inertias, partitioning its weakly coupled subsystems, or simplifying its mathematical representation without loss of accuracy.

It can eventually be noted that the dynamic models proposed and described within this Thesis, if intended for system design, might be used also for long term simulation of the designed system.

While the dynamic models realized are specifically developed to assess new arrangements within complex energy systems in order to have a tool that help predicting the transient behaviour in off design operating conditions and for control design, it is quite common that these systems in real world will be operated very often under steady state conditions or with high time constant transients.

To this extent a detailed dynamical model might be too accurate for the scope, the computation might be too demanding and the modelling approach would thus result improper.

In this sense the dynamic model of the newly designed system setup can also be used to derive characteristic maps that define the different and possible steady state operating conditions and these maps can be eventually introduced within a code where the main energy fluxes of the system may be evaluated, for example on hourly bases, hence recurring to a queasy steady simulation.

2.5 Summary

In this Chapter the overall methodologies applied to develop the Work of Thesis are illustrated. The scope of the work is to define an object-oriented library of computer models aimed at the dynamic simulation of power systems. A specific software (Matlab®/Simulink®) is chosen for the scope due to its capabilities in developing custom blocks with high degree of mathematical complexity based on *S-function*, which allows executing specific function written in the Matlab® language while Simulink® is performing the simulation of the complete system, thus determining an equation based modeling approach.

Characteristics sought in the models blocks is their flexibility, scalability and the possibility to be coupled to many other components to create advanced system designs. Scope of the Work is in fact to provide a flexible tool that might allow for system design, off design and transient operation analysis and control development.

Refernces

1 Curlett P., Felder J.L., *Object-Oriented Approach for Gas Turbine Engine Simulation*, NASA-TM-106970. Lewis Research Center, National Aeronautics and Space Administration, Cleveland, OH, 1995.

2 Doebelin E.O., *System Dynamics – Modeling, Analysis, Simulation, Design*, Marcel Dekker Inc., 1998.

3 Karnopp D.C., Margolis D.L., Rosenberg R.C., *System Dynamics: modeling and simulation of Mechatronic Systems*. New York: John Wiley & Sons Inc., 2000.

4 Guzzella L., Onder C.H., *Introduction to Modelling and Control of Internal Combustion Engine Systems*, Springer, 2004.

5 Moskwa J.J., Munns S.A., Rubin Z. J., *The Development of Vehicular Powertrain System Modeling Methodologies: Philosophy and Implementation*. SAE Technical Paper 971089.

6 Ali M., Moskwa J.J., *Developing a Generalized Modular Structure for Dynamic Engine Simulation*. SAE Technical Paper 2002-01-0202.

7 Canova M., *Fluid Systems Dynamics Modeling for Control: Internal Combustion Engines Case Studies*, Ph. D Thesis, Industrial Engineering Department, University of Parma, Italy 2006.

8 Shapiro A.H., *The dynamics and thermodynamics of compressible fluid flow*, Vol I., The Ronald Press Company, New York, 1953.

9 Vaja I., *Modellazione e simulazione finalizzate al controllo di una centrale solare termoelettrica a collettori parabolici lineari: il progetto "Archimede"*. Master Thesis, Industrial Engineering Department, University of Parma, 2007 (in Italin), sponsored by ENEA.

10 Menta B., *Studio tecnico-economico e simulazione di un impianto cogenerativo applicato ad un complesso scolastico*. Master Thesis, Industrial Engineering Department, University of Parma, Italy, 2006 (in Italian).

11 Salati L., *Studio di fattibilità e valutazione tecnico-economica di un impianto cogenerativo a biomassa applicato ad un complesso agrituristico*. Master Thesis, Industrial Engineering Department, University of Parma, Italy, 2006 (in Italian).

12 Favaro V., *Simulazione del comportamento di un edificio a basso consumo di energia: confronto tra diverse soluzioni impiantistiche*. Master Thesis, Industrial Engineering Department, University of Parma, Italy, 2007 (in Italian).

13 Augenti C., Gambarotta A., Pagliarini G., Rainieri S., Vaja I., *Economic feasability analysis of a CCHP system in a tertiary sector application*. ASME-ATI Conference, Milano 2006.

14 Vaja I., Augenti C., Gambarotta A., Pagliarini G., Rainieri S., *Aspetti economici di un impianto trigenerativo applicato al settore terziario*. 61° Congresso Nazionale ATI, Perugia – Italia 12-15 settembre 2006. (in Italian).

15 Elmqvist H., Mattsson S.E., *An introduction to the physical modeling language Modelica*, Proceedings of the 9th European Simulation Symposium, ESS'97, Oct 19-23, Passau, Germany, 1997

16 Pfafferott T., Schmitz G., *Modelling and transient simulation of CO_2-refrigeration systems with Modelica*, International Journal of Refrigeration 27 pp.42–52, 2004.

17 Miche M., Lafossas F.A., Guillemin J., *Enhanced Phenomenological Modelling of Conventional and HCCI Diesel Combustion using Algorithms for Automatic Calibration.* SAE Paper 2007-24-0036, ICE 2007, Capri, Naples, Sept. 16-20, 2007.

18 Izenbrandt J., Goudappel E., *Simulation of the AVV 1 cycle with GateCycle*, ECOS 2003 conference, Copenhagen Denmark, Jun.30-Jul.2, 2003.

19 Falcone C., *Utilizzo delle biomasse per la produzione di energia elettrica: studio di fattibilità di un impianto per la combustione di pollina*, Master Thesis, Industrial Engineering Department, University of Parma, Italy, 2007 (in Italian).

20 Moita R. D., Matos H. A., Fernandes C., Nunes C. P., Prior J. M., *Dynamic modelling and simulation of a cogeneration system integrated with a salt recrystallization process*, , Computers and Chemical Engineering 29 (2005) 1491–1505.

21 Cennerilli S., Sciubba E., *Application of the CAMEL process simulator to the dynamic simulation of gas turbines*, Energy Conversion and Management 48 (2007) 2792–2801.

22 Cennerilli S., Fiorini P., Sciubba E., *Application of the Camel process simulator to the dynamic simulation of gas turbines*, ECOS 2006 Proceedings, Vol. 1, pp. 355-363.

23 Traverso A., *TRANSEO: A New Simulation Tool for Transient Analysis of Innovative Energy Systems*, Ph.D. Thesis, TPG-DiMSET, University of Genova, Italy, 2004.

24 Ersal T., Faty H.K., Rideout D.G., Louca L.S., Stein J.L., *A review of proper modelling techniques*, Journal of Dynamic Systems, Measurement, and Control, vol. 130, Nov. 2008.

25 Gonzalez-Bustamante J.A., Sala J.M., Lopez-Gonzalez L.M., Mıguez J.L., Flores I., *Modelling and dynamic simulation of processes with 'MATLAB'. An application of a natural gas installation in a power plant*, Energy 32 (2007) 1271–1282.

26 Curlett P., Felder J.L., *Object-Oriented Approach for Gas Turbine Engine Simulation, NASA-TM-106970*, Lewis Research Center, National Aeronautics and Space Administration, Cleveland, OH, 1995.

27 Falchetta M., Gambarotta A., Vaja I., Cucumo M., Manfredi C., *Modeling and simulation of the thermo and fluid dynamics of the "Archimede Project" solar power station*, ECOS 2006 Int. Conference, Creta – Greece 12-14 Lug. 2006.

28 Karcanias, *Modeling and simulation in technological and emerging fields: emerging challenges*, Sim-Serv Conference, Modeling and Simulations: Challenges, Oct. 2004

29 Ersal T., Faty H.K., Rideout D.G., Louca L.S., Stein J.L., *A review of proper modelling techniques*, Journal of Dynamic Systems, Measurement, and Control, Nov. 2008, vol. 130.

CHAPTER
THREE

A LIBRARY OF MODELS FOR THE DYNAMIC SIMULATION OF ENERGY SYSTEMS

The present Chapter reports a collection of components that have been realized during this Ph.D work at the Industrial Engineering Department of the University of Parma.

All the proposed models have been developed with the common characteristic of being flexible, fast scalable and suitable to be used to build up full dynamic models of complex and advanced energy conversion systems, some example of which will be presented in the next Chapters.

Not for all the components, however, the dynamic behaviour has been considered: for some energy systems elements, classified as 'not state determined', dynamic phenomena have been neglected leading to the realization of quasi-steady components. The dynamics of the whole plants will be simulated by the 'state determined' components, intended as those elements where some sort of storage is possible (of energy, mass, momentum etc.). The cause-effect approach used to create the complete model will lead to alternating the 'not state determined' elements with 'state determined' elements, favouring the numerical stability of the complete mathematical models since algebraic loops are in most of the cases avoided.

The scalability and flexibility of the component models are considered as fundamental requirements in the modelling activity, since it is author's belief that each model should be promptly and easily used in a wide range of situations with different design (i.e. size) and considering different working fluids. An analysis of the dialog windows created for each component and reported in the following Paragraphs reveals in fact that many parameters are required to configure precisely the component according to the application.

To be noted that the modeling approaches here applied to the different components of interest are not unique and that many other techniques may be followed but the one proposed here are those that have been believed to be the most appropriate case to case.

To be noted that the modeling approaches applied in the work are not the only possible, since other techniques may be used: the solutions proposed here are those that are thought to be the most appropriate for the scope.

Nomenclature

c_p	Specific heat at constant pressure [J/kg K]
c_v	Specific heat at constant volume [J/kg K]
d	Diameter [m]
f	Friction factor [-]
$\bar{g}_f^0$	Free Gibbs energy molar at standard conditions [kJ/kmol]
h	Specific enthalpy [kJ/kg]
$\bar{h}$	Molar enthalpy [kJ/kmol]
k	Thermal conductivity [W/mK]
m	Mass [kg] – Polytrophic exponent [-]
$\dot{m}$	Mass flow rate [kg/s]
q	Heat transfer rate [W]
q'	Heat transfer rate per unit length [W/m]
q''	Heat Flux [W/m^2]
s	Specific Entropy [kJ/kg K]
t	Time [s] - Thickness [m]
u	Speed [m/s] –Specific internal energy [J/kg]
$\bar{u}$	Molar internal energy [kJ/kmol]
x	Vapour mass fraction [-]
A	Area [m^2]
Bi	Biot number [-]
D_h	Hydraulic diameter [m]
J	Inertia [kg m^2]
Ja	Jacob number [-]
L	Length [m]
Nu	Nusselt number [-]
P	Power [kW]
Pr	Prandtl number [-]
Re	Reynolds number [-]
S	Surface area [m^2]
T	Temperature [K]
U	Heat exchange coefficient [W/m^{2}K]
X	Molar fraction
X_{tt}	Martinell Factor [-]

Greek symbols

α	Convection heat transfer coefficient [W/m^{2}K] – Air fuel mass ratio [-]
ε	Emissivity[-], Relative error [-], Turbine pressure ratio [-]
σ	Stefan-Boltzmann constant [-]
η	Efficiency [-]
θ	Crank angle
μ	Viscosity [kg/s m]
τ	Torque [Nm]
φ	Air fuel equivalence ratio [-]
ω	Angular speed [rad/s]
φ	

Abbreviations and subscripts

a	Air
abs	Absolute
avg	Average
b	Burning
cond	Conduction
conv	Convection
cr	Critical
df	Dumping factor
exp	Experimental
f	Fluid, Fin, Fuel
h	Hydraulic
i	Insulation
irr	Irradiation
in	Inlet
m	Mechanical
bmip	Brake mean indicated pressure
mod	Model
n	Nominal
l	Liquid
out	Outlet
p	Pipe
prod	Products
rad	Radiative
react	Reactants
t	Thermal
tf	Transfer fluid
v	Vapour
x	Axial abscissa
y	Longitudinal abscissa
w	Wind, Wall, Water
C	Compressor
CC	Combustion Chamber
F	Fuel
HTF	Heat transfer fluid
ICE	Internal Combustion Engine
MGT	Micro Gas Turbine
N	Negative
ORC	Organic Rankine Cycle
P	Positive, Pump
R	Reduced
S	Sun
T	Turbine

3.1 Overview of the libraries

In the present Chapter a comprehensive set of models for components that may be used within energy conversion systems (mainly power generating systems) is presented and discussed. The aim is to create a wide library that could be used to pick up blocks in order to create complete models of energy systems that the user is keen to investigate. In Chapter 4 and 5 in fact some examples will be provided showing how the single blocks can be properly bounded together creating a system of interest and results of transient simulations are provided demonstrating the capabilities of the tool.

As seen in the previous Chapter, when a physical system is being modelled two main classes of objects that can be considered:

- Reservoirs, characterized by one or more states that represent the "stored" amount of level variables;
- Flow Control Devices which determine the amount of properties that flow through them, typically as a result of differences between reservoir levels.

These definitions, already discussed, can fall in the broader categories of *state determined* and *not state determined models*, the first including the “reservoirs” systems and the latter including “flow control devices”, depending on whether or not it is possible to define differential equations expressed in terms of the state variables of the system.

When considering energy systems and power systems, as for example a steam plant or a gas turbine plant, it is a good practice to split the elements of the plant in two categories:

- Heat exchanger devices;
- Fluid machinery elements.

The distinction between these two categories is crucial and allows introducing some simplifications in the analysis of the corresponding models.

Any power cycle, besides a working fluid, requires a series of heat exchangers and fluid machines to operate. In a simple steam cycles heat exchanger devices may be assumed to be the evaporator and the condenser while the fluid machines are the turbine and the pump.

In general it can be stated that heat exchangers are all those elements where the working fluid exchanges energy with the surrounding only in thermal form, i.e. any exchange of work can be neglected. At a first sight, also the effects of friction can be neglected hence considering the process as perfectly isobaric. This assumption will often be adopted in the analyses that follow. The thermal or mass capacitance of the system, i.e. its capacity of accumulating either thermal energy or mass can be considered or not. Taking into account these phenomena will certainly lead to start from energy or mass conservation equations that will contain time derivatives of some variables that can then be considered as state variables. Heat exchangers in this case are to be considered as *state determined* models where the behaviour in time of the fluid temperature (or specific enthalpy) as well as the mass flows through the boundaries is not a linear function of the actual inputs, but depends also on the history of the system since capacitances are taken into account. These systems can therefore be considered as reservoirs where level variables can be fluid temperatures.

It should be noted that a volume can be associated to heat exchangers, and hence the possibility to store mass. In this case the pressure within the heat exchanger is assumed to uniformly distributed, but its evolution in time is determined by the amount of mass stored within the component hence the pressure is a state variable of the system or, equivalently, a ‘level’ variable of the reservoir. In some cases, as in the example of the organic fluid evaporator, the capability in determining the pressure dynamics through mass and energy storage has been lumped to an associated volume (the drum) while the only level variables associated to the actual heat exchanger are merely the fluid temperatures and flow rates (see Par. 3.2.3 and 3.2.4).

The other main category of components identified in the power systems analysis is fluid machines. Differently from the heat exchangers, they are assumed to be ideally adiabatic, that is the heat flux exchanged between the working fluid and the surrounding is neglected. The only significant energy flux exchanged between fluid and components occur in the form of mechanical work leading to a pressure change (either positive or negative): these components therefore cannot be considered isobaric. A common assumption in this case is that the dynamic phenomena within the fluid occur much faster than the rate of change in the thermodynamic boundary conditions which take place in the reservoirs to which the fluid machineries (or fluid control devices) may be connected. With this assumption, the processes occurring in the fluid can be modeled as quasi-steady processes and static maps can be used to describe the behaviour of these devices. This approach is typical of *not state determined* modeling techniques and the model outputs are determined by applying algebraic correlations, often empiric in nature and usually highly nonlinear, and no accumulation phenomena are considered. Fluid machines in fact, in system dynamic analysis, are usually considered to behave exactly as flow controlling devices and the actual mass flow rate flowing through them (flow variable) will be determined by the pressure existing at inlet and outlet of the device (the pressure as seen can be considered as a level variable determined by the dynamic processes occurring within the reservoirs, i.e. heat exchangers and their associated volumes).

Within this framework, therefore, all the models presented will be divided into the two main categories of *state determined* and *not state determined* in the broad sense definition introduced here.

According to this classification, the library of component models of energy systems will be divided into these two main categories.

The sub-library 'state determined components' will contain the following components:

- thermal solar collector;
- single phase heat exchanger;
- heat exchanger with phase change;
- drums;
- constant pressure combustion chamber;
- rotating shafts dynamics;
- General fluid Receiver;
- ICE intercooler.

The sub-library "not state determined" will contain models of the following components:

- compressor;
- turbines;
- pump;
- valve;
- heat exchanger with no thermal dynamics;
- in cylinder combustion processes (in ICE).

The complete customized library of components, whose detailed description is provided in the Paragraphs that follow, is visible in Fig. 3.1 that displays the ‘Simulink$^{®}$ Library Browser’ interface. The ‘Energy Systems Library’ contains the two mentioned sub-libraries referring to ‘not state determined’ and ‘state determined’ components. It is possible to notice that, analogously to any other standard Simulink$^{®}$ block, all the created models can be dragged and dropped in a new Simulink$^{®}$ workspace in order to be properly linked together to simulate the desired system. Examples of this will be provided in Chapter 4 where it is also described the sub-library ‘Complete Power Systems’ that appears in the main ‘Energy Systems Library’.

As general characterization the model referring to the ‘state determined’ sub-library will be marked with black shadows in order to make them easily distinguishable from the components referring to ‘not state determined’ sub-library.

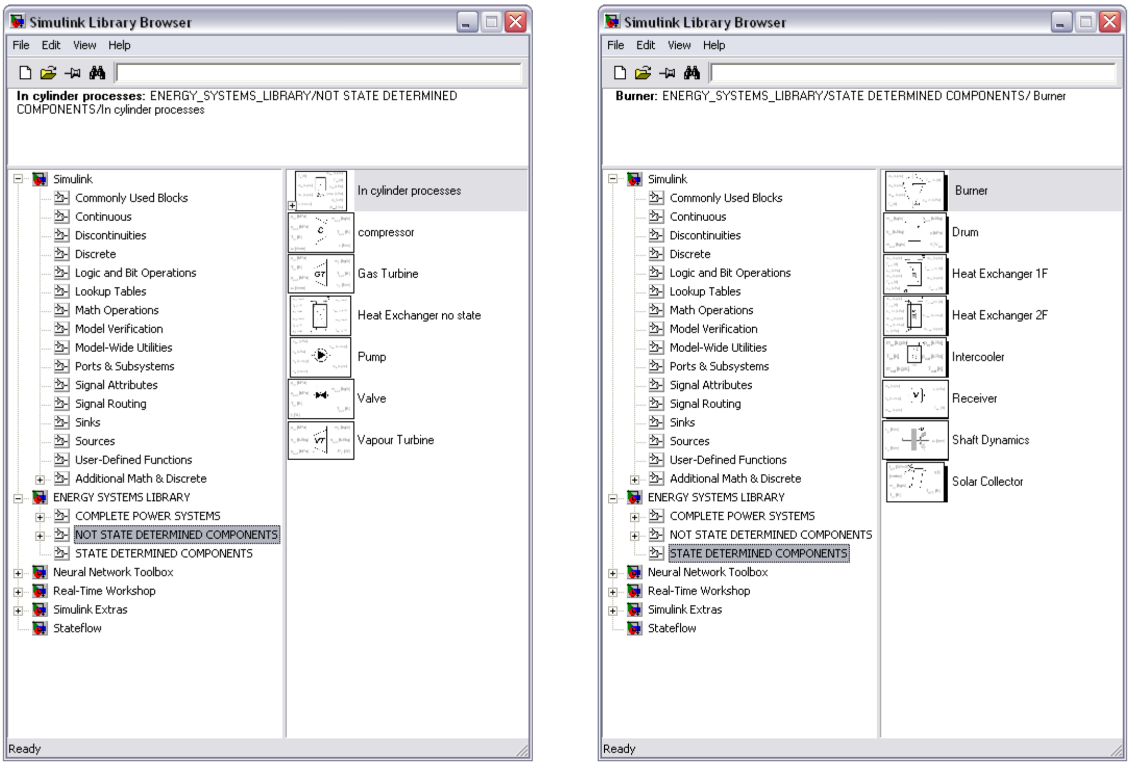

In cylinder processes: ENERGY_SYSTEMS_LIBRARY/NOT STATE DETERMINED COMPONENTS/In cylinder processes

Burner: ENERGY_SYSTEMS_LIBRARY/STATE DETERMINED COMPONENTS/ Burner

(a) (b)

Fig. 3.1. The custom ‘Energy Systems library’ accessible from the ‘Simulink$^{®}$ Library Browser’: detail of (a) the ‘not state determined’ sub-library and (b) of the ‘state determined’ sub-library.

3.1.1 The state equation

In the following a general insight on the way equation of state have been considered in realizing the models proposed in the present Chapter is given. As already observed, the state equation of a fluid can be described with simple correlations only when the fluid can be considered as a perfect gas or as an incompressible liquid. The state equation cannot be defined analytically when the fluid is in the liquid to vapour phase change and usually empirical correlations are provided in this case.

Since the aim of the work was not to describe the fluid behaviour but rather to describe the system behaviour, the easiest way to implement the state equation has appeared that of using already compiled databases of fluid thermodynamic properties.

Among the many available in commerce, REFPROP® database, developed by NIST (National institute of Standard and Technology, USA) has been chosen for the scope of this work. REFPROP® is an acronym for REFerence fluid PROPerties and provides tables and plots of the thermodynamic and transport properties of fluids commonly used in industrial applications and their mixtures, with an emphasis on refrigerants and hydrocarbons. REFPROP® is based on the most accurate pure fluid and mixture models currently available. It implements three models for the thermodynamic properties of pure fluids: equations of state explicit in Helmholtz energy, the modified Benedict-Webb-Rubin equation of state, and an extended corresponding states (ECS) model [1]. Mixture calculations employ a model that applies mixing rules to the Helmholtz energy of the mixture components; it uses a departure function to account for the departure from ideal mixing. Viscosity and thermal conductivity are modeled with either fluid-specific correlations, an ECS method, or in some cases the friction theory method.

These models are implemented in a suite of Fortran® subroutines. They are written in a structured format and have been tested on a variety of compilers.

Routines are provided to calculate thermodynamic and transport properties at a given (T,ρ,x) state. Iterative routines provide saturation properties for a specified (T,x) or (P,x) state. Flash calculations describe single- or two-phase states given a wide variety of input combinations [(P,h,x), (P,T,x), etc].

Even though a separate graphical user interface, designed for the Windows operating system, can provides a convenient means of accessing the models, and it allows generating tables and plots for user-specified mixtures or a number of predefined mixtures (air and the commercially available refrigerant blends), the software has been chosen for its compatibility with the Matlab® platform.

A specific Fortran® file, called refpropm.f90, is in fact available to link Matlab® with the routines used in REFPROP®. The Fortran® routines are called externally by typing with proper arguments the Matlab® function `refpropm.m`, developed by Lennart Vamling at the Chalmers University of Technology in Sweden and modified by Johannes Lux of the German Aerospace Center. This function allows to use the entire REFPROP® database from Matlab®, hence allowing calculations of fluid state properties from any Matlab® based model code. The function returns the required fluid properties given a state point (defined by two specified and known state properties) and given the pure fluid considered or the fluid mixture composition (if the substance is not a pure fluid). Examples of call of the REFPROP® routines from Matlab® are provided below:

1)
```
cp_g=refpropm('C','T',T_g,'P',p_g,'CO2','water','nitrogen','oxygen',[0.091 0.074 0.742 0.093]);
```

In this case the specific heat at constant pressure is provided at a given temperature and pressure for a known mixture of gases that constitute the exhaust gas composition of a natural gas fired ICE.

2)
```
[h4,T4]=refpropm('HT','P',p_min,'S',pt3_1.s,’toluene’);
```

In this second case specific enthalpy and temperature are calculated at a given pressure and specific entropy for toluene.

The coder is indeed highly flexible and suitable for the application of interest. However a trial of accuracy has been conducted before using it in order to assess the errors that arise using inverse functions.

Particularly for the three fluid states of interest within fluid power systems analysis (liquid, two-phase and vapour), given two state properties (pressure p and temperature T for liquid and vapour regions, vapour fraction x and pressure p for the two-phase region) two new properties have been calculated (as for example specific enthalpy h and density ρ). Starting from these last properties the former have been calculated, according to the following procedure:

- liquid and vapour: $(p',T') \to (h,\rho) \to (p'',T'');\ e_p = \dfrac{p''-p'}{p'},\ e_T = \dfrac{T''-T'}{T'};$
- two phase region: $(p',x') \to (h,\rho) \to (p'',x'');\ e_p = \dfrac{p''-p'}{p'},\ e_x = \dfrac{x''-x'}{x'}.$

If the functions used by the software were not approximate the same starting values should be observed, as h and ρ describe the same state point and the relative errors would appear nought. Some errors however occur in computing inverse functions and can be observed from Tab. 3.1, derived for water.

Field	Property	Relative error [%]
Liquid	p=100 kPa	$3.4420\cdot10^{-8}$
	T=300 K	$3.2211\cdot10^{-13}$
Vapour	p=100 kPa	$1.8716\cdot10^{-11}$
	T=500 K	$1.8417\cdot10^{-11}$
Two-phase	p=100 kPa	-0.0897
	x=0.5	0.0064

Tab. 3.1. Relative error due to inverse functions of the REFPROP® database for water.

Similar results have been gathered for other fluid families and for other state parameters and demonstrate how the error committed by recurring to inverse functions is negligible in the single phase regions and quite more significant in the two phase region. This analysis shows that a broad use of inverse functions in this region should be done carefully.

The REFPROP® database therefore has been integrated into many of the components described and in general in all the cases when specific fluid properties were required for calculation, with the double advantage of always considering precise values of the properties (rather than introducing approximating mean values also in the liquid or gas fields of the fluids considered) and relieving from the need to upload and interpolate on wide data bases.

3.2 The 'state detrmined' library

In this Paragraph all the components appearing in the 'state determined' library will be described in detail. Particular emphasis has been placed upon describing the heat exchangers where finite volume discretization techniques have been applied.

The activity of modelling heat exchangers with this approach started with a relatively simple model of solar collector then leading, with subsequent upgrades, to an advanced model of a counterflow heat exchanger where phase change is also considered to model condensers and evaporators.

3.2.1 Dynamic model of a Thermal Solar Collector

Many steady state models of solar collector devices have been proposed in literature. They have the advantage of simplicity, thus requiring low computing time, but, on the other hand, these in general lead to an overestimation of up to 10% of the energy delivered by the collector, as the thermal losses along the receiving pipe are not properly evaluated [4].

Other studies [5] propose three dimensional models of the thermal and hydro-dynamic fields during unsteady conditions, suitable for very detailed analysis of the flow and thermal distribution within the pipe and allowing for example to assess the effects of fins in the local parameters or the laminar mixed convection in the collector entrance region. These models appear indeed inadequate for overall thermal simulations of a solar system.

The model here proposed allows assessing the behaviour of a solar thermal collector under time varying mass flow rates of the heat transfer fluid (*HTF*) as well as the treatment of spatial non uniform solar radiation and heat transfer coefficients. The procedure is based on splitting the solar collector into n_x nodes along the axial direction and into 2 thermal nodes perpendicular to flow direction, resulting in $2 \times n_x$ system of partial differential equations [6]. A peculiarity of the proposed procedure is the possibility to define, through specific simulation parameters, both the degree of collector axial discretization and time discretization. This allows to define, by simply tuning the simulation parameters, very detailed thermal dynamic models as well as less detailed models of the exchanger (suitable for estimating overall thermal performances). Similar procedures, which also consider more than two longitudinal nodes, are proposed in [7,8] but the methods used to solve the model equations are not suitable for varying fluid mass flow rates.

The simulation of the thermal behaviour of a solar collector is an interesting issue as it implies the treatment of time-dependent weather conditions as well as time varying inlet fluid mass flow rates. This becomes important especially where these variables affect not only the dynamics within the collector but also of other energy systems if the solar thermal collector is integrated in a network where it is necessary to cover reliably the energy demand of a end user, residential or industrial.

A reliable precise and not too time consuming dynamic model of solar collector can be therefore a useful tool to study Integrated Energy Systems.

The aim of the work is also to develop a method of analysis and modeling of thermal energy systems which can be generalized not only to solar thermal collectors but also to other systems that implies heat exchanges under transient conditions.

3.2.1.1 The system

The analyzed solar collector is of unglazed type and features a metal receiving pipe thermally linked to fins, in order to enhance solar heat absorption. Pipe and fins are of the same material and the model features a library with the physical properties (expressed as function of temperature) of different metals (such as copper and iron) in order allow considering different collector set ups. A scheme of a single pipe of the solar collector under analysis is proposed in Fig. 3.2, where the receiving pipe is perfectly connected to the fins at each side (no thermal resistance is assumed in the heat transfer between fins and pipe). This system can be considerd the basic element of a flat plate solar collector.

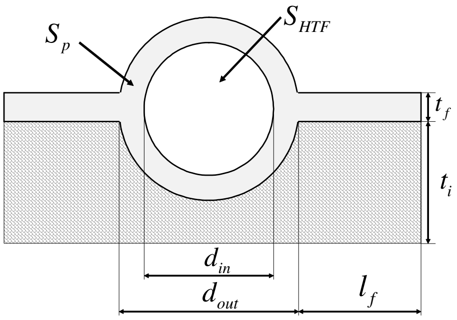

Fig. 3.2. Cross section of a pipe of the thermal solar collector.

The collector has a thermal insulation in the back side. Properties of the insulation are not introduced in the model as the back side of the collector is considered ideally adiabatic. This means assuming the insulation to be ideal and that heat losses on the back side can be neglected compared to the heat losses in the upper side of the collector

Surface colour of the external side may be considered for both the pipe and the fins, in order to reduce heat reradiated from the collector and to enhance the absorption of the solar radiation. Properties of three different types of external paintings are loaded in the model, and their variation with temperature is considered: black paint, which may be used in the simplest collectors, Black Chrome and Cermet, if more advanced setups are being modeled.

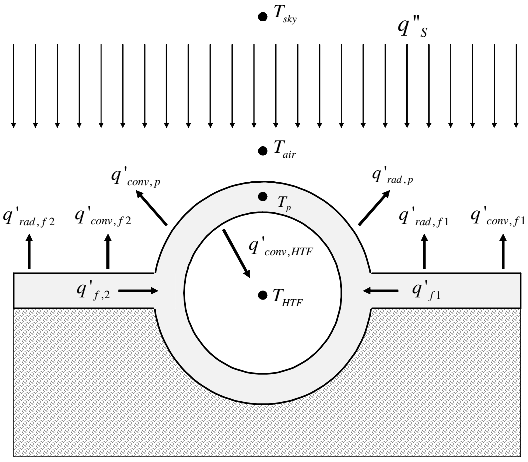

Fig. 3.3. Main heat fluxes and temperatures within the receiving pipe.

The main heat fluxes within each pipe of the collector were defined as represented in the scheme of Fig. 3.3. The solar radiation upon the collector, q''_S, provides heat to the external side of the pipe and fins. Heat from the fins (q'_f) is transferred to the main pipe contributing to increase the heat flow to the *HTF*.

The increase in the pipe and fins temperature causes heat losses. These are mainly due to convection ($q'_{conv,f}$, $q'_{conv,p}$) with external air flowing upon the collector at wind speed u_w, and due to radiation ($q'_{rad,f}$, $q'_{rad,p}$); in this case heat is transferred from the collector to the 'sky', which is assumed at the 'sky' temperature T_{sky}.

The balance among heat fluxes allows determining the net heat delivered to the heat transfer fluid ($q'_{conv,HTF}$), which is exchanged between the pipe internal side and the liquid mainly due to convection.

3.2.1.2 Modeling the solar collector

In the present section a detailed description of the proposed model is provided. Some assumptions are first presented as well as a classification of the model.

The main equations are then introduced referring to a simple collector with only three axial volumes and the procedure is then generalized leading to the definition of the overall solving system in matrix form. The procedure of integration through finite difference method is then described along with the main equations used to describe the heat streams within each control volume.

The collector pipe, which length is L, is split up into n_x segments (axial discretization) with length Δx. Each element defines a control volume according to the finite volume method of discretization. For each segment and at each instant of simulation t, energy conservation equations are applied to both the metal pipe (which local temperature is $T_p(t,x)$) and the heat transfer fluid flowing within it (which temperature is $T_{HTF}(t,x)$); the component therefore presents a 2 node distribution in the y direction. Temperatures at each equidistant node are calculated by the model and the value at an intermediate position may be determined by linear interpolation. A scheme of the generic pipe element is provided in Fig. 3.4, which refers to a longitudinal section of the receiving pipe, where the main heat fluxes are highlighted.

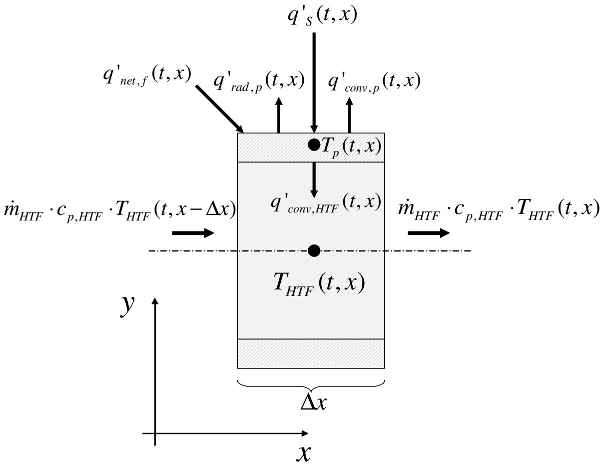

Fig. 3.4. Heat fluxes in a element of the receiving pipe.

The state of the system is represented by the nodal temperature of both HTF and pipe at each instant of the simulation. Temperatures at the following time step can be obtained by integration of differential equation expressed in terms of derivative of the nodal temperatures.

In Fig. 3.5 the block diagram of the model of solar collector is schematically proposed with input outputs and state variables.

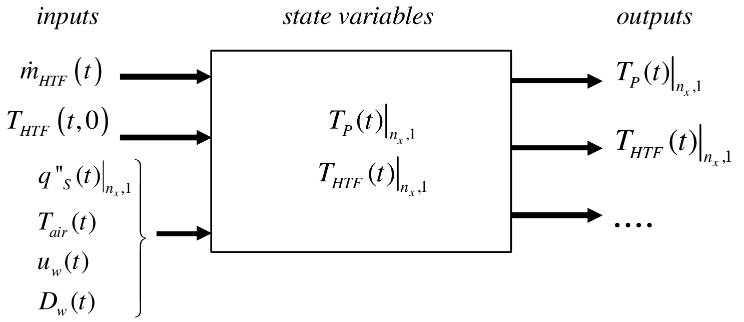

Fig. 3.5. Block diagram of the solar collector model.

Inputs to the system at each time of simulation are represented by:

- heat transfer fluid mass flow rate through the collector ($\dot{m}_{HTF}(t)$);
- heat transfer fluid temperature at the collector inlet ($T_{HTF}(t,0)$);

Further inputs are represented by meteorological variables, which also influence the change in time of the state and output variables. These are assumed to be uncontrollable external inputs:

- solar radiation to the collector ($q''_S|_{n_x,1}(t)$), that is represented by a vector containing the actual value of the radiation upon each segment of the discretized collector (this allows considering spatial non uniform solar radiation and to study transient simulations such as clouds passing);
- air temperature ($T_{air}(t)$);
- wind speed ($u_w(t)$);
- wind direction, with respect to collector orientation ($D_w(t)$).

Several outputs can be generated by the model such as the local radiative or convective heat losses, the energy stored, etc. Among the model outputs, the system state variables (pipe and HTF nodal temperature) are certainly the most interesting to be taken into account, allowing to know not only the fluid output temperature but also the fluid and pipe temperature at each node and instant of simulation, allowing to analyze the effects of varying input values on temperature distributions. These results could be hardly achieved by testing real components, where only the fluid output temperature is usually acquired. In this case therefore the output equation assumes the simplified form:

$$\overline{Y}(t) = \overline{X}(t) \tag{3.1}$$

It is possible to note that the size of both input and output vectors depend on the number of discrete volumes considered n_x; the length of the input vector is $5+n_x$ while the output vector is $2 \times n_x$, in the hypothesis of considering the nodal temperature of fluid and pipe as outputs.

The dimensions of the solving system of equations also depend on the number of nodes considered, as the overall number of state variables is, $2 \times n_x$. A specific procedure is therefore created in order to allow this flexibility in the number of model inputs/outputs, as well as in the dimensions of the system of equations. The procedures are therefore implemented in Matlab®, in order to exploit its capabilities in matrix calculation, while the system graphical interface is realized within the Simulink® environment.

The proposed model of solar collector also features an internal solving procedure, instead of the embedded Simulink® solvers, based on the solution of a set of differential equations, written in terms of the derivative of the state variables with respect of time, according to a forward finite difference approach, thus providing a discrete state *S-Function*:

$$\frac{dX}{dt} \simeq \frac{X_{t+\Delta t} - X_t}{\Delta t} \tag{3.2}$$

The following assumptions were made to generate the model:

- temperatures within the receiver (fluid, metal pipe and fins) are function of space and time;
- thermal capacitance of both the fluid and metal pipe are considered;
- the axial conductive heat flux is negligible [25];
- solar radiation is function of space and time;
- heat transfer due to conduction between pipe/HTF and pipe/air has been neglected;
- convective and radiation losses are considered only in the upper side of the collector, and the lower side is supposed perfectly insulated;
- the heat transfer fluid is liquid;
- thermodynamic properties of the HTF, the external air and metal pipe are function of the local node temperature;
- turbulent, transitional or laminar flow are considered to model convective heat transfer both in the HTF side and in the external air side of the pipe;
- the receiving pipe is considered to be as a single stretched pipe;
- metal pipe and fin temperature is assumed to be uniform at each node, according to the assumption of lumped thermal capacitance.

The hypothesis of lumped capacitance is quite stringent and not always valid: in order to be sure that the assumption will not cause errors, the Biot number is calculated both on the HTF and air side for each element of the pipe. The Biot number in fact provides a measure of the temperature drop in a solid exposed to convection, relative to the temperature difference between the surface and the fluid [30]. The dimensionless Biot number is defined as follows:

$$Bi = \frac{hL}{k} \tag{3.3}$$

If $Bi \ll 0.1$, it is reasonable to assume a uniform temperature distribution across the solid at any time during a transient process. This condition allows to assume that the resistance to conduction within the solid is much less that the resistance to convection across the fluid boundary layer, and hence the assumption of uniform temperature is reasonable. The Biot number therefore is calculated in the model for the solid system made up of the metal pipe and the side fins linked to it; whenever the condition $Bi<<0.1$ is not satisfied during simulation, the model stops and an error message is displayed.

The model could be considered as a *white box* as all phenomena occurring within the component are studied referring to physical equations, but the fact that many of these rely on empirical coefficients or correlations leads to consider it as a *grey box*. In the following section a description of the main equations is provided as well as the methodology used in order to be able to consider a variable number of inputs and state variables of the system.

3.2.1.3 The balance equations

For each control volume (Fig. 3.4) partial differential equations in discrete form may be written for the metal pipe and HTF respectively with proper boundary conditions, based on application of energy conservation. These equations have to be linked together in a system, depending on the number of volumes considered.

In Fig. 3.6 a very simple collector is considered where the longitudinal discretization is based on 3 elements only (n_x=3).

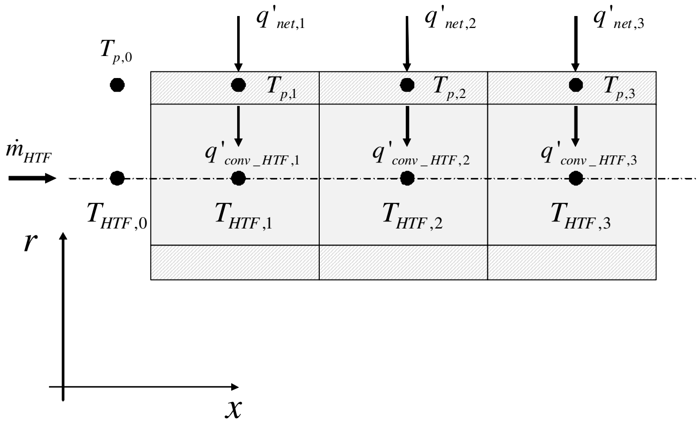

Fig. 3.6. Receiving pipe with three axial nodes.

Energy balance at each node of the system leads to the following set of six (2×n_x) equations:

$$\begin{cases} q'_{net,1} - q'_{conv\_HTF,1} = m_p c_{p_{p,1}} \dfrac{\partial T_{p,1}}{\partial t} \\ q'_{net,2} - q'_{conv\_HTF,2} = m_p c_{p_{p,2}} \dfrac{\partial T_{p,2}}{\partial t} \\ q'_{net,3} - q'_{conv\_HTF,3} = m_p c_{p_{p,3}} \dfrac{\partial T_{p,3}}{\partial t} \\ q'_{conv\_HTF,1} - \dot{m}_{HTF} c_{p_{HTF,1}} \left(T_{HTF,1} - T_{HTF,0}\right) = m_{HTF} c_{p_{HTF,1}} \dfrac{\partial T_{HTF,1}}{\partial t} \\ q'_{conv\_HTF,2} - \dot{m}_{HTF} c_{p_{HTF,2}} \left(T_{HTF,2} - T_{HTF,1}\right) = m_{HTF} c_{p_{HTF,2}} \dfrac{\partial T_{HTF,2}}{\partial t} \\ q'_{conv\_HTF,3} - \dot{m}_{HTF} c_{p_{HTF,3}} \left(T_{HTF,3} - T_{HTF,2}\right) = m_{HTF} c_{p_{HTF,3}} \dfrac{\partial T_{HTF,3}}{\partial t} \end{cases} \tag{3.4}$$

where variables have the following meaning:

- q'_{net} is the heat exchanged between the pipe and the external environment: with reference to Fig. 3.4, for a generic element of the pipe at an axial abscissa *x*, is:

$$q'_{net}(x) = q'_S(x) + q'_f(x) - q'_{rad,p}(x) - q'_{conv,p}(x) \tag{3.5}$$

where $q'_f(x)$ is the overall thermal contribution of the fins;

- $q'_{conv,HTF}$ is the heat exchanged between the pipe and the heat transfer fluid flowing within it. In steady state condition, at a generic axial node *x*, is:

$$q'_{conv,HTF}(x) = q'_{net}(x) \tag{3.6}$$

- m_p is the total mass of the pipe and its linked fins; for a discrete element of length Δx is:

$$m_p = \rho_{p,x} S_p c_{p_{p,x}} \Delta x \tag{3.7}$$

where S_p is the actual surface of the cross section of pipe and its linked fins (Fig. 3.2);

- m_{HTF} is the total mass of the fluid contained within each element of pipe; for a discrete element of length Δx is:

$$m_{HTF} = \rho_{HTF,x} S_{HTF} c_{p_{HTF,x}} \Delta x \tag{3.8}$$

where S_{HTF} is the pipe internal cross section (Fig. 3.2).

The system of equations (3.4) can be rearranged and written, in matrix form, as:

$$\left|\Phi\right|_{6,1} = \left|K\right|_{6,6} \cdot \left|\dot{T}\right|_{6,1} \tag{3.9}$$

where *Φ* is the nodal thermal flux vector, *K* is the heat capacitance matrix and $\dot{T}$ is the vector containing the nodal temperature derivatives. Eq. (3.9) represents the State Equation for the three nodes collector: at each time of simulation the state of the system is known and the only unknowns are the time derivatives of the state variables. It is possible to rewrite it according to the finite difference approach (Eq. (3.2)) as follows:

$$\frac{\partial T_p}{\partial t} \simeq \frac{T_p\big|_{t+\Delta t} - T_p\big|_t}{\Delta t} \tag{3.10}$$

$$\frac{\partial T_{HTF}}{\partial t} \simeq \frac{T_{HTF}\big|_{t+\Delta t} - T_{HTF}\big|_t}{\Delta t} \tag{3.11}$$

Substituting the previous in Eq. (3.9) the only unknowns become the values of the state variables at the next step of simulation (time discrete simulation) which can be defined once a time interval *Δt* is defined (system parameter).

It is clear that the number of unknowns at each time steps is consistent with the number of balance equations written, and the system can be solved performing some matrix calculations, including matrix inversions.

The vector of unknowns for the simple collector with three axial nodes is provided below:

$$\begin{bmatrix} T_{p,1}\big|_{t+\Delta t} \\ T_{p,2}\big|_{t+\Delta t} \\ T_{p,3}\big|_{t+\Delta t} \\ T_{HTF,1}\big|_{t+\Delta t} \\ T_{HTF,2}\big|_{t+\Delta t} \\ T_{HTF,3}\big|_{t+\Delta t} \end{bmatrix} \tag{3.12}$$

The system of equations (3.4), obtained for a collector with only three nodes, can be rewritten for a generic solar collector where a higher number of nodes is defined. If n_x is the number of discrete elements, the system features a number of equations equal to the number of state variables, that are 2×n_x, with the following form:

$$\left|\Phi\right|_{2\cdot n_x,1} = \left|K\right|_{2\cdot n_x,2\cdot n_x} \cdot \left|\frac{T\big|_{t+\Delta t} - T\big|_t}{\Delta t}\right|_{2\cdot n_x,1} \tag{3.13}$$

In Fig. 3.7 a scheme of the way the model operates to set up the system of equations (3.13) and to solve it is reported.

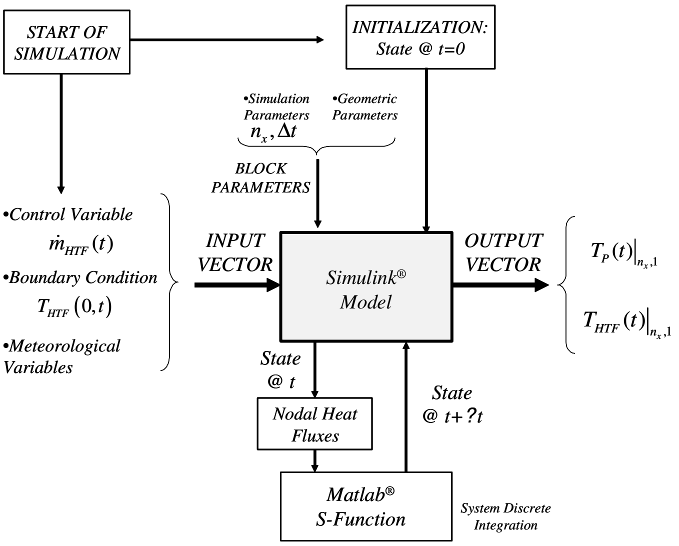

Fig. 3.7. Flow diagram of the main procedures of the model performed at each time step of simulation.

The core of the system is the Simulink® model, which also represent the model graphical interface.

At start of simulation the system initialization procedure provides the system with the initial value of the state variables. The Simulink® block recalls at each time step of simulation the S-Function which also dialogs with external functions that perform the calculation of the thermal fluxes at each node; again this calculation is realized in matrix form. A detailed description of the equations used to determine the net value of the heat fluxes is given in the next section.

The Matlab® script compiled within the S-Function allows to define, at each time step of simulation, the system of equations (3.13). The procedure is parameterized with reference to the number of thermal nodes considered (n_x) which constitutes a parameter for the Simulink® block in order to allow the simulation. Another block parameter is the discrete time step of integration Δt used by the discrete state S-function to perform the integration of the system and to calculate the state vector at the next time step. The internal procedure of numerical integration is able to operate regardless of the Simulink® solver integration time step. The S-Function therefore provides the Simulink® block with the value of the state variables at simulation time $t+\Delta t$.

The whole procedure is also influenced by the instantaneous value of the input variables, previously described. The *HTF* mass flow rate has been ticked in Fig. 3.7 as a control variable. In the physical system in fact a variation of the outputs (i.e. the fluid temperature at the collector outlet) is usually achieved by acting on the amount of fluid circulating within the collector, through proper fluid control devices (pumps or valves). This allows to respond to changes of the uncontrollable external inputs, such as the solar irradiation.

The model produces an output vector containing the temperatures of both the receiving pipe and the heat transfer fluid at each node of discretization.

Further parameters to be provided to the block are geometric data. These include pipe length (*L*), inner and outer diameter (d_{in}, d_{out}), fin length and thickness (l_f, t_f), pipe orientation, pipe material, type of selective absorber and type of heat transfer fluid.

These parameter, as well as the simulation parameters (n_x and Δt) are introduced through a block mask, shown in Fig. 3.8 (b). Fig. 3.8 (a) shows instead the Simulink® interface of the realized solar collector model. All the meteorological variables but the actual irradiance are provided within a vector. The solar irradiance has is in fact a special input whose vectorial dimensions and whose behaviour with time may follow special patterns (as in the case cloud passage is simulated, as from Fig. 3.14-Fig. 3.16.

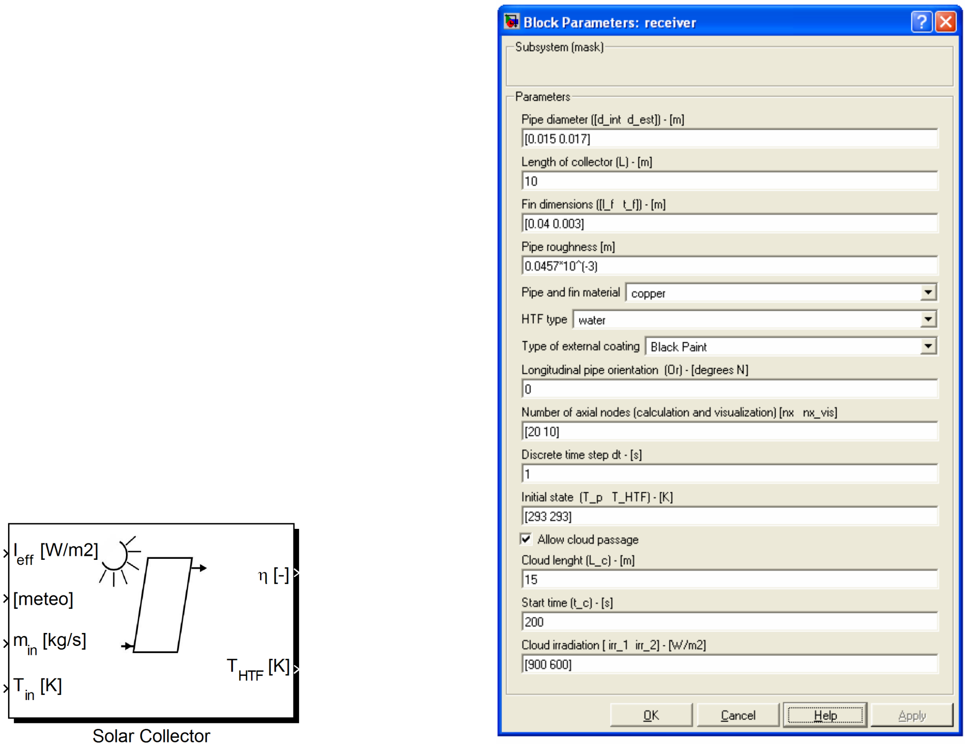

Pipe diameter ([d_int d_est]) - [m]: [0.015 0.017]
Length of collector (L) - [m]: 10
Fin dimensions ([l_f t_f]) - [m]: [0.04 0.003]
Pipe roughness [m]: 0.0457*10^(-3)
Pipe and fin material: copper
HTF type: water
Type of external coating: Black Paint
Longitudinal pipe orientation (Or) - [degrees N]: 0
Number of axial nodes (calculation and visualization) [nx nx_vis]: [20 10]
Discrete time step dt - [s]: 1
Initial state (T_p T_HTF) - [K]: [293 293]
☑ Allow cloud passage
Cloud lenght (L_c) - [m]: 15
Start time (t_c) - [s]: 200
Cloud irradiation [irr_1 irr_2] - [W/m2]: [900 600]

(a) (b)

Fig. 3.8. Simulink® model of the thermal solar collector (a) and block dialog mask (b).

3.2.1.4 Heat transfer equations

In the procedure proposed for the dynamic simulation of the solar collector, the Matlab® S-Funcion (where the system of partial differential equations is written and numerically integrated) calls external functions that perform the calculation of the heat fluxes, based on the instantaneous value of the HTF and pipe temperatures and on the value of the external inputs.

The effects of the local flow conditions are taken into account by calculating the local convection coefficients at each node on the basis of the local nodal temperature and the fluid flow conditions. Indeed the finest is the discretization the more acceptable is the approximation of assuming constant heat transfer coefficients over the discrete volume.

Values of heat fluxes are then provided to the S-Function in a proper format in order to allow placing the terms in the correct position within the main solving system of Eq. (3.13). Again the entire procedure of calculation of the heat fluxes is parameterized on the number of thermal nodes defined.

The heat transfer equations therefore are solved in matrix form in order to provide the main solving system with a vector of values consistent with the number of state variables.

The main equations used for heat transfer calculations have been obtained from literature [10,30] and are briefly described below for the receiving pipe.

- Convective heat transfer between pipe and heat transfer fluid:

$$q'_{conv,HTF} = h_{HTF}\left(T_p - T_{HTF}\right) \tag{3.14}$$

where the convection heat transfer coefficient can be determined from the dimensionless Nusselt number:

$$Nu = \frac{h_{HTF} D}{k_{HTF}} \tag{3.15}$$

At each node the Nusselt number is calculated depending on whether the flow is laminar or not: in case of laminar flow *Nu*=4.36 while in case of transitional and turbulent flow regime (Re>2300) Nusselt number can be determined from the Gnielinski correlation [10]:

$$Nu_{HTF} = \frac{(f/8)(\mathrm{Re}-1000)\,\mathrm{Pr}_{HTF}}{1+12.7\sqrt{f/8}\left(\mathrm{Pr}_{HTF}^{\;2/3}-1\right)} \tag{3.16}$$

where *f* is the friction factor.

- Convective heat transfer between pipe and external air:

$$q'_{conv,p} = \overline{h}_{air}\,x\left(T_p - T_{air}\right) \tag{3.17}$$

The profile of the pipe has been assumed as a flat slab in case of longitudinal air stream and the properties are calculated at film temperature.

The local convection heat transfer coefficient can be determined from the local Nusselt number:

$$Nu_x = \frac{h_x x}{k_{air}} \tag{3.18}$$

Once again at each node the Reynolds number is calculated and the Nusselt number is determined depending on the flow conditions.

In case of laminar flow:

$$Nu_x = 0.332 \,\mathrm{Re}_x \,\mathrm{Pr}^{1/3} \quad \mathrm{Pr} > 0.6 \tag{3.19}$$

In case of turbulent flow:

$$Nu_x = 0.0296 \,\mathrm{Re}_x^{4/5} \,\mathrm{Pr}^{1/3} \quad 0.6 < \mathrm{Pr} < 60 \tag{3.20}$$

- The radiative losses are calculated for long concentric cylinders under the hypothesis of radius of external cylinder being much bigger than internal cylinder.

$$q_{rad} = \varepsilon_p \sigma \pi \frac{d_{out}}{2} \left(T_p^{\,4} - T_{sky}^{\,4} \right) \tag{3.21}$$

The external cylinder, which receives heat through radiation from the collector pipe, is the ‘sky’, and the ‘sky’ temperature has to be calculated:

$$T_{sky} = -100.4 + 1.269 T_{air} \tag{3.22}$$

The net heat from finned surfaces measures the actual heat that contributes heating the receiving pipe and in turns the heat transfer fluid.
For each fin placed aside the receiving pipe, the following correlation may be written:

$$q'_{f1} = q'_S - q'_{conv,f} - q'_{rad,f} \tag{3.23}$$

The different terms that appear in the previous equation can be calculated according to correlations analogous to those proposed for the receiving pipe. The heat transfer equations are defined assuming a fin temperature equal to the pipe temperature, which is consistent with the hypothesis of lumped capacitance for the pipe and fins body (i.e. no heat resistance to conduction has been assumed between fin and pipe).

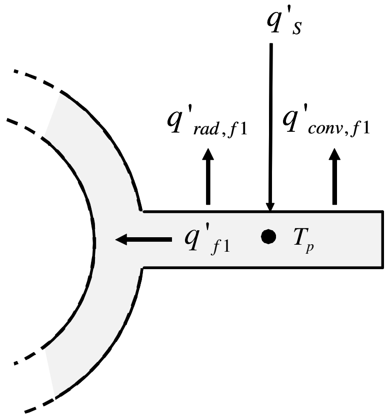

Fig. 3.9. Heat fluxes in the fins.

3.2.1.5 Model validation

To assess the validity of the proposed model the results of some simulations have been compared to data gathered from a test facility where a real solar collector have been tested.

These data derive from literature: in a study by Tripanagnostopoulos et. al. [9] experimental results from testing of three flat plate solar collectors with black, blue red and brown absorber, with and without glazing are presented. The purpose of the study was to compare the different types of external colouring and for different collector types, in order to evaluate experimentally the effect of differently coloured absorbers on the collector efficiency. One of the collectors tested has geometric characteristics compatible with the presented model. Such collector is unglazed with back insulation, made with copper pipes with 0.01m internal diameter and 0.012m external diameter, placed parallel at a distance 0.08m each other and in thermal contact with a thin copper fin. The collector has been coloured externally with black paint.

The collector described was purposely constructed for the experiment and was tested outdoors, in steady state operating conditions during noon, with variable input water temperature while the water mass flow rate was fixed to 0.02kg/s. Thermocouples were used to measure input and output temperatures, as well as some intermediate temperatures. Solar radiation intensity at the collector plane and wind speed were also measured during the experiment. Solar irradiation q''_S was always greater than 800W/m^2 and wind speed u_W was below 2m/s.

From the data recorded graphs have been created for each type of collector were the collector steady state efficiency ($\eta_C = \frac{\dot{m}_{HTF} c_{P_{HTF}} \left(T_{out} - T_{in}\right)}{q"_S \, S_C}$) has been plotted as function of the ratio $\frac{\Delta T}{q"_S} = \frac{\left(T_{in} - T\right)}{q"_S}$. The collector efficiency measures the amount of the solar energy to the collector effectively transferred to the fluid.

The geometric parameters of the real collector described in [9] have been introduced into the model, black paint has been considered for external collector colouring and the same inputs as the real system have been considered for the simulation (meteorological data and fluid mass flow rate). A set of simulations have been performed with different water inlet temperatures and the steady state model outputs have been used to calculate the collector efficiency. Values obtained from the model have been plotted in the graph of Fig. 3.10 which also reports the curve of the measured data.

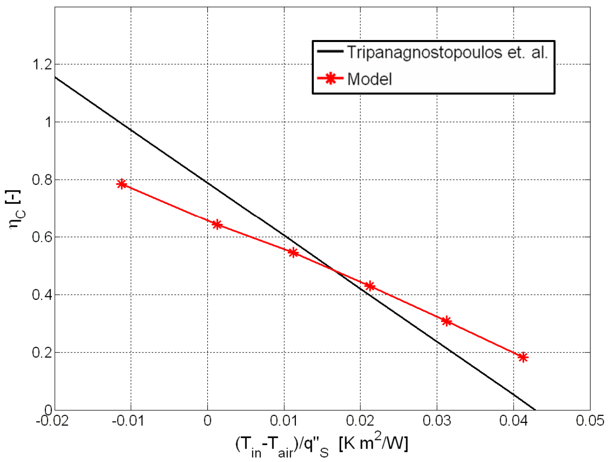

Fig. 3.10. Steady state efficiency results of the tested collector and the model.

To assess the accuracy of the model with respect to the result from the real collector, the actual model output were compared with the output of the real system. Model output (the fluid temperature at collector outlet) was compared with the fluid temperature leaving the real collector. The error ($\varepsilon_{abs} = T_{out}\big|_{\exp} - T_{out}\big|_{\mathrm{mod}}$) is displayed in Fig. 3.11 (a): it can be observed that an absolute error of only few degrees Kelvin in the fluid temperature exists between the experimental data and results from the model:

In Fig. 3.11 (b) the relative error is plotted, as:

$$\varepsilon = \frac{T_{out}\big|_{\exp} - T_{out}\big|_{\mathrm{mod}}}{T_{out}\big|_{\exp}} \cdot 100 \tag{3.24}$$

The agreement between the results from the model and the data from the experimental facility appears good, confirming that the correlations used to describe the main heat transfer phenomena occurring within the collector are appropriate. It also demonstrates the validity of the method used to create and solve the system of equations, at least in steady state conditions. Unfortunately a validation of the behaviour of the model under unsteady condition has not been possible so far for the lack of experimental data.

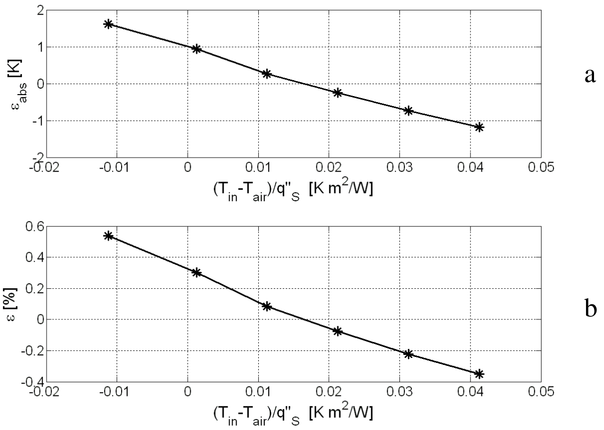

Fig. 3.11. Absolute error (a) and relative error (b) between fluid outlet temperature measured from experimental setup and calculated from the model.

3.2.1.6 Simulations

Following the described validation, some simulations have been performed with the model proposed. Among the several inputs that may affect the behaviour of the system indeed the HTF mass flow rate circulating through the collector and the net solar irradiation are those that have major effects in determining changes in the fluid outlet temperature, which represent the main output variable. Results of two simulations are therefore proposed in this section.

In the first simulation a step change in the fluid mass flow rate is imposed. At simulation time *t*=2000s the mass flow rate circulating within the receiving pipe suddenly decreases from the initial value of 0.025kg/s to 0.015kg/s, as shown in Fig. 3.12 (a). In this case the solar radiation has been assumed to be uniform and equal to 1000W/m^2.

The collector under analysis is characterized by a 20m long copper receiving pipe with high performance black-chrome selective absorber; the heat transfer fluid is water.

As initial condition (model initialization) it is assumed collector and HTF temperature equal to 293K; as boundary condition the HTF temperature at the receiver inlet section is set again at 293K during the whole duration of simulation.

The model has been simulated referring to an axial discretization Δx=2m (n_x=10) and a time discretization Δt=5s (simulation parameters).

The response of the system to the step change in the fluid mass flow rate is shown in Fig. 3.12 (b), where the temperature of the fluid, as well as of the receiving pipe, are plotted with respect to time: both temperatures refer to the outlet section of the receiver. It can be observed that, starting from the same temperature for both pipe and HTF at *t*=0s (model initialization), a sudden increase in the pipe temperature allows the HTF temperature to rise, but at a slower rate. Steady state conditions are reached after about 1000s of simulation. When the step change in the HTF mass flow rate circulating within the pipe is imposed, a new transient condition in the fluid and pipe temperature can be observed; the reduced mass that circulates within the receiver allows a further rise in the temperatures.

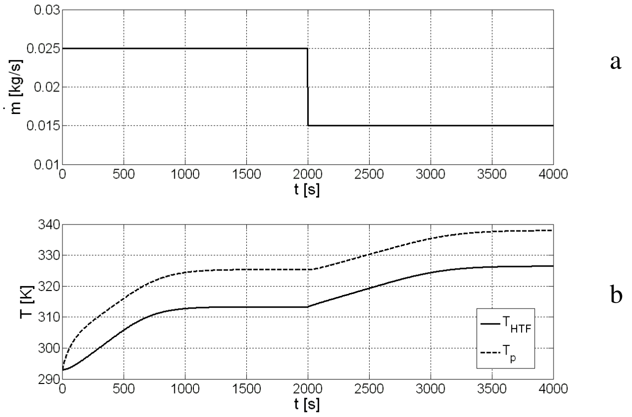

Fig. 3.12. (a) Step change in the HTF mass flow rate – (b) Response in the HTF and pipe temperature in the outlet receiver section

The procedure that has been created for simulating the thermal behavior of the solar collector allows creating more complete representations of the temperature distribution within the system and three dimensional graphs can be plotted which allow to evaluate the temperature distribution for each cross section of the pipe according to the axial discretization imposed. The model in fact returns the values of HTF and pipe temperature not only in the outlet section of the receiver but also for each axial node.

In Fig. 3.13 (a) the fluid temperature is plotted with respect to time of simulation and collector length. It can be observed that the temperature profile at the outlet section (at L=20m from inlet) corresponds to that shown in Fig. 3.12 (b), which in fact may be considered as a section of the three-dimensional plot of Fig. 13. It can also be noticed how the temperature profile in the first node (at a distance L=2m from inlet) is almost flat and close to the water entering temperature set to 293K.

An analogous pattern of the temperatures, with respect to time of simulation and receiver length, is proposed in Fig. 3.13 (b) for the pipe.

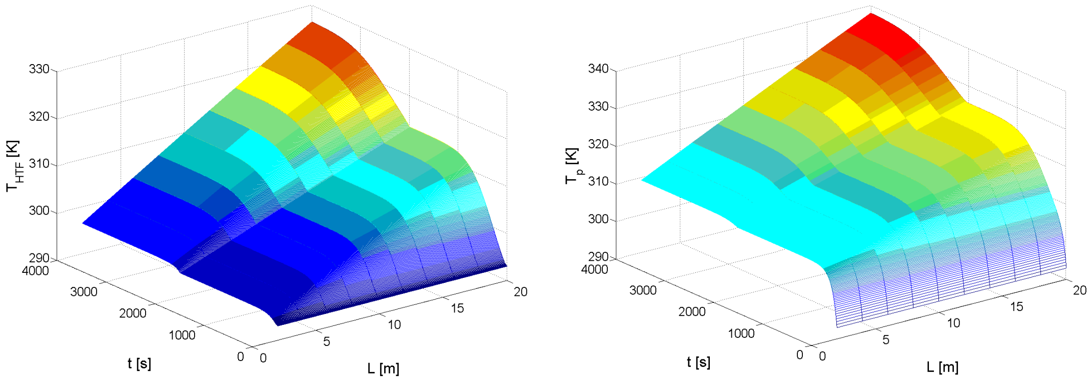

(a) (b)

Fig. 3.13. Temperature distribution of the heat transfer fluid (a) and pipe wall (b) due to a step change in the HTF mass flow rate, as function of time and distance from collector inlet.

In the second set of results here presented, which refer to the same collector described above, the heat transfer fluid mass flow rate has been assumed to be constant and equal to 0.02kg/s, while a variation with time in the solar radiation has been considered (Fig. 3.15 and Fig. 3.16).

The results reported allow to assess the effects on the fluid and pipe temperatures due to clouds passage, imposed at simulation time t=250s, which determines a sharp decrease in the solar radiation to the collector, as shown in Fig. 3.14 where net solar radiation is plotted with respect to time of simulation and collector length. Cloud shade is assumed to be 15m long and with a speed of 0.5m/s: the solar irradiation at clear sky condition is assumed 1100W/m^2 and the value decreases to 300W/m^2 when cloud is passing. The cloud moves longitudinally along the collector (under the hypothesis that the receiving pipe does not make bends) and it starts shading the receiver from the inlet. It is possible to observe that at each point along the pipe the reduction in the solar radiation (as well as the subsequent increase to the original value) occur at a time that is proportional to the distance from collector inlet. A special procedure for evaluating cloud passing upon the collector has been set up and cloud parameters can be introduced in the Simulink® block dialog window (Fig. 3.8).

The three dimensional graphs allow in this case to appreciate the temperature distribution of both fluid and pipe with respect to time and space, due to the non uniform solar radiation caused by the cloud: the HTF temperature is plotted as function of time and distance from pipe inlet in Fig. 3.15 while the pipe wall temperature is reported in Fig. 3.16.

The results have also been proposed in this case with two different sets of the simulation parameters, in order to demonstrate how different degrees of discretization may be considered for the same physical system, depending on the accuracy required.

In Fig. 3.15 (a) and in Fig. 3.16 (a) a spatial discretization of Δx=4m was assumed (n_x=5, thus the solving system features 10 equations) with a time discretization Δt=50s. The computational time required for the simulation of such system is 3.2s on a Pentium® IV desktop computer.

A finer simulation is proposed in Fig. 3.15 (b) and Fig. 3.16 (b) were Δx is 0.5m (then n_x=40, with 80 equations to be solved at each time step of simulation) and Δt=1s; the time required for simulation in this case is 19.5s.

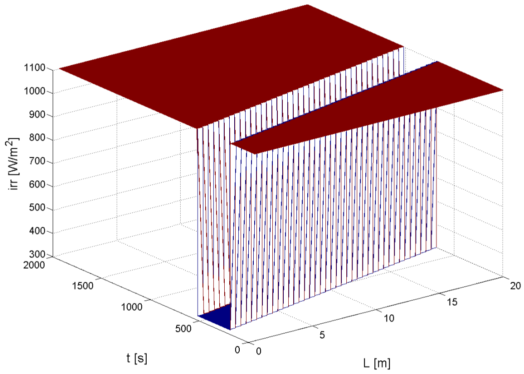

Fig. 3.14. Solar radiation to the collector due to cloud passage.

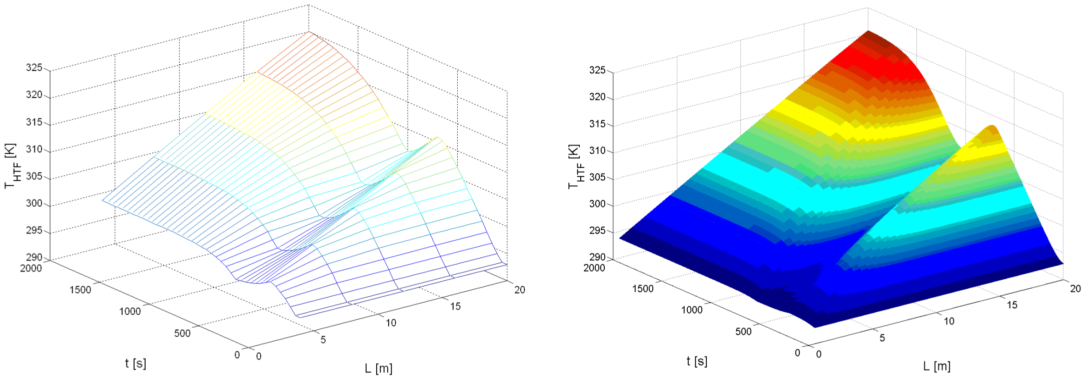

(a) (b)

Fig. 3.15. Heat transfer fluid temperature distribution during cloud passage with two different degrees of spatial and time discretization.

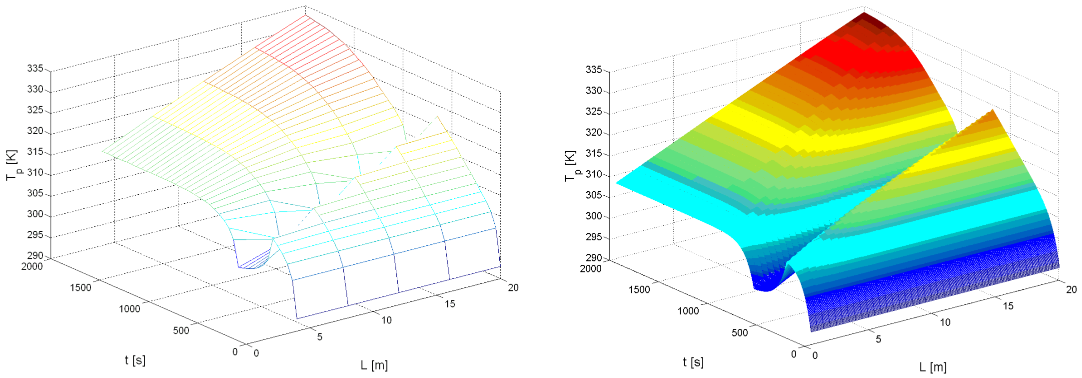

(a) (b)

Fig. 3.16. Pipe wall temperature distribution during cloud passage with two different degrees of spatial and time discretization

The results of simulation shown in Fig. 3.15 (a) and (b), for the same physical system but with different spatial and time discretization, have been compared. The plot of Fig. 3.17 has been obtained as the difference of the value of the HTF temperature calculated with the two different sets of simulation parameters, for each corresponding combination of simulation time *t* and distance from collector inlet *L*. ΔT_{HTF}, reported in the *z*-axis of Fig. 3.17, is the difference between the fluid temperature calculated through the rough discretization (n_x=5, Δt=50s) and the temperature calculated with the fine discretization (n_x=40 Δt=1s).

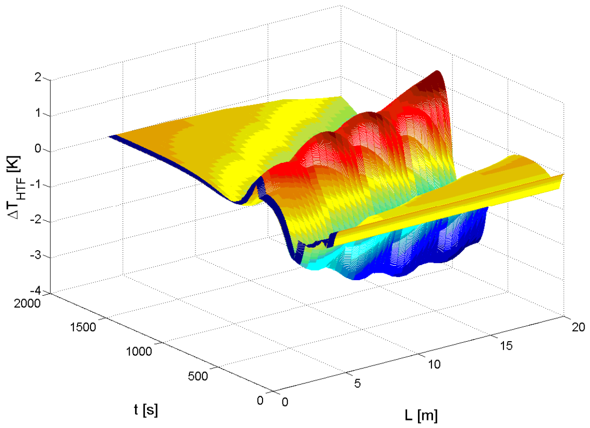

Fig. 3.17. Difference in the HTF temperature calculated with two different degrees of spatial and time discretization.

It can be observed that differences exist between the results obtained with the two sets of simulation parameters. During the transient condition caused by the cloud passing, the rough model lags a little in calculating the decrease in HTF temperature. The opposite occurs when the cloud uncovers the collector and the fine model is quicker in demonstrating the increase in the fluid temperature. This effect is certainly due to the higher time step assumed for the rough model (50 s instead than 1 s), but also the spatial discretization has some implications: the temperature difference is however contained within few degrees Kelvin.

It can also be noticed from Fig. 3.17 that the steady state values of the HTF temperature calculated with the two different degrees of discretization do not show significant difference and both models provide the same steady state fluid temperature, as can be expected.

For general applications of the model, roughest discretization degrees may therefore be accepted, also considering the much lower computational time required when the number of axial nodes is reduced and time interval is increased. Whenever precise description of transient phenomena is required, the model can provide much higher calculation performances of the same physical system, by simply tuning the simulation parameters through the block dialog mask.

3.2.2 Dynamic model of a counterflow heat exchanger with no phase change

In this section the model of a counterflow heat exchanger is presented. The model is developed under the hypothesis that the two fluids are in single phase so that they do not experience phase change while flowing through the component. Both liquid and gas phases are considered for the fluids, so the exchange may take place between a gas and a liquid, two gases or two liquids.

The exchanger has been, for sake of simplicity, represented as a typical counterflow straight pipe in pipe component, despite it is well known that different and more complex designs are usually adopted in order to enhance heat exchange and to reduce overall dimensions of the system. This assumption simplifies the resulting dynamic problem to a great extent, and is commonly adopted when heat exchanger dynamic modelling is considered [19,24].

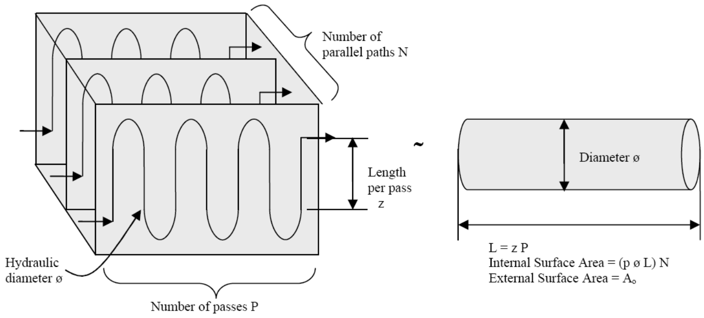

Fig. 3.18. Developement of a compact heat exchanger into a Unidirectional pipe.

This straight pipe in pipe design of the evaporator has been split into n_x longitudinal lumped volumes, each of length Δx, that are the places where the conservation equations are applied in analogy to the model of solar collector. For each discrete volume three nodes can be defined in the radial direction: one referring to the fluid within the internal pipe (referred to as *f1*) one to the state of the metal constituting the metal pipe (referred to as *p*) one referring to the state of the fluid in the annulus (*f2*), according to the scheme of Fig. 3.19. The discretization adopted therefore brings to a 2D model since variation of state parameters are evaluated both in the axial and radial direction. The discretization nodes are located at the centre of the different control cells that have been identified for the pipe and the two fluids.

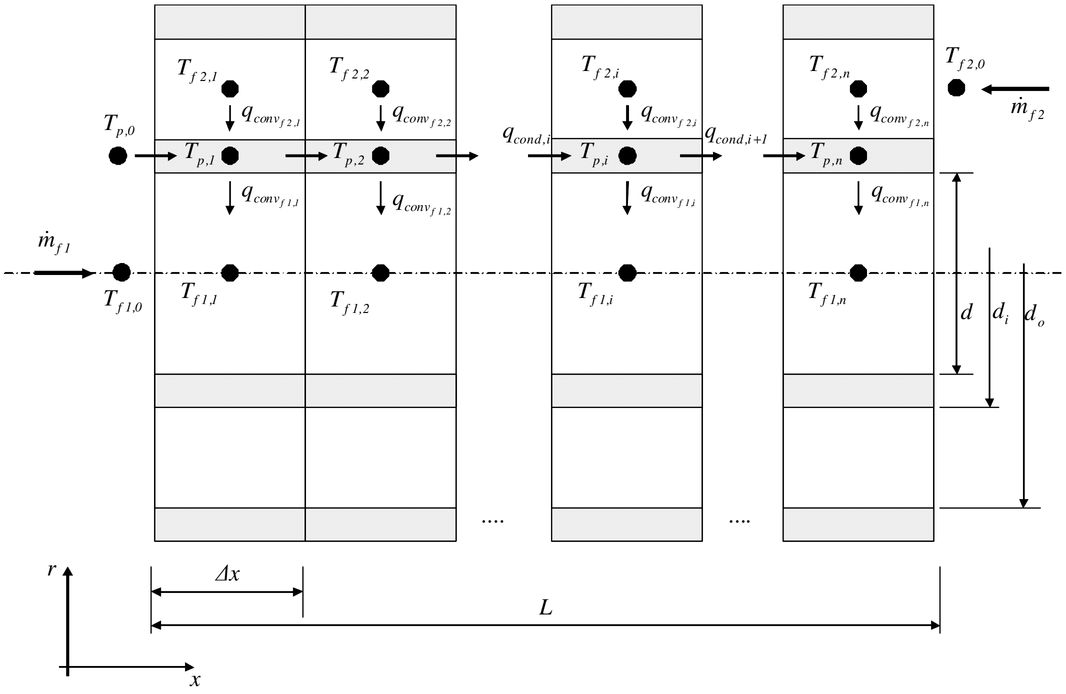

Fig. 3.19. Discretization assumed for the pipe in pipe counterflow heat exchanger and main heat fluxes involved.

The assumptions introduced in the analysis of the evaporator are the following:

- thermodynamic properties of both the metal pipe and the fluids are function of space and time;
- thermal capacitance of both the metal pipe and the fluids are considered;
- the axial conductive heat fluxes have been neglected for the fluids [25] but have been considered for the metal pipe;
- the external pipe is assumed to be ideally insulated hence heat losses are neglected;
- head losses are neglected for both the pipes; the assumed negligible pressure drop within the pipe renders redundant the momentum conservation equation that is hence not applied to the cells of fluid [24];
- heat transfer due to conduction between fluids and pipe has been neglected;
- turbulent, transitional or laminar flow are considered to model convective heat transfer for fluids;
- lumped thermal capacitance is assumed for both the metal pipe and the fluids hence just on thermal node can be defined;
- no mass accumulation is considered for the fluids;
- energy accumulation is considered in both the metal pipe and the two fluids.

This approach in representing heat exchangers is similar to that adopted in many other works as for example [26], where the dynamic model of a gas-gas counterflow heat exchanger used for regeneration of micro gas turbine cycles is proposed and modelled with an analogous approach based on axial discretization of the equivalent straight tube in tube system.

In the following pages the main cardinal equations adopted in each control volume of the system are presented.

- Anulus

As from Fig. 3.19 it can be observed that for each control volume referring to the fluid in the external annular region an energy balance equation can be applied in order to determine the associated fluid temperature. The energy fluxes involved are the convective heat exchange between the fluid and internal pipe along with the term related to transport. In this case, being the fluid assumed as incompressible and no continuity equation was applied to the different nodes (this assumption is considered valid also in case of gas, since mass accumulation has been neglected), the fluid mass flow rate entering and leaving each control volume are the same, but the temperature is different, hence a global net energy apport can be considered referring to the transport phenomena.

The overall energy balance equation at a given node *i* and time *t* is provided by the following:

$$\dot{m}_{tf2}\overline{c}_{p_{f2,i}}\left(T_{f2,i+1}-T_{f2,i}\right)-q_{conv_{f2,i}}=\overline{\rho}_{f2}V_{f2}\overline{c}_{p_{f2,i}}\frac{\partial T_{f2,i}}{\partial t} \qquad (3.25)$$

Retyping the previous differential equation according to a finite difference forward approach, given a finite time interval *Δt*, and rearranging the terms, the only unknown becomes the node temperature at new simulation time *t+ Δt*:

$$T_{f2,i}{}^{t+\Delta t} \simeq T_{f2,i}{}^{t} + \Delta t \frac{\dot{m}_{f2}{}^{t}\overline{c}_{p_{f2,i}}{}^{t}\left(T_{f2,i+1}{}^{t} - T_{f2,i}{}^{t}\right) - q_{conv_{f2,i}}{}^{t}}{\overline{\rho}_{f2}{}^{t}V_{f2}\overline{c}_{p_{f2,i}}{}^{t}} \tag{3.26}$$

- Pipe wall

Each anular control volume of the metal pipe is subject to a series of heat fluxes. Convective heat exchange takes places both in the external and internal side, with the two fluids, but axial conduction is also considered hence each control volume receives or provides heat to the neighbouring metal anuli. The overall energy balance equation, referring to the generic node *i* and at time *t*, can be written as follows:

$$q_{conv_{tf,i}} - q_{conv_{f,i}} + q_{cond_{p,i}} = \rho_{p,i}V_p\overline{c}_{p_{p,i}}\frac{\partial T_{p,i}}{\partial t} \tag{3.27}$$

where $q_{cond_{p,i}}$ expresses the net conductive heat flux at the i^{th} node.

Rewriting the previous equation the pipe nodal temperature can be determined:

$$T_{p,i}{}^{t+\Delta t} \simeq T_{p,i}{}^{t} + \Delta t \frac{q_{conv_{tf,i}}{}^{t} - q_{conv_{f,i}}{}^{t} + q_{cond_{p,i}}{}^{t}}{\rho_{p,i}{}^{t}V_p\overline{c}_{p_{p,i}}{}^{t}} \tag{3.28}$$

- Internal pipe

For each fixed in space control volume defined within the inner pipe the fluid *f1* flows receiving heat from the metal pipe with the effect of rising its temperature. Application of the energy conservation equation leads to a formulation very similar to (3.26) achieved for the annulus:

$$T_{f1,i}{}^{t+\Delta t} \simeq T_{f1,i}{}^{t} + \Delta t \frac{\dot{m}_{f1}{}^{t}\overline{c}_{p_{f1,i}}{}^{t}\left(T_{f1,i+1}{}^{t} - T_{f1,i}{}^{t}\right) - q_{conv_{f1,i}}{}^{t}}{\overline{\rho}_{f1}{}^{t}V_{f1}\overline{c}_{p_{f1,i}}{}^{t}} \tag{3.29}$$

Equations (3.26), (3.28) and (3.29) hence represent the state equation of the system. The proposed model of the evaporator is therefore state determined and the number of state parameters defined is functional to the number of axial nodes considered. The overall state parameters are therefore:

- n_x axial temperatures for the fluid in the anulus $T_{f2,i}$;
- n_x axial metal pipe wall temperatures $T_{p,i}$;
- n_x axial temperatures for the fluid in the inner pipe $T_{f1,i}$;

The mentioned state equations have been implemented in the *m-sfunction* that constitutes the core of the model and solved together leading to a linear system of partial differential equations. The system of $3\times n_x$ have been implemented in matrix form for ease of solution and computational speed due to the Matlab® capabilities of handling matrix calculations, in analogy to what seen for the thermal solar collector:

$$\left|\Psi\right|_{3n_x,1} = \left|K\right|_{3n_x,3n_x} \cdot \left|\dot{\Phi}\right|_{3n_x,1} \tag{3.30}$$

where Ψ is the nodal thermal flux vector, K is the heat capacitance matrix and $\dot{\Phi}$ is the vector containing the nodal state variables derivatives (either temperatures or enthalpies). As already observed at each time of simulation the state of the system is known and the only unknowns are the time derivatives of the state variables, hence the system corresponding to Equations (3.26), (3.28) and (3.29) is as follows:

$$\left|\Phi^{t+\Delta t}\right|_{3n_x,1} = \left|\Phi^{t}\right|_{3n_x,1} + \Delta t \frac{\left|\Psi\right|_{3n_x,1}}{\left|K\right|_{3n_x,3n_x}} \tag{3.31}$$

The model block operates in analogy to the thermal solar collector, in accordance to the scheme of Fig. 3.7. A proper set of the values of the state parameters at start of simulation is therefore required for system initialization and the vector $\left|\Phi^{t=0}\right|_{3n,1}$ containing the nodal transfer fluid and pipe temperatures must be provided.

Proper boundary conditions must also be introduced and these are represented by some of the inputs of the block, particularly $T_{f1,in}{}^{t}$, $T_{p,in}$ (this parameter is assumed not to change with time) and $T_{f2,in}{}^{t}$. The main inputs, outputs and state variables of the model are represented in the scheme of Fig. 3.20.

The system inputs are characterized by the parameter representing the two fluids at heat exchanger input, particularly their temperature, pressure and mass flow rate must be known, and the fluid pressures is introduced since many properties depend also upon pressure.

The output generated by the system can be any of the state variables but of particular interest, in the view of linking the heat exchanger to other components in a complex network, the state of the fluids leaving the exchanger must be provided, as the temperature of the two fluids. Due to the counterflow design this temperature will be the one calculated at the node with index 1 for the fluid flowing in the annulus, as from Fig. 3.19.

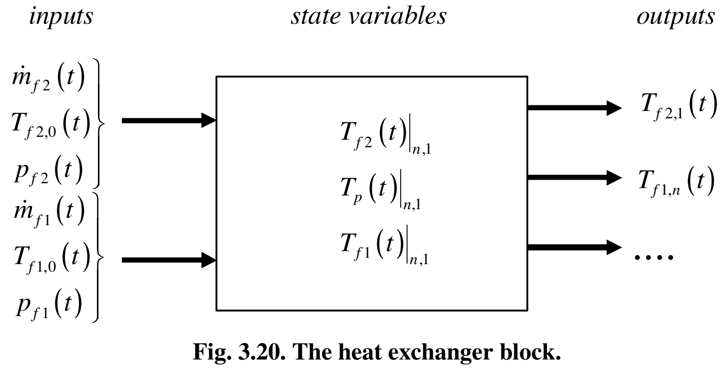

Fig. 3.20. The heat exchanger block.

Once the system has been fully defined the correlations to calculate the actual thermal fluxes must be introduced, in order to properly compile the vector K of Eq. (3.30). The section that follows illustrates therefore the main correlations adopted.

To be noted that the model of the counterflow heat exchanger, while could be considered as a *white box* model since it is based on application of conservation equations, actually recurs to empirical or semi-empirical correlations in order to numerically evaluate the actual thermal heat fluxes at each time of simulation and also an empirical form of the state equation is employed in the organic fluid side. These consideration brings to consider the model, if not as purely *black box*, as a *grey box*.

3.2.2.1 Heat flux correlations

- Convection between fluid in the annulus and pipe

According to the scheme of Fig. 3.19 the transfer fluid flows within an anular duct characterized by the diameters d_o and d_i. For such a duct it is possible to define the hydraulic diameter $d_h=4A/P$, and hence the Reynolds number:

$$Re=\frac{4\dot{m}d_h}{\pi\left(d_o^2-d_i^2\right)\mu} \tag{3.32}$$

In case of laminar flow the Nusselt number depends upon the diameter ratio: $Nu=f(D_i/D_o)$ while in case of transitional and turbulent flow the Gnielinski correlation can be adopted [30]:

$$Nu_{tf}=\frac{(f/8)(\mathrm{Re}-1000)\mathrm{Pr}_{tf}}{1+12.7\sqrt{f/8}\left(\mathrm{Pr}_{tf}^{2/3}-1\right)} \tag{3.33}$$

where f is the friction factor that, for a smooth pipe can be determined by Petukhov correlation [30]:

$$f=(0.79\ln\mathrm{Re}-1.64)^{-2} \tag{3.34}$$

The convection coefficient can then be calculated as:

$$h=\frac{Nu_{tf}\ \lambda}{D_h} \tag{3.35}$$

hence the nodal convective heat flux, as:

$$q_{conv,i}=h\left(T_{f2,i}-T_p\right)\pi d_i\Delta x \tag{3.36}$$

- Axial pipe wall conduction heat flux

Fourier law has been applied to the bounding pipe control volumes in order to take into account the axial heat flow that may be, in some cases, not negligible:

$$q''_{cond} = -\lambda_p \left(\frac{\partial T}{\Delta x} \right)_p \tag{3.37}$$

The previous can be rewritten according to finite difference approach and at a given time of simulation for the generic node *i*, the net conductive heat flux can be defined by the following:

$$q_{cond,i} = -\lambda_p \left(\frac{T_{p,i} - T_{p,i-1}}{\Delta x} + \frac{T_{p,i} - T_{p,i+1}}{\Delta x} \right) \frac{\pi \left(d_i^2 - d_o^2 \right)}{4} \tag{3.38}$$

- Convection between pipe and fluid in the inner pipe

The approach is similar to that adopted for the anular region, where the fluid is always assumed to be single phase and Nu=4.36 in the laminar region otherwise the Gnielinsky correlation (3.33) applies. Equation (3.36) still remains valid to compute the actual convective heat flux with reference to proper heat exchange surface:

$$q_{conv,i} = h\left(T_p - T_{f1}\right) \pi d \Delta x \tag{3.39}$$

3.2.2.2 The Simulink® model

The Simulink® model of the evaporator has been realized through the compilation of a specific *m-sfunction* where the overall system of equation in matrix form (3.30), are compiled and solved. As seen the number of equations that constitutes these two systems is a function of the number of nodes n_x into which the evaporator has been discretized (n_x) which is therefore a very important parameter of the block and is widely utilized within the constituting *s-function* in order to preallocate properly the dimension of the different matrixes and vectors that have to be filled with the different heat fluxes and thermal nodal capacitances

Fig. 3.21 (a) depicts the Simulink® model of the realized heat exchanger and Fig. 3.21 (b) reports the block dialog window. It is possible to observe that many parameters have to be provided in order to characterize both the component and the discretization procedure.

A first set of parameters are required in order to specify which fluids will have to be used as heat exchanging media, the material adopted for the metal pipe and many geometric parameters that define the evaporator design.

Next some important discretization parameters need to be provided, as the number of nodes n_x considered for axial discretization. As for the thermal solar collector (Par.3.2.1) the user can in fact set the "quality" of the geometric discretization. Since the differential equations, expressed as time derivatives of the state variables, have also been discretizred in time according to the finite difference forward approach, the discrete time step interval *Δt* has also to be provided. The block therefore will be called by Simulink® solver only at the specified time interval. This approach is typical of discrete solution methods.

The last set of parameters required by the block, being the system aimed at numerically integrating in time a set of differential equations, is the system initialization that is the value of the state parameters at time *t=0*. For sake of simplicity just one value is provided for each category of state parameters and that value is then adopted and propagated to all the nodes.

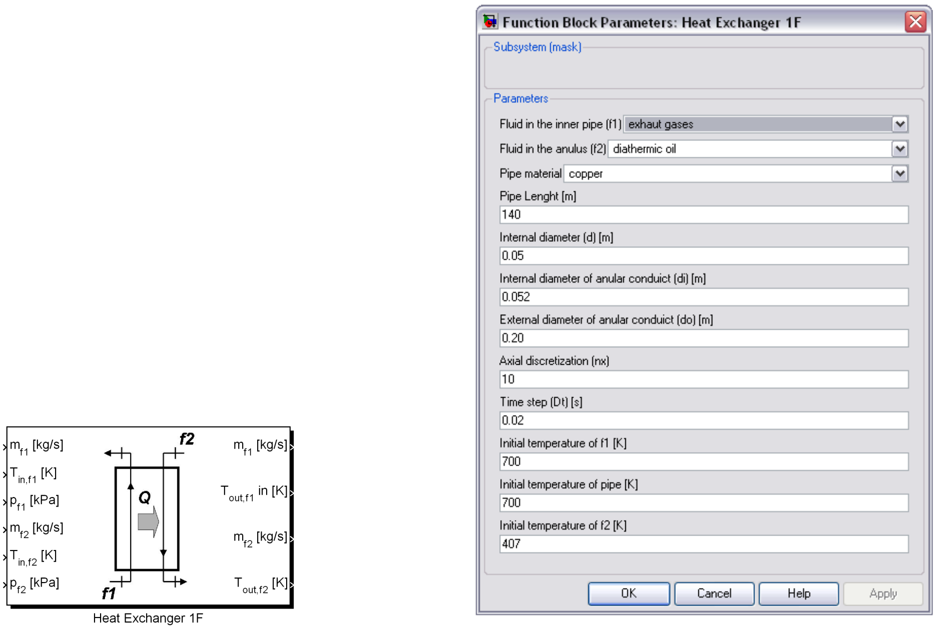

Function Block Parameters: Heat Exchanger 1F

Fluid in the inner pipe (f1): exhaut gases
Fluid in the anulus (f2): diathermic oil
Pipe material: copper
Pipe Lenght [m]: 140
Internal diameter (d) [m]: 0.05
Internal diameter of anular conduict (di) [m]: 0.052
External diameter of anular conduict (do) [m]: 0.20
Axial discretization (nx): 10
Time step (Dt) [s]: 0.02
Initial temperature of f1 [K]: 700
Initial temperature of pipe [K]: 700
Initial temperature of f2 [K]: 407

(a) (b)

Fig. 3.21. Simulink® model of the heat exchanger with no phase change (a) and block dialog mask (b).

Examples of simulations of the model are provided in Chapter 5 where the component is applied to the combined ICE-ORC system and used to transfer the heat available in the engine exhaust gases to a diathermic oil that is then fed to the ORC.

3.2.3 Dynamic model of a counterflow heat exchanger with phase change

Following the single phase heat counterflow heat exchanger a counterflow evaporator or condenser is here presented. The overall geometry of the heat exchanger is similar to the one presented in Par. 3.2.2 but it is now considered the possibility for the fluid flowing in the internal pipe to undergo phase change. This kind of components are key elements in defining the dynamics and overall behaviour of vapour cycles (particular attention is paid within this Thesis to Organic Rankin Cycles, but this model can be used also for steam cycle or heat pumps). Whit reference to ORCs in fact it should be observed that while models of pumps and turbines are readily available in literature and the methodology for their representation based on performance maps is quite uniquely accepted, the correct representation of dynamics in evaporator and condenser is not straightforward [21] and different approaches can be adopted.

The one chosen here, analogous to the one presented for the simple heat exchanger, is based on the finite difference method by applying the energy conservation and mass conservation equations in differential form. The model should be characterized by a sufficient flexibility such to allow simple generalization of the design since the evaporator is the crucial component in determining the overall dynamic and behaviour of ORCs.

Again the straight pipe in pipe design of the heat exchanger has been split into n_x longitudinal lumped volumes, each of length Δx, that are the places where the conservation equations are applied. For each discrete volume three nodes can be defined in the radial direction: one referring to the state of the transfer fluid in the annulus, one to the state of the metal constituting the metal pipe and one referring to the organic fluid within the internal pipe (if the exchanger is intendended for applications within Organic Rankine Cycles, as in the examples that will follow), according to the scheme of Fig. 3.22.

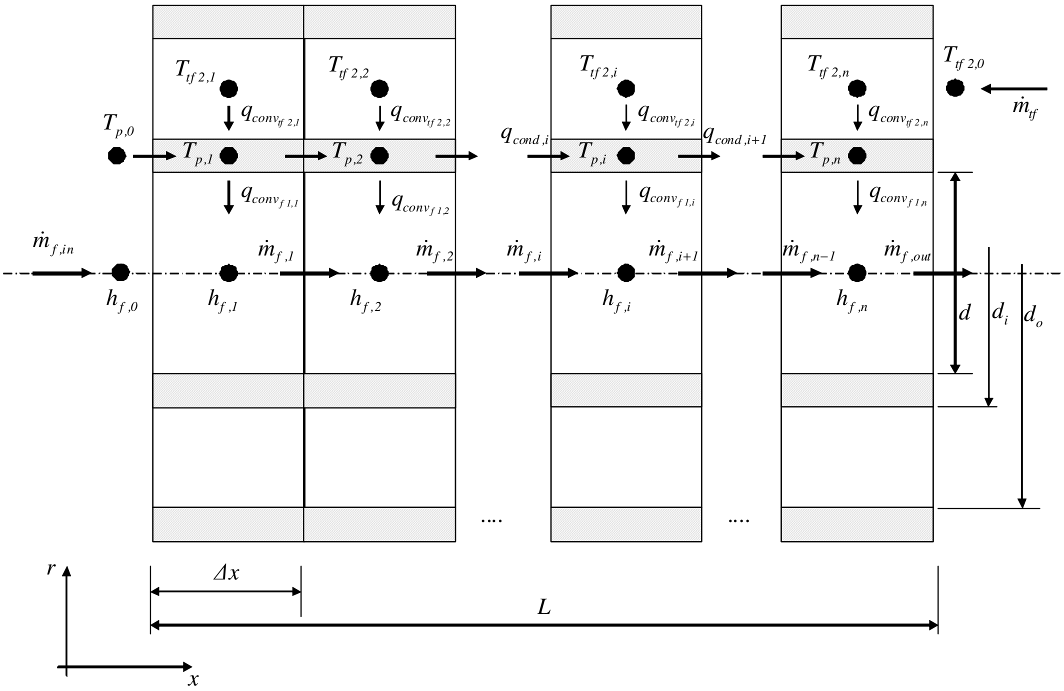

Fig. 3.22. Discretization assumed for the pipe in pipe counterflow heat exchanger with phase change and main heat fluxes involved.

The assumptions adopted in the analysis are similar to those imposed in the case of simple heat exchanger with no phase change but now mass conservation equations are also applied in the internal pipe: it has been assumed that mass can be accumulated within the lumps of the pipe containing the organic fluid due to the significant density variations that occur along the pipe due to transition from subcooled liquid to vapour.

The literature proposes similar approaches in representing dynamic behaviour of evaporators or condensers. In [19] for example it is briefly described a discretized model for the evaporator of an organic Rankine cycle. The approach is quite similar to the one adopted here but in that case the momentum equation has been also applied to the entire inner pipe length, that is the momentum equation has not been applied for each cell of the discretized pipe but just one momentum balance has been considered for the entire mass contained within the pipe in order to determine the actual pressure existing in the pipe. A different approach has been considered here for determining the pressure living within the pipe and its evolution with time related to the conditions existing within the pipe and the hot drum is introduced for the scope (see next Paragraph).

Another interesting work on the topic is [27] where a very detailed numerical simulation of the thermal and fluid dynamic behaviour of a double pipe heat exchanger to be used as either evaporator or condenser is proposed. The governing equations applied are again momentum, continuity and energy conservation inside the internal tube and the annulus, together with energy conservation for the pipe, analogously to what proposed here. The model proposed in [27] however is much more detailed since further radial nodes are considered. Energy conservation equations have in fact been applied to the external tube and insulation, hence dropping the hypothesis of ideally insulated system, plus a finer representation of their temperature is achieve by introducing a radial discretization. The procedure, while substantially similar to the one proposed here, is much more accurate but it was believed that, for the scope of the present work, the rougher discretization proposed could be sufficient to provide an enough accurate picture of the main dynamical phenomena taking place within the evaporator.

The cardinal equations applied to the presented model of evaporator with phase change are substantially similar to the ones introduced for the exchanger with no phase change in Par 3.2.2 for the fluid in the annulus (that is here assumed to be always single phase) and to the metal pipe, and Equations (3.25)-(3.28) still apply.

Important differences are instead introduced to the cells comprised in the internal pipe since now the fluid is assumed to be able to experience phase change and mass accumulation can take place. The cardinal equations considered for the internal pipe are then described, and the case of an evaporator is described even though analogous considerations can be made for a condenser.

- Internal pipe

For each control volume fixed in space defined within the internal pipe, where the organic fluid flows and exchanges heat with the metal pipe in order to evaporate or condensate, either the energy conservation equation and the continuity equation are applied, the latter being necessary to determine the actual fluid mass flow rate flowing out each control volume. The heat provided to the fluid has the effect of rising the liquid temperature, in the first part of the metal pipe and then to vaporize it and eventually to superheat the vapour, if the pipe dimensions and the thermal flow would allow for that. From when the organic fluid begins to change its phase the density can no longer be considered constant and at each node but decreases significantly, and the actual fluid mass stored in each control volume will be substantially different. For these reasons, under unsteady phenomena (i.e. in the startup when the fluid starts to vaporize or at any time when there is a change in one of the inputs of the systems) the fluid mass flow rate entering and leaving each control volume may be different. With reference to Fig. 3.23, considering the i^{th} node of the pipe, $\dot{m}_{f_{i-1}} \neq \dot{m}_{f_i}$.

The continuity equation can be expressed in the following differential form at the i^{th} node of the pipe and at time t:

$$\dot{m}_{f,i-1} - \dot{m}_{f,i} = V \frac{\partial \rho_i}{\partial t} \tag{3.40}$$

and recurring to the backward finite difference approach the mass flow rate leaving each node can be calculated as follows:

$$\dot{m}_{f,i}{}^{t} \simeq \dot{m}_{f,i-1}{}^{t} - V\frac{\rho_i^{t} - \rho_i^{t-\Delta t}}{\Delta t} \tag{3.41}$$

Solving the continuity equation first is necessary since the organic fluid mass flow rate entering and leaving each cell of the pipe is required, for the energy balance that can be defined by the following equation, expressed in enthalpy form for convenience:

$$q_{conv_{tf,i}} + \dot{m}_{f,i-1}h_{f,i-1} - \dot{m}_{f,i}h_{f,i} = V_f\frac{\partial\left(\rho_{f,i}h_{f,i} - p_f\right)}{\partial t} \tag{3.42}$$

Neglecting the term $V_f\frac{\partial p_f}{\partial t}$, passing to the finite difference and extracting the unknown, it is possible to obtain the following equation, where $\dot{m}_f = \rho_f V$:

$$h_{f,i}{}^{t+\Delta t} \simeq h_{f,i}{}^{t} + \Delta t\frac{q_{conv_{f,i}}{}^{t} + \dot{m}_{f,i-1}{}^{t}h_{f,i-1}{}^{t} - \dot{m}_{f,i}{}^{t}h_{f,i}{}^{t}}{\rho_{f,i}{}^{t}V_f} \tag{3.43}$$

Equations (3.25), (3.27), (3.40) and (3.42) represent the state equation of the system. The proposed model of the evaporator is therefore *state determ*ined and the number of state parameters defined is a function of the number of axial nodes considered. The overall state parameters are therefore:

- n_x axial temperatures for the heat transfer fluid in the annulus $T_{tf,i}$;
- n_x axial metal pipe wall temperatures $T_{p,i}$;
- n_x axial enthalpies for the fluid experiencing phase change in the internal pipe $h_{f,i}$;
- n_x organic fluid masses stored within axial internal pipe control volumes $m_{f,i}$..

The mentioned state equations have been implemented in the *m-sfunction* that constitutes the core of the model and solved together leading to a linear system of partial differential equations. The system of 4×n_x equations have been implemented in matrix form in analogy to what seen for the heat exchanger with no phase change (Eq. (3.30)).

Proper boundary conditions must be introduced and these are represented by some of the inputs of the block, particularly $T_{tf,in}{}^{t}$, $T_{p,in}$ (this parameter is assumed not to change with time), $h_{f,in}{}^{t}$ and $\dot{m}_{f,in}{}^{t}$.

The Simulink® block can be schematically represented as in Fig. 3.23. The system inputs are characterized by the parameter representing the transfer fluid and organic fluid state at the evaporator input, particularly their temperature, pressure and mass flow rate must be known. The output generated by the system can be any of the state variables but of particular interest, in the view of linking the evaporator to other components in a complex network, the state of the fluids leaving the exchanger must be provided, i.e. the organic fluid mass flowrate leaving the last cell and the associated nodal temperature, as well as the temperature of the transfer fluid leaving the exchanger. Due to the counterflow design this temperature will be calculated at the node with index 1, as from Fig. 3.22.

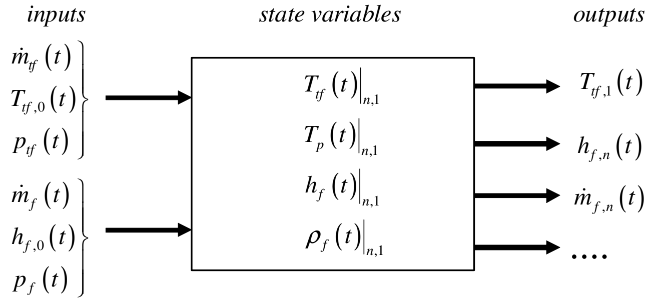

Fig. 3.23. The evapoarator block.

Once the system has been fully defined the correlations to calculate the actual thermal fluxes must be introduced and are illustrated in the section that follows. While the correlations adopted in the annulus and for the conduction heat flux in the pipe are substantially the same introduced in Par. 3.2.2.1 through Equations (3.32) to (3.38), new correlations must be introduced to evaluate the conductive heat flux in the internal pipe between organic fluid and metal wall in order to take into account of the possible phase change.

3.2.3.1 Heat flux correlations in the internal pipe heat exchange with evaporating-condensing fluid

Under normal operating conditions the organic fluid enters the heat exchanger as subcooled liquid and leaves the exchanger as saturated or superheated vapour if the component operates as evaporator, conversely it may enter as satured or superheated vapour and live as liquid if the component operates as condenser. For this reason different fluid phase regions may exist within the i^{th} cell of the internal pipe of the evaporator and different heat exchange correlations apply depending on whether the fluid is single phase ($h_i<h_l$ or $h_i>h_v$) or two phase ($h_l<h_i<h_v$).

In case of single phase the approach is similar to that adopted for the anular pipe, where the fluid is always assumed to be single phase, and Nu=4.36 in the laminar region otherwise the Gnielinski correlation (3.33) is applied.

In the two-phase fluid region the Chen correlation is instead adopted for determining the Nusselt number [28,29].

$$Nu = Nu_{Dc} + Nu_{Db} \tag{3.44}$$

Nu_{Dc} expresses the Nusselt number for vaporization in forced convection, written from the Dittus-Boelter correlation [30]:

$$Nu_{Dc} = 0.023\,\mathrm{Re}_l^{0.8}\,\mathrm{Pr}_l^{0.4}\,F \tag{3.45}$$

where F is a correction empirical factor that takes into account of the characteristics of the fluid flow and calculated from the Martinelli factor X_{tt} [30]:

$$\mathrm{X}_{tt}=\left(\frac{1-x}{x}\right)^{0.9}\left(\frac{\rho_v}{\rho_l}\right)^{0.5}\left(\frac{\mu_l}{\mu_v}\right)^{0.1} \tag{3.46}$$

and:

$$\begin{aligned} F &= 2.35\left(\frac{1}{X_{tt}}+0.213\right)^{0.736} && \text{if } \mathrm{X}_{tt}<10 \\ F &= 1 && \text{if } \mathrm{X}_{tt}>10 \end{aligned} \tag{3.47}$$

The Reynolds number for the liquid can be calculated as:

$$\mathrm{Re}_l=\frac{4\dot{m}(1-x)}{\pi d\mu_l} \tag{3.48}$$

Nu_{Db} represents instead the Nusselt number in case of nucleation boiling, and can be expressed according to the following:

$$Nu_{Db}=0.00122\ S\ Ja^{0.24}\ \mathrm{Pr}_l^{0.21}\left(\frac{\rho_l}{\rho_v}\right)^{0.24}\left(\frac{d\Delta p}{\sigma}\right)^{0.5}\left(\frac{\rho_l d^2\Delta p}{\mu_l^2}\right)^{0.5} \tag{3.49}$$

In the previous correlation S is a factor smaller than 1 defined by the following empirical correlation:

$$S=\frac{1}{1+2.53\cdot 10^{-6}\,\mathrm{Re}_{2F}^{1.17}} \tag{3.50}$$

and takes into account of the decreasing importance of nucleation with increasing two phase Reynolds number Re_{2F}, defined as:

$$\mathrm{Re}_{2F}=\mathrm{Re}_l\,F^{1.25} \tag{3.51}$$

The Jacob number in Eq.(3.49) can be defined as:

$$Ja=\frac{c_l\Delta T_e}{H_{lv}} \tag{3.52}$$

where $\Delta T_e=T_p-T_{vs}$ is the difference between pipe wall temperature and fluid saturation temperature, and H_{lv} is the latent heat of vaporization.

The term Δp of equation (3.49) expresses the difference between vapour saturation pressure at the wall temperature and the liquid hydrostatic pressure:

$$\Delta p = p_{vs}\left(T_p\right) - p_l \tag{3.53}$$

Once the Nusselt number is calculated from Eq.(3.44), the convection coefficient can finally be defined as:

$$h = \frac{Nu\ \lambda_l}{d} \tag{3.54}$$

and the actual overall convective thermal flow exchanged between pipe and evaporating organic fluid, regardless if in the single phase or two phase region, can be expressed as:

$$q_{conv,i} = h\left(T_p - T_f\right)\pi d \Delta x \tag{3.55}$$

To model the heat exchange between pipe and organic fluid some issue related to discontinuities in the functions defining the heat exchange coefficients must be taken into account. It should be noted in fact that when the organic fluid is single phase the fluid exchanges sensible heat with the pipe wall, while when phase change occurs the latent heat is involved, which is usually on order of magnitude higher than sensible heat [27]. This implies that, due to the discretized approach adopted, in neighbouring organic fluid control volumes the heat transfer coefficient may experience a step change if the fluid is first subcooled (node i) then it starts to vaporize (node $i+1$) or, equally, it is ending the vaporization process (node i) and in the following node ($i+1$) it is completely in the vapour field. These discontinuities in the correlations adopted cause serious stability problems to the solution of the explicit set of equations presented in this section. For this reason a "dumping" coefficient is introduced in order to make smoother the change in the heat transfer coefficient and, while representing an approximation, it turns out to be extremely useful in reducing stability concerns of the model and rising computational speed. It must also be considered that, as stated in [29], the validity of Chen correlation for x>0.85 is limited, hence the approximation can be accepted. It will be also shown that the effect of approximating the step change in the convection coefficient with a ramp is negligible.

Fig. 3.24 reports the heat transfer coefficient as function of the vapour fraction x in the two phase region as from the Chen correlation and in the hypothesis of smoothing the step change for $x=0$ and $x=1$. The "dumping coefficient", dc, is assumed to be the Δx, from $x=0$ and $x=1$, in which the two phase convection coefficient is approximated as a straight line linking the convection coefficient calculated from Chen at $x= \Delta x$ and $x=1-\Delta x$ and the convection coefficient for the liquid at $x=0$ and for the vapour at $x=1$. In Fig. 3.24 for example the "dumped" convection coefficient is calculated with $dc=0.1$ and, in fact, the Chen correlation is adopted in the range $0.1<x<0.9$, otherwise two straight lines approximate the convection coefficient linking the values in a smoother way to the liquid and vapour coefficients. The example refers to a pipe with d=0.02m where a mass flow rate of 0.1kg/s of water at atmospheric pressure vaporizes due to the pipe wall temperature assumed constantly at 120°C.

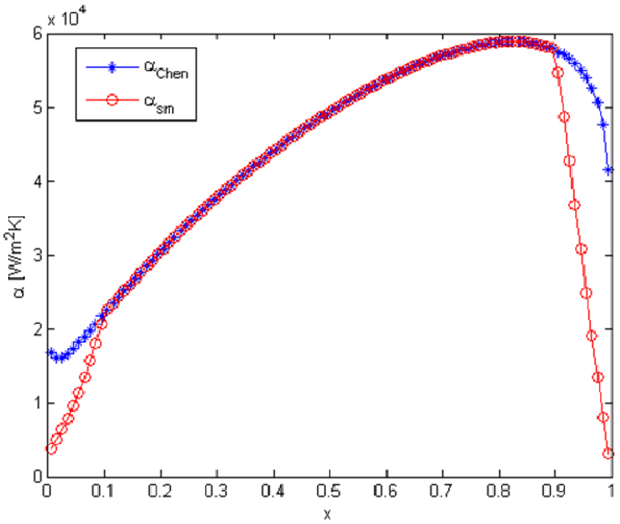

Fig. 3.24. Heat transfer coefficient in the two phase zone as function of vapour fraction.

Before proceeding further with illustrating the complete Simulink® model of the evaporator some of the strongest assumptions introduced in the model have also to be verified.

One of these is the hypothesis of lumped thermal capacitance for the metal that has brought to assuming the temperature of each pipe element related to any discretized volume to be at constant and uniform temperature. As shown in Par.3.2.1.2 this hypothesis can be accepted as far as $Bi<<0.1$. In the case under analysis the condition $Bi<<0.1$ is verified both with reference to the transfer fluid – pipe and with organic fluid – pipe heat transfer convection coefficient, hence the assumption of lumped thermal capacitance for the metal pipe can be accepted.

The second strong hypothesis introduced in the analysis is that of constant pressure within the pipe where the organic fluid flows. Besides the pressure losses due to friction between the flowing fluid and the pipe which, within some extent can reasonably be neglected, another important phenomena occurs when a fluid that undergoes phase change flows within a straight pipe, that has been called here "backpressure of inertia" [31].

It is well known that, for a fluid that undergoes phase change, as for the organic fluid flowing within the evaporator inner pipe, the fluid density changes within the flow stream both because of friction and because of heat exchange processes. Applying Bernulli equation to the straight and constant cross section circular pipe, and neglecting the effects of friction, a decrease in the fluid density corresponds to a decrease in the fluid hydrostatic pressure being conversely increased the fluid speed and hence its volumetric flow ratio. For this reasons, also in the hypothesis of completely neglecting friction, a pressure drop along the pipe should still be considered.

The backpressure of inertia can be calculated according to the following equation from the inlet to the outlet section of the evaporator, with reference to the evaporating fluid:

$$\Delta p = p_{f,in} - p_{f,out} = \rho_{f,in} c_{f,in}^{\ 2} \left(\frac{\rho_{f,in}}{\rho_{f,out}} - 1 \right) \tag{3.56}$$

For all the geometries considered in the present study the fluid speed at the evaporator inlet section, $c_{f,in}$ has always been limited to values smaller than 3m/s and the corresponding backpressure of inertia turned out to be limited to at most 6% of the pressure at the inlet section, $p_{f,in}$: its effect have been neglected for sake of simplicity. In the future model upgrades will however consider the phenomena by introducing the momentum conservation equation.

3.2.3.2 The Simulink® model

The Simulink® model of the heat exchanger with phase change has been realized through the compilation of a specific *m-sfunction* where the overall system of state equations in matrix form are compiled and solved. Again the total number of equations that constitutes these two systems is a function of the number of axial nodes.

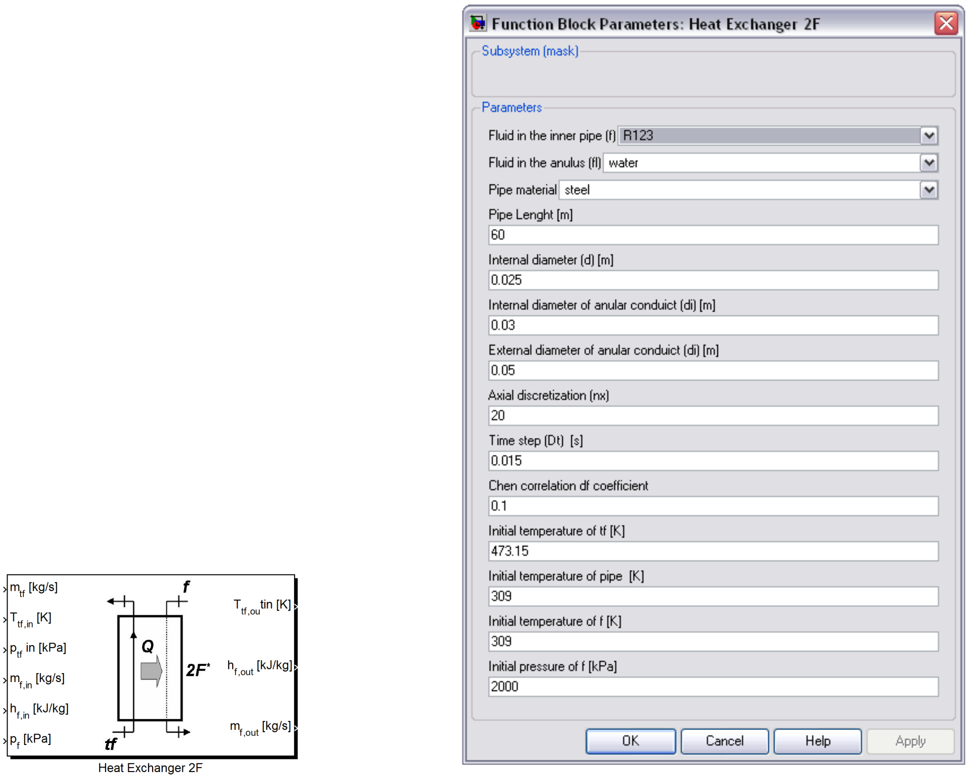

Fluid in the inner pipe (f) R123
Fluid in the anulus (fl) water
Pipe material steel
Pipe Lenght [m]
60
Internal diameter (d) [m]
0.025
Internal diameter of anular conduict (di) [m]
0.03
External diameter of anular conduict (di) [m]
0.05
Axial discretization (nx)
20
Time step (Dt) [s]
0.015
Chen correlation df coefficient
0.1
Initial temperature of tf [K]
473.15
Initial temperature of pipe [K]
309
Initial temperature of f [K]
309
Initial pressure of f [kPa]
2000

(a) (b)

Fig. 3.25. Evaporator block Simulink® dialog window.

Fig. 3.25 depicts the Simulink® block dialog windows. It is possible to observe that, as in the case of heat exchanger with no phase change, many parameters have to be provided in order to characterize both the component and the discretization procedure.

Among the parameters that were not included in the dialog window of the heat exchanger with no phase change, the dumping factor for the convection coefficient in the two phase field is now required. For the initialization procedure of the model a parameter to compile the vector of nodal enthalpies for the organic fluid is now required. The latter can be compiled once the organic fluid pressure is known, (and given the nodal temperature at start of simulation) and this parameter must also be provided for initialization. Knowing the organic fluid pressure and temperature at $t=0$ also allows to determine the vector of nodal densities, or, equally, of nodal masses, for the organic fluid side of the pipe thus providing initialization to the last set of state variables required for integrating the continuity equation. Given these parameters the state of the system at start of simulation X_0 is then fully defined.

The proposed evaporator model has been validated recurring to data found in literature, since no testing facilities were available for actual components. The data used for the scope are those provided by Takamatsu et. al. [32] and provide steady state distribution of some peculiar variables along the pipe abscissa for a pipe in pipe straight evaporator in geometry and principle much similar to the model here defined.

The model of the evaporator has been therefore provided with the same geometry:

- L=5.52m;
- d=7.9·10^{-3}m;
- d_i=9.5·10^{-3}m;
- d_o=16·10^{-3}m.

and the same input signals, constant in time:

- p_{tf}=101.325kPa;
- $T_{tf,in}$=56°C;
- $\dot{m}_{tf}$ =214kg/m^{2}s;
- p_f=1140kPa;
- $T_{f,in}$=27°C;
- $\dot{m}_f$ =290kg/m^{2}s;

The transfer fluid employed is water while R22 is employed as evaporating fluid, since the system proposed in [32] is the evaporator for refrigerating plants.

The simulation has been run keeping the input values constant while a steady state condition has been reached by the model (after about 180s of simulation); the discretization parameters were n=20 and Δt=0.1s, while different dumping factors for the convection coefficient in the two phase zone have been assumed in order to assess its influence on the simulation results.

Fig. 3.26 to Fig. 3.28 show the results of validation. In Fig. 3.26 the transfer fluid temperature distribution along the pipe length is displayed; it is possible to appreciate little difference between the results provided by the model and measured data. Indeed reducing the convection coefficient dumping factor help to improve accuracy, since the actual convection coefficient between the organic fluid and the pipe with high dumping is underestimated in the first part of the pipe hence the transfer fluid temperature results higher than the real one and vice versa in the end part of the pipe where the organic fluid has high values of title x. The overall result is however satisfactory, and it can be concluded that the effects of the damping coefficient, while not completely negligible, are marginal.

The same tendency can be observed also from Fig. 3.27 which refers to the pipe wall temperature and again good approximation of the model to the experimental data can be appreciated. It can be observed how both the model and the experimental data provide a nearly constant wall temperature in the region where fluid phase change occurs.

Even more comforting are the plots of Fig. 3.28 that refer to the organic fluid vapour fraction and very good accuracy is provided by the model.

Unfortunately no experimental data on dynamic behaviour of real evaporator have been found in literature, and therefore no validation in transient processes has been possible so far.

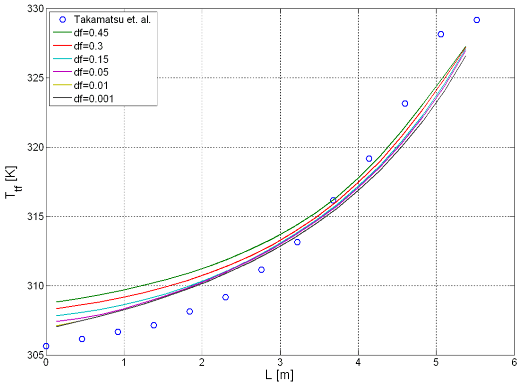

Fig. 3.26. Transfer fluid temperature measured at varying distance from pipe inlet by Takamatsu et. al. [32] (dots) and calculated from the model with different values of damping coefficient.

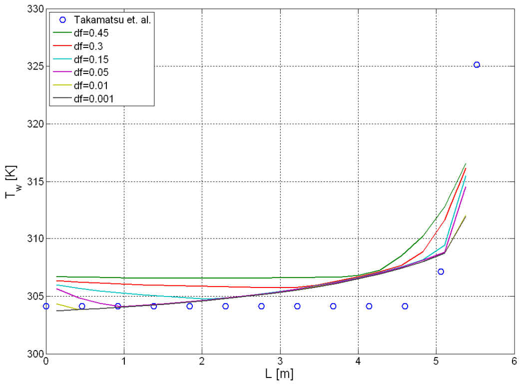

Fig. 3.27. Pipe wall temperature measured at varying distance from pipe inlet by Takamatsu et. al. [32] (dots) and calculated from the model with different values of damping coefficient.

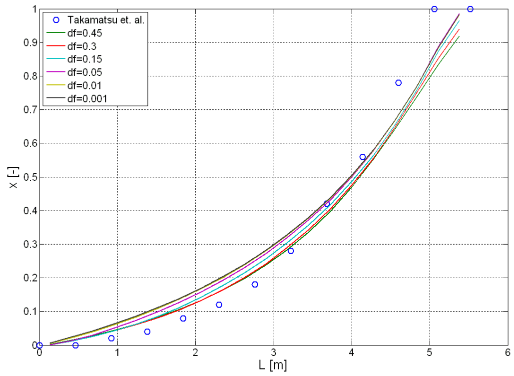

Fig. 3.28. Organic fluid vapour fraction measured at varying distance from pipe inlet by Takamatsu et. al. [32] (dots) and calculated from the model with different values of damping coefficient.

3.2.4 The hot drum

As seen in the previous section the proposed model of evaporator requires, as input, the pressure existing on the organic fluid side of the exchanger, that can change with time. The actual pressure existing within the evaporator can be calculated by balances applied to the hot drum, a component that has the double effect of providing the expander with satured vapour and determining the pressure existing within the drum which is in turn assumed to be equal to the pressure dynamics of the evaporator system. Within the drum hence the saturation condition exist: liquid can be assumed to lay in the bottom and vapour to occupy the left volume and is sucked by the expander or other vapour utilizes.

The component can be defined as a 0D state determined *white box* (besides the equation of state, which is by nature empirical, all other equations adopted come from cardinal equations) and has the input, outputs and state variables shown in Fig. 3.29.

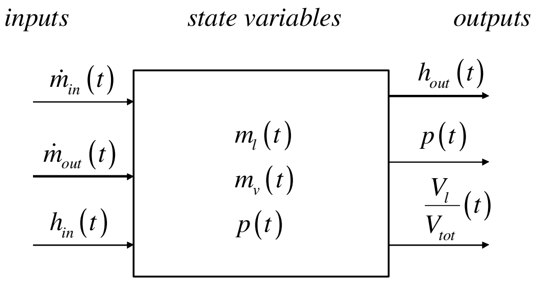

Fig. 3.29. Schematic block for the hot drum.

Inputs of the model are the mass flow rate entering and leaving and the enthalpy of the fluid coming from the evaporator (or condenser). The outputs calculated by the model are the enthalpy of the fluid leaving (that, if possible, is equal to the enthalpy of satured vapour at the pressure existing within the component), the pressure and the liquid volume fraction with respect to the overall drum volume.

3.2.4.1 Mathematical model

The following equations are considered:

- Mass balance:

The difference in the mass flow rates entering and leaving the drum must result in a mass change in time. Expressing this principle with finite difference approach, the mass stored within the component can be calculated in the next step of simulation *t+Δt*:

$$m_l^{t+\Delta t} + m_v^{t+\Delta t} = m_l^{t} + m_v^{t} + \Delta t\left(\dot{m}_{in}^{\ t} - \dot{m}_{out}^{\ t}\right) \tag{3.57}$$

where the total mass is expressed as sum of the vapour and liquid masses.

- Energy balance

The overall energy balances states that the energy flow entering the system with the organic fluid coming from the evaporator (or condenser), and the energy flow leaving the drum (that, if possible, is achieved by subtracting saturated vapour), must result in a system energy change in time. Expressing the energy conservation equation according to the finite difference approach, the internal energy at next step of simulation can be expressed through the following equation:

$$m_l^{t+\Delta t} u_l^{t+\Delta t} + m_v^{t+\Delta t} u_v^{t+\Delta t} = m_l^{t} u_l^{t} + m_v^{t} u_v^{t} + \Delta t\left(\dot{m}_{in}^{\ t} h_{in}^{\ t} - \dot{m}_{out}^{\ t} h_{out}^{\ t}\right) \tag{3.58}$$

- Volume conservation

Indeed another physical condition to be considered is that volume of the liquid phase and vapour phase must equal the overall drum internal volume, that is assumed constant in time (rigid walls):

$$\frac{m_v^{t+\Delta t}}{\rho_v^{t+\Delta t}} + \frac{m_l^{t+\Delta t}}{\rho_l^{t+\Delta t}} = V_{TOT} \tag{3.59}$$

- State equations

Since the component features a number of 7 state variables (m_l, m_v, p, u_l, u_v ρ_l and ρ_v), four equations are needed for system closure. These equations come from applying different times the fluid equation of state that is in fact used to determine:

$$\begin{cases} \left(u_v^{t+\Delta t}, \rho_v^{t+\Delta t}\right) = f\left(p^{t+\Delta t}, x=1\right) \\ \left(u_l^{t+\Delta t}, \rho_l^{t+\Delta t}\right) = f\left(p^{t+\Delta t}, x=0\right) \end{cases} \tag{3.60}$$

The Simulink® model of the hot drum component and its dialog window interface are shown in Fig. 3.30. To be noted that the parameters required are geometrical parameters and parameters required for initializing the system at simulation time *t*=0.

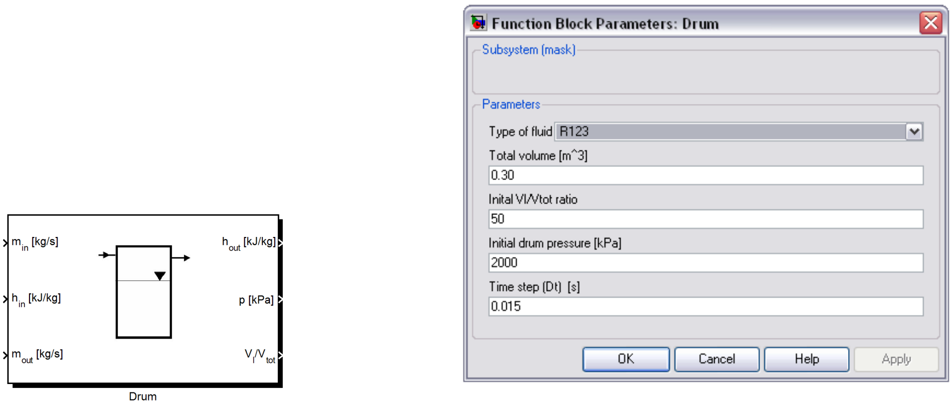

Type of fluid: R123

Total volume [m^3]: 0.30

Inital Vl/Vtot ratio: 50

Initial drum pressure [kPa]: 2000

Time step (Dt) [s]: 0.015

(a) (b)

Fig. 3.30. Simulink® model of the drum (a) and block dialog mask (b).

The existence of state parameters implies that initialisation parameters should be provided so, the Simulink® block dialog musk must include, besides geometrical and physical parameters as drum size and fluid adopted, also the initial values of pressure, mass of liquid and mass of vapour at simulation time *t=0*.

To be noted that, among the different parameters to be provided to the model, the overall volume of the drum has significant effect on determining the time evolution of the main system outputs. Fig. 3.31 shows for example the effects played by drum volume in the dynamic response due to a step change in one of the system inputs; R123 is considered as organic fluid. It can be noted that, as expected, the smallest the drum volume, the faster is the system response.

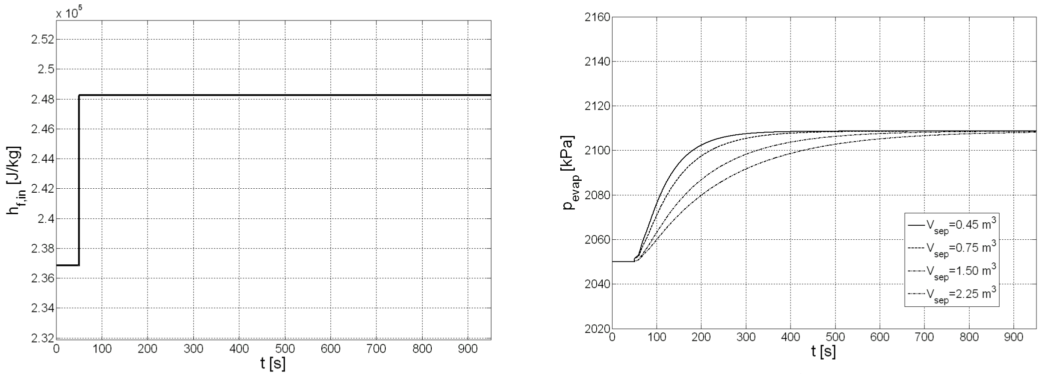

(a) (b)

Fig. 3.31. Pressure response in the hot drum (b) due to a step change in the enthalpy flow of the fluid entering (a) at varying drum volumes.

3.2.4.2 Dynamic behaviour of the drum-evaporator subsystem

The mutual interaction between hot drum and evaporator are strong and the dynamic behaviour of each component cannot be really separated from the other. In fact what happens within the evaporator has effect on the evaporator outputs as for example the organic fluid mass flow rate or enthalpy, which in turn, affects the energy and mass conservation equations of the hot drum that would result in a new pressure within the component, that is fed backward to evaporator and so on.

Evaporator and hot drum have therefore been tested together and the following plots are proposed as example of their mutual interactions. The model of the evaporator linked to the model of the hot drum in the Simulink® environment is proposed in Fig. 3.32.

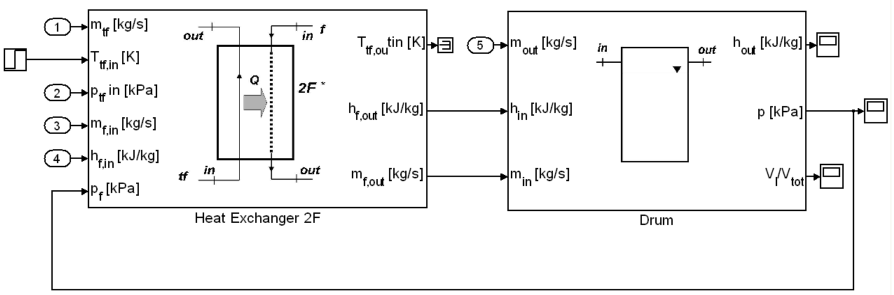

Fig. 3.32. Simulink® model of an evaporator-hot drum system.

The system has been operated using the following geometry of the evaporator:

- L=95m;
- d=45·10^{-3}m;
- d_i=50·10^{-3}m;
- d_o=85·10^{-3}m.

The organic fluid employed is R123 and the transfer fluid is diathermic oil. The drum volume is assumed to be 0.75m^3, while the number of nodes adopted for the axial discretization of the evaporator is n=20. The number of nodes has been chosen as a result of a convergence analysis.

In Tab. 3.2 the value of pressure existing within the evaporator-drum system at varying number of nodes is reported. It can be observed that the higher the number of axial nodes considered the lower is the system pressure. This is a consequence of the fact that the organic fluid specific enthalpy entering the drum is lower when a low number of nodes is considered since it is evaluated as average over a bigger control volume (the length of each pipe *cv* is bigger). It can also be noticed that increasing from 20 to 30 nodes the pressure change is negligible and usually, when smaller than 5%, it can be assumed that convergence is reached.

n	***P_{vap}* [kPa] (steady state)**	**Relative variation [%]**
5	1586	-
10	1885	+18.85
20	2051	+8.81
30	2104	+.258

Tab. 3.2. Analysis of convergence on the number of nodes of the axial discretization of the evaporator.

After reaching steady state operating conditions one of the main system external inputs is changed with a step. In this example the temperature of the heat transfer fluid is changed and this has effects on both the hot drum (Fig. 3.35) and the evaporator (Fig. 3.34).

It can be observed that the decreasing transfer fluid temperature determines a decrease in the pipe wall temperature (that is sharper close to the transfer fluid inlet, Fig. 3.35 (b)) which in turn determine a decrease in the organic fluid specific enthalpy and temperature (Fig. 3.35 (d) and (e)). The decreased energy flow that the evaporator provides through the organic fluid to the drum causes a decrease in the pressure existing within the system (Fig. 3.34 (a)) which in turn causes a fraction of the liquid present within the component to evaporate (Fig. 3.34 (b)).

At the end of transient all values stabilizes into a new steady state; to be noted that the pressure and hence the saturation temperature within the evaporator are at a lower value. Interesting is also Fig. 3.35 (e) which shows the nodal organic fluid mass flow leaving each discretized cell within the evaporator. To be remembered that the organic fluid mass flow rate entering the evaporator does not change with time. The sudden drop in the wall temperature make the vapour within some cells to condensate thus reducing the actual mass flow rate through these cells, resulting in an overall decrease in the organic fluid mass flowrate in the two phase region. The subsequent fall in the evaporating pressure causes start of vaporization in some cell were, at the previous pressure level, liquid phase still existed. Part of the mass contained within these cells is then discharged, causing an increase in the leaving mass flow rate in all the following cells. To be noted that when steady state conditions are reached the mass flow rate flowing through each cell remains constant. Also it can be appreciated that no changes in the mass flow rate can be observed, even during transients, in the zone where only liquid exist (whose density is independent from existing pressure and temperature within small changes of these parameters).

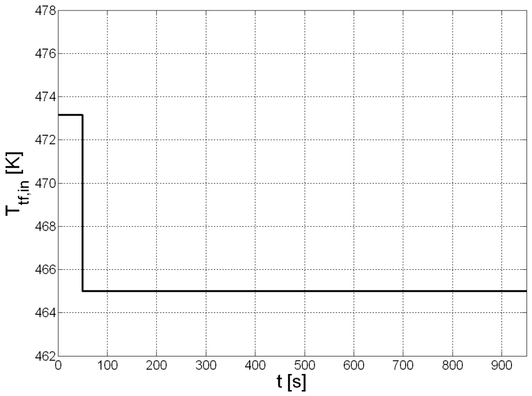

Fig. 3.33. Change in temperature of the transfer fluid entering the evaporator.

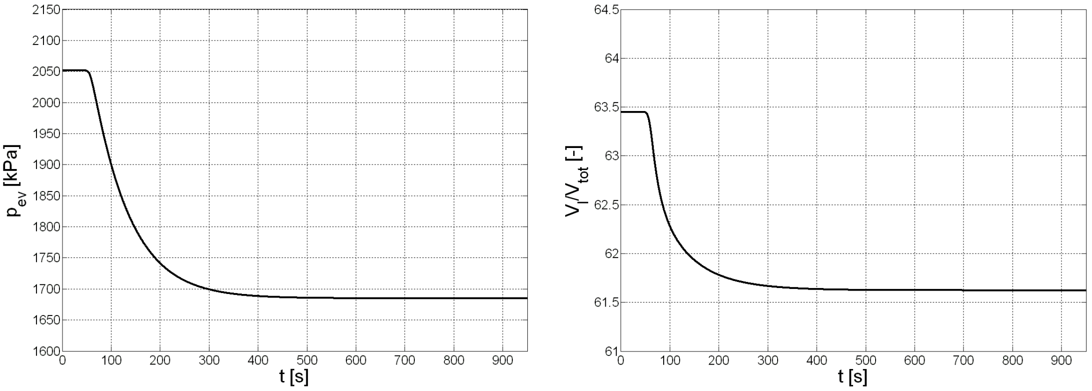

(a) (b)

Fig. 3.34. Hot drum response: pressure (a) and liquid volume fraction (b).

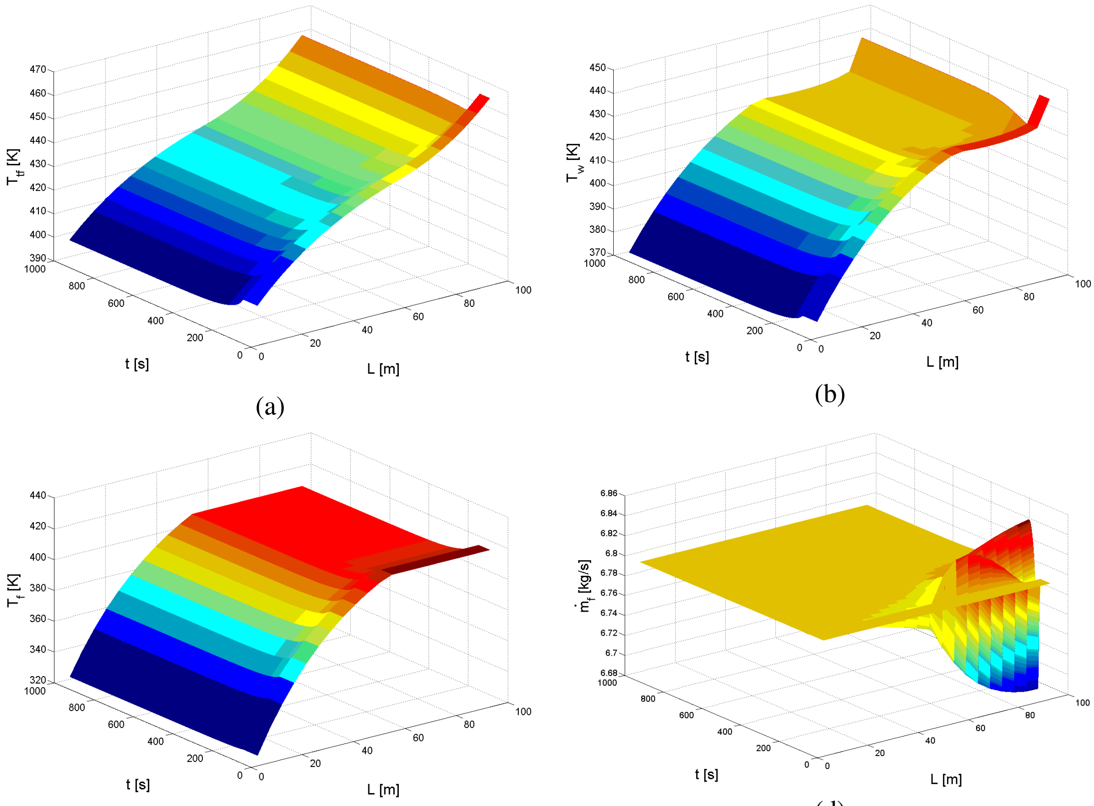

(a) (b)

(c) (d)

Fig. 3.35. Evaporator response: (a) transfer fluid temperature, (b) pipe wall temperature, (c) organic fluid temperature and (d) organic fluid mass flow rate. Distribution with time and as function evaporator abscissa.

3.2.5 Model of a constant pressure combustion chamber

The model of another important “reservoir” is here presented. The constant pressure combustion chamber (CC) is considered since it can be widely applied in the analysis of gas turbine systems.

The component can be at a first view modeled as a constant pressure heat exchanger where a stream of gases of defined composition enters with a certain temperature and enthalpy for leaving the chamber with higher temperature, but at the same pressure. The rise in sensible specific enthalpy occurs due to the oxidation of a fuel that is added and contributes, with its energy content at increasing the system overall energy. This particular heat exchanger does not require an hot exchanging media to rise the working fluid temperature, as in the examples presented in the previous sections, but rather requires a combustible. To be noted that for the representation of a closed Joule cycle the single phase heat exchanger presented in Par. 3.2.2 can be used, while the component presented here is introduced to simulate those plants where internal combustion processes are considered.

The combustion chamber is modeled here as a constant volume capacity. Air/fuel mixture is assumed to be perfectly homogeneous in each point of the CC and the combustion reactions to be instantaneous [36]. Therefore, differently to the heat exchangers presented in the previous sections, a simplified 0D model is proposed here and the property distribution within the chamber is homogeneous. The component is still *state determined* and can be considered as *white box* since only cardinal equations are applied, even though the combustion process is modelled through an empirical combustion coefficient η_b.

A block diagram of the model of the CC is shown in Fig. 3.36.

Inputs of the system are the air mass flow rate entering the CC ($\dot{m}_{in}$), its temperature (T_{in}), the fuel mass flow rate ($\dot{m}_f$) and the mass flow rate of gases leaving the combustion chamber ($\dot{m}_{out}$).

The State vector of the system is represented by the air/fuel mass stored within the volume of the CC (m_{CC}), its internal energy (U_{CC}) and the internal energy stored as heat within the combustion chamber walls (U_w).

Outputs of the model are the pressure in the combustion chamber (p_{CC}), the temperature of the exhaust gases leaving the system (T_{out}), and, if required, the combustion chamber wall temperature (T_w).

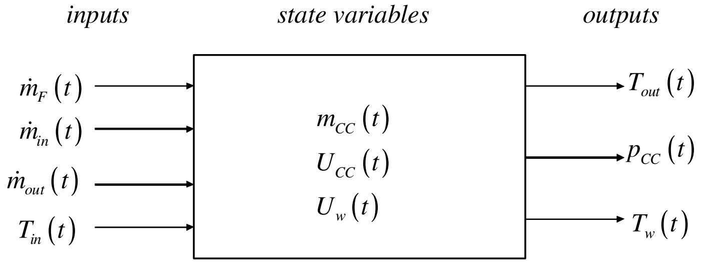

Fig. 3.36. Block Diagram of the combustion chamber model.

It should be noted that, while pressure is assumed to be uniform within the component at a given time instant (hence the heat exchange process is assumed to be isobaric) pressure may change in time and therefore the overall heat exchange may take place as a sequence of constant pressure processes. The pressure changes in time is due to the accumulation of mass that may occur in transients, due to accumulation of energy that may lead to an increase in the gas temperature. These phenomena may occur in unsteady operation conditions.

Since the vector of state variables has three elements, three state equations in scalar form are needed. These equations are the mass conservation equation, the energy equation applied to the mass of burnt gas within the combustion chamber, and the energy equation applied to the walls of the combustion chamber applied in zero dimensional form. The spatial distribution of the state variables is therefore neglected and interest is placed only upon their change in time, realizing therefore a purely thermodynamic model where the fluid dynamics is neglected (i.e., the momentum equation is not considered).

The CC has been modelled as a constant volume with semi-permeable walls. Application of the mass conservation equation in differential form to the control volume of the combustion chamber gives:

$$\frac{dm_{CC}}{dt} = \sum \dot{m}(t) = \dot{m}_{in}(t) + \dot{m}_F(t) - \dot{m}_{out}(t) \tag{3.61}$$

Application of the energy equation to the mass of burnt gases within the combustion chamber, assuming that the work exchanged is zero (the CC has constant volume), gives:

$$\frac{dU_{CC}}{dt} = q_{chem} - q_{w,in} + \dot{H}_{in} - \dot{H}_{out} \tag{3.62}$$

where:

$$q_{chem} = \dot{m}_F H_{vi} \eta_b \tag{3.63}$$

and represent the heat provided to the system through the combustion of the fuel added at any instant of simulation. The combustion is assumed to be instantaneous and homogeneous but not perfect, since a combustion efficiency η_b is introduced.

The total enthalpy flow entering and leaving the combustion chamber are calculated from the temperatures according to the following:

$$\dot{H} = \dot{m} c_p T \tag{3.64}$$

$q_{w,in}$ in Eq. (3.62) is the heat flux from the burning zone to the combustion chamber walls. This term appears in the energy equation applied to the walls, whose temperature T_w is assumed uniform and constant:

$$\frac{dU_w}{dT} = q_{w,in} - q_{w,out} = \frac{dT_w}{dt} m_w c_{p,w} \tag{3.65}$$

Terms $q_{w,in}$ and $q_{w,out}$ can be calculated assuming the convective heat fluxes between the burned gas within the CC and the chamber walls (Eq(3.66)), and between the walls and the environment (Eq.(3.67)):

$$q_{w,in} = h_{in} A_{w,in} (T_3 - T_w) \tag{3.66}$$

$$q_{w,out} = h_{out} A_{w,out} (T_w - T_1) \tag{3.67}$$

Definition and solution of the Output Equations are achieved through integration of the State Equations, at each time step *t*:

$$m_{CC} = m_{CC,0} + \int_{t=t_0}^{t} \dot{m}_{CC} dt \tag{3.68}$$

$$U_{CC} = U_{CC,0} + \int_{t=t_0}^{t} \dot{U}_{CC} dt \tag{3.69}$$

$$U_w = U_{w,0} + \int_{t=t_0}^{t} \dot{U}_w dt \tag{3.70}$$

This requires the definition of initial values for the vector of state variables (initialization):

$$\overline{X}_0 = \overline{X}(t_0) = [m_{CC,0}, U_{CC,0}, U_{w,0}] \tag{3.71}$$

The Output Equation (that is algebraic) can now be solved at each time instant in order to generate the vector of output variables:

$$p_{CC} = \frac{m_{CC} R T_{CC}}{V_{CC}} \tag{3.72}$$

$$T_3 = \frac{U_{CC}}{m_{CC} c_{p,g}} \tag{3.73}$$

$$T_w = \frac{U_w}{m_w c_{p,w}} \tag{3.74}$$

In this case, seen the limited number of equations and states involved in the model, a different modelling approach has been adopted and instead that compiling code function, icon programming has been preferred using predefined Simulink® operational blocks. The resulting model of the combustion chamber is presented in Fig. 3.37 (a) while Fig. 3.37 (b) shows the block dialog window.

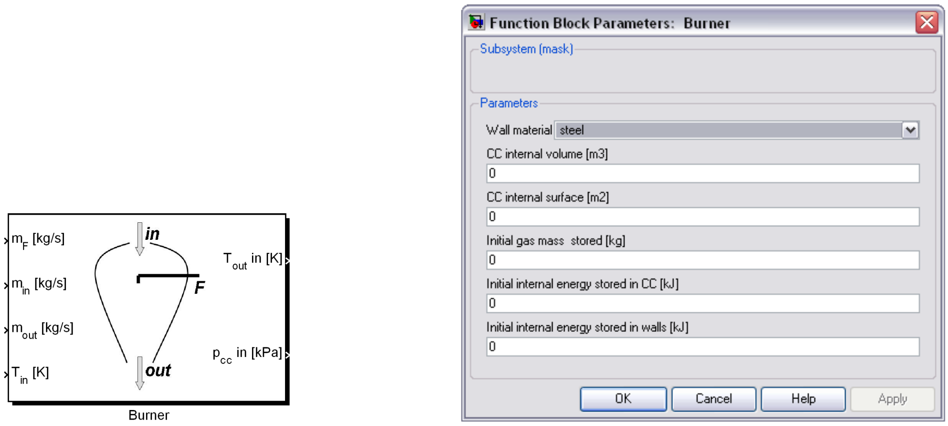

Wall material: steel

CC internal volume [m3]: 0

CC internal surface [m2]: 0

Initial gas mass stored [kg]: 0

Initial internal energy stored in CC [kJ]: 0

Initial internal energy stored in walls [kJ]: 0

(a) (b)

Fig. 3.37. Simulink® model of the combustion chamber (a) and block dialog mask (b).

3.2.6 Model of a Receiver.

Receivers are important components in determining the overall dynamics of a fluid system. Fluid receivers may appear in many different ways in complex system, i.e. they can be tanks, reservoirs, manifolds and others. The common characteristic is that they are elements of fixed volume whose purpose is to accumulate and release mass and energy. The model will be employed for example in the next chapter to represent the intake and exhaust manifold of the cogenerative ICE.

Receivers are typically modeled as lumped-parameter systems where the state variables are assumed to be uniformly distributed over their volume (0D). Considering systems operating with perfect gas mixtures, the state variables are the stored mass and internal energy. These parameters determine the gas pressure and temperature which are the outputs of the system, while inputs are represented by mass flow rate and specific enthalpy content of the gases entering and leaving the volume, according to the casual block of Fig. 3.38 [33].

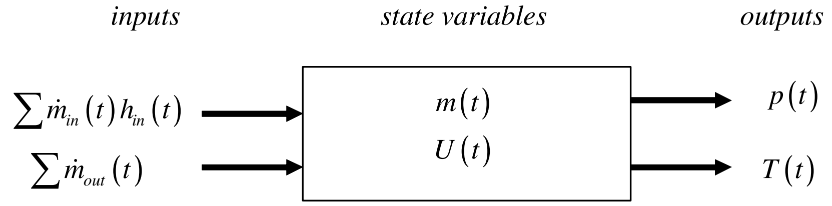

Fig. 3.38. Block Diagram of the receiver model.

The component is simulated following a filling and emptying method where the state variables are derived from integration of the mass and energy conservation equations, expressed in the following form [34]:

$$\frac{d}{dt} m(t) = \sum \dot{m}_{in} - \sum \dot{m}_{out} \tag{3.75}$$

$$\frac{d}{dt} U(t) = \sum \dot{m}_{in}(t) h_{in}(t) - \sum \dot{m}_{out}(t) h_{out}(t) - \dot{Q}(t) \tag{3.76}$$

where multiple inflows and outflows are assumed for generality. $\dot{Q}(t)$ represent the heat subtracted to the gas mass due to heat exchange with the surroundings.

For a perfect gas it is possible to recall the equations:

$$U(t) = m(t) c_v T(t) \tag{3.77}$$

$$h_{in}(t) = c_p T_{in}(t) \tag{3.78}$$

$$h_{out}(t) = c_p T_{out}(t) \tag{3.79}$$

where the out gas temperature T_{out} is the same of the gas stored within the component (T). The specific heats have not here assumed to depend on time since, if the system operates within limited temperature ranges, they can be assumed as constant values as first approximation. However, if the gas composition is known, the REFPROP® database can be used to determine exact values of the constant heats as function of existing pressure and temperature.

Rearranging Eq.(3.76) according to Eqs. (3.77)-(3.79) it is possible to gather the following:

$$\frac{d}{dt}T(t)=\frac{\sum \dot{m}_{in}(t)h_n(t)-\sum \dot{m}_{out}(t)h_{out}(t)-u(t)\frac{dm}{dt}-\dot{Q}(t)}{m(t)c_v} \tag{3.80}$$

that, in case of considering just one input and output flow, leads to the next equation:

$$\frac{d}{dt}T(t)=\frac{RT(t)}{c_v p(t)V}\left[\dot{m}_{in}(t)c_pT_{in}(t)-\dot{m}_{out}(t)c_pT(t)-c_v\left(\dot{m}_{in}(t)-\dot{m}_{out}(t)\right)T(t)-\dot{Q}(t)\right] \tag{3.81}$$

Applying the state equation, given by the ideal gas law if the gases are modeled as ideal, the pressure within the receiver can be calculated once determined the actual mass stored within the component and its temperature, given the constant volume capacity *V*:

$$p(t)V=m(t)RT(t) \tag{3.82}$$

The heat flux $\dot{Q}(t)$ that appears in Eq. (3.80) can be neglected, thus leading to the assumption of adiabatic system, in some circumstances as in those cases when the temperature difference between gas stored and environment is limited (as in the case of intake manifolds of ICEs) or when the surface to volume ratio of the receiver is small. Otherwise $\dot{Q}(t)$ can be calculated recurring to simplified heat exchange correlations (heat is lost mainly due to radiation and convection).

The convective term is expressed as a function of the convection coefficient α, the receiver surface S and the difference between stored gas and reservoir wall temperatures:

$$\dot{Q}_{conv}=\alpha S\left(T-T_w\right) \tag{3.83}$$

The Gnielinky correlation (3.16) applies for the Nusselt number. The Reynolds number and Nusselt number can be calculated given an equivalent diameter for the receiver and considering it like a pipe (the approximation applies for stirred receivers).

The radiative term of the heat exchange between gases and chamber wall is given by the Stefan-Boltzmann correlation [30]:

$$\dot{Q}_{irr}=\varepsilon_0\sigma_0\left(T^4-T_w^{\ 4}\right) \tag{3.84}$$

where ε_0 is the grey body emissivity factor (comprised between 0 and 1) and σ_0 is the Stefan-Boltzmann constant.

The realized Simulink® block and the corresponding dialog window are displayed in Fig. 3.39; a full set of parameters are to be provided when the heat exchange option is selected in order to comply with the heat exchange correlations. Parameters must also be provided for initialization (i.e., internal pressure and temperature at start of simulation).

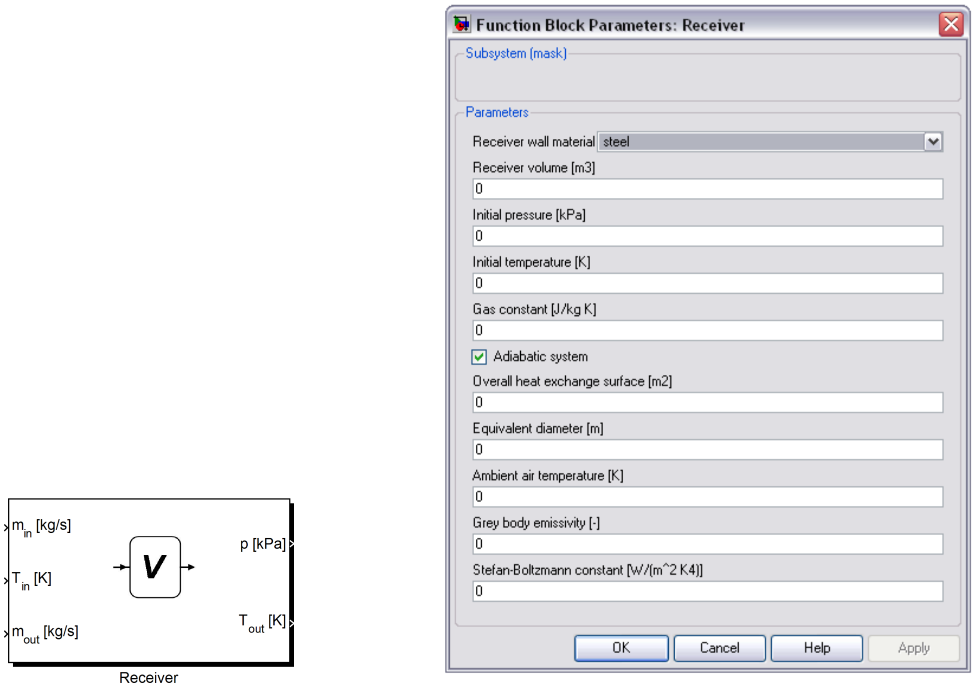

Function Block Parameters: Receiver

Subsystem (mask)

Parameters

Receiver wall material: steel

Receiver volume [m3]: 0

Initial pressure [kPa]: 0

Initial temperature [K]: 0

Gas constant [J/kg K]: 0

☑ Adiabatic system

Overall heat exchange surface [m2]: 0

Equivalent diameter [m]: 0

Ambient air temperature [K]: 0

Grey body emissivity [-]: 0

Stefan-Boltzmann constant [W/(m^2 K4)]: 0

(a) (b)

Fig. 3.39. Simulink® model of the receiver chamber (a) and block dialog mask (b).

3.2.7 Dynamic equilibrium of a rotating shaft

When rotating masses are connected through a shaft, their actual angular velocity should be determined in time and it is subjected to the effect of positive or negative torques applied to it.

The shaft system can fall in the ‘state determined’ library since the corresponding model is *state determined* (a differential state equation can be introduced with reference to the state variable that is the angular speed) and *white box* (since the applied state equation comes from Newton’s second law applied to rotating systems). The system can at the end be considered as a reservoir due to its ability to store and accumulate kinetic energy.

The system input/output is shown in Fig. 3.40.

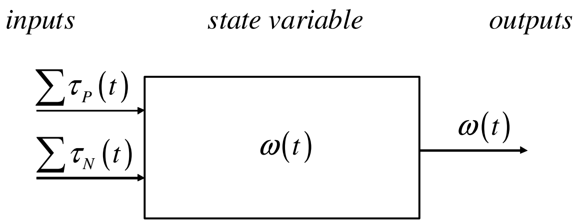

Fig. 3.40. Block Diagram of the rotating shaft model.

The model requires therefore as inputs the positive torque and net negative torque applied to the shaft and in turns the output generated is just the state variable, and the system instantaneous rotational speed is provided, due to integration of the following differential equation:

$$\frac{d}{dt}\omega = \frac{1}{J}\left(\sum \tau_P - \sum \tau_N - F\omega\right) \tag{3.85}$$

where the combined action of viscous and friction forces of rotor and load can be calculated as a function of the rotational speed.

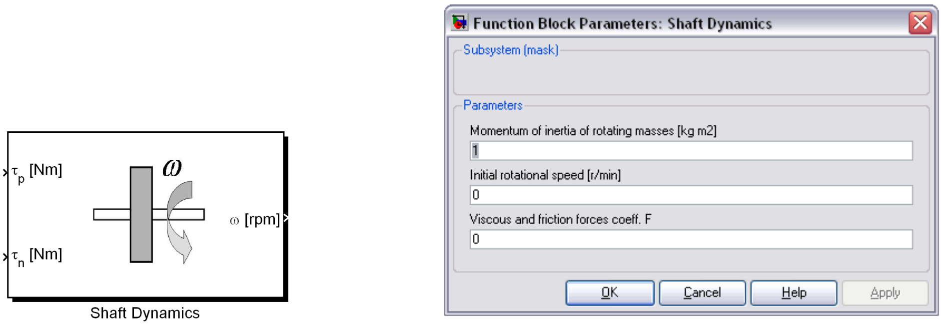

Momentum of inertia of rotating masses [kg m2]: 1

Initial rotational speed [r/min]: 0

Viscous and friction forces coeff. F: 0

(a) (b)

Fig. 3.41. Simulink® model of the Shaft dynamics (a) and block dialog mask (b).

The realized Simulink® block, shown with its dialog window in Fig. 3.41, can be applied in different instances. One example is the complete model of CHP-MGT (see Par. 4.4) where the positive torque is just the torque provided by the turbine and the negative torque is the sum of the compressor torque and the torque applied by the generator. In this case the electric generator has been modelled using the electric components of the SimPower Systems library of Simulink® that features a series of electrical circuits and electromechanical devices in order to built and simulate power systems. The considered electrical machine is assumed to be able to operate in either generator or motor mode depending on the sign of the mechanical torque, and is a permanent magnet synchronous machine, linked to a three-phase power converter based on diodes connected in a bridge configuration (to generate a continuous current that can eventually be fed to a DC/AC converter for AC network). This scheme is typical of distributed generation units, since it doesn't require to operate the Gas Turbine at a constant speed synchronised with the AC grid frequency [37]. In this case, when coupled to the MGT, the torque provided to the electrical machine is always positive and a three phase current is generated. The equations implemented in the component to represent the electric system are summarized below [38]:

$$\begin{cases} \dfrac{d}{dt} i_d = \dfrac{1}{L_d} v_d - \dfrac{R}{L_d} i_d + \dfrac{L_q}{L_d} p\omega_r i_d \\ \dfrac{d}{dt} i_q = \dfrac{1}{L_q} v_q - \dfrac{R}{L_q} i_q - \dfrac{L_d}{L_q} p\omega_r i_d - \dfrac{\lambda p\omega_r}{L_q} \\ \tau_e = 1.5p\left[\lambda i_q + \left(L_d - L_q\right) i_d i_q\right] \end{cases} \tag{3.86}$$

Indeed a detailed model of the generator coupled to the Gas Turbine would not allow real time simulations, because of the high frequencies of the transient phenomena occurring within the generator model that would require a very small simulation time step. Therefore a detailed model of this component, based on Eq. (3.86), has been used outline only to derive the generator characteristic that allows calculation the negative torque required by the generator.

The shaft dynamics block will also appear in the CHP-ICE model (Par.3.2.7) where it is used for the simulation of turbocharger group dynamics, thus determining the actual rotational speed, to estimate correctly the transient response of the system: turbocharger dynamics has a relevant effect on the whole dynamics of the ICE.

3.2.8 Intercooler

Intercooler heat exchangers are a components commonly adopted in ICE applications: it will be applied to the model of cogenerative ICE described in Chapter 4. The approach followed to describe this particular heat exchanger is different from that applied to the other heat exchangers described so far and is based on a simplified quasi-steady technique. The model proposed here comes from the model activity developed within the research group on ICE modeling at the Industrial Engineering Department of the University of Parma and the simplifications and assumptions introduced are due to fast simulation and to guarantee proper cause-effect correlation with the other components in the ICE layout [i.e. 33-35]. The method of analysis consists of combining quasi-steady and filling and emptying techniques to create a grey-box model where certain parameters are determined empirically [35]. This allows to study the dynamics of the component with a reasonable accuracy in steady state conditions. The heat flux within the heat exchanger (that is usually of compact cross-flow design) is evaluated by applying the *ε-NTU* method and the outlet temperature is obtained through the definition of effectiveness ε. For compact heat exchangers, theoretical and experimental results suggest to relate this variable to the Number of Transfer Units *NTU*, a dimensionless parameter depending mainly on exchange surface area and overall heat transfer coefficient [30]. The methodology for calculating the air output temperature will be further described in Par.3.3.7.

Cause and effect constrain impose to associate to the heat exchanger a defined volume with storage capabilities, hence state parameters will be defined and for this reason the component is considered to be a reservoir and falls in the ‘state determined’ sub-library. Similarly to a receiver in fact , the block requires as inputs the mass flow rates into and out of the component, as well as the inlet temperature. However, the output signals are quite different, since both the inlet and outlet pressures are present. The reason is explained in Figure 4.16, where a causality diagram shows that the model of the heat exchanger is made of three elementary components: an inlet and outlet manifold, and a core. The first two blocks are considered as receivers, while the core is a flow control device which determines the mass flow rate through the device and the temperature drop of the fluid [33, 35], where all the heat is assumed to be exchanged in the core and the receivers are introduced to avoid algebraic loops in calculations and are modeled as adiabatic receivers (see Par. 3.2.6).

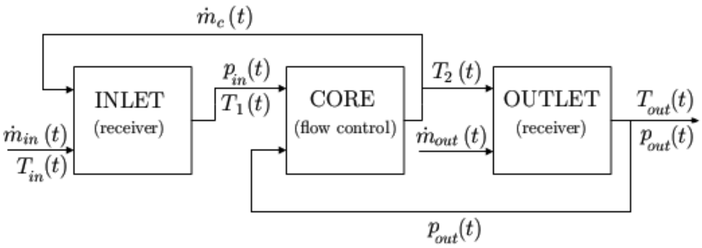

Fig. 3.42. Causality diagram for the ICE intercooler model.

A simplified relation is used to evaluate the pressure drop across heat exchangers in turbulent flow:

$$\Delta p = \frac{k_1 \dot{m}^2 + k_2 \dot{m}}{k_3} \tag{3.87}$$

where k_1 and k_2 are introduced for accounting of distributed and concentrated pressure losses respectively and k_3 takes account of inertial phenomena. The block then calculates the pressure difference between inlet and outlet at a given air mass flow rate

The overall block input, output and state are reported in Fig. 3.43 while the corresponding Simulink® block is in Fig. 3.44.

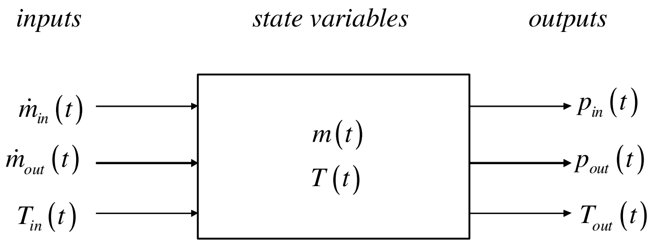

Fig. 3.43. Block Diagram of the intercooler.

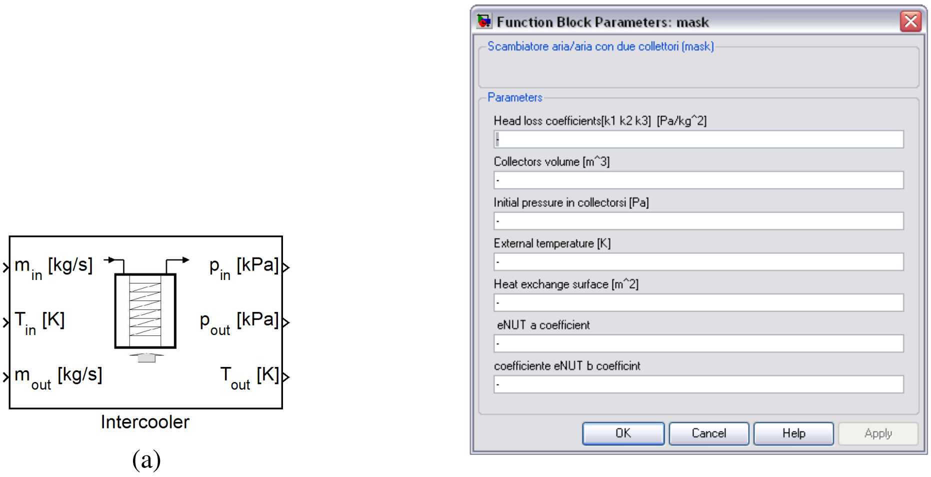

Scambiatore aria/aria con due collettori (mask)

Parameters

Head loss coefficients[k1 k2 k3] [Pa/kg^2]: -

Collectors volume [m^3]: -

Initial pressure in collectorsi [Pa]: -

External temperature [K]: -

Heat exchange surface [m^2]: -

eNUT a coefficient: -

coefficiente eNUT b coefficint: -

(a) (b)

Fig. 3.44. Simulink® model of the intercooler (a) and block dialog mask (b).

3.3 The ‘not state determined’ library

A description of the main ‘not state determined’ components is here reported.

3.3.1 Dynamic air compressor

The dynamic air compressor is modelled as a component without state variables, thus neglecting its capability of storing mass, energy or momentum. The model is therefore based on the steady-state compressor characteristic maps and no state parameters are defined. The output vector $\bar{Y}(t)$ at time *t* only depends on the value of the input vector $\bar{U}(t)$ at the same time instant, according to a purely algebraic equation. In this case therefore the dynamic behaviour of the component is neglected since no differential equations are introduced and a quasi-steady approach is followed.

The characteristic maps of the compressor represent the correlation that exist between mass flow rate, compression ratio efficiency and rotational speed, as shown in Fig. 3.45, where the abscissa refers to the air mass flow rate, the *y*-axis to the compression ratio and a set of curves are reported as iso-efficiency or iso-shaft rotational speed.

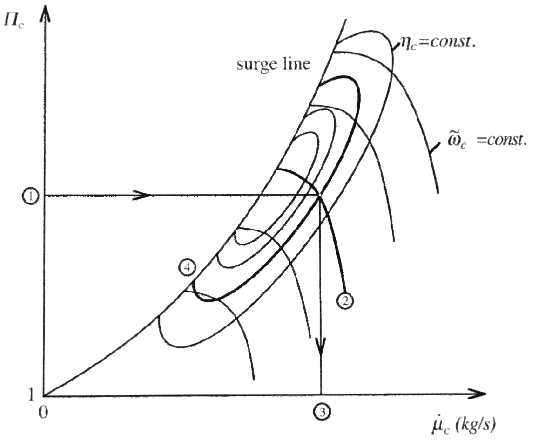

Fig. 3.45. Compressor characteristic maps.

Input and output variables of the proposed compressor model are schematically shown in Fig. 3.46.

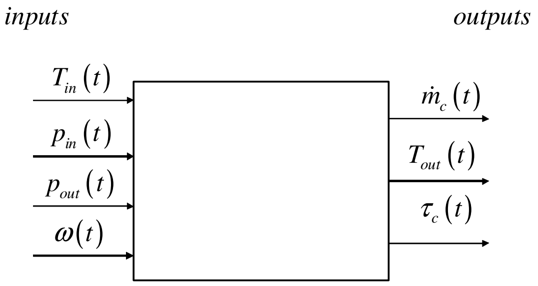

Fig. 3.46. Block diagram of the Compressor model.

From the dimensional analysis a set of 4 parameters can be defined to characterize the Compressor, which have to be introduced referring to specific thermodynamic conditions:

- Pressure ratio: $\beta = \frac{p_{out}}{p_{in}}$;
- Reduced speed: $\omega_R = \omega \sqrt{\frac{T_0}{T_{in}}}$;
- Reduced mass flow rate: $\dot{m}_{R,C} = \frac{p_0}{p_{in}} \sqrt{\frac{T_{in}}{T_0}} \dot{m}_C$;
- Reduced power: $P_{R,C} = P_C \frac{p_0}{p_{in}} \sqrt{\frac{T_0}{T_{in}}}$;

where p_0 and T_0 are the reference pressure and temperature assumed at compressor inlet when deriving the actual compressor maps and are usually provided by the manufacturer.

It can be noticed that the reduced compressor power can be used instead of the compressor isentropic efficiency η_c, since:

$$P_{R,c} = \dot{m}_{R,c} \overline{c}_p T_{in} \left(\beta^{\frac{k-1}{k}} - 1 \right) \frac{1}{\eta_c} \tag{3.88}$$

The reduced parameters can be used to define the implicit form of the compressor characteristic equations as:

- Compressor mass flow rate characteristic:

$$f_1\left(\beta, \dot{m}_{R,C}, \omega_R\right) = 0 \tag{3.89}$$

- Compressor efficiency characteristic:

$$f_2\left(\eta_C, \dot{m}_{R,C}, \omega_R\right) = 0 \tag{3.90}$$

These forms of the compressor characteristics are preferred for the extrapolation and interpolation procedures, starting from the values provided in the compressor maps, in order reduce the model computational time. Indeed the compressor maps are used in the proposed procedure to define the parameters used in the analytical equations.

The mass flow rate characteristic of the compressor can be defined in the following form, according to [39]:

$$\beta\left(\dot{m}_{R,c}, \omega_R\right) = \beta_{\max}(\omega_R) - c_c(\omega_R)\left[\dot{m}_{R,c} - \dot{m}'_R(\omega_R)\right]^2 \tag{3.91}$$

The parameters β_{max}, c_c and $\dot{m}_R'$ depend only on the compressor speed ω. They can be expressed through a set of third order polynomials in ω, where all the equation coefficients can be derived from the compressor characteristic curves.

The Compressor mass flow rate is given by the following equation, where the second case is a crude model for suction, if the surge line is crossed [39]:

$$\dot{m}_C = \begin{cases} \dot{m}'_R + \sqrt{\dfrac{\beta_{\max} - \beta}{c_c}} & \text{if } \beta > \beta_{max} \\ 0 & \text{otherwise} \end{cases} \tag{3.92}$$

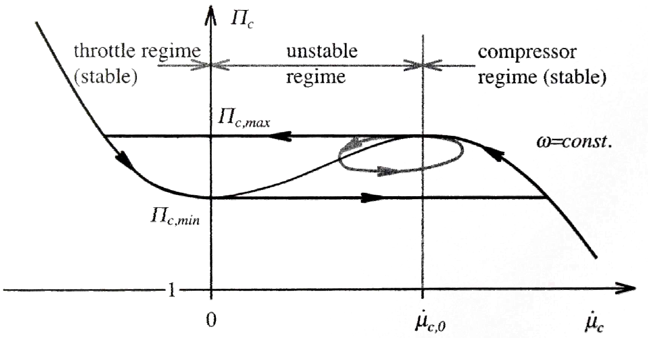

Fig. 3.47. Compressor characteristic maps with reference to surge.

The efficiency characteristic may be expressed in the following parameterized form [39], where the orthogonal transformation has been introduced to represent the ellipses of the Compressor efficiency (in the β- $\dot{m}_R$ plane), with good accuracy far from the maximum efficiency conditions:

$$\eta_C\left(\beta, \dot{m}_{R,C}\right) = \eta_{C,\max} - \chi^T\left(\beta, \dot{m}_{R,C}\right) \cdot Q \cdot \chi\left(\beta, \dot{m}_{R,C}\right) \tag{3.93}$$

where:

$$\chi^T(\beta, \dot{m}_{R,C}) = \left[\beta - \beta_{\max}, \dot{m}_{R,C} - \dot{m}_{R,\max}\right] \tag{3.94}$$

Values for $\dot{m}_{R,\max}$, β_{max}, $\eta_{C,max}$ and Q can be also defined from the compressor maps, and the "max" subscript indicates the operation point where the compressor reaches maximum efficiency. In this case the influence of the rotational speed is expressed through the reduced mass flow rate.

The air temperature at the compressor outlet can be computed according to the following equation:

$$T_{out} = T_{in}\left[1 + \left(\frac{\beta^{\frac{k-1}{k}} - 1}{\eta_C}\right)\right] \tag{3.95}$$

The net power P_c required by the compressor is given by combining Eq.(3.88) with the expression of the reduced power. Torque can then be calculated as:

$$\tau_C = \frac{P_C}{\omega} \tag{3.96}$$

The Simulink® model of the compressor is shown in Fig. 3.48 (a) while Fig. 3.48 (b) displays the block dialog mask. It can be observed that by properly feeding the model with the parameters required to define the explicit analytical correlations introduced to represent the mass flow rate and efficiency characteristics, with values derived from experimental characteristics curves, the model will be properly fitted to describe the desired compressor component.

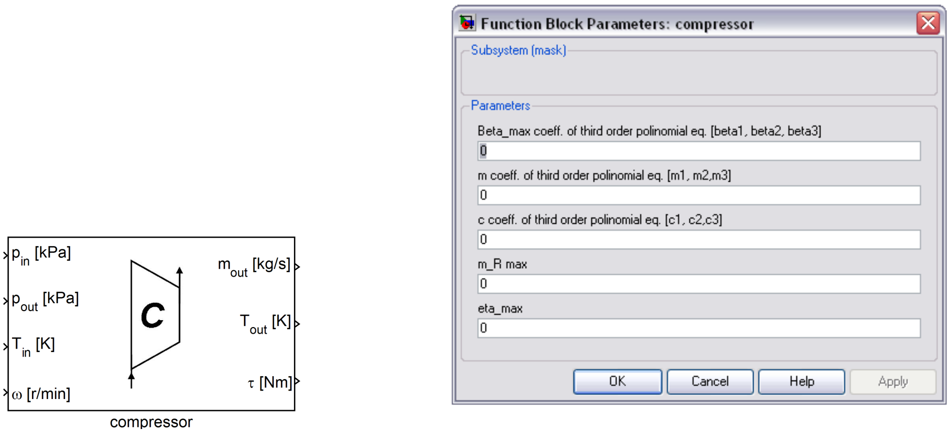

Beta_max coeff. of third order polinomial eq. [beta1, beta2, beta3]
0

m coeff. of third order polinomial eq. [m1, m2,m3]
0

c coeff. of third order polinomial eq. [c1, c2,c3]
0

m_R max
0

eta_max
0

(a) (b)

Fig. 3.48. Simulink® model of the compressor (a) and block dialog mask (b).

3.3.2 Turbine

As for the Compressor, the turbine is modeled as a component with no state, based upon steady-state characteristic curves. Inputs/outputs of the system are shown in Fig. 3.49. Here again, as for the compressor, the rotational speed as well as the pressure ratio are input variables, while mass flow rate and efficiency (from which power and torque can be derived) are outputs. Changes in specific heats are assumed to depend not only on temperatures, but also on composition.

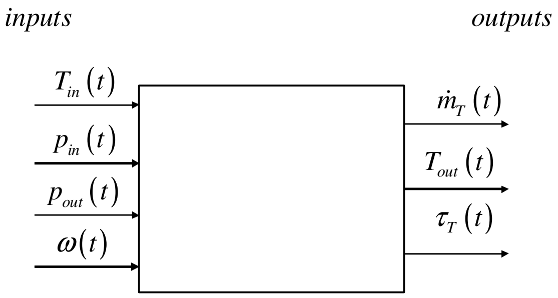

Fig. 3.49. Block diagram of the gas turbine model.

Reduced parameters can be introduced for the turbine, as:

- Expansion ratio: $\varepsilon = \dfrac{p_{in}}{p_{out}}$;
- Reduced speed: $\omega_R = \omega\sqrt{\dfrac{T_0}{T_{in}}}$;
- Reduced mass flow rate: $\dot{m}_{R,T} = \dfrac{p_0}{p_{in}}\sqrt{\dfrac{T_{in}}{T_0}}\dot{m}_T$;
- Reduced turbine power: $P_{R,T} = P_T\dfrac{p_0}{p_{in}}\sqrt{\dfrac{T_0}{T_{in}}}$.

Two analytic characteristic equations can be defined in terms of the reduced parameters:

- Turbine mass flow rate characteristic:

$$f_1\left(\varepsilon, \dot{m}_{R,T}, \omega_R\right) = 0 \tag{3.97}$$

- Turbine efficiency characteristic:

$$f_2\left(\eta_T, \dot{m}_{R,T}, \omega_R\right) = 0 \tag{3.98}$$

It should be noted however that for turbine the characteristics defined in (3.97) and (3.98) are very weak function of the turbine rotational speed, hence the following simplified correlations usually apply:

$$f_1\left(\varepsilon, \dot{m}_{R,T}\right) = 0 \tag{3.99}$$

$$f_2\left(\eta_T, \dot{m}_{R,T}\right) = 0 \tag{3.100}$$

It can be also noted that the turbine isentropic efficiency is related to the turbine power, since:

$$P_{R,T} = \dot{m}_{R,T}\bar{c}_p T_{in}\left(1-\varepsilon^{\frac{1-k}{k}}\right)\eta_T \tag{3.101}$$

A further significant parameter is the cinematic ratio:

$$c_{us} = \frac{u}{c_s} = \frac{r_T\omega}{c_s} \tag{3.102}$$

where r_t is the turbine wheel radius, u is the impeller tangential speed and c_s is the isentropic gas speed, defined as follows:

$$c_s = \sqrt{2\overline{c}_p T_{in}\left[1-\varepsilon^{\frac{1-k}{k}}\right]} \tag{3.103}$$

and represents the gas velocity that would be obtained through an isentropic expansion from the inlet to the outlet conditions existing upstream and downstream the turbine.

A common approach in modeling the behaviour of a gas turbine mass flow rate characteristic is that of approximating the turbine behaviour similar to an orifice [39,40].

The turbine mass flow rate can be calculated according to the following relationship, which is based on the turbine characteristic curve in the ($\dot{m}-\varepsilon$) plane:

$$\dot{m}_{R,T} = A_O c_T \psi \frac{p_{in}}{\sqrt{RT_{in}}} \tag{3.104}$$

A_O is the flow open area which in the general case may be assumed to vary with the actual rotational speed, c_T is the turbine flow coefficient while ψ can be defined as function of the turbine pressure ratio:

$$\psi = \begin{cases} \sqrt{\dfrac{2k}{k-1}\left[\varepsilon^{-2/n} - \varepsilon^{n+1/n}\right]} & \text{if} \quad \varepsilon \le \left(\dfrac{2}{n+1}\right)^{n-1/n} \\ \left(\dfrac{2}{n+1}\right)^{1/n-1} \sqrt{\dfrac{2k}{k-1}\dfrac{m-1}{m+1}} & \text{otherwise} \end{cases} \tag{3.105}$$

where n is the coefficient of an equivalent polytrophic expansion that approximates initial and final state of the fluid flowing through the turbine. The second correlation have been introduced to take into account of the chocking field.

Turbine efficiency can be calculated as a function of the turbine cinematic ratio, according to the following:

$$\eta_T(c_{us}) = \eta_{T,\max}\left[2\frac{c_{us}}{c_{us,\max}} - \left(\frac{c_{us}}{c_{us,\max}}\right)^2\right] \tag{3.106}$$

where parameters $\eta_{T,max}$ and $c_{us,max}$ have to be identified from the actual turbine efficiency map, the latter defined as the isentropic exit velocity at maximum efficiency. In the Eq.(3.106) the dependency of the Turbine efficiency from the reduced mass flow rate and pressure ratio, according to the definition of turbine efficiency characteristic, is related to the definition of c_{us}.

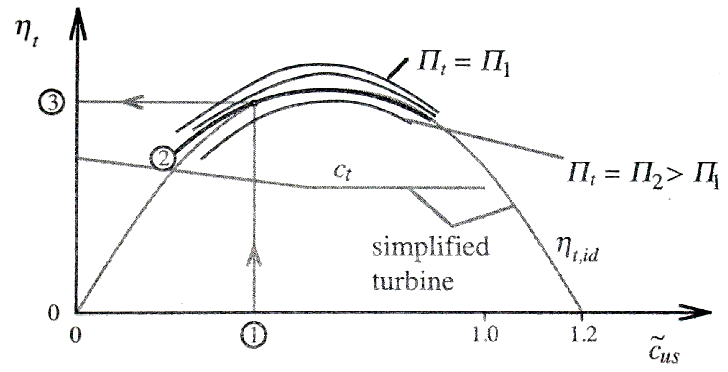

Fig. 3.50. Typical turbine efficiency characteristic as function of cinematic ratio.

The gas temperature at the turbine exit is given by the well-known relationship:

$$T_{out} = T_{in} \frac{\varepsilon^{\frac{1-k}{k}}}{\eta_t} \tag{3.107}$$

As for the air compressor (Par. 3.3.1), the turbine net power P_t can be derived combining Eq.(3.101) with the definition of reduced power. The torque can then be calculated as:

$$\tau_T = \frac{P_T}{\omega} \tag{3.108}$$

Although the model is applied to a fixed geometry turbine, its principles can be easily extended to characterize variable geometry turbines (VGT) where the throat area of the nozzles is modified, resulting in a change in expansion ratio for the same mass flow rate. One way to model the turbine flow in the presence of a variable inlet geometry is to use equations (3.104) and (3.105) where the coefficients A_0 and n, are a function of a normalized geometry setting, that should result as further input to the model.

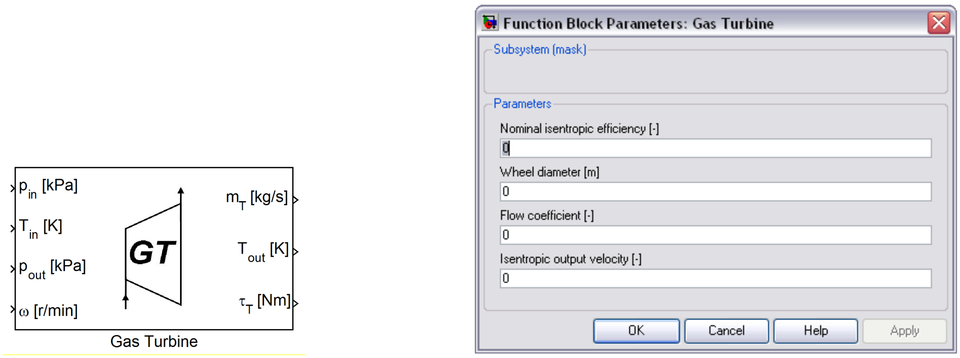

Nominal isentropic efficiency [-]: 0
Wheel diameter [m]: 0
Flow coefficient [-]: 0
Isentropic output velocity [-]: 0

(a) (b)

Fig. 3.51. Simulink® model of the turbine (a) and block dialog mask (b).

3.3.3 Model of a vapour expander

A model of an expander to be utilized within a vapour power cycle is here presented. Since within this work the vapour cycles of interest are Organic Rankine cycles, the expander considered is typical for that application. Hence an axial, dynamic, single stage turbine with *R=0* is described, where *R* represent the ratio of fluid enthalpy drop in the rotor with respect to overall available enthalpy.

As for the gas turbine also the organic fluid turbine is modelled according to a *black box*, *not state determined* approach.

Overall block input and outputs (no state parameters are defined in this case) is shown in Fig. 3.52.

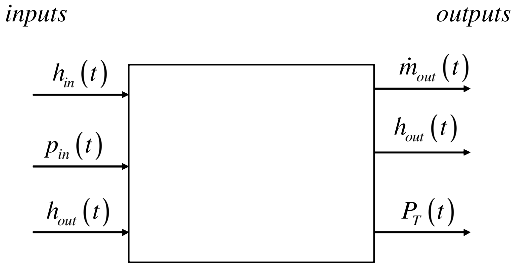

Fig. 3.52. Block diagram of the vapour turbine model.

In the mathematical model an approach similar to that followed for the gas turbine has been applied and for the mass flow rate characteristic it has once again been neglected the influence of rotational speed, according to the general correlation (3.99), and it has be approximated the relationship between mass flow rate and expansion ration as the turbine were an orifice. The following a semi empirical formulation of the Stodola equation [21] applies when a vapour expander is considered:

$$\dot{m} = K\sqrt{\rho_{in}p_{in}\left[1-\left(\frac{1}{\varepsilon}\right)^2\right]} \tag{3.109}$$

where $K=c_d{\cdot}A$ is the product between the coefficient of discharge and the equivalent nozzle cross area at the inlet.

To be noted that Eq. (3.109), unlike the two Equations (3.105) introduced for the gas turbine, has general validity and is capable to approximate also the condition of chocking that may occur given some inlet/outlet pressure ratios. Fig. 3.53 is a plot of Eq. (3.109) and refers to the turbine that will be employed in the example of ORC complete unit described in Chapter 5, as well as the other figures that follow in this section.

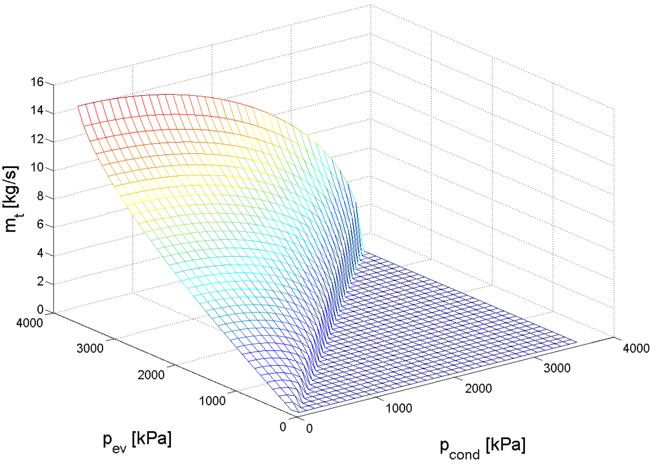

Fig. 3.53. The Stodola equation providing the turbine mass flow rate given the pressure at condenser and evaporator.

Therefore, given the *K* factor, Eq. (3.109) can provide a full representation of the mass flow rate characteristic of the expander at any operating condition. Particularly, since aim of the work is to realize a general model, a preprocessing routine is introduced in the turbine block that determines the equivalent *K* from the following equation (which is a reverse form of equation (3.109)), given the nominal operating parameters of the turbine (subscipts *n*):

$$K_{eq} = \frac{\dot{m}_n}{\sqrt{\rho_n p_n\left[1-\left(\frac{1}{\varepsilon_n}\right)^2\right]}} \qquad (3.110)$$

In Fig. 3.54 the mass flow rate characteristic curves are shown and the nominal operating conditions are highlighted by the * symbol. The curves reported are orthogonal sections of the surface of Fig. 3.53.

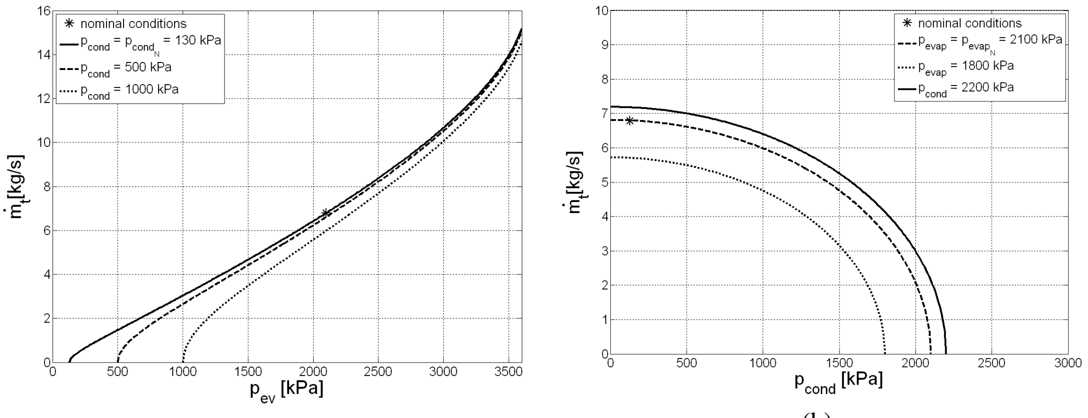

(a) (b)

Fig. 3.54. Expander mass flow rate characteristic curves at varying evaporator pressure and for three values of condenser pressures (a) and at varying condenser pressure and for three values of evaporator pressures.

As in the case of gas turbine, for the vapour turbine the rotational speed parameter is neglected in the efficiency characteristic and the general correlation (3.100) is applied through a polynomial function of second grade analogous to Eq. (3.106) that can be defined given the operational point at maximum efficiency.

From the turbine efficiency the power can be calculated as:

$$P_T = \dot{m}_T \eta_T \left(h_{in} - h_{out}\big|_s \right) \tag{3.111}$$

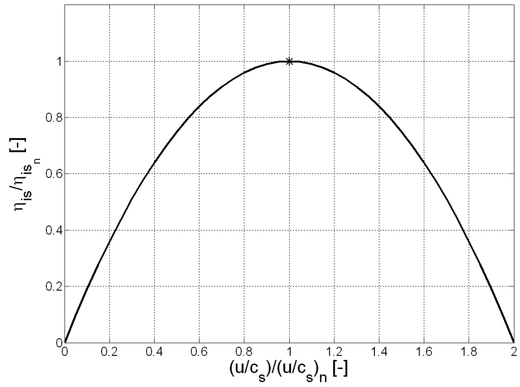

Fig. 3.55. Turbine efficiency characteristic curve.

Fig. 3.56 reports the Simulink® model of the turbine which is based on a *m-sfunction* (where the characteristics equations are implemented at each time step), as well as the block dialog mask. It can be observed how, among the parameters, nominal operating values of the main variables must be provided. These values are employed within an initialization function that calculates the parameters that appear in the nominal characteristic curves. It can be easily appreciated the flexibility of the model proposed that can provide representation of any desired turbine by simply tuning these parameters. Despite this is achieved by using simplified forms of the characteristic equations, for the scope of present work generality is a more desired requirement than a too detailed description of the component.

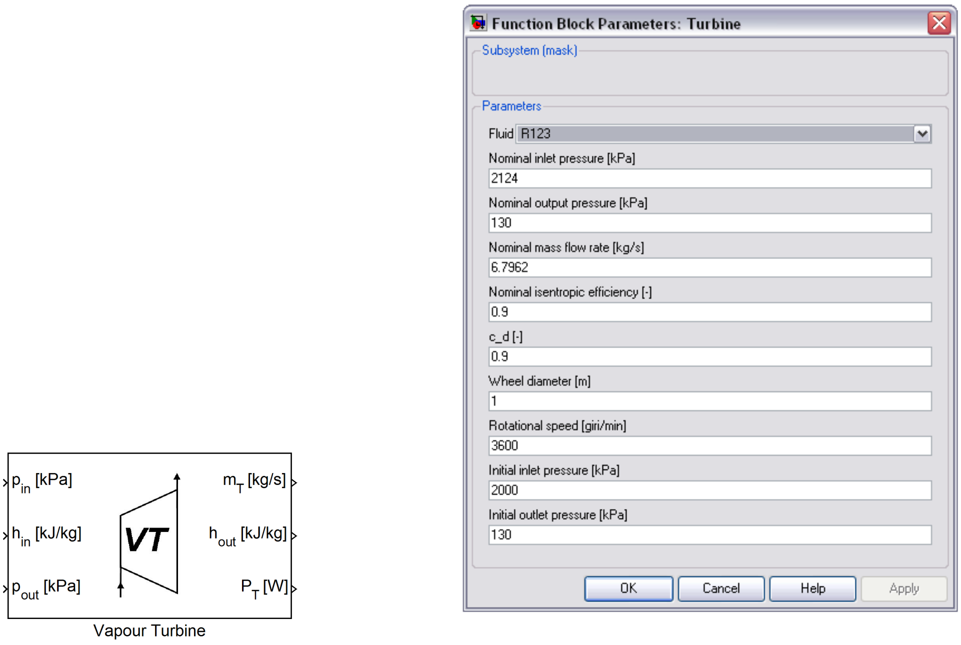

Function Block Parameters: Turbine

Subsystem (mask)

Parameters

Fluid R123

Nominal inlet pressure [kPa]
2124

Nominal output pressure [kPa]
130

Nominal mass flow rate [kg/s]
6.7962

Nominal isentropic efficiency [-]
0.9

c_d [-]
0.9

Wheel diameter [m]
1

Rotational speed [giri/min]
3600

Initial inlet pressure [kPa]
2000

Initial outlet pressure [kPa]
130

(a) (b)

Fig. 3.56. Simulink® model of the vapour turbine (a) and block dialog mask (b).

3.3.4 The pump

The pump model here proposed will find applications in all the cases where the head (*y*) of an incompressible fluid needs to be raised. One interesting application of the pump model is within vapour power cycles (particularly Organic Rankine Cycles), hence the modeling approach will be focused at creating a component suitable for the purpose. The pump considered will be therefore radial, dynamic, single stage.

As for the other fluid machines also the pump has been modeled according to a *black box*, *not state determined* approach. In this case the idea not to define one single specific pump but rather to produce a model that could realistically represent different pumps and can be easily scaled has led to simplifying the characteristic curves as shown below.

Overall block input and outputs (no state parameters are defined in this case) is shown in Fig. 3.57.

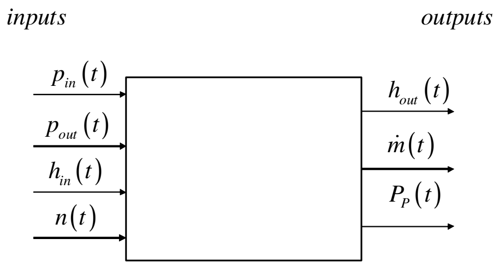

Fig. 3.57. Block diagram of the pump model.

- Pump flow rate characteristic:

The general expression of the volumetric flow rate characteristic is the following:

$$f_1\left(y, \omega_p, \dot{V}\right) = 0 \tag{3.112}$$

Usually the flow rate characteristic for a pump is reported on a $y - \dot{V}$ plane at different values of the pump rotational speed.

In this case the nominal characteristic curve is plotted given the nominal flow rate, and head, at the nominal rotational speed, from the following:

$$y = \frac{y_n - y_{0_n}}{\dot{V}_n^2}\dot{V}^2 + y_{0_n} \tag{3.113}$$

where y_{0_n} is the pump head at nominal rotational speed when no flow rate is allowed.

Starting from the curve plotted at the nominal rotational speed, as from Eq. (3.113), analogous curves at different rotational speed can be determined applying proper scaling rules:

$$\begin{aligned} \dot{V}' &= \dot{V}\left(\frac{\omega}{\omega'}\right) \\ y' &= y\left(\frac{\omega}{\omega'}\right)^2 \end{aligned} \tag{3.114}$$

In the case of pumps in fact, the dependency from the rotational speed of the flow rate characteristic cannot be neglected and ω_P appears in the general characteristic equation (3.112).

Fig. 3.58 reports the flow rate characteristic curves at nominal operating point. The nominal curve is highlighted and more curves at different rotational speed are also plotted. The curve, as well as that of Fig. 3.59, refers to the actual pump employed in the ORC model of Chapter 4.

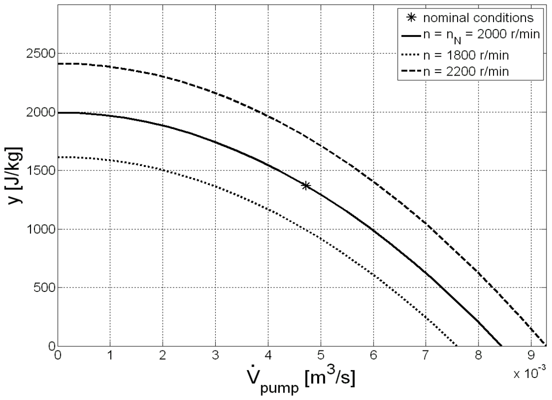

Fig. 3.58: Pump flow rate characteristics.

- Pump efficiency characteristic:

The general expression of the efficiency characteristic is the following:

$$f_2\left(\eta_p, \omega_p, \dot{V}\right) = 0 \tag{3.115}$$

As for the flow rate characteristic, the pump isentropic efficiency has been approximated by a polynomial curve on the $\eta_p - \dot{V}$ plane, given the nominal values and according to the following:

$$\eta_p = -\frac{\eta_{p_n}}{\dot{V}_n^2}\dot{V}^2 + 2\frac{\eta_{p_n}}{\dot{V}_n}\dot{V} \tag{3.116}$$

Starting from pump efficiency, the pump required power can be easily computed, and then the curves can be once again scaled recurring to scaling rules of the type:

$$\begin{aligned} \dot{V}' &= \dot{V}\left(\frac{\omega}{\omega'}\right) \\ P' &= P\left(\frac{\omega}{\omega'}\right)^3 \end{aligned} \tag{3.117}$$

In Fig. 3.59 the efficiency characteristic curves are shown for a given a nominal operating point. The nominal curve is highlighted and several curves at different rotational speed are also plotted.

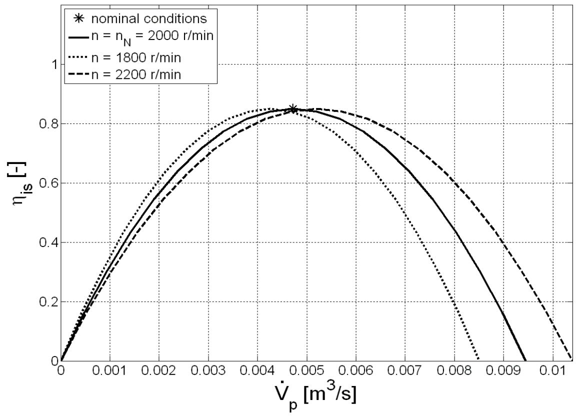

Fig. 3.59. Pump efficiency characteristics.

Fig. 3.60 reports the realized Simulink® model of the pump which is based on a *m-sfunction* where the characteristics equations are implemented at each time step, as well as the block dialog mask. It can be observed how, among the parameters, nominal operating values of the main variables must be provided. This values are employed within an initialization function that calculates the parameters that appear in the nominal characteristic curves of Eqs. (3.113) and (3.116). It can be easily appreciated the flexibility of the model proposed that can provide representation of any desired pump by simply tuning these parameters.

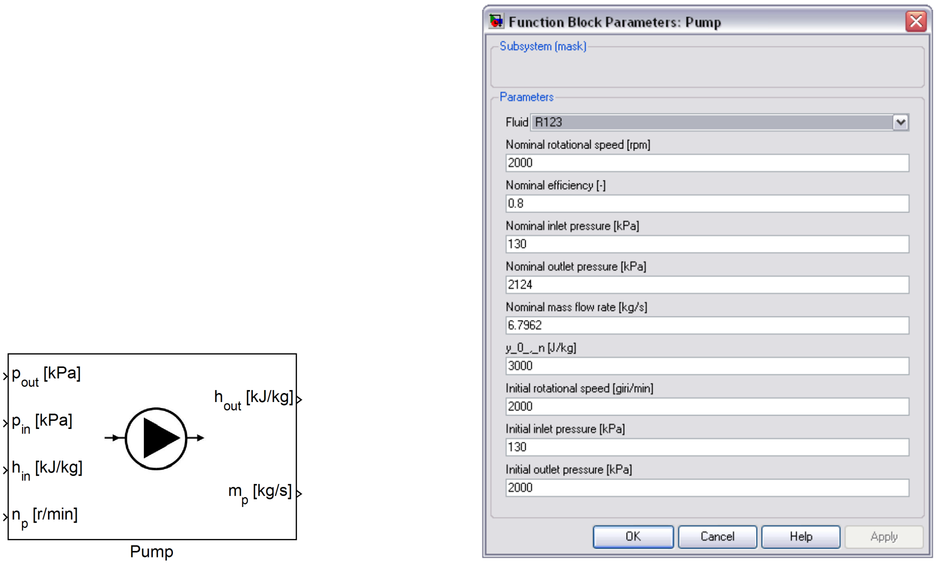

Function Block Parameters: Pump

Subsystem (mask)

Parameters

Fluid: R123

Nominal rotational speed [rpm]: 2000

Nominal efficiency [-]: 0.8

Nominal inlet pressure [kPa]: 130

Nominal outlet pressure [kPa]: 2124

Nominal mass flow rate [kg/s]: 6.7962

y_0_._n [J/kg]: 3000

Initial rotational speed [giri/min]: 2000

Initial inlet pressure [kPa]: 130

Initial outlet pressure [kPa]: 2000

(a) (b)

Fig. 3.60. Simulink® model of the pump (a) and block dialog mask (b).

3.3.5 ICE in-cylinder combustion process

The in-cylinder combustion processes of a generic ICE have been modeled through a specifically developed code for calculating the chemical equilibrium composition of the products and the flame temperature for a combustion reaction of a generic fuel with air, for a C-H-O-N system, in both cases of constant volume and constant pressure combustion. After its validation the code has been used for the development of a zero-dimensional model that simulates the compression and expansion strokes in a cylinder of an internal combustion engine, calculating the thermodynamic state and chemical equilibrium composition of the reacting mixture of gases at each simulation step, defined by a finite increase in the engine shaft crank angle [41]. Empirical correlations have then been introduced to take account of the heat exchange between gases and cylinder walls to make the complete engine cycle closer to the real cycles (only the “closed valves” process is assessed).

3.3.5.1 Combustion reaction and chemical equilibrium

The combustion reaction of a generic $C_nH_mO_r$ fuel with air can be written as following, considering n product species after combustion:

$$C_nH_mO_r+\left(\frac{n+\frac{m}{4}-\frac{r}{2}}{\varphi}\right)O_2+\frac{79}{21}\left(\frac{n+\frac{m}{4}-\frac{r}{2}}{\varphi}\right)N_2\rightarrow N_p\left(X_a a+...+X_i i+...X_n n\right) \tag{3.118}$$

where φ is the equivalence ratio, defined as:

$$\varphi = \frac{\alpha_{st}}{\alpha} \tag{3.119}$$

A great number of product species n can be considered for combustion processes (The CEC code developed by NASA can consider up to 400 species [42]) however, to keep the system complexity to a reasonable degree, the only dissociation reactions reported below are considered:

- $CO_2 \leftrightarrow CO + \frac{1}{2}O_2$
- $H_2O \leftrightarrow H_2 + \frac{1}{2}O_2$
- $OH \leftrightarrow \frac{1}{2}O_2 + \frac{1}{2}H_2$
- $HO \leftrightarrow \frac{1}{2}O_2 + \frac{1}{2}N_2$
- $\frac{1}{2}O_2 \leftrightarrow O$
- $\frac{1}{2}N_2 \leftrightarrow N$
- $\frac{1}{2}H_2 \leftrightarrow H$

This leads to considering that the following 11 as products of the combustion reaction:

- Carbon Dioxide: CO_2;
- Carbon Monoxide: CO;
- Water: H_2O;
- Molecular Hydrogen: H_2;
- Molecular Oxygen: O_2;
- Molecular Nitrogen: N_2;
- Hydroxide: OH;
- Nitric oxide: NO;
- Atomic Hydrogen: H;
- Atomic Oxygen: O;
- Atomic Nitrogen: N;

It has also been assumed that the system is closed (neither heat nor mass transfer occurs) and that the combustion reaction is complete, meaning that all the fuel reacts with the oxidizer to form products.

The chemical equilibrium is invoked by applying the second law of thermodynamics, thus maximizing the entropy of the products mixture, or equivalently minimizing the Gibbs free energy G, defined as [43]:

$$G = H - TS \tag{3.120}$$

For a generic reactant system:

$$aA + bB + \ldots \leftrightarrow eE + fF + \ldots \tag{3.121}$$

the chemical equilibrium is given by the following equation:

$$\frac{\left(\frac{p_e}{p^0}\right)^e\left(\frac{p_f}{p^0}\right)^f\cdots}{\left(\frac{p_a}{p^0}\right)^a\left(\frac{p_b}{p^0}\right)^b\cdots}=e^{\frac{-\Delta G_T^0}{R_u}} \tag{3.122}$$

where p_i is the partial pressure of the i^{th} specie and the standard-state Gibbs function change ΔG_T^0 is defined as following:

$$\Delta G_T^0=\left(e\overline{g}_{f,E}^0+f\overline{g}_{f,F}^0+\ldots-a\overline{g}_{f,A}^0-b\overline{g}_{f,B}^0-\ldots\right)_T \tag{3.123}$$

The standard state is defined, according to IUPAC standards, by a pressure p^0=100kPa [44]. The reference temperature T_{ref}=298K has been chosen according to the CHEMKIN database [45], which was used as reference for all the thermodynamic state variables of interest.

The equilibrium composition of the mixture at a given temperature and pressure, according to the assumptions made, is determined by the following 12 unknowns:

$$X_{CO_2},\ X_{CO},\ X_{H_2O},\ X_{H_2},\ X_{O_2},\ X_{N_2},\ X_{OH},\ X_{NO},\ X_{O},\ X_{N},\ X_{H},\ \mathrm{N}_{prod} \tag{3.124}$$

where X_i is the molar fraction of the i^{th} specie, and N_{prod} is the total number of moles.

These 12 unknowns are determined solving the following non-linear system of 12 equations:

$$
\begin{cases}
\dfrac{X_{CO} \cdot X_{O_2}}{X_{CO_2}} \cdot \left(\dfrac{p}{p_{atm}} \right)^{\frac{1}{2}} = e^{-\left(\frac{\bar{g}^0_{fCO} - \bar{g}^0_{fCO_2}}{RT} \right)} \\
\dfrac{X_{H_2} \cdot X_{O_2}^{\frac{1}{2}}}{X_{H_2O}} \cdot \left(\dfrac{p}{p_{atm}} \right)^{\frac{1}{2}} = e^{-\left(\frac{\bar{g}^0_{fH_2O}}{RT} \right)} \\
\dfrac{X_{H_2}^{\frac{1}{2}} \cdot X_{O_2}^{\frac{1}{2}}}{X_{OH}} \cdot \left(\dfrac{p}{p_{atm}} \right)^{\frac{1}{2}} = e^{-\left(\frac{\bar{g}^0_{fOH}}{RT} \right)} \\
\dfrac{X_{N_2}^{\frac{1}{2}} \cdot X_{O_2}^{\frac{1}{2}}}{X_{NO}} \cdot \left(\dfrac{p}{p_{atm}} \right)^{\frac{1}{2}} = e^{-\left(\frac{\bar{g}^0_{fNO}}{RT} \right)} \\
\dfrac{X_O}{X_{O_2}^{\frac{1}{2}}} \cdot \left(\dfrac{p}{p_{atm}} \right)^{\frac{1}{2}} = e^{-\left(\frac{\bar{g}^0_{fO}}{RT} \right)} \\
\dfrac{X_N}{X_{N_2}^{\frac{1}{2}}} \cdot \left(\dfrac{p}{p_{atm}} \right)^{\frac{1}{2}} = e^{-\left(\frac{\bar{g}^0_{fN}}{RT} \right)} \\
\dfrac{X_H}{X_{H_2}^{\frac{1}{2}}} \cdot \left(\dfrac{p}{p_{atm}} \right)^{\frac{1}{2}} = e^{-\left(\frac{\bar{g}^0_{fH}}{RT} \right)} \\
X_{CO_2} + X_{CO} = \dfrac{n_C}{N_{prod}} \\
2X_{CO_2} + X_{CO} + X_{H_2O} + 2X_{O_2} + X_{OH} + X_{NO} + X_O = \dfrac{n_O}{N_{prod}} \\
2X_{H_2O} + 2X_{H_2} + X_{OH} + X_H = \dfrac{n_H}{N_{prod}} \\
2X_{N_2} + 2X_{NO} + X_N = \dfrac{n_N}{N_{prod}} \\
X_{CO_2} + X_{CO} + X_{H_2O} + X_{H_2} + X_{O_2} + X_{N_2} + X_{OH} + X_{NO} + X_O + X_N + X_H = 1
\end{cases}
\tag{3.125}
$$

where the first 7 equations represent the chemical equilibrium of the considered dissociation reactions, while the last 5 equations represent respectively: the conservation of the total number of carbon atoms; the conservation of the total number of oxygen atoms; the conservation of the total number of hydrogen atoms; the conservation of the total number of nitrogen atoms and the conservation of mass.

From Dalton's law that for the i^{th} specie of a mixture it can be also written:

$$X_i = \frac{p_i}{p} \tag{3.126}$$

where p is the total pressure of the mixture.

The analytic solution of non-linear systems of algebraic equations is generally impossible, thus a numerical approximate solution is necessary.

Scope of the analysis, besides determining the actual gas composition during the combustion process, is also to determine the in-cylinder thermodynamic state.

The whole combustion phase of the engine can be split in a series of discrete constant volume combustions, where the volume at each step is determined by the crank-piston correlation.

The adiabatic flame temperature is determined by applying the first law of thermodynamics, that, for an isolated constant-volume system can be written in the following form:

$$U_{react}(T_i, V)=U_{prod}(T_{ad}, V) \tag{3.127}$$

Under the assumption that every product of combustion can be considered as an ideal gas, Eq. (3.127) can be rewritten for T_{ad} as:

$$T_{ad} = \frac{\sum_{react} N_i \left[\bar{h}^0_{f,i} + \bar{c}_{p,i} \left(T_i - T_{ref} \right) \right] - \sum_{prod} N_j \left[\bar{h}^0_{f,j} + \bar{c}_{p,j} \left(-T_{ref} \right) \right] - N_{react} R_0 T_i}{\sum_{prod} N_j \bar{c}_{p,j} - N_{prod} R_0} \tag{3.128}$$

The constant pressure specific heat has been considered a function of the sole temperature; a mean value has been used, determined at a mean temperature between the initial and the adiabatic flame temperature:

$$\bar{T} = \frac{T_i + T_{ad}}{2} \tag{3.129}$$

The error made considering the specific heat as a constant value in Eq.(3.128) is very small, while the equation itself is notably simplified, resulting in a greater simplicity of the program and a lower computational load.

It can be noted however from Eq.(3.128) that the adiabatic flame temperature depends on the chemical composition of the system. However, from (3.125), it can be observed that in turn the equilibrium chemical composition depends on the adiabatic flame temperature, since the molar Gibbs function of the i^{th} specie $\bar{g}^0_{f_i}(T)$ is a function of the temperature. An iterative procedure is then required, starting from a given initial guess value for the adiabatic flame temperature. Moreover, the numerical solution of the non-linear system of equations (3.125) requires itself another initial guess value of the equilibrium composition of the products. Therefore the program uses two iterative procedures, which make the real-time on-line running of the program not feasible, even if computational load and the running time were as low as possible. The program for the solution of the combustion process therefore could not have been employed directly into the in-cylinder combustion block due to high computational time but will be employed in a pre-processing operation to derive characteristic maps that cover wide operational conditions that will be in turn introduced into the model, reliving it from the two combined iterative solution procedures.

Starting from the initial guess of the adiabatic flame temperature, the equilibrium composition of the system is determined by solving the non-linear system of equations (3.125); using this composition, Eq.(3.128) is applied and a new final temperature is calculated. This calculated temperature is then compared with the previous one used for the determining the equilibrium composition; the process is then repeated until the difference between these two values is equal or less than a user-set value (default is 1K). The initial and final volume (in case of constant pressure combustion) or pressure (in case of constant volume combustion) of the system is determined using the equation of state of ideal gases.

$$pV = NR_0T \tag{3.130}$$

The numerical solution was obtained utilizing the *fsolve* function embedded in the *Optimization Toolbox* contained in the Matlab® environment. *fsolve* transforms the solving of a non-linear system of equations into a least-squares optimization problem, using the *Gauss-Newton* [46] and *Levenberg-Marquardt* [47] algorithms.

The default solving algorithm is the *Gauss-Newton* one: however this algorithm is implemented into *fsolve* so that automatically switches to the *Levenberg-Marquardt* algorithm when either the step length goes below a threshold value (1e-15) or when the condition number of the Jacobian matrix is below 1e-10. The condition number is a ratio of the largest singular value to the smallest. The difference between the two algorithms is the strategy used for the determination of the next point of function evaluation; while the *Gauss-Newton* method uses a *line search* strategy, the *Levenberg Marquardt* algorithm uses a *trust-region* method.

The main problem when using approximate numerical solutions lies in the need for initial values of the unknowns, which must be not too different from the real solution if a good convergence is to be achieved.

The *Gauss-Newton* method implemented into *fsolve* has proven to be able to solve the non-liner system of equations in a wide range of temperature values: however, it has been found that it is very difficult to find a solution of the system for temperatures of less than 750K for which there is very little if no dissociation at all. In this temperature range, to avoid numerical problems due to the bad conditioning of the problem, only two dissociation reactions were considered, eliminating those reactions that did not yield almost any product. The considered reactions were:

- $CO_2 \leftrightarrow CO + \frac{1}{2}O_2$
- $H_2O \leftrightarrow H_2 + \frac{1}{2}O_2$

The non-linear system of equations describing the chemical equilibrium condition is then reduced to:

$$
\begin{cases}
\dfrac{X_{CO}\cdot X_{O_2}}{X_{CO_2}}\cdot\left(\dfrac{p}{p_{atm}}\right)^{\frac{1}{2}}=e^{-\left(\frac{\bar{g}^0_{fCO}-\bar{g}^0_{fCO_2}}{RT}\right)}\\
\dfrac{X_{H_2}\cdot X_{O_2}^{\frac{1}{2}}}{X_{H_2O}}\cdot\left(\dfrac{p}{p_{atm}}\right)^{\frac{1}{2}}=e^{-\left(\frac{\bar{g}^0_{fH_2O}}{RT}\right)}\\
X_{CO_2}+X_{CO}=\dfrac{n_C}{N_{prod}}\\
2X_{CO_2}+X_{CO}+X_{H_2O}+2X_{O_2}=\dfrac{n_O}{N_{prod}}\\
2X_{H_2O}+2X_{H_2}=\dfrac{n_H}{N_{prod}}\\
2X_{N_2}=\dfrac{n_N}{N_{prod}}\\
X_{CO_2}+X_{CO}+X_{H_2O}+X_{H_2}+X_{O_2}+X_{N_2}=1
\end{cases}
\tag{3.131}
$$

The results obtained from the program were validated by comparing them with the data obtained with the *TPEQUIL* software [43], which is based on the algorithms developed by Olikara and Borman [48], and considers the same 11 species considered here (3.124).

Fig. 3.61 and Fig. 3.62 show the comparison between the developed program results and the *TPEQUIL* data. As can be noted, the data corresponds perfectly, and the realized Matlab® program is capable of finding the correct solution even for extremely lean mixtures ($\varphi \leq 0.2$), for which the adiabatic flame temperature is lowest. The only major difference is found for the molar fraction of the monoatomic hydrogen *H*, which, when present, is higher than the one obtained with the TPEQUIL program.

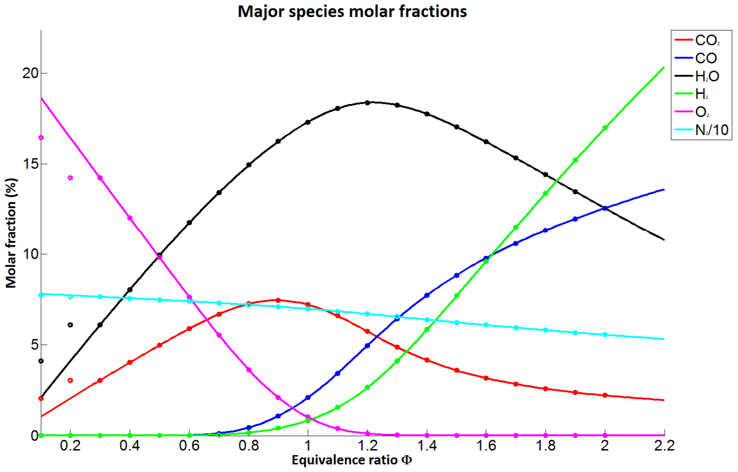

Fig. 3.61. Validation of the code (lines) by comparison with data obtained with *TPEQUIL* (dots): major species molar fractions at different values of the equivalence ratio. The chart data refers to constant volume Methane (CH_4) combustion; starting temperature T_i is 298 K and starting pressure p_i is 101325 Pa.

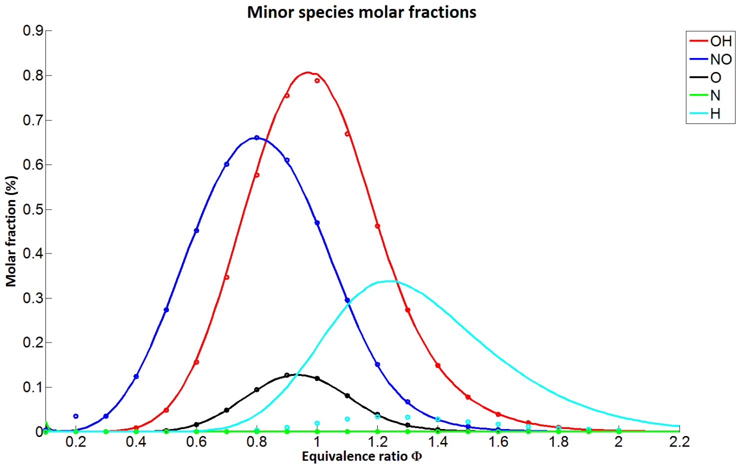

Fig. 3.62. Validation of the realized code (lines) by comparison with data obtained with *TPEQUIL* (dots): minor species molar fractions at different values of the equivalence ratio. The chart data refers to constant volume Methane (CH_4) combustion; starting temperature T_i is 298 K and starting pressure p_i is 101325 Pa.

3.3.5.2 In-cylinder processes pre-processing tool

Starting from the developed and validated methodology for the calculation of adiabatic flame temperature and gas composition described in the previous Section, a specific code has be compiled allowing the solution of the compression and combustion strokes of an ICE.

The following hypotheses were assumed:

- all considered quantities are not space-dependent (0-D modeling);
- the mixing between fuel and air is perfect;
- the combustion reaction takes place without any delay;
- all the dissociation reactions reach instantaneously the chemical equilibrium;
- the combustion process is modeled as a sequence of instantaneous constant-volume reactions which involve a fraction of the total amount of fuel.

Due to the approach followed the code allows knowing the thermodynamic state of the system at any given discrete crank angle step (or time step, if the rotational speed is known), and some graphs are plotted below to show the evolution of the system during the two considered engine strokes.

Since aim of the present work is however generate a set of data to be provided to a model of the ICE combustion process to be inserted in a Mean Value engine model, the only values referring to the system state at BDC, just before the exhaust valve opening, are of interest.

In the procedure, the effect of work and heat exchanged by the gas with the surroundings will also be evaluated, thus the system can no longer be considered insulated but just closed.

As for the compression stroke, the step by step gas temperature is evaluated from the state in the previous step by considering an isentropic process, since the assumption of an ideal engine makes the process both reversible and adiabatic (there are neither friction losses nor heat exchange); hence for the i^{th} simulation step it can be stated that:

$$T_s = T_{s-1}\left(\frac{V_{s-1}}{V_s}\right)^{k-1} \tag{3.132}$$

where s indicates the generic step in which the process has been divided.

The pressure is easily evaluated applying the state equation of ideal gases, since at each simulation step the volume remains constant.

Boundary condition to be provided is the air temperature at start of compression resulting for example as the temperature existing in the intake manifold of the engine.

The rate of change in the combustion chamber volume can be calculated referring to the crank mechanism.

For the expansion stroke the temperature of the system at each step is calculated as the adiabatic flame temperature resulting from the combustion of the fuel burned during the current step, starting from a mixture whose composition is determined by the equilibrium composition of the system at the previous step conditions; the amount of fuel involved in the constant volume combustion of each simulation step is given by a Fuel Burning Rate curve (FBR) that must be provided and is the black box representation of the way the fuel combustion evolves in time within the combustion chamber, and can be selected to simulate either a spark-ignition or compression-ignition ICE.

The work done by the gas can approximately calculated as:

$$W = \overline{p}dV \tag{3.133}$$

where dV is the volume variation between two consecutive simulation steps, and $\overline{p}$ is the mean value in the step of the in-cylinder pressure, evaluated as:

$$\overline{p} = \frac{p_{s-1} + p_s}{2} \tag{3.134}$$

Heat transfer through the cylinder walls is an important process in determining overall performance, of an internal combustion engine. It affects the indicated efficiency because it reduces the cylinder temperature and pressure, and thereby decreasing the work transferred on the piston per cycle [49].

The followed approach for the instantaneous heat transfer coefficient, developed by Annand [50], allows to calculate the instantaneous convective heat exchange coefficient, as function of crank angle, according to the following:

$$U(\theta) = a\frac{k}{D}Re^b \tag{3.135}$$

The *a* constant represents the level of convective heat transfer, varies with intensity of charging motion and combustion chamber design. At normal combustion, it varies from 0.25 to 0.8 and increases directly with increasing the intensity of charging motion. The index *b* varies from 0.7 to 0.8 [50]. Reynolds number is formed with a characteristic speed equal to the mean piston velocity u_p, a characteristic length equal to the *D* cylinder bore, gas density and dynamic viscosity as follows:

$$Re(\theta)=\frac{\rho(\theta)u_p(\theta)D}{\mu(\theta)} \tag{3.136}$$

The instantaneous cylinder volume area and piston speed are calculated as a function of crank angle.

Taking account of both the work and heat exchange the first law of thermodynamic (3.127) can be rewritten as:

$$U_{react}(T_{init},V_{init})=U_{prod}(T_f,V_f)+W+Q \tag{3.137}$$

Remembering the equation of state of ideal gases and the definition of enthalpy, Eq. (3.137) can be rewritten as:

$$H_{react}-H_{prod}-R_u(N_{react}T_{init}-N_{prod}T_f)-W-Q=0 \tag{3.138}$$

Substituting Eq.(3.128) in Eq.(3.138) the final gas temperature (referred to a generic step) can be calculated:

$$T_f=\frac{\sum\limits_{react}N_i\left[\bar{h}^0_{f,i}+\bar{c}_{p,i}\left(T_i-T_{ref}\right)\right]-\sum\limits_{prod}N_j\left[\bar{h}^0_{f,j}+\bar{c}_{p,j}\left(-T_{ref}\right)\right]-N_{react}R_0T_i-\bar{p}dV-Q}{\sum\limits_{prod}N_j\bar{c}_{p,j}-N_{prod}R_0} \tag{3.139}$$

3.3.5.3 The in-cylinder model

Starting from the pre-processing tool described in the previous section a series of maps can be compiled to represent the final state of the gases at the end of the compression and expansion strokes.

The block overall inputs and outputs are represented as from Fig. 3.63.

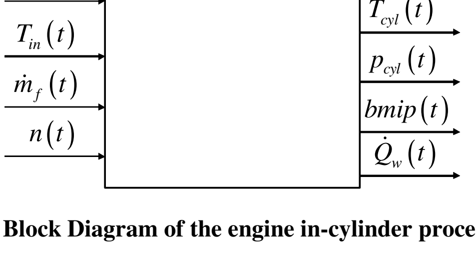

Fig. 3.63. Block Diagram of the engine in-cylinder processes model.

It can be observed that, since the model features four independent inputs, the maps to be provided to the engine will be four dimensional matrixes. In the figures that follows the maps, referring to the stationary cogenerative natural-gas fired ICE that will be further illustrated in Chapter 4, are presented. Since the engine is supposed to operate constantly at 1000r/min for generator synchronization, the dependency on the rotational speed is dropped and the maps are reported as function of the only three independent variables $\dot{m}_{in}$, φ and T_{in}.(where φ can be calculated stating from $\dot{m}_{in}$ and $\dot{m}_f$).

Four matrixes are provided to calculate the main four model outputs: the temperature and pressure existing within the cylinder at BDC (T_{cyl} and p_{cyl}), the engine mean indicated pressure, calculated being known the pressure during the whole cycle (see for example Fig. 3.66) and the heat exchanged by the gas to the cylinder wall, that is assumed to be entirely transferred to the engine refrigerant water ($\dot{Q}_w$).

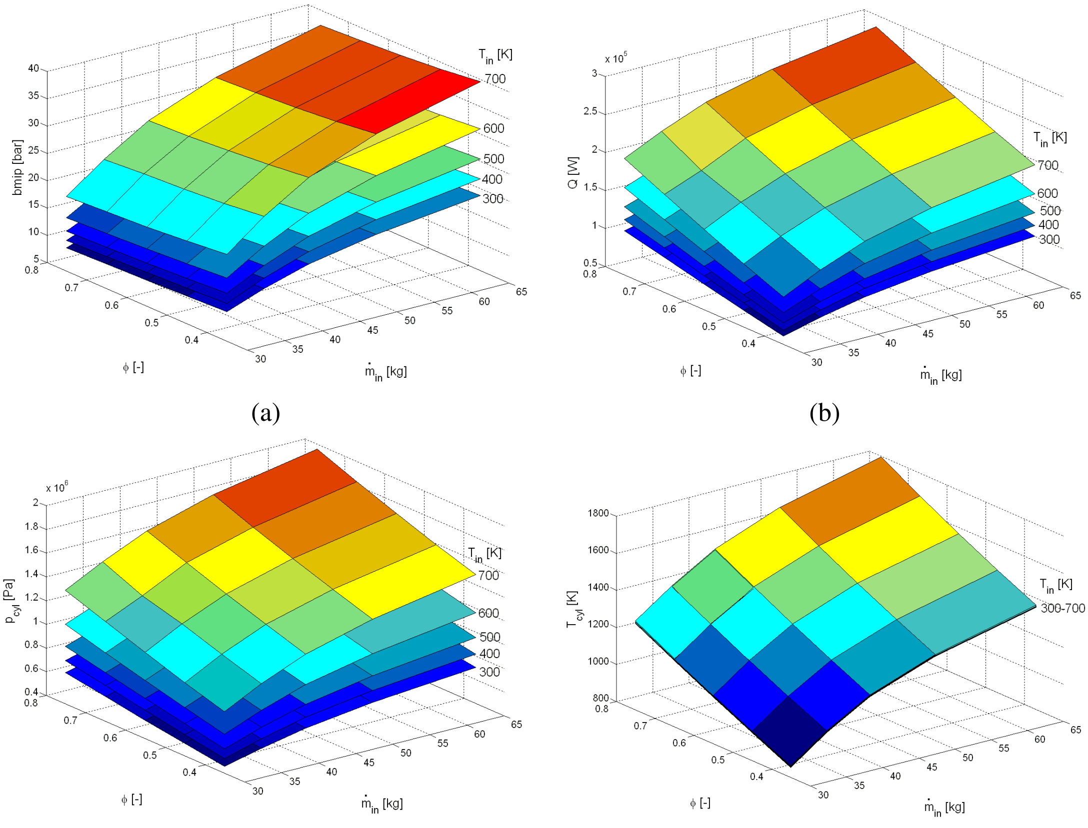

(a) (b)

(c) (d)

Fig. 3.64. Performance maps provided to the in-cylinder model with reference to a stationary cogenerative natural gas fired ICE: (a) *bmip*, (b) heat exchanged between gas and cylinder walls, (c) in-cylinder pressure at BDC and (d) in-cylinder temperature at BDC. Values at different engine intake air mass flow, fuel equivalence ration and inlet air temperature.

The gas composition (at equilibrium) could also be provided as overall model output, since the pre-processing software, as seen, also allows to know the amount of the different species at each time.

Example is provided in Fig. 3.65 for the same engine of Fig. 3.66, where the species evolution during a whole closed valves cycle is presented at nominal operating conditions.

It can be observed that, due to the lean combustion, no CO is found at the end of cycle an some oxygen is still left at the end of combustion. The NO formation appears limited due to the low temperatures; its presence appears to decline moving towards the BDC since only the chemical equilibrium is considered. With the decreased temperature, that is reached due to gas expansion, the chemical equilibrium leads to nearly no NO formation even though it is well known that for nitrogen oxides the characteristic formation and dissociation times are usually much higher than the typical ICE cycle frequency. The evolution of nitrogen oxides, that is here only evaluated as function of gas temperature, is therefore probably misleading and for a better representation a chemical dynamics approach should be preferred.

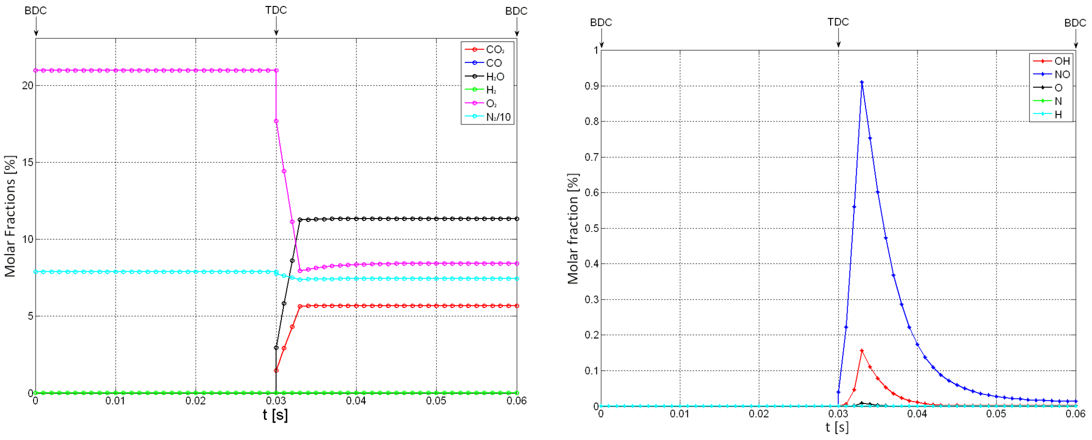

(a) (b)

Fig. 3.65. Evolution of chemical species as function of cycle time

Some other plots are here reported to show the capabilities of the developed tool. Fig. 3.66 and Fig. 3.67, which again refer to the stationary ICE that will be illustrated in Chapter 4, show some characteristics of the engine cycle.

Fig. 3.66 represent the typical engine *p*-*V* diagram and is here reported only for the compression and expansion strokes. The temperature evolution, and the heat exchanged by the gas with the engine walls, are reported in Fig. 3.67. In this first release of the model heat exchange is assumed to occur only in the expansion stroke.

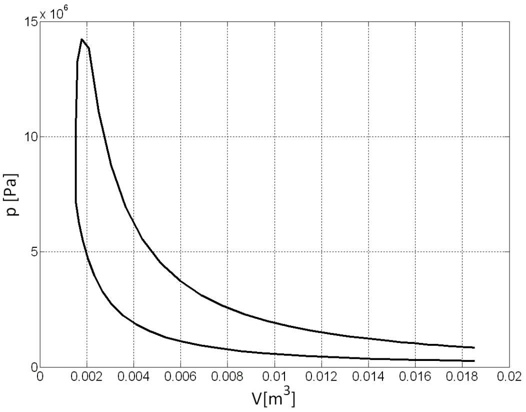

Fig. 3.66. ***p-V*** **diagram of the compression and expansion stroke for the engine considered.**

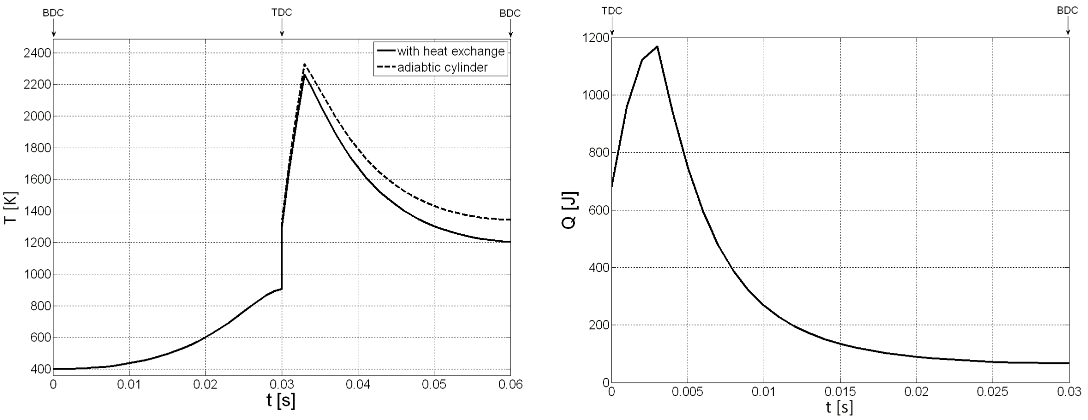

(a) (b)

Fig. 3.67. (a) in-cylinder gas temperature and (b) gas-cyclinder heat exchanged as function of cycle time.

To be noted that the proposed model features some important simplifications that need to be mentioned. The first hypothesis is that not mechanical losses are accounted, hence the *mip* is only calculated; the introduction of an empirically calculated mechanical efficiency is necessary to calculated the *mep*, hence the actual engine power.

No pumping effects are considered (the open vales strokes have here not been considered) so the effect of possible losses are not accounted for in this model release.

Also no dynamics in the heat exchange between gas and cylinder walls is considered. As a consequence the available heat in the engine refrigerant is considered to be a function of the gas temperature.

Besides these simplifications the procedure introduced has the big advantage of allowing to built precise models of the combustion processes within ICEs recurring to cardinal laws (as the energy conservation equations and chemical species conservation equations) and avoiding to recur to large set of experimental data on the engine analyzed, as it is common practice to model the combustion processes in fast and mean ICE models.

The model can therefore be considered as *white-box*, but the introduction of empirical coefficients leads to consider it *grey-box* at right. The Simulink® interface of the proposed model is visible in Fig. 3.68.

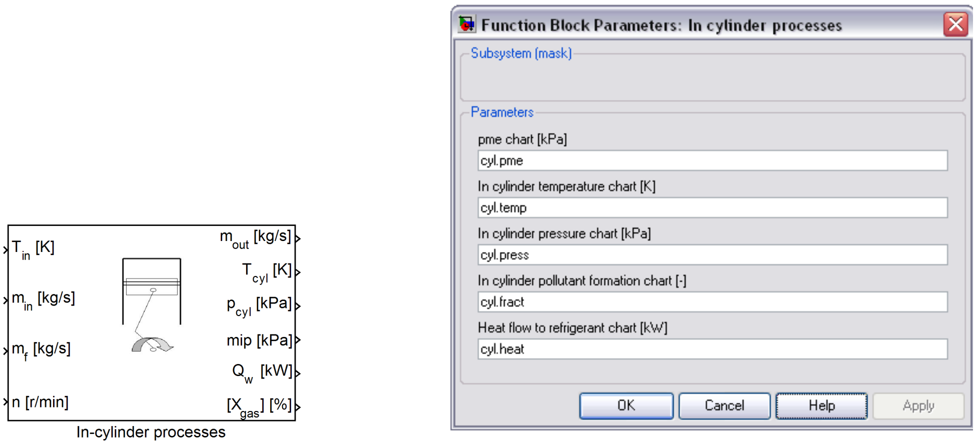

pme chart [kPa]: cyl.pme

In cylinder temperature chart [K]: cyl.temp

In cylinder pressure chart [kPa]: cyl.press

In cylinder pollutant formation chart [-]: cyl.fract

Heat flow to refrigerant chart [kW]: cyl.heat

(a) (b)

Fig. 3.68. Simulink® model of the in-cylinder combustion processes (a) and block dialog mask (b).

3.3.6 Valves and restrictions

In fluid systems, besides compressors, turbines, pumps, etc., other flow control devices are usually used, as valves and orifices of different nature, that differ from the above mentioned elements since no moving exchange useful technical work with the fluid. From a system dynamics standpoint, these blocks determine the mass and energy flow rates through the component as functions of the instantaneous value of the upstream and downstream state variables [33]. For these components no spatial effects are relevant in the study and flow phenomena are modeled as zero dimensional steady-state resistances by means of purely algebraic equations of the following form:

$$\dot{m} = f_1\left(p_{in}, p_{out}, T_{in}, \xi\right) \tag{3.140}$$

$$T_{out} = f_1\left(p_{in}, p_{out}, T_{in}, \xi\right) \tag{3.141}$$

which give mass flow rate and exit temperature as function of upstream and downstream pressure, inlet temperature and opening degree ξ (if referring to a valve with variable flow section) [34].

No state variables are associated to the system and hence the model is of ‘not state determined’ type.

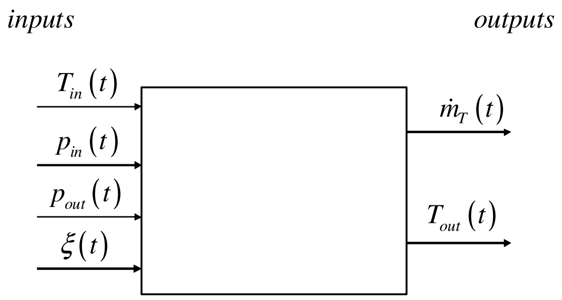

Fig. 3.69. Block Diagram of a valve component.

The relation between the input and output parameter is usually nonlinear and depends strongly on the nature of the fluid and the geometry of the system. In case of compressible fluid the key assumption to build the model equation is to separate the behaviour in two parts:

- no losses occur in the accelerating part (pressure decrease) up to the throat: all the potential energy stored in the flow is converted isentropically into kinetic energy;
- after the narrowest point the flow is fully turbulent and all the kinetic energy is dissipated into thermal energy; therefore, no pressure recovery takes place.

Recurring to the well known thermodynamic relations for isentropic expansion, the following flow equation, analogous to the one adopted for the turbine mass flow rate characteristic, can be written for perfect gases:

$$\dot{m} = \frac{C_d A p_{in}(t)}{\sqrt{RT_{in}(t)}} \psi\left(\frac{p_{in}(t)}{p_{in}(t)}\right) \tag{3.142}$$

where the function ψ is defined according to the pressure ratio existing between valve inlet and outlet section:

$$\psi\left(\frac{p_{in}(t)}{p_{in}(t)}\right) = \begin{cases} \sqrt{\frac{2k}{k-1}\left[\left(\frac{p_{in}(t)}{p_{in}(t)}\right)^{\frac{2}{k}} - \left(\frac{p_{in}(t)}{p_{in}(t)}\right)^{\frac{k+1}{k}}\right]} & \text{if } p_{out} \geq p_{cr} \\ \sqrt{\left(\frac{2}{k+1}\right)^{\frac{k+1}{k-1}}} & \text{if } p_{out} < p_{cr} \end{cases} \tag{3.143}$$

The critical back pressure p_{cr} where the flow reaches sonic conditions, is given by:

$$p_{cr} = p_{in}\left(\frac{2}{k-1}\right)^{\frac{k}{k-1}} \tag{3.144}$$

The gas exit temperature can be calculated assuming an equivalent polytrophic expansion:

$$T_{out}(t) = T_{in}(t)\left(\frac{p_{in}(t)}{p_{out}(t)}\right)^{\frac{m-1}{m}} \tag{3.145}$$

The flow area A in Eq. (3.142) is a geometric function of the valve opening degree ξ while the valve discharge coefficient C_d , that expresses turbulent and friction losses, is usually determined experimentally since the complex nature of the flow makes it extremely complicate to define a general theoretical expression. The polytrophic exponent m of Eq. (3.145) is also determined experimentally through available data for the valve under study.

The model block is presented in Fig. 3.70.

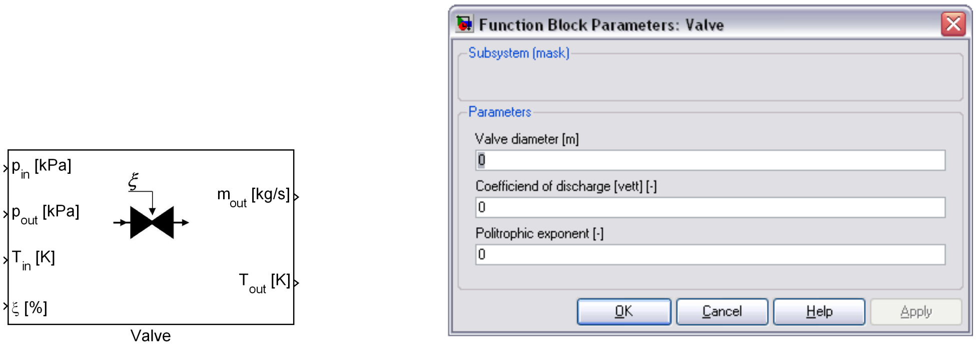

Valve diameter [m]: 0

Coefficiend of discharge [vett] [-]: 0

Politrophic exponent [-]: 0

(a) (b)

Fig. 3.70. Simulink® model of the valve (a) and block dialog mask (b).

3.3.7 The static heat exchanger

Besides the dynamic heat exchangers presented in Paragraphs 3.2.1-3.2.2-3.2.3 that belong to the 'state determined' library, a simpler 'static' model for an heat exchanger was developed to be used within energy systems where the thermal dynamics of the heat exchange process is expected to play a minor role in the overall system response. The component is the included in the 'not state determined' sub-library since it performs a static calculation of output temperatures of the fluids through purely algebraic equations.

The overall component inputs/outputs (Fig. 3.71) are nearly the same as those introduced for the more complex heat exchangers previously presented and this allows an easy switch of the 'static' heat exchanger to the 'dynamic' one when required.

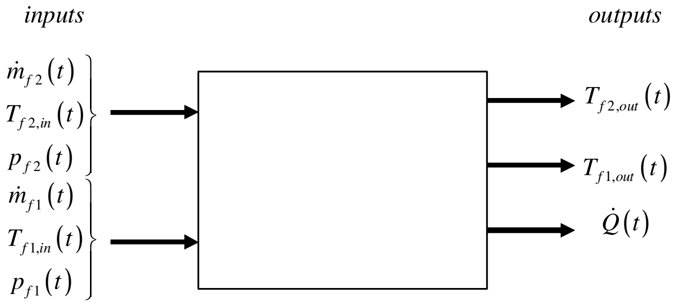

Fig. 3.71. Block Diagram of heat exchanger with no states.

The exchanger with no state is considered to be a cross flow Compact Heat Exchanger (CHE), of plate-and-fins type for gas-gas heat exchange processes, where *f1* and *f2* indicates the two fluids experiencing heat exchange.

Typical correlations for heat exchangers have been considered for building up the model [30,51], and the behaviour of the heat exchanger is represented through the *ε–NTU* approach [51], where *ε* is the exchanger Effectiveness.

The exchanger effectiveness ε can be defined as follows:

$$\varepsilon = \frac{Q}{Q_{\max}} = \frac{C_{f1}\left(T_{f1,in} - T_{f1,out}\right)}{C_{\min}\left(T_{f1,in} - T_{f2,in}\right)} = \frac{C_{f2}\left(T_{f2,out} - T_{f2,in}\right)}{C_{\min}\left(T_{f1,in} - T_{f2,in}\right)} \tag{3.146}$$

where:

$$C_{\min} = \min\left\{C_{f2}, C_{f1}\right\} = \min\left\{\dot{m}_{f2}c_{p,f2}, \dot{m}_{f1}c_{p,f1}\right\} \tag{3.147}$$

By defining an initial value of the *ε* coefficient, the model is able to calculate a first approximation value of the gases output temperature, $T_{f1,out}$ and $T_{f2,out}$. These values are then used to calculate the average temperature of the fluids within the exchanger. The thermodynamic properties of the fluid can then be calculated as functions of these average temperatures.

In the case of the heat exchanger the cinematic viscosity and Prandtl number have to be evaluated. The Reynolds number is estimated to calculate the friction factor *f* and the Colburne factor $j_H(\mathrm{Re}) = St \cdot \mathrm{Pr}^{2/3}$ (through look-up tables that have been built up starting from experimental data available in the open literature). The Colburne factor, along with the Prandtl number, allows to determine the convection coefficient:

$$h = St \cdot c_p \cdot G \tag{3.148}$$

The efficiency of the finned surface $\eta_0 = 1 - A_f/A(1 - \eta_f)$ (where η_f is the efficiency of a single fin) is calculated in order to determine the overall heat transfer coefficient *U*.

Calculation of the overall heat coefficient, based on the air surface area, leads to the following equation:

$$\frac{1}{U_{f2}} = \frac{1}{\eta_{0,f2} \cdot \alpha_{f2}} + \frac{1}{\left(\dfrac{A_{f1}}{A_{f2}}\right) \cdot \eta_{0,f1} \cdot \alpha_{f1}} \tag{3.149}$$

The Number of Thermal Units (*NTU*) can now be calculated as:

$$NTU = \frac{A_{f2}U_{f2}}{C_{\min}} \tag{3.150}$$

Empirical correlations for the evaluation of heat exchanger effectiveness are available in the open literature for a variety of heat exchangers, allowing to calculate the *ε* factor as function of *NTU*. For Cross flow single pass heat exchangers with both fluids unmixed the following equation can be used [52]:

$$\varepsilon = 1 - \exp\left\{ \left(\frac{1}{C_r} \right) \cdot NTU^{0.22} \cdot \left[\exp\left(-C_r \cdot NTU^{0.78} \right) - 1 \right] \right\} \tag{3.151}$$

where C_r is the heat capacity ratio of the fluids, defined as $C_r = C_{min}/C_{max}$.

This value of ε can be used to calculate the new values of $T_{f1,out}$ and $T_{f2,out}$. Calculations of the thermodynamic properties should then be done again and the whole procedure repeated. Of course, if a good approximation for the value of the ε factor is defined in the first step, a single iteration can provide sufficiently accurate results.

The overall heat flow exchanged can then be calculated as:

$$\dot{Q} = \dot{m} c_{p,f} (T_{f,out} - T_{f,in}) \tag{3.152}$$

Fig. 3.72 proposes the Simulink® model of the heat exchanger.

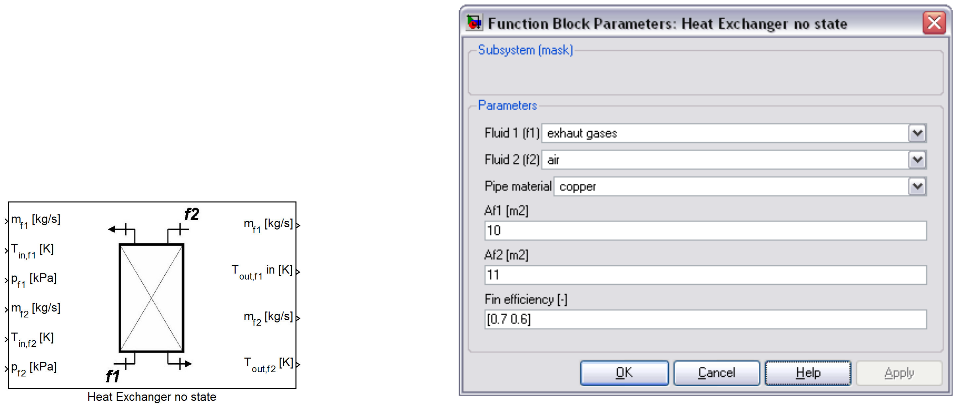

Fluid 1 (f1) exhaut gases
Fluid 2 (f2) air
Pipe material copper
Af1 [m2] 10
Af2 [m2] 11
Fin efficiency [-] [0.7 0.6]

(a) (b)

Fig. 3.72. Simulink® model of the heat exchanger with no state (a) and block dialog mask (b).

3.4 Summary

A comprehensive library of models for fluid components has been here presented: it features a series of model some of which have high general applicability (like the valve or the receiver models) while other have been designed for certain specific applications (like for example the ICE in-cylinder combustion processes). Aim of the work was to provide a set of reliable model that could be easily used and linked together to generate complete and functional overall models of complex power units. The realized model components can be quickly and easily picked up from the specific libraries created within the Simulink® browser and interconnected with other standard Simulink® block, if necessary to enhance the model functionality.

Due to the lack of test facilities and available data on the performances of the different components analyzed, not all the presented models have been effectively validated: a comprehensive validation of the models, both in steady state and off design conditions, is part of the future work planned to enhance the proposed library.

To be noted that the Simulink® library is dynamic. This means that any modifications or improvement provided to the models described herein (for example because of a specific calibration of some empirical coefficient for the availability of experimental data) would automatically be passed to any existing Simulink® model where the improved block is employed, greatly simplifying the process of trial of the modifications introduced since prompt feedback on its functionality is provided.

Refernces

1 Lemmon E., Huber M., McLinden M., NIST Reference Fluid Thermodynamic and Transport Properties REFPROP 8, NIST Standard Reference Database 23, 2007.

2 Vaja I., *Modellazione e simulazione finalizzate al controllo di una centrale solare termoelettrica a collettori parabolici lineari: il progetto "Archimede"*. Master Thesis, Industrial Engineering Department, University of Parma, Italy, 2007 (in Italian)., sponsored by ENEA.

3 Gambarotta A., Vaja I., *Dynamic model of a thermal solar collector*, Paper 364, EUROSIM 2007 Int. Conference, Ljubljana – Slovenia, 9-13 Settembre 2007.

4 Schnieders J., Comparison of the energy yield prediction of stationary and dynamic solar collector models and the model's accuracy in the description of a vacuum tube collector, Solar Energy, 1997; 61:179-190.

5 Ouzzane M., Galanis N., *Numerical analysis of mixed convection in inclined tubes with external longitudinal fins*, Solar Energy, 2001; 71:199-211.

6 Hilmer F., Vajen K., Ratka A., Ackermann H., Fuhs W., Melsheimer O., *Numerical solution and validation of a dynamic model of solar collectors working with varying fluid flow rate*, Solar Energy, 1999; 65:305-321.

7 Kamminga W., *The approximate temperatures within a flat-plate solar collector under transient conditions*, International Journal of Heat and Mass Transfer, 1985; 28:433-440.

8 de Ron A. J., *Dynamic Modelling and verification of a flat plate solar collector*, Solar Energy, 1980; 24:117-128.

9 Tripanagnostopoulos Y., Soulitis M., Nousia T., *Solar Collectors with colored absorbers*, Solar Energy, 2000; 68:343-356.

10 Tiwari G.N., *Solar Energy – Fundamentals, Design, Modelling and Applications*. Alpha Science International, 2002.

11 Wei D., Lu X., Lu Z., Gu J., *Performance analysis and optimization of organic Rankine cycle (ORC) for waste heat recovery*, Energy Conversion and Management 2007; 48:1113-1119

12 Madhawa Hettiarachchi H.D., Golubovic M., Worek W.M., Ikegami Y., *Optimum design criteria for an Organic Rankine cycle using low-temperature geothermal heat sources*, Energy 2007; 32:1698–1706.

13 Wei D., Lu X., Lu Z., Gu J., *Experimental evaluation of an autonomous low-temperature solar Rankine cycle system for reverse osmosis desalination*, Desalination 2007; 203:366–374.

14 Larjola J., *Electricity from industrial waste heat using high-speed organic Rankine cycle (ORC)*, Int. J. of Production Economics, 1995;41:227-235.

15 Invernizzi C., Iora P., Silva P., *Bottoming micro-Rankine cycles for micro-gas turbines*, Applied Thermal Energy 2007;27:100-110.

16 Danov S.N., Gupta A. K., *Modeling the Performance Characteristics of Diesel Engine Based Combined-Cycle Power Plants – Part I: Numerical Model*, Journal of En U. Drescher, D. Bruggermann, Fluid selection for the Organic Rankine Cycle (ORC) in biomass power and heat plants, Applied Thermal Energy 27 (2007) pp. 223-228gineering for Gas Turbines and Power, 2004;126:28-34.

17 Micheli D., Reini M., *On bottoming a micro turbine with a micro ORC section: Part b) micro-combine cycle plant performance evaluation*. In Proceedings of ECOS 2007, Padua, Italy, June 25-28, 2007, p.1035-1041.

18 Drescher U., Bruggermann D., *Fluid selection for the Organic Rankine Cycle (ORC) in biomass power and heat plants*, Applied Thermal Energy 2007; 27:223-228.

19 Wei D., Lu X., Lu Z., Gu J., *Dynamic modelling and simulation of an organic Rankine cycle (ORC) for waste heat recovery*, Applied Thermal Engineering, Article in press, 2007.

20 Colonna P., van Putten H., *Dynamic modeling of steam power cycles. Part I - Modeling paradigm and validation*, Applied Thermal Engineering 2007; 27:467-480.

21 Colonna P., van Putten H., *Dynamic modeling of steam power cycles. Part II – Simulation of a small simple Rankine cycle system*, Applied Thermal Engineering 2007; 27:2566-2582.

22 Kane M., Favrat D., Gay B., Andrei O., *Scroll Expander Organic Rankine Cycle (ORC) Efficiency Boost of Biogas Engines*, Proc. of ECOS 2007, A. Mirandola et al., eds., Padua, Italy, vol.2, pp.1017-1024, 2007.

23 Yamamoto T., Furuhata T., Arai N., Mori K., Design and Testing of the Organic Rankine Cycle, Energy 2001; 26:239-251.

24 Bestrin R., Vermeulen A. G. *Mathematical modeling and analysis of vapour compression system*, International Report, University of Technology, Eindhoven Nedherland, Aug. 2003.

25 Prabhankar P.R., *Two dimensional configuration analysis of a flat plate solar collector*, Ph. D. thesis in Mechanical Engineering, University of Oklahoma, USA, 1975.

26 Traverso A., *TRANSEO: A New Simulation Tool for Transient Analysis of Innovative Energy Systems*, Ph.D. Thesis, TPG-DiMSET, University of Genova, Italy, 2004.

27 García-Vallardes O., Pérez-Segarra C. D., Rigola J., Numerical simulation of double-pipe condensers and evaporators, International Journal of Refrigeration 2004; 27:656-670.

28 X. Jia, Tso C.P., Chia P.K., Jolly P., *A distributed model for prediction of the transient response o fan evaporator*, International Journal of Refrigeration, 1995; 18:336-342.

29 Comini G., Cortella G., *Fondamenti di trasmissione del calore*, SGE. 2005 (in Italian).

30 Incroprera F.P., De Witt D.P., *Fundamentals of Heat and Mass Transfer*, John Wiley & Sons. 2001.

31 Acton O., Caputo C., *Collezione Macchine a Fluido, Vol. I: Introduzione allo studio delle macchine*, UTET 1979.

32 Takamatsu H., Momoki S., Fujii T., a correlation for forced convective boiling heat transfer of pure refrigerants in a horizontal smooth tube. Int. J. Heat and Mass Transfer 1993;36(13):3351-60.

33 Canova M., *Fluid Systems Dynamics Modeling for Control: Internal Combustion Engines Case Studies*, Ph. D Thesis, Industrial Engineering Department, University of Parma, Italy 2006.

34 Canova M., Fiorani P., Gambarotta A., Tonetti M. *A real-time model of a small turbocharged Multijet Diesel engine: application and validation*, 7th SAENA Int.Conf.on Engines for Automobiles, SAE paper n.2005-24-65, Capri (NA), Sept. 2005.

35 Canova M., Gambarotta A., *Automotive Engine Modeling for Real-Time control using an object-oriented simulation library*, Proceedings of the 4th International Conference on Control and Diagnostics in Automotive Applications, paper 03A2035, Sestri Levante, Giu. 2003.

36 Cennerilli S., Fiorini P., Sciubba E., *Application of the Camel process simulator to the dynamic simulation of gas turbines*, ECOS 2006 Proceedings, Vol. 1, pp. 355-363

37 Van Tichelen P., Weyen D., *Optimised Use of an Internal-Combustion Engine with a Variable-Speed Synchronous Generator and Rectifier*, IEEE International Conference on Power Electronic Drives and Energy Systems for Industrial Growth, 1998 Proceedings, Vol. 2, pp. 659-664.

38 Grenier, D., Dessaint L.-A., Akhrif O., Bonnassieux Y., and LePioufle B., *Experimental Nonlinear Torque Control of a Permanent Magnet Synchronous Motor Using Saliency*, IEEE Transactions on Industrial Electronics, Vol. 44, No. 5, October 1997, pp. 680-687

39 Guzzella L., Onder C. H., *Introduction to Modeling and Control of Internal Combustion Engine Systems*, Springer Verlag, Berlin, 2004.

40 Amman M., Fekete N., Amstutz A., Guzzella L., *Control-Oriented Modeling of a Turbocharged Common-Rail Diesel Engines*, Proceedings of the International Conference CDAuto01, 2001.

41 Taburri M., *La simulazione dei processi di combustione nei sistemi energetici: realizzazione ed applicazioni di un modello in Simulink basato sugli equilibri chimici*. Master Thesis, Industrial Engineering Department, University of Parma, Italy, 2007 (in Italian).

42 Gordon S., McBride B.J., *Computer program for calculation of complex chemical equilibrium compositions, rocket performance, incident and reflected shocks and Chapman-Jouget detonations*, Nasa, 1976. NASA SP-273, 1976.

43 Turns, S.R. *An introduction to combustion concepts and applications*, McGraw-Hill, 2000.

44 McNaught A.D., Wilkinson A., *Compendium of Chemical Terminology*, online version. IUPAC, 1997. see: http://old.iupac.org/publications/books/author/mcnaught.html.

45 Kee R.J.,. Rupley F.M, Miller J.A., *The Chemkin thermodynamic database*, Sandia Report, 1991. SAND87-8215B.

46 Nocedal J., Wright S.J., *Numerical Optimization*. New York, Springer, 1999.

47 Marquardt D.W., *An algorithm for least-squares estimation of non-linear parameters*. J. Soc. Indust. Appl. Math., Vol. 11, 2,1963.

48 Olikara C., Borman A.L., *A computer program for calculating properties of equilibrium combustion products with some application to IC engines*, SAE paper 750468,1975.

49 Sanli A., Ozsezen A.N., Kilicaslan I., Canakci M., *The influence of engine speed and load on the heat transfer between gases and in-cylinder walls at fired and motored conditions of an*

IDI diesel engine, Applied Thermal Engineering 28, pp.1395–1404, 2008.

50 Annand W.J.D, Ma T.H., *Instantaneous heat transfer rates to the cylinder head surface of a small compression-ignition engine*, Proceedings of the IMechE, Part D: Journal of Automobile Engineering 185, pp.976–987 1971.

51 Kays W.M., London A.L., *Compact heat exchangers*, 3rd ed., McGraw-Hill, New York, 1984.

52 Hung W.W., *Dynamic simulation of gas-turbine generating unit*, IEEE Proceedings 1991,138(4).

CHAPTER FOUR

APPLICATION OF THE LIBRARIES OF MODELS

In this Chapter an insight is provided to the way the different model components, belonging to the 'State determined and 'Not state determined' libraries presented in Chapter 3, can be properly coupled together in order to create complete models of energy systems.

The blocks described are therefore picked up from the libraries created and dropped in workspaces where they are linked according to the physical causality that exists between the real components.

Some examples are provided and the focus is here on common and well known energy systems, i.e. plants or power units that are widely known and studied, to demonstrate how the developed component models can apply for the simulation of whole systems.

A brief description is first provided to a simple complete model of a cogenerative Micro Gas Turbine unit (Par. 4.1). More emphasis is placed upon the description of the Organic Rankine Cycle power unit and the cogenerative Internal Combustion Engine, presented in Par. 4.2 and Par. 4.3 respectively, since the analysis of these power system will be further discussed in Chapter 5 where some possible integration will be analyzed.

Each one of the described power units models (the MGT, ORC and ICE) will be incorporated in independent Simulink® blocks that will eventually be used to create the 'Complete Power Systems' library that comes along with the two already presented libraries, constituting the third sub-library of the main 'Energy Systems' library, visible in the Simulink® root.

Nomenclature

m	Mass [kg]
$\dot{m}$	Mass flow rate [kg/s]
n	Rotational speed [r/min]
p	Pressure [Pa]
s	Specific entropy [kJ/kg K]
t	Time [s]
H	Head [m]
R	Specific gas constant [kJ/kg K]
$\dot{Q}$	Heat flux [MW]
T	Temperature [K]
V	Volume [m^3]
$\dot{V}$	Volume flow rate [m^3/s]

Greek symbols

β	Pressure ratio [-]
λ_v	Volumetric efficiency [-]
ρ	Density [kg/ m^3]

Abbreviations and subscripts

a	Air
amb	Ambient
co	Condenser
cyl	Cylinder
e	Electrical
eng	Engine
ev	Evaporator
exh	Exhaust
f	Fuel
g	Gas
in	Inlet
mep	Mean effective pressure
mip	Mean indicated pressure
out	Outlet
t	Thermal
tf	Transfer fluid
w	Water
BDC	Bottom dead centre
C	Compressor
CC	Combustion chamber
CHE	Compact heat exchanger
CHP	Combined heat and power
HRB	Heat recovery Boiler
ICE	Internal combustion engine
IM	Intake manifold
MGT	Micro Gas Turbine
ORC	Organic Rankine cycle
R	Regenerator
T	Turbine
TDC	Top dead centre

4.1 Complete model of a regenerated cogenerative Micro Gas Turbine (MGT) system

In this section the libraries of components described in the previous chapter are utilized to create a dynamic model capable of fast simulation of a CHP system based on a Micro-Gas Turbine (MGT) with regeneration. The model is intended not only for stand alone operation, but is also suitable to study the integration of the MGT system with other components in a complex energy system network. Particular attention is paid to define off design operation of the system, since a Micro CHP system barely operates at design conditions, but often is called to satisfy time-varying loads [1].

Dynamic models of Gas Turbine power plants are often used to design control systems [2] or for off design performance analyses [3]. Other applications may concern the prediction of plant transient to limit test costs, for fault diagnosis, or to generate time series of transient condition data which are hardly available for industrial gas turbines that work mainly in steady state conditions [4]. Accurate dynamic models of micro turbines are also appreciated to study transient and long term stability of distributed generation systems [5] and to assess the optimal configuration to minimize fuel consumption, increase energy efficiency and reduce operational costs [6]. Gas turbine units are able to cope quickly to sudden changes in power demand, and a model which allows to predict the behaviour of MTG units within an energy network including other generation sources seems a very important tool to assess the performances of the system. A comprehensive work on the dynamic modelling of Micro Gas Turbine systems is the Ph.D. Thesis of A. Traverso [7] where different and advanced plant configurations based on Micro Gas Turbines is presented.

When a CHP system is inserted in an existing energy grid, several options can be considered to fulfil energy requirements. The electric energy can be produced partially by the CHP unit and partially purchased from the external power grid. The heat can be generated by the waste heat of the CHP plant (even with afterburning). The issue becomes more complex if a CCHP system is considered: the cooling load can be satisfied by an absorption chiller driven either by the waste heat of a gas turbine or by afterburning [8].

The example presented here refers to an early work [9] and was developed when advanced dynamic models of the heat exchangers were still not fully developed hence the simpler heat exchangers with no state presented in the previous Chapter have been introduced to represent the heat exchange processes that occur in the regenerator and HRB, well aware of the approximation introduced. Examples of the full dynamics of the heat exchange processes are however provided in the following Paragraphs and Chapter.

4.1.1 The micro gas turbine system

Micro Gas Turbines for cogeneration purposes are often aeroderivative to reduce costs. The gas turbine considered in the presented model is a single-shaft, natural gas fired, Turboméca Artoise IIC6 derived from the helicopter SE 313B Alouette II produced by Aerospatiale. The compressor is single staged centrifugal while the turbine is axial with two stages.

The MGT is coupled with a high frequency electric generator: compressor, turbine and generator are mechanically coupled on a single-shaft without gearbox. Exhaust gases are sent to a regenerator and a boiler for waste heat recovery. A scheme of the CHP system is shown in Fig. 4.1.

The regenerator is a surface heat exchanger, since involved gases (compressed air and exhaust gases) are not mixed up and their compositions and pressures are different. The exchanger is a cross flow Compact Heat Exchanger (CHE), of plate-and-fins type with strip fins on the air side and plain fins on the exhaust gas side.

The boiler, used for district heating purposes, is –as the regenerator- a CHE in cross flow. In this case the heat exchange is between a hot gas and a liquid (water). Since the convection coefficient on the water side is high, finned surfaces are not required and the heat exchanger is then of fin-tube type with continuous plate fins on the gas side and elliptical pipes.

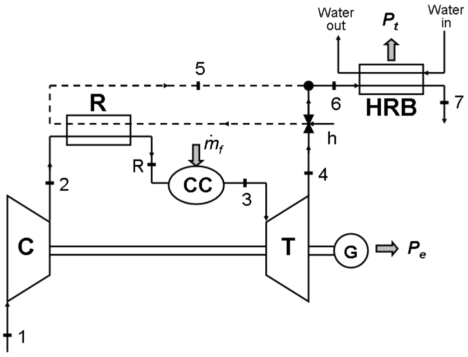

Fig. 4.1. Scheme of the micro gas turbine with regeneration and HRB.

Air at atmospheric pressure and temperature (p_1 and T_1) enters the plant at the compressor inlet (1), and is compressed (2) and preheated before enter the combustion chamber through a regenerator (R) which allows to recover the enthalpy of the exhaust gases at the turbine exit (4). Fuel is then mixed with the air in the combustion chamber (CC), bringing the hot gas mixture to state (3). Then exhaust gases are expanded through the turbine to produce mechanical power. Apart from the fraction used to drive compressor, turbine power output is converted into electric power through the generator coupled to the turbine shaft.

Hot exhaust gases can be used both to preheat the compressed air through the regenerator and to feed the Heat Recovery Boiler (HRB) to heat water for district heating purposes. A bypass valve at the turbine exit allows the plant control system to direct defined fractions of the exhaust gases (at state 4) to both heat exchangers, according to the operating conditions of the plant. After passing through the regenerator (5) exhaust gases -with lower enthalpy- are sent to the HRB.

The plant operating conditions therefore can be changed not only by changing the fuel mass flow rate, but also by acting on the bypass valve, making possible to vary the ratio between mechanical and thermal power output of the plant. This allows the system to cover a wide operating range of power-to-heat values.

The regenerated Joule cycle is plotted in Fig. 4.2 for the considered system operating at nominal operating conditions with full regeneration.

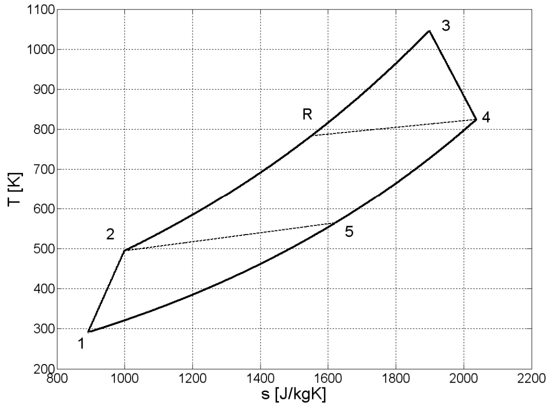

Fig.2

Fig. 4.2. Regenerated Joule cycle for the MGT system.

4.1.2 The MGT model

The Simulink® interface of the developed model is shown in Fig. 4.3. Main components (such as the compressor, the combustion chamber, the turbine, the regenerator and the HRB) can be easily recognized. Overall system inputs are highlighted by the red source blocks (S).

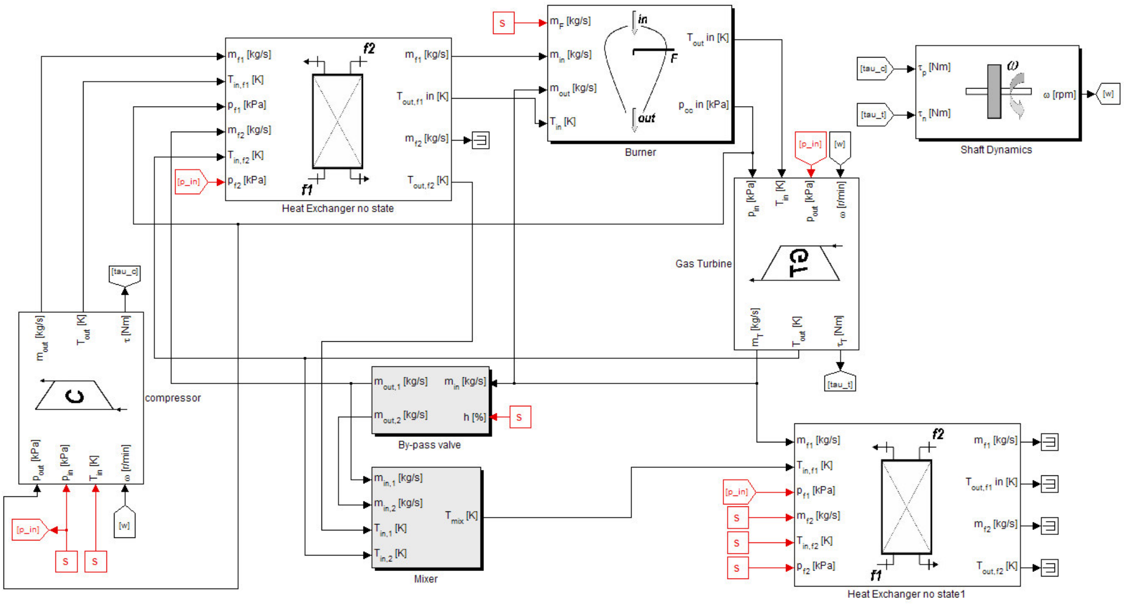

Fig. 4.3. Simulink® model of the Micro Gas Turbine unit.

The most important independent variables of the whole system are the fuel mass flow rate and the opening degree of the by-pass valve, and these inputs can be externally actuated for system control. Other external inputs are the air temperature and pressure and these are usually considered to be constant during a simulation, as well as the conditions of the fluid entering the HRB and heated from the MGT turbine exhaust gases. Many outputs can be considered when operating on a Micro Gas turbine system but when it comes to energy systems analysis usually the main energy fluxes and efficiencies are of interest. For these reason electrical power and electrical efficiency, along with thermal power and thermal efficiency, are highlighted as overall system outputs in Fig. 4.4 where the Simulink® block of the whole MGT plant of Fig. 4.3 is presented.

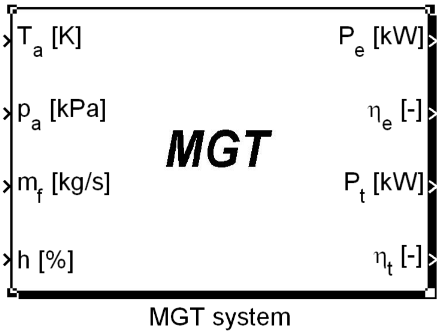

Fig. 4.4. Simulink® block model of the Micro Gas Turbine unit. Upper level.

In order to verify the model capabilities several simulations were developed in different operating conditions.

In the following graphs the main parameters of the system are represented during a transient operating condition defined by a step change in the fuel mass flow rate, which increases from 0.028 to 0.035 kg/s at

t=5 s. Simulations are proposed for three different values of the recirculation valve opening degree h, varying from 100% (i.e., turbine exhaust mass flow rate is entirely sent to the Regenerator) to 60%.

In Fig. 4.5 the main system outputs mentioned herein (overall CHP electrical and thermal efficiencies of the system, along with the net output electrical and thermal power) are represented. The time response to the step change in the fuel mass flow rate is very fast and the MGT unit can be considered as a quick unit in responding to transients, the main inertias lying in the energy and mass storage of the combustion chamber and rotational inertia of compressor, turbine and generator shaft.

To be noted that the adoption of the heat exchangers with no state to model the regenerator and the HRB brought to neglect the thermal inertia of the fluids and materials of components thus the time response of the thermal power available is as fast as the mechanical response of the system.

It can also be observed that while, as expected, higher electrical power is achieved for high recirculation ratios through the regenerator, the opposite happens for the thermal power: low recirculation ratios enhance the enthalpy of the flue gases to the HRB. This can be noted also from Fig. 4.6, where relevant temperatures are shown with reference to the cycle of Fig. 4.1.

Fig. 4.6 also shows that, as consequence of the increase in fuel mass flow rate, temperature at the regenerator outlet may decrease (T_R). This depends on both the increase of the compressor mass flow rate (Fig. 4.7) and the decrease of the Turbine exit temperature (T_4). The highest reduction of the temperature T_4 is obtained for h=60% and depends on the increase of the air/fuel ratio, which brings to a reduction in the CC outlet temperature T_3, and an increase in the turbine adiabatic efficiency.

In Fig. 4.7 compressor and turbine mass flow rates are plotted along with the adiabatic compression and expansion efficiencies. It can be observed that the time required to reach a steady-state value for the mass flow rate is higher for the turbine than for the compressor and this is a consequence of the mass storage capability of the combustion chamber that is interposed between these components.

Even if no experimental data were available for a comparison, theoretical results show a qualitative agreement with the expected behaviour of the system. It is apparent that a proper experimental validation of the calculation procedure has to be developed in the next future: however, these first simulations allowed to prove the flexibility of the proposed MTG model.

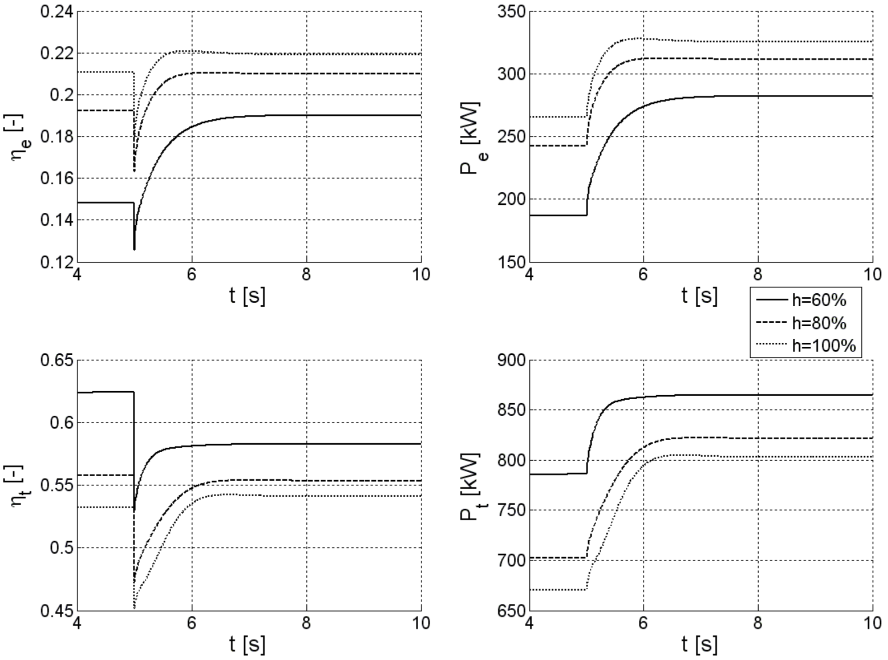

Fig. 4.5. Mechanical and thermal overall efficiencies and net output power evaluated from the model in transient operating conditions.

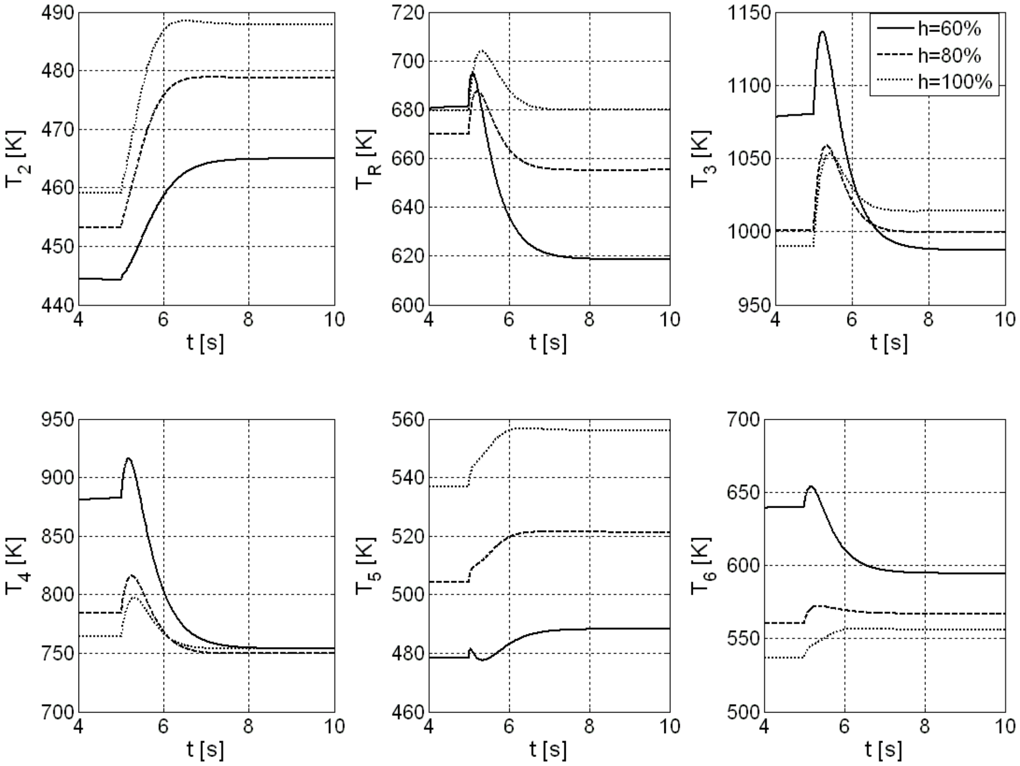

Fig. 4.6. Gas temperatures evaluated by the model for the thermodynamic cycle in transient operating conditions.

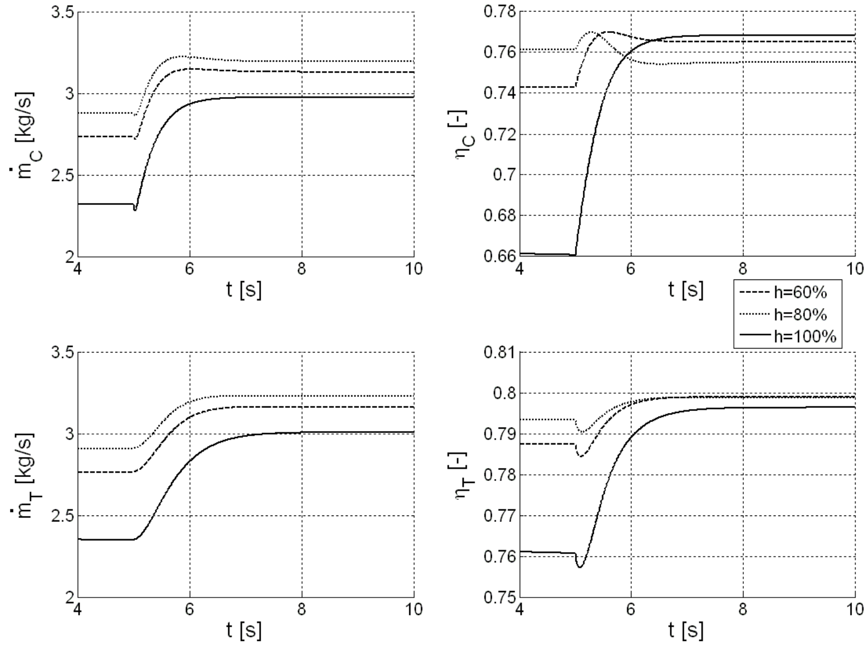

Fig. 4.7. Turbine and compressor mass flow rates and adiabatic efficiencies evaluated by the model in transient operating conditions.

4.2 Dynamic model of an Organic Rankine Cycle (ORC)

In this Paragraph a detailed dynamic model of an Organic Rankine Cycle (ORC) power unit is described.

Organic Rankine Cycles are vapour power cycles that can employ different working fluids in order to exploit low grade thermal heat sources to generate useful work. Many applications and studies exist that demonstrate the feasibility of these systems and the possibility for them to be applied to different industrial processes [10-13]. An interesting application of ORCs is their coupling with other prime movers utilizing their waste heat, thus realizing a combined power unit, with the effect of enhancing the overall system efficiency [14-16]. Since the ORC system generates additional power without requiring extra fuel, the specific pollutant emissions of the combined plant are reduced.

Organic fluids are to be preferred to water when the power required from the power cycle is limited and the heat source temperature is low. Water-steam cycles would not give satisfactory performances due to the low volume flows, that would increase leakage losses in the axial steam turbine lowering the overall cycle efficiency. Moreover organic fluids often have lower heat of vaporization compared to water and they can follow better the heat source to be cooled, lowering the temperature difference between exchanging fluids, thus reducing the irreversibility at the evaporator. This means that higher electrical power can be generated from an heat source [13]. Furthermore turbines for organic cycles can provide high efficiencies also at part loads [18] and are usually less complex (1 or 2 stages, for an axial turbine) because the enthalpy change of the fluid is lower [13]. ORC systems exhibit great flexibility, high safety and low maintenance requirements especially in recovering low-medium grade waste heat from industrial processes or power plants [10].

Evaporators for Organic Rankine cycles are usually simple components designed as heat exchangers often with direct use of hot gases released by the thermal source (without an intermediate fluids such as diathermic oils) and with one level of evaporating pressure [14,16]. This design will be adopted in the model here presented for the evaporator and condenser.

Organic Rankine Cycles therefore are expected to play a significant role in enhancing the overall efficiency of different thermal systems or processes. An example to this is provided in Chapter 5 where the proper coupling of an ORC with a stationary internal combustion engine is considered in order to recovery in mechanical form part of the energy that is downloaded by the engine through its main hot streams (exhaust gases and refrigerant).

In order to gather a deep understanding of the way ORC operate and to design new energy conversion systems were ORCs can find their place for the recovery of low-medium temperature heat from exhaust heat sources, a proper detailed dynamic model of the Organic Rankine Cycle power plant has been developed and will be illustrated within this section [17].

Few examples of complete dynamic models of ORC system have been found in literature. The most complete is provided in [19] where two alternative approaches for creating a dynamic model for an ORC to be used for the design of control and diagnostics systems are proposed. The model has been developed in Modelica® language and simulated with Dymola®. The paper focus is on the model of the evaporator which, in fact, is the key component to be represented. The two modeling approaches adopted for this component, based on moving boundary and discretization techniques, are compared in terms of accuracy, complexity and simulation speed.

Compared to experimental data, simulations evidenced that while both models have good accuracy, the moving boundary model is faster, therefore more suitable for control design applications. Since the aim of this work is system design, as will be shown in Chapter 5, the discretized approach is here preferred, as it allows a broader understanding and representation of the phenomena occurring within the evaporator for both the transfer fluid and the organic fluid.

Another extensive work in the field of dynamic modelling of Rankine cycles is that described in [21,22]; despite the work does not refer to organic fluids but to ordinary steam Rankine cycles, it provides an interesting approach for the designing of components of steam power plants. The presented software called SimECS, developed at the Delft University of Technology, is a modular, hierarchical and causal paradigm, which means that systems are formed by components which in turn are formed by modules with predefined causal interactions. SimECS therefore is based on elementary modules that in turn can be appropriately combined to obtain main components. For example, the superheater component is composed of:

- fluid flow modules (resistive and storage) to model the hot and cold fluid streams and to take into account of energy and mass accumulation within the control volumes as well as flow resistance;
- fluid resistive thermal modules to model the heat transfer between the fluid and the metal surfaces
- a solid storage thermal module to model the thermal energy accumulation in the metallic parts.

All the main phenomena occurring within the heat exchangers are then lumped within single logical blocks that describe the physical phenomena through implementation of proper physical relations and conservation laws in the lumped parameters form. While the approach seems very interesting in terms of modularity, it again does not seem to provide the desired accuracy in describing the process that is sought here.

4.2.1 The system

ORCs are power cycles based on the Rankine vapour cycle typical of steam power plant. In the case of ORCs however a different fluid is employed in place of water that allows some benefits under certain circumstances. Particularly, the fluids employed (typically hydrocarbons or refrigerants) have low boiling points and high specific volume of the vapour at the typical pressures adopted in the evaporation, that make the stream at the expander inlet suitable for a efficient expansion, reducing the leakage losses that would occur if water were used instead. These cycles in fact are usually adopted when the thermal power of the heat source and its temperature are limited; under these circumstances the steam volumetric flow rate would be too low, in case of adopting water as working fluid, and the overall cycle efficiency would be compromised by the extremely low expansion efficiency.

Besides the different fluid that can be adopted in ORCs, the overall cycle layout can be considered conceptually similar to that of a steam power cycle.

As displayed in Fig. 4.8, which refers to a simple Organic Rankine cycle with no regeneration, reheating or superheating, the fluid is first heated and evaporated through the evaporator, and then expanded in order to convert its pressure energy into useful mechanical work. A condenser is then necessary in order to desuperheat and condensate the fluid which then passes trough the feeding pump which provides the liquid with the required head.

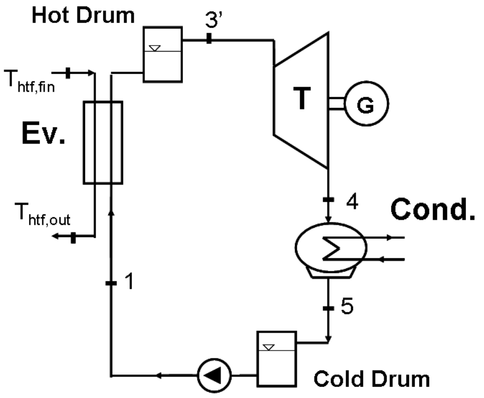

Fig. 4.8. Schematic layout of an Organic Rankine Cycle.

Due to the simple design of the main heat exchangers (evaporator and condenser) which, as seen, especially for the smallest plants, can be designed as simple counterflow tube in tube heat exchangers, two moisture separators (drums) have also been considered. The first separator is at the the evaporator exit and is used when the organic fluid vapour is not totally dry in order to avoid that the liquid droplets that are carried by the vapour stream are dragged into the expander. Analogously, another moisture separator is considered at the condenser outlet and in this case its use is to separate the vapour fraction that might be mixed to the liquid hence avoiding the presence of vapour at the pump suction. These separators are intended as simple components and designed as tanks; the presence of these elements is considered also in some cycle setups as those described in [10,19,20].

The dynamic model of the entire system therefore will be realized by assembling together the models of the different subcomponents that have been identified. Indeed more advanced designs of the cycle could be considered (see also Par. 5.1 and 5.2): particularly thermal regeneration is a common practice when it comes to organic Rankine cycles that utilize fluids of the overhanging type. This condition is not only favourable because it allows to have dry expansions at nearly every operating condition without superheating, but also it makes convenient to regenerate the cycle by sub cooling the vapour at the end of expansion (if the *T-s* diagram is overhanging the fluid is superheated at turbine exit). The regeneration in these cases may be realized without vapour extraction from the turbine, but via a direct regeneration, similarly to what happens in the Brayton-Joule cycles.

Other cycle designs may involve recurring to other heat exchangers, besides the evaporator or the regenerator, in order to recovery heat from other low temperature heat sources and providing a preheating of the organic fluid that allows overall efficiency enhancing, as will be shown in the next Chapter.

4.2.2 Example: the complete Organic Rankine Cycle dynamic model

Different model blocks from the created ‘Energy Systems’ library have been properly linked creating a complete Organic Rankine Cycle plant according to the configuration presented in Fig. 4.8.

The Simulink® model of the plant is presented in Fig. 4.9, where it is possible to recognize the main components introduced as the pump, organic fluid evaporator, hot drum, turbine, condenser and cold drum. It can be observed that the overall external inputs of the complete ORC plant are:

- Heat transfer fluid temperature, pressure and mass flow rate;
- Refrigerant temperature, pressure and mass flow rate.

It can also be appreciated how the evaporator-hot drum and condenser-cold drum constitute the two main places of energy and mass storage of the plant while the two flow control devices (feed pump and turbine) are positioned in between them.

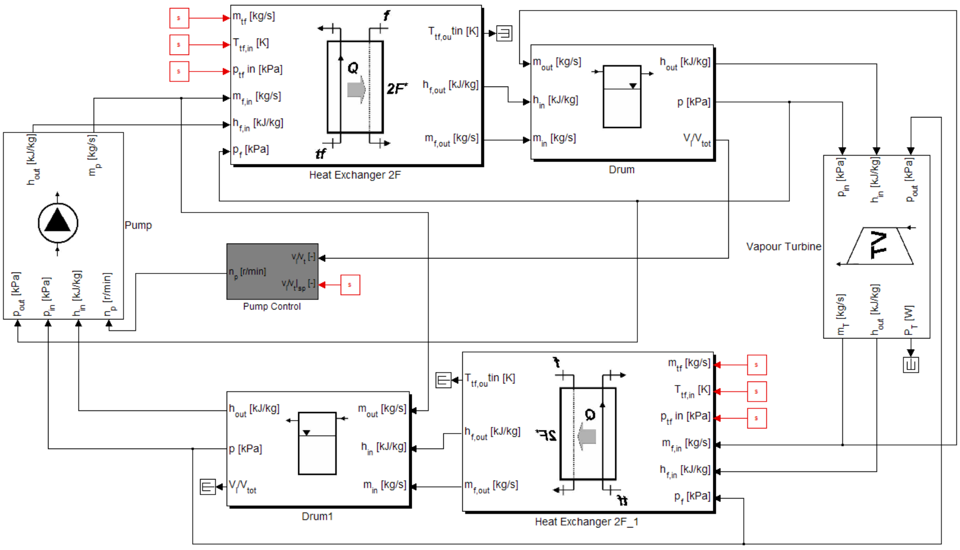

Fig. 4.9. Simulink® model of the ORC power plant.

One component that has not previously described and had to be introduced to guarantee stable operation of the system is the controller of the pump speed. It should be noted in fact that an open loop operation of these plants would not be feasible [22], since if the mass flow rate from the pump were not controlled during transients and off design operation the drums would experience rapid emptying of full filling which is not acceptable in ordinary operations. For this reason a proper controller has be introduced in order to keep constant the level in the hot drum acting on the pump rotational speed.

The implemented PID controller (Fig. 4.10) features also a *Rate Limiter* introduced to simulate the pump actuator delay in responding to a step input in the desired rotational speed.

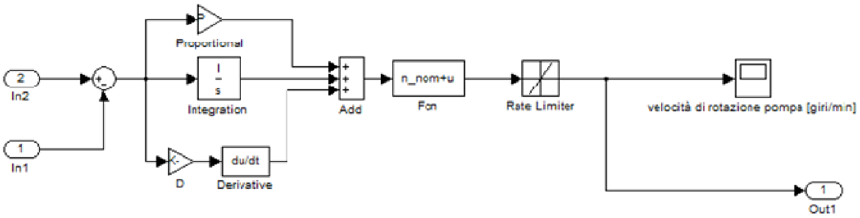

Fig. 4.10. PID controller of the hot drum level.

The whole ORC model built up with the library blocks can be masked within a single block that constitutes the full ORC plant, displayed in Fig. 4.9 The ORC model block will turn useful in the next chapter as it can quickly be coupled to the model of an ICE. In Fig. 4.11 the main system independent inputs and overall outputs are highlighted. Inputs of interest are represented by the main characteristics of the two heat transfer fluids necessary to vaporize and condense the organic fluid, that are the actual driving forces of the plant. Outputs are represented by the mechanical power and efficiency along with the temperatures of the two above mentioned transfer fluids.

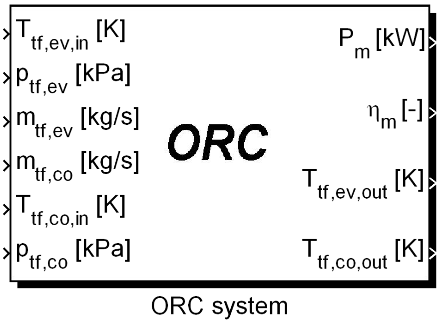

Fig. 4.11. Simulink® interface of the Organic Rankine Cycle unit. Upper level.

A set of simulation results is proposed in the following pages for the complete ORC plant. The organic fluid employed for the cycle is R123 while hot diathermic oil is the heat transfer medium to the evaporator while water is used to cool the condenser. A 20 nodes axial discretization is assumed for the heat exchangers as consequence to the convergence analysis conducted in Chapter 3 for the evaporator. The example there reported in fact refers to just the geometry that will be here adopted.

Simulation have been conducted imposing a step change in one of the main overall external inputs, the heat transfer fluid mass flow rate to the evaporator (Fig. 4.12) starting from a steady state operating condition, while all the other external inputs remained constant.

The sudden increase in the heat transfer fluid mass flow rate, not being changed its temperature, determines an increase in the energy flow input to the system.

Fig. 4.13 (a) and (b) demonstrates how the pressure existing within hot and cold drum, and hence in the evaporator and condenser, changes due to the increased heat transfer fluid mass flow rate that in fact, determines an increase in the organic fluid temperature leaving the evaporator (Fig. 4.14 (c)).

The volume fraction within the hot drum however remains nearly constant after the transient (Fig. 4.13 (d)) and this is due to the action of the controller on the pump speed (Fig. 4.13 (c)).

Cycle net power delivered and thermodynamic efficiency are presented in Fig. 4.13 (e) and (f), where the net power has been calculated from the turbine power and the pump power and taking into account of electrical efficiencies for generator and motor.

Fig. 4.14 displays the 3D plots where main state variables of the evaporator are plotted with respect to simulation time and distance from exchanger inlet. It can be observed how the organic fluid mass flow rate changes in time as consequence of the controller's action on the main pump.

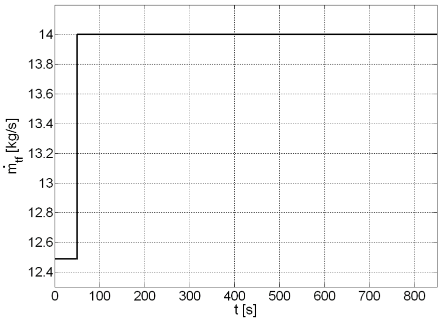

Fig. 4.12. Imposed step change to the transfer fluid mass flow rate.

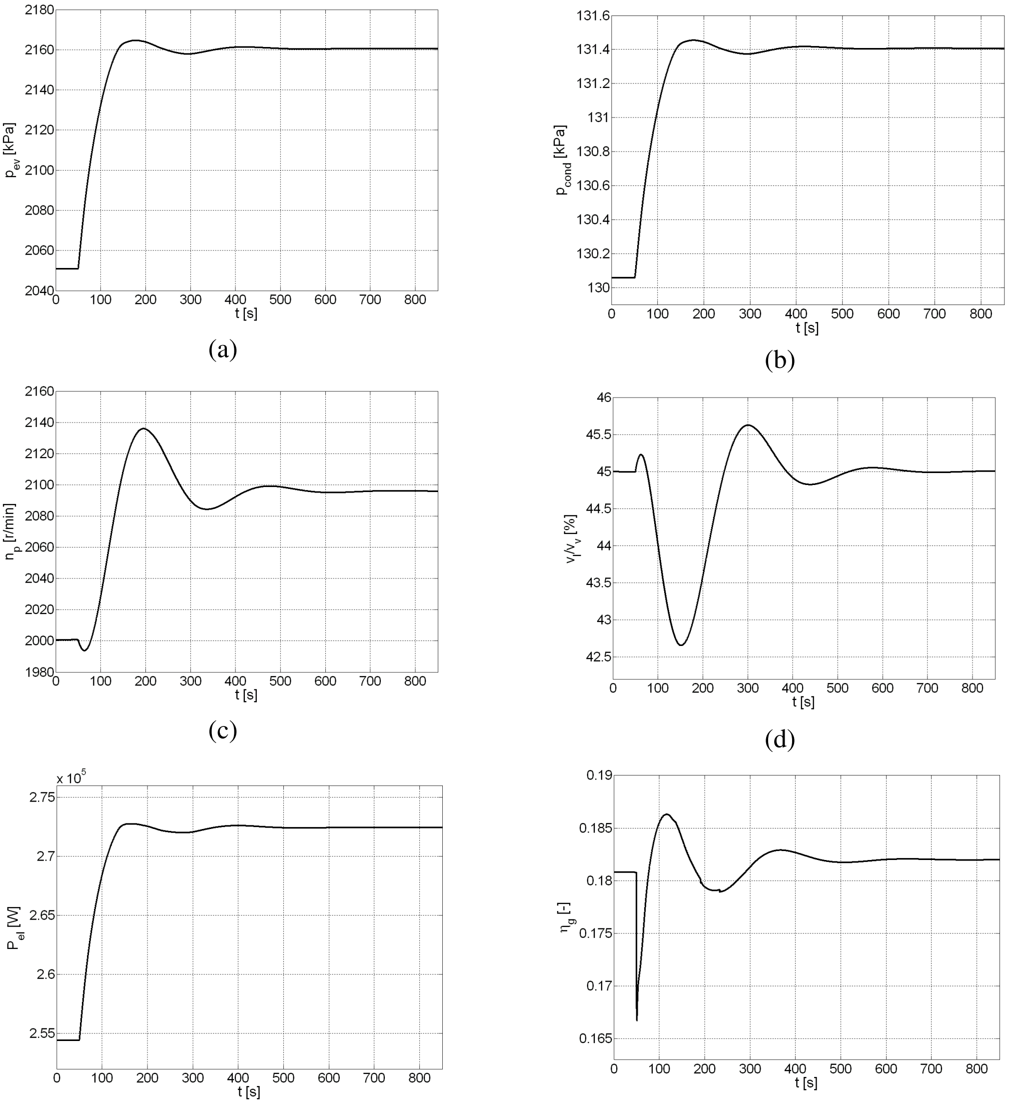

(a) (b)

(c) (d)

(e) (f)

Fig. 4.13. System response: hot drum pressure (a), cold drum pressure (b), pump rotational speed (c), liquid volume fraction in the hot drum (d), generated electrical power (e) and overall cycle efficiency (f).

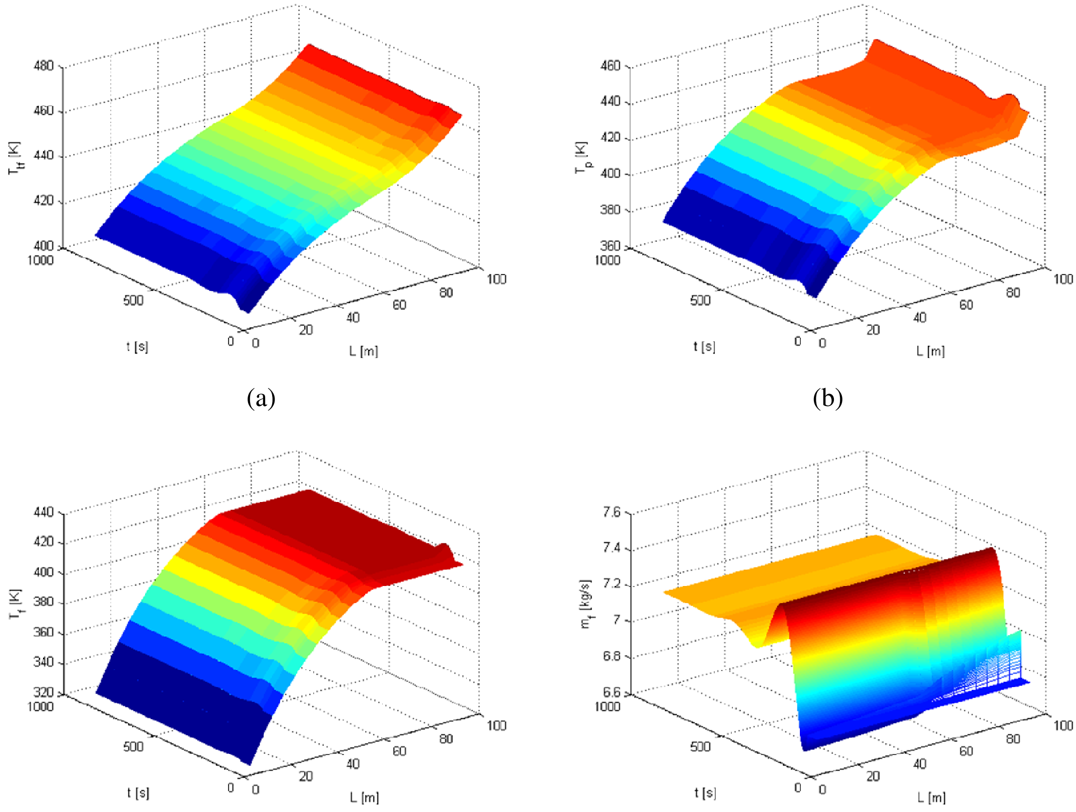

(a) (b)

(c) (d)

Fig. 4.14. Evaporator response: transfer fluid temperature (a), pipe wall temperature (b), organic fluid temperature (c), organic fluid mass flow rate (d) as function of time and distance from evaporator inlet.

4.3 Model of a CHP ICE

In the present Paragraph an example is provided where the developed libraries of components are employed to built up a complete dynamic model of a stationary cogenerative industrial alternative Internal Combustion Engine (ICE). The here presented model in fact, besides proving the applicability of the libraries of components created to the simulation of an ICE, will be also used in Chapter 5 as base component of a complex ICE-ORC combined power unit.

The methodology and approach here applied in modeling the ICE comes from the experience developed within the Department on real-time simulation of fast automotive ICEs for control-oriented applications, witnessed by many publications, as [23-28] to quote the most recent. The literature has also been widely surveyed in these years on the topic, and an overview is here reported.

The work of control oriented ICE modelling typically requires the introduction of proper simplifications in building up the theoretical models that should allow to catch the overall system behaviour avoiding a detailed description of some aspects [29,31,32]. These models usually have to combine physical –and chemical– principles (generally based on conservation laws) with an empirical description of processes and components (usually through quasi-steady representations based on suitable characteristic maps) with reference to averaged values of thermodynamic parameters ("Mean Value Models", MVM, [29]).

First works appeared on control-oriented ICE models were mainly based on quasi-steady techniques or on transfer functions, and therefore relied largely on steady state empirical data. The introduction of filling-and-emptying methods allowed to overcome some drawbacks of the quasi-steady approach, taking account of low frequency transient processes which happen in intake and exhaust manifolds [33]. Since then it was apparent that a proper mixture of filling-and-emptying methods with a quasi-steady approach applied to specific engine components (e.g., valves, restrictions, and even to turbocharger turbine and compressor) would be the most suitable way to simulate engine transients. It is well known, however, that these models are not able to follow high frequency phenomena (related to a cycle-to-cycle basis), and the thermodynamic parameters are represented by corresponding values averaged over several engine cycles.

The simulation of in-cylinder processes introduces several difficulties. If spark ignited combustion may be well described by means of a two-zone approach (at least as regards control-oriented models), Diesel engine combustion is apparently more complicated, since it is highly not homogeneous. In this case the simulation of the spray and of the subsequent diffusive combustion usually requires a multidimensional model, which cannot be used in control-oriented applications: therefore, simplified models were proposed since the beginning. A “real thermodynamic cycle” was introduced by Watsonnd Marzouk [33], based on the definition of a proper fuel burning function (taking account of heat transfer from the cylinder through Woschni's correlation): the overall thermodynamic effects of the combustion process is described by an apparent heat release rate, which in any case have to be defined on the basis of experimental data. Once again, they followed a quasi-steady approach joined with a filling-and-emptying technique for the intake and exhaust system.

For the simulation of intake and exhaust flows quasi-steady, filling-and-emptying or wave-action techniques [29,31], more or less mixed together, are widely proposed.

Wave-action techniques can be classified as multidimensional CFD methods which allow for a detailed description of gas flows through Partial Differential Equations (PDE), since both time and spatial derivatives are considered. This approach leads to distributed parameters *white-box* models with state variables, which are able to tackle with high frequency transients (typically defined on a cycle-by-cycle scale, i.e., with a crank angle resolution).

At present real-time simulation require Filling-and- Emptying (F&E) and Quasi-Steady (QS) methods, allowing to build up 0-D, lumped parameter, cycle averaged, Mean Value Models [29,30]. The model of ICEs developed within the research group are based on this approach which is followed also to built up the industrial CHP-ICE here presented. The F&E approach is typically used for the simulation of capacitances (i.e., volumes) which allow the accumulation of energy and mass: QS models are widely used for the simulation of resistance (i.e., valves, junctions, etc.) which don’t allow any accumulation of energy or mass

It is well known that the advantages in terms of computing time offered by F&E and QS techniques have to be paid through the introduction of empirical correlations, which are used to take account of those processes and phenomena that cannot be properly described by these approaches. However, a QS approach still remains the only practical solution for the simulation of specific components (e.g., turbocharger compressor and turbine), where 3-D calculations would be the only significant alternative.

As seen a wide literature is available for automotive engines but much less experiences can be recalled when it comes to simulation of industrial alternative internal combustion engines. This is indeed because these engines are less demanding in terms of control strategies and barely are called to operate in transient conditions. Common approaches are therefore to represent their behaviour by means of just some empirical overall correlations that describe their behaviour in terms of fuel consumption-power generated then leading to simple quasi-steady models where the entire system is just reduced to a transfer function. Since aim of the present work on energy system is more focused on plant design rather than operational analyses (i.e. what is the fuel consumption if the engine is operated for a certain number of hours at full load and some other hours at partial load, as proposed in some previous works [34-35]) a comprehensive object based model of the engine plant is considered to be the suitable tool to design, test and enhance solutions that are intended to improve the energy conversion performances of the unit.

The schematic block diagram of the engine modeled is presented in Fig. 4.15, where it is also recognizable the cause effect correlation between the blocks, and appears simpler than common modern automotive engines since many components, like variable geometry turbocharger (VGT), exhaust gas recirculation systems (EGR), VVA/VVT systems and aftertreatment devices (i.e., catalysts, particulate traps, etc.) are typically not employed in stationary low-medium speed natural gas fired ICEs. The main components considered in defining the plant layout are therefore an air compressor, an intercooler, throttle valve, intake manifold, combustion chamber, exhaust valves, exhaust manifold and turbine.

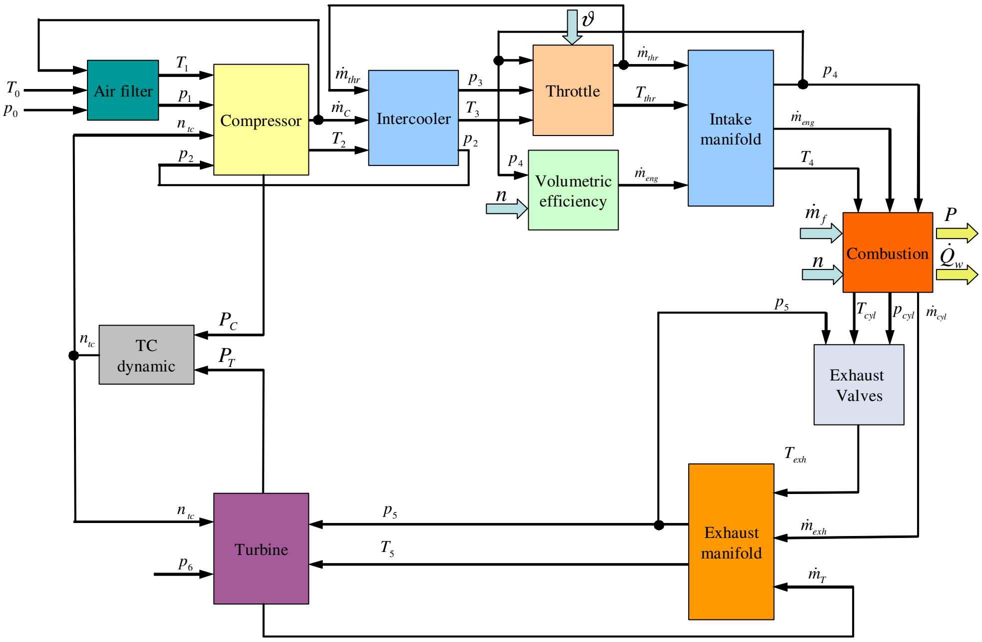

Fig. 4.15. Causality diagram of the modeled ICE.

The engine modeled is the four stroke spark ignition, natural gas fired supercharged engine of which main geometrical data and operational parameters at nominal conditions, are listed in Tab. 4.1.

Engine Power	3000	kW
Rated Electrical efficiency	41.8	-
mep	17.7	bar
Engine speed	1000	min^{-1}
Bore/stroke	260/320	mm
Displacement	~200	l
Fuel consumption	7000	kW
Exhaust gas temperature	~470	°C
Exhaust mass flow	15673	kg/h
Combustion air mass flow	15154	kg/h
Engine jacket temperatures	79/90	°C
Engine jacket flow	~90	m^3/h

Tab. 4.1. Main parameters of the modeled cogenerative ICE.

While nearly all the blocks visible in Fig. 4.15 appear in the library of components, thus allowing a quick assembling of the whole ICE model, the "Volumetric Efficiency" block is a special component introduced to take account of the actual air mass trapped by the engine at each cycle. The engine volumetric efficiency λ_v is in fact defined as the ratio of the air mass trapped within the cylinder ant the air mass that would be contained in the cylinder at *BDC* given the thermodynamic state existing in the intake manifold (p_{IM}, T_{IM}).

Once known the value of λ_v the actual mass flow rate to the cylinder is given, for a 4 strokes engine, by the known correlation:

$$\dot{m} = \frac{\lambda_v p_{IM} V_d n}{120 R T_{IM}} \tag{4.1}$$

where n is the engine rotational speed in [r/min] and V_d is the engine displacement in [m^3].

An empirical correlation from Hendricks [36] is used in this instance to evaluate λ_v given the pressure existing upstream the intake valve, according to the linear correlation:

$$\lambda_v(p) = S_i p - Y_i \tag{4.2}$$

where the coefficients have to be determined by means of experimental data.

As highlighted MVM of ICEs, where QS components appear, as in the case under investigation, require large sets of experimental data to setup all the empirical functions introduced. The unavailability of such data for the industrial ICE studied, forced to introduce some further simplifications and to apply some scaling techniques to the main components of which data were available only for automotive engines.

Many correlations regarding pressure losses of the gas flowing through main components (as the intercooler or the air filter) have been implemented recalling [37] while parameters concerning the heat exchange correlations in the intercooler have been gathered from [38].

A total new approach have been applied instead to define the in-cylinder processes automotive applications. So far, the models developed within the Department, used a set of correlations defined on a combination of 2nd order polynomial and exponential functions, whose coefficients are evaluated through a least square method on the basis of experimental data. The characterization of the in-cylinder processes therefore was fully *black-box* and based on data gathered from bench test of the engine to be modeled.

A different approach is here proposed and, as highlighted in Par. 3.3.5, the cycle *bmip* and in-cylinder temperature and pressure at end of expansion are gathered through the introduction of energy conservation equation and chemical species conservation equations by applying an approach that, if not totally *white-box* due to the introduction of chemical constants, is however *grey-box*. The main advantage of this approach is that it allows to get sufficient information of the combustion process just knowing the geometrical data of the engine that can simply be obtained from commercial datasheets, therefore no specific test data, which are often hard to obtain, have been used at all.

Other components of the engine subjected to a deep review are those defining the supercharging unit.

It is first to be noted that the industrial engine here considered adopts two separate turbocharging units, one for each bank of the *V* arranged cylinders. Nevertheless, since the model is fully averaged, one equivalent turbocharger has been introduced. No data however were available for this component and, as seen, both the compressor and turbine models need data input to be fully characterized. Some method have therefore been adopted to properly scale the characteristic maps of an automotive turbocharger, that were the only ones available, in such a way to describe the components employed in the cogenerative ICE.

By application of the *Π* Theorem it is possible to introduce some dimensionless groups of parameters that define the behaviour of turbo machineries [39]. For an air compressor, for example, the group π_1 is function of the volumetric flow rate and displays that $\dot{V}$ is a linear function of the rotational speed n:

$$\pi_1 = \frac{\dot{V}}{nD^3} \tag{4.3}$$

or, equivalently:

$$\pi_1 = \frac{\dot{m}\sqrt{T_1}}{p_1}\frac{R\sqrt{T_1}}{nD^3} \tag{4.4}$$

where it is recognizable the term $\frac{\dot{m}\sqrt{T_1}}{p_1}$ representing the corrected mass flow rate.

The group π_2 can be introduced showing that the head depends on the square of the tip blade speed:

$$\pi_2 = \frac{gH}{(nD)^2} \propto \frac{gH}{u^2} \tag{4.5}$$

where:

$$gH = \int \frac{\partial p}{\rho} = \frac{k}{k-1} R T_1 \left(\beta^{\frac{m-1}{m}} - 1 \right) \tag{4.6}$$

The group π_3 can eventually be introduced with reference to compressor power:

$$\pi_3 = \frac{\dot{V}}{nD^3} \frac{gH}{\left(nD\right)^2} = \frac{P}{\rho n^3 D^5} = \frac{\pi_1 \pi_2}{\rho} \tag{4.7}$$

Once π_3, π_3 and π_3 have been determined for the known compressor, the flow rate, pressure ratio and power for the new compressor can be calculated:

$$\dot{V} = \pi_1 n D^3 \tag{4.8}$$

$$\beta = \left(\pi_2 \left(nD\right)^2 \frac{k-1}{k} \frac{1}{RT_1} + 1 \right)^{\frac{m}{m-1}} \tag{4.9}$$

$$P = \pi_1 \pi_2 n^3 D^5 \tag{4.10}$$

The new compressor characteristic maps can then be built up by properly scaling the known maps of an automotive compressor (i.e. Fig. 4.16 and Fig. 4.17). Although this is an approximation, it is believed that the error committed is negligible and this was an easier way to gather proper maps for the compressor model. The maps are reported as function of the corrected mass flow rate defined as from Par. 3.3.1.

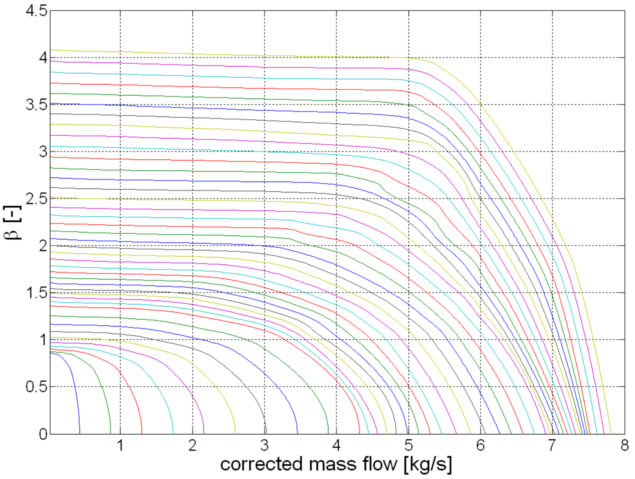

Fig. 4.16. Compressor mass flow rate characteristic for stationary heavy duty ICE.

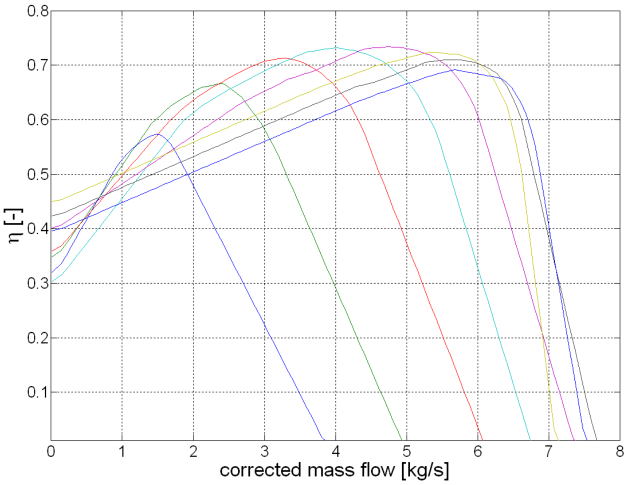

Fig. 4.17. Compressor efficiency characteristic for stationary heavy duty ICE.

Once a full set of parameters and characteristic curves has been gathered, these values have been used to characterize the single components that, picked up from the created libraries of customized models, have been employed to reproduce in Simulink® the engine lay-out, as from Fig. 4.18.

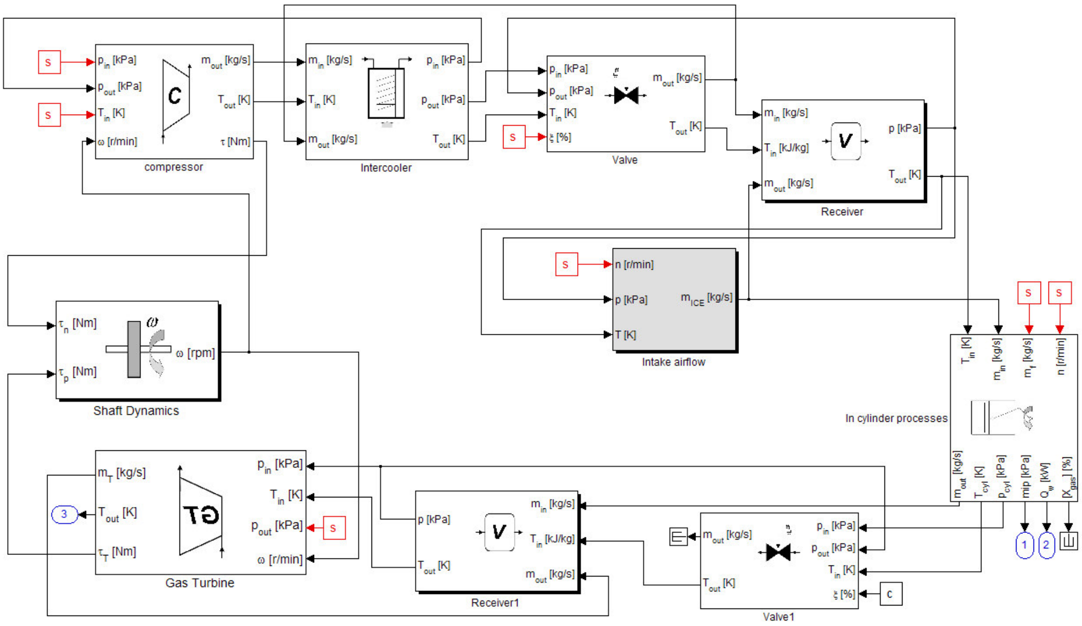

Fig. 4.18. Simulink® model of a cogenerative alternative IC engine.

As the MGT and the ORC, also the ICE model has been fitted into one Simulink® block that in fact constitutes the upper model block of the cogenerative ICE (Fig. 4.19). It can be easily observed how the main system inputs are represented by the temperature and pressure of the ambient air, along with the combustion fuel mass flow rate (which is assumed to be an independent input since the natural gas is introduced via electronic actuated injectors), the throttle valve opening grade and the engine rotational speed. The latest have to be determined by merging the engine load curve and the engine characteristic. In industrial ICEs, especially those destined to power generation applications, if synchronous generators are employed, as in the case under analysis, are managed to keep constant the rotational speed with varying loads.

Again many outputs could be recalled from the models but the ones highlighted in the block of Fig. 4.19 are those relevant for the matching with other components, as it will be clearer by going through Chapter 5. Therefore, besides the mechanical and thermal power and efficiencies, also the main energy streams associated to the exhaust gases and refrigerant are considered.

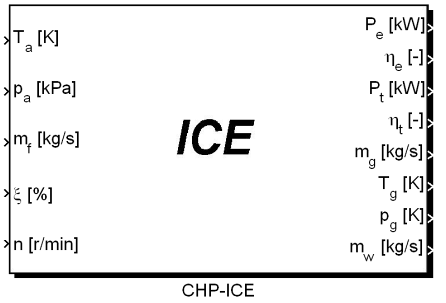

Fig. 4.19. Simulink® interface of the ICE unit. Upper level.

4.3.1 Steady state operational characteristics

In this section some steady state operational characteristics of the modeled engine will be analyzed. Since the engine is supposed to be operated at full throttle under any circumstance and the rotational speed is assumed to be 1000r/min for generator synchronization, the only two overall external inputs that may affect engine operation are (changes in ambient air pressure are neglected):

- $\dot{m}_f$: injected fuel mass flow rate [kg/s];
- T_{amb}: ambient air temperature at compressor inlet [K].

To be noted that only the fuel mass flow rate is a controllable input while the ambient air temperature is an uncontrollable input that however may significantly affect the overall engine performances, as will be shown in the following.

A first set of plots is proposed to represent the steady state engine performances given a range of fuel flow rate varying from 0.06 to 0.16kg/s of methane, when the rated fuel mass flow rate is 0.14kg/s. The ambient air temperature is in this case fixed at 298K.

Fig. 4.20 shows the engine output energy fluxes versus actual fuel mass flow rate. It can be observed that both the mechanical power (P_{ICE} and the thermal power ($\dot{Q}$) display a nearly linear pattern. Fig. 4.20 (a) particularly can be considered as a representation of the Willans line for the engine under analysis; it is common in literature in fact to attribute a linear dependency between actual engine power (or *bmip*, in this case equivalent since the engine speed is kept constant) for heavy duty engines [40-41] the line should cross the x axes in a positive abscissa that represent the fuel consumption at the idle, that is the mechanical losses of the engine. In the example here presented the extension of the line would reach the origin of the axes of the $\dot{m}_f - P_{ICE}$ plane (the plot axes have purposely been extended up to the origin to show this trend of the "Willans line") consistently with the assumption placed on the model of no engine mechanical losses to be accounted for. This demonstrates therefore that the model proposed overestimates the net power output and future work will be done to take into account of the engine mechanical losses. However, the pattern of the engine power characteristic is consistent to the expected behaviour.

The increasing steady state performances of the engine at rising fuel mass flow rate can be appreciated also from Fig. 4.21 (that represent the in cylinder pressure at BDC prior to exhaust valve opening) and Fig. 4.22 (that displays the performances of the engine turbo-charger). Fig. 4.22 (a) shows the mechanical turbine power and the compressor power which are equal since the data are provided at steady state operation when the turbo-charger equilibrium is reached. The power increases with the fuel mass flow rate as well as the rotational speed (Fig. 4.22 (b)) which also determines an increase in the air flow elaborated by the compressor and the gas flow that expands through the turbine (the difference is the fuel mass flow rate, Fig. 4.22 (d)). In Fig. 4.22 (c) it can also be observed as the turbine and compressor isentropic efficiencies approximate the optimum values when the fuel mass flow rate is close to the rated.

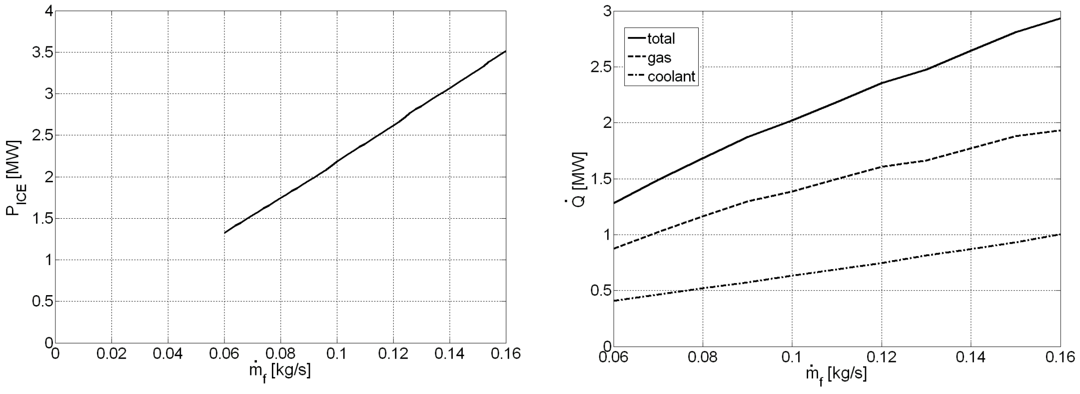

(a) (b)

Fig. 4.20. Main ICE output energy fluxes at varying fuel mass flow rate: (a) mechanical power, (b) thermal power.

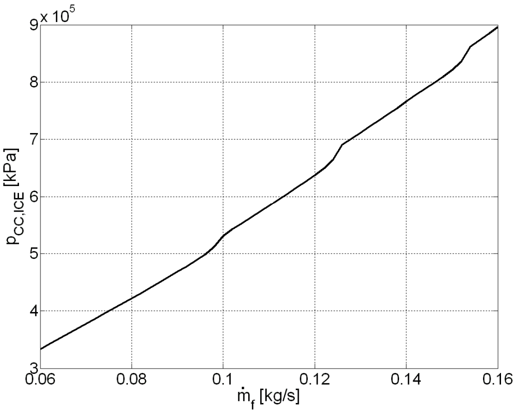

Fig. 4.21. Combustion chamber pressure at BDC at varying fuel mass flow rate.

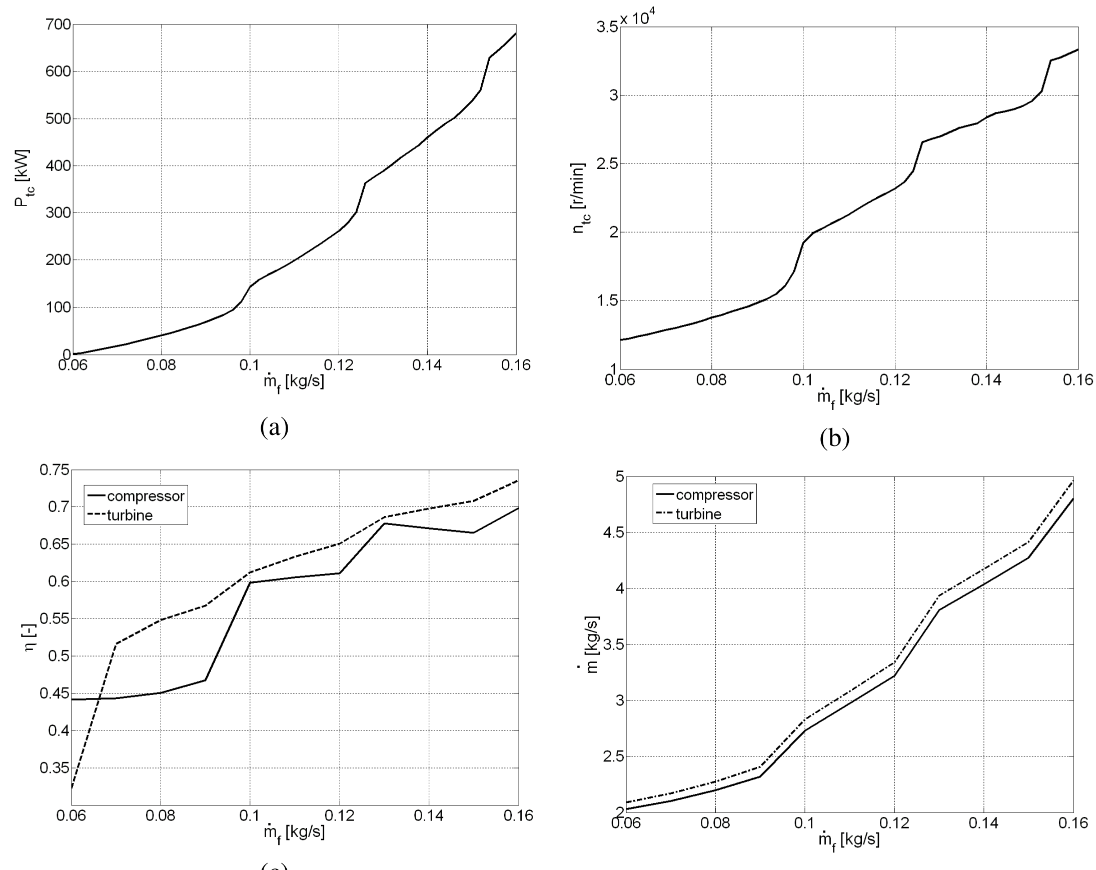

(a) (b)

(c) (d)

Fig. 4.22. Turbo-charger characteristics at varying fuel mass flow rate: (a) compressor and turbine power, (b) turbo-charger rotational speed, (c) compressor and turbine isentropic efficiencies, (d) compressor and turbine gas mass flow rate.

A similar set of plots is proposed to highlight the non negligible influence of the ambient air temperature on the operating conditions of the engine; T_{amb} is assumed in the range 263-313K while the fuel mass flow rate is the rated.

From Fig. 4.23 one can observe how the increasing air temperature determines a decrease in the mechanical power generated and, conversely, an increase in the overall thermal power available, as suggested in literature (for example [42]). The effect, while moderate, is however perceivable and it accounts for a change of about 2% in the mechanical power and 7% in the thermal power. This variation has effects on the engine mechanical an thermal efficiencies since the energy input, given by the unchanging fuel mass flow rate, is the same (Fig. 4.23 (c)).

This decay of engine performances with air temperature is due to the decreasing air mass flow rate that is introduced in the combustion chamber (Fig. 4.24) due to its decreased density.

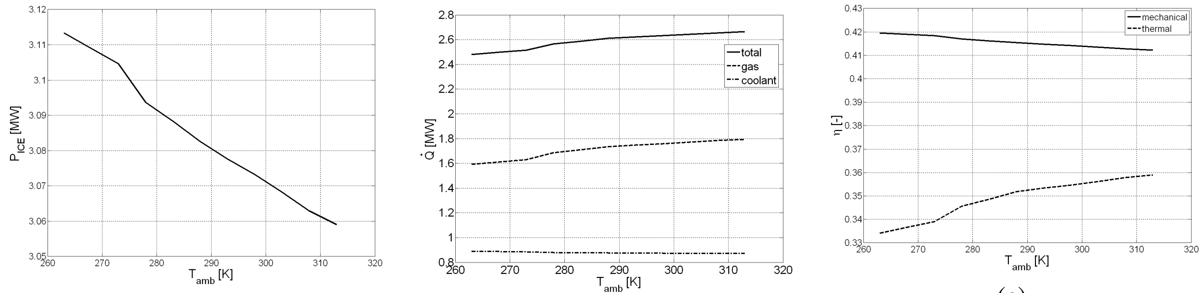

(a) (b) (c)

Fig. 4.23. Main ICE performances at varying ambient air temperature: (a) mechanical power, (b) thermal power, (c) engine mechanical and thermal efficiency.

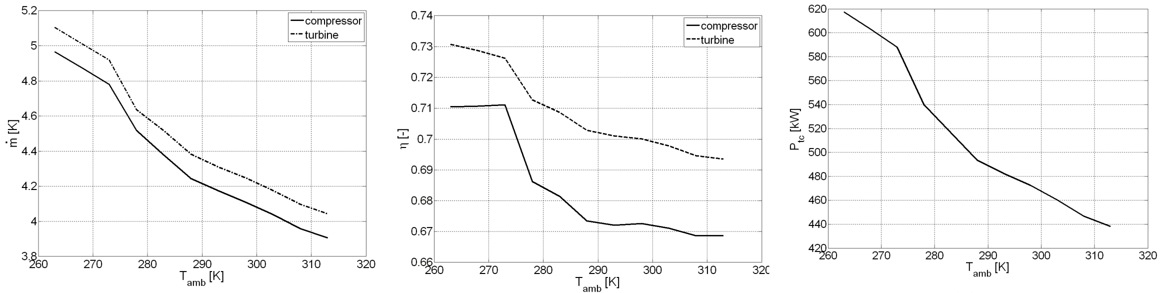

(a) (b) (c)

Fig. 4.24. Turbo-charger characteristics at varying ambient air temperature: (a) compressor and turbine gas mass flow rate, (b) compressor and turbine isentropic efficiencies, (c) compressor and turbine power.

4.3.2 Transient response

In this section the behaviour of the CHP-ICE model is presented in response to a step change in the fuel mass flow rate from 0.14 to 0.08kg/s that takes places at simulation time t=20s when the engine is running at stationary conditions. The ambient air temperature is constant at 298K and the engine rotational speed is again 1000r/min with full throttle.

Fig. 4.25 (a) gives the engine power: it is possible to observe how promptly the engine responds in terms of mechanical power to the step change in the fuel mass flow rate. This is a consequence of the quasi-steady way the in cylinder processes are introduced in the model, hence a sudden decrease in the fuel mass flow rate determines the sharp decrease in the in cylinder pressure (Fig. 4.26 (a) displays the combustion chamber pressure at BDC prior to exhaust valve opening) that in turn causes a decrease in the *bmip* and then P_{ICE}. To be noted that, besides the first and sharp decrease in p_{CC} and P_{ICE}, they keep decreasing for some time afterwards as a consequence to the response on the turbo-charger unit (Fig. 4.27) that is slower due to dynamics of the intake and exhaust manifolds.

Fig. 4.25 (b) shows the response in term of available thermal power from the *ICE*. While it is reasonable to assume that the power available in the exhaust gases may provide the very fast response proposed by the plots, as a consequence of the way the temperature of the gases decreases (Fig. 4.26 (b)) the sharp decrease in the available heat flow from the engine refrigerant seems unreal. This behaviour is due to the fact that thermal inertia of the engine body has been neglected and the heat exchanged between gases and cylinder walls is assumed to be a function of the in cylinder gas temperature that, again, changes instantaneously with $\dot{m}_f$.

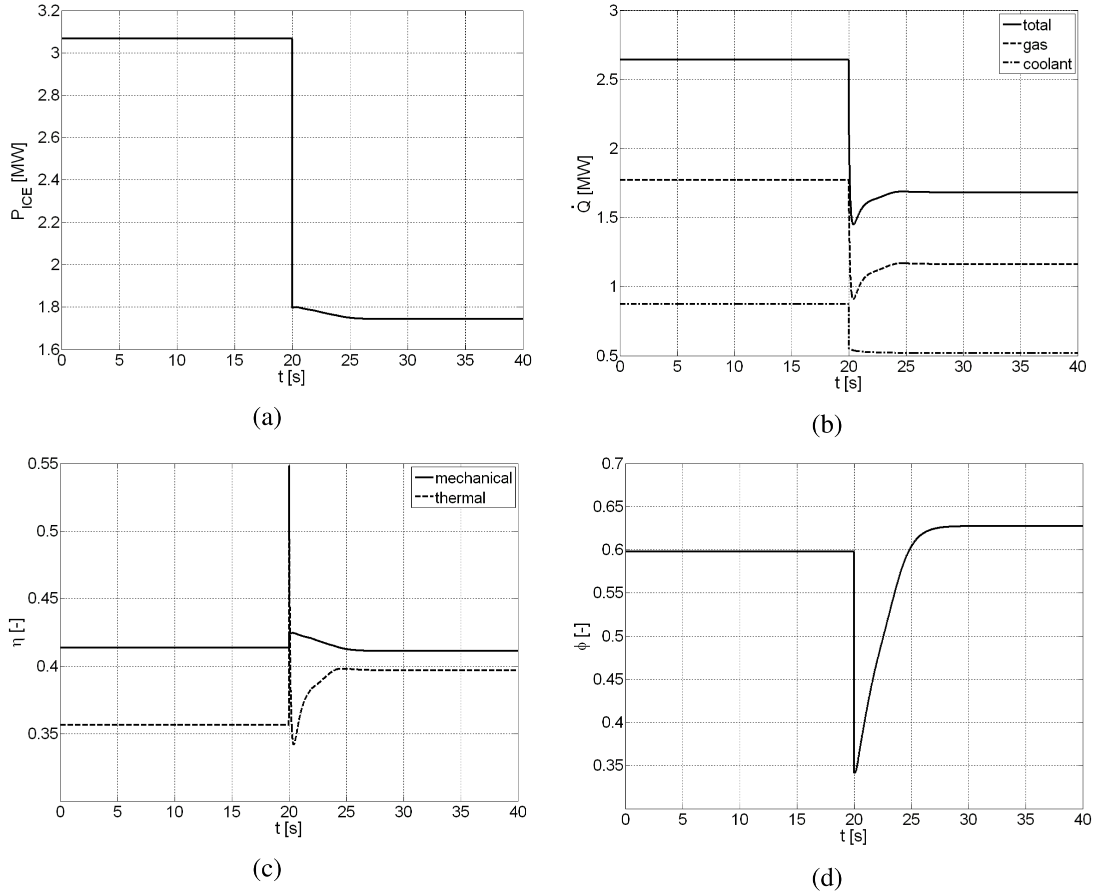

(a)

(b)

(c)

(d)

Fig. 4.25. Main ICE performances due to a step change in $\dot{m}_f$: (a) mechanical power, (b) thermal power, (c) engine mechanical and thermal efficiency, (d) combustion air-fuel equivalence ratio.

The engine mechanical and thermal efficiency are proposed in Fig. 4.25 (c) and they both increase as the engine is brought to operate closer to nominal conditions ($\dot{m}_f$=0.14kg/s).

The fuel air equivalence ratio is displayed in Fig. 4.25 (d) and it is possible to see the sharp change when the step change in $\dot{m}_f$ occur, and this is because the air flow from the compressor had no time to adjust and then, after the transient phenomena have expired, how it stabilizes a value slightly higher that that observed before the transient. The engine operates with nearly the same air fuel ratio in both circumstances and this determines nearly identical in cylinder gas temperatures at BDC (Fig. 4.26 (b)) while the pressure decreases in the combustion chamber (Fig. 4.26 (a)) due to the reduced total gas mass trapped within the cylinder.

The unchanged temperature in the exhaust manifold (that is close to the in cylinder gas temperature but decreased due to expansion through the exhaust valves) with decreased pressure, determines a lower pressure drop through the turbine (the turbine exhaust is always at atmospheric pressure, since the pressure losses in the gas heat exchanger have been neglected) which in turn is cause for a higher gas temperature at turbine outlet (Fig. 4.26 (b)) which is one of the cause for overall thermal efficiency increase (Fig. 4.25 (c)).

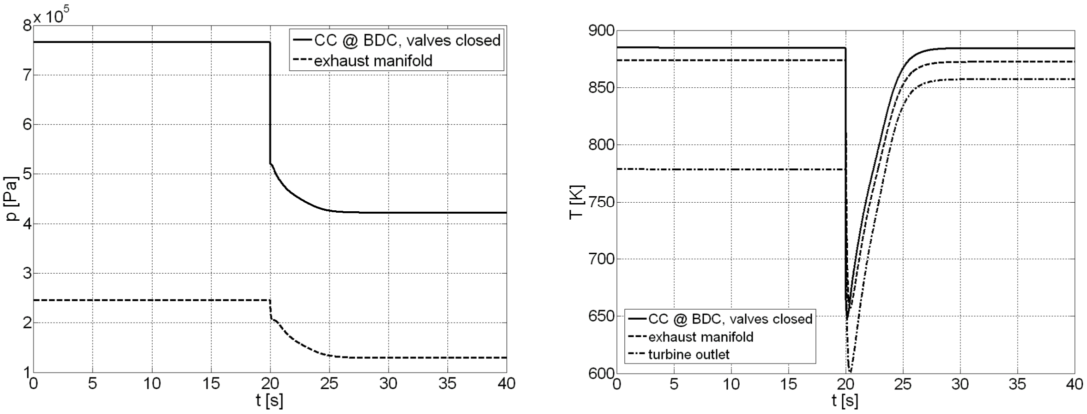

(a) (b)

Fig. 4.26. Conditions in the exhaust manifold due to a step change in $\dot{m}_f$: (a) in cylinder and manifold pressure, (b) in cylinder, manifold and turbine outlet temperatures.

The response of the turbo-charging unit has a time lag similar to that of the pressure adjustment in the manifolds. Fig. 4.27 (a) also shows how, during the transient, some mismatch between the turbine and compressor power arise that determines adjustment in the rotational speed.

As already observed the compressor and turbine isentropic efficiencies decrease when moving away from nominal mass flow rates and rotational speed (Fig. 4.27 (b)). The mass flow rates are proposed in Fig. 4.27 (d) and it is possible to observe that the compressor model responds with some instability at the fast decrease in the available positive power coming from the turbine being the pressure in the intake manifold still not decreased, condition that is typical of surge.

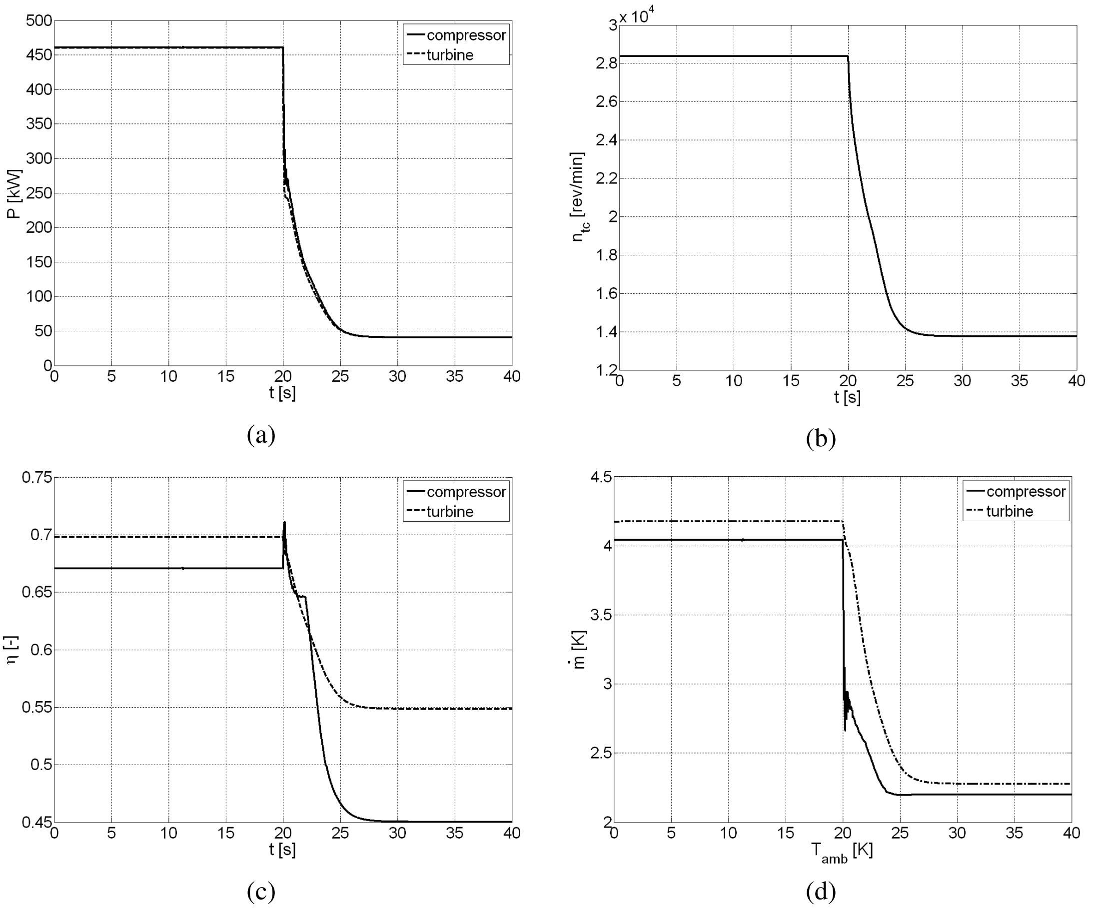

(a)

(b)

(c)

(d)

Fig. 4.27. Turbo-charger characteristics due to a step change in $\dot{m}_f$: (a) compressor and turbine power, (b) turbo-charger rotational speed, (c) compressor and turbine isentropic efficiencies, (d) compressor and turbine gas mass flow rate.

4.4 Summary

In the Chapter examples have been provided on the way the base component models presented in Chapter 3 can be utilized to generate complete power systems dynamical models. The presented power systems models, while necessarily featuring some approximations (some of which come from the hypothesis placed on creating the component models and some other come from simplifications in the system lay-out), can still be believed to provide interesting information in predicting the behaviour in off-design and transient operation of the systems analyzed. Once again a full validation of the models have not be possible so far, even though it is planned as future enhancement.

The presented complete models of energy power systems (MGT, ORC and ICE) have been grouped together in a new Simulink® sub-library ('Complete Power Systems'), presented in Fig. 4.28. To be noted that this new library, that features only the three presented blocks, can easily be extended according to the research needs whenever new complete systems are to be analyzed and that, in any case, new complete power systems models can be built up recurring to the base components available in the ‘State Determined’ and ‘Not State Determined’ libraries.

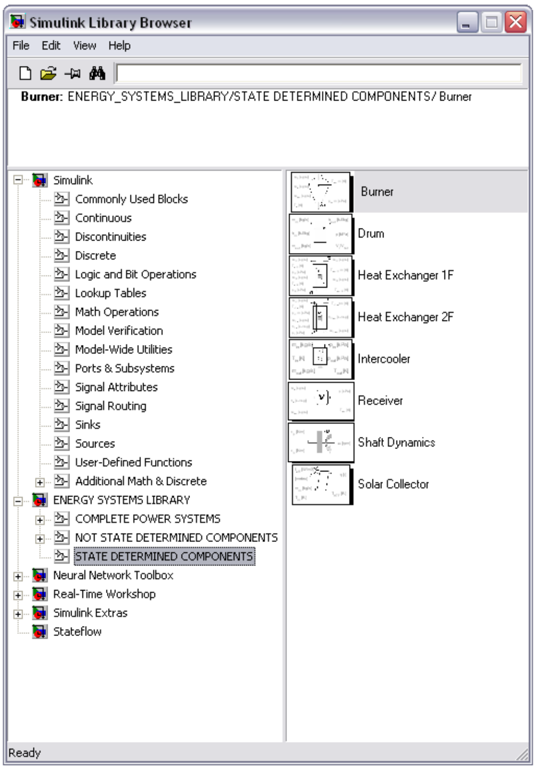

Fig. 4.28. The custom ‘Energy Systems library’ accessible from the ‘Simulink® Library Browser’: detail of the ‘Complete Power System’ sub-library.

Refernces

1 Cennerilli S., Fiorini P., Sciubba E., *Application of the Camel process simulator to the dynamic simulation of gas turbines*, ECOS 2006 Proceedings, Vol. 1, pp. 355-363.

2 Youhong Y., Chen L., Sun F., Wu C., *Matlab/Simulink-based simulation for digital-control system of marine three-shaft gas-turbine*, Applied Energy, 80 (2005) 1-10.

3 Youhong Y., Chen L., Sun F., Wu C., *Neural-network based analysis and prediction of a compressor’s characteristic performance map*, Applied Energy, article in press.

4 Simani S., Fantuzzi C., *Dynamic system identification and model-based fault diagnosis of an industrial gas turbine prototipe*, Mechatronics 16 (2006) 341-363.

5 Jurado F., *Non-linear modeling of micro-turbines using NARX structures on the distribution feeder*, Energy Conversion and Management 46 (2005) 385-401.

6 Augenti C., Gambarotta A., Pagliarini G., Rainieri S., Vaja I., *Economic feasability analysis of a CCHP system in a tertiary sector application*, ASME-ATI 2006 Conference Proceedings, Milano 2006

7 Traverso A., *TRANSEO: A New Simulation Tool for Transient Analysis of Innovative Energy Systems*, Ph.D. Thesis, TPG-DiMSET, University of Genova, Italy, 2004.

8 X.Q. Kong, R.Z. Wang, X.H. Huang, Energy optimization model for a CCHP system with available gas turbines, Applied Thermal Engineering 25 (2005) 377-391.

9 Gambarotta A., Vaja I., *A Real Time Dynamic Model of a Micro-Gas Turbine CHP System with Regeneration,* Paper POWER2007-22098, ASME POWER Int. Conference, San Antonio – Texas, 17-19 Luglio 2007.

10 Wei D., Lu X., Lu Z., Gu J., *Performance analysis and optimization of organic Rankine cycle (ORC) for waste heat recovery*, Energy Conversion and Management 2007; 48:1113-1119

11 Madhawa Hettiarachchi H.D., Golubovic M., Worek W.M., Ikegami Y., *Optimum design criteria for an Organic Rankine cycle using low-temperature geothermal heat sources*, Energy 2007; 32:1698–1706.

12 Wei D., Lu X., Lu Z., Gu J., *Experimental evaluation of an autonomous low-temperature solar Rankine cycle system for reverse osmosis desalination*, Desalination 2007; 203:366–374.

13 Larjola J., *Electricity from industrial waste heat using high-speed organic Rankine cycle (ORC)*, Int. J. of Production Economics, 1995;41:227-235.

14 Invernizzi C., Iora P., Silva P., *Bottoming micro-Rankine cycles for micro-gas turbines*, Applied Thermal Energy 2007;27:100-110.

15 Danov S.N., Gupta A. K., *Modeling the Performance Characteristics of Diesel Engine Based Combined-Cycle Power Plants – Part I: Numerical Model*, Journal of En U. Drescher, D. Bruggermann, Fluid selection for the Organic Rankine Cycle (OR(C) in biomass power and heat plants, Applied Thermal Energy 27 (2007) pp. 223-228gineering for Gas Turbines and Power, 2004;126:28-34.

16 Micheli D., Reini M., *On bottoming a micro turbine with a micro ORC section: Part (b) micro-combine cycle plant performance evaluation*. In Proceedings of ECOS 2007, Padua, Italy, June 25-28, 2007, p.1035-1041.

17 Laurenti L., *Sviluppo di un modello dinamico in Simulink® per la simulazione di impianti a ciclo Rankine a fluidi organici*. Master Thesis, Industrial Engineering Department, University of Parma, Italy, 2008 (in Italin).

18 Drescher U., Bruggermann D., *Fluid selection for the Organic Rankine Cycle (OR(C) in biomass power and heat plants*, Applied Thermal Energy 2007; 27:223-228.

19 Wei D., Lu X., Lu Z., Gu J., *Dynamic modelling and simulation of an organic Rankine cycle (ORC) for waste heat recovery*, Applied Thermal Engineering, Article in press, 2007.

20 Yamamoto T., Furuhata T., Arai N., Mori K., *Design and Testing of the Organic Rankine Cycle*, Energy 2001; 26:239-251.

21 Colonna P., van Putten H., *Dynamic modeling of steam power cycles. Part I - Modeling paradigm and validation*, Applied Thermal Engineering 2007; 27:467-480.

22 Colonna P., van Putten H., *Dynamic modeling of steam power cycles. Part II – Simulation of a small simple Rankine cycle system*, Applied Thermal Engineering 2007; 27:2566-2582.

23 A.Gambarotta, *A control-oriented library for the simulation of automotive Diesel engines*, 3rd Intern.Conf.on Control and Diagnostics in Automotive Applications, paper 01A3039, Sestri Levante, 7/2001.

24 Canova M., Gambarotta A., *Automotive Engine Modeling for Real-Time control using an object-oriented simulation library*, Proceedings of the 4th International Conference on Control and Diagnostics in Automotive Applications, paper 03A2035, Sestri Levante, Giu. 2003.

25 Canova M., Fiorani P., Gambarotta A., Tonetti M. *A real-time model of a small turbocharged Multijet Diesel engine: application and validation*, 7th SAENA Int.Conf.on Engines for Automobiles, SAE paper n.2005-24-65, Capri (NA), Sept. 2005.

26 Fiorani P., Gambarotta A., Lanfranco E., Tonetti M., *A real-time model for the simulation of transient behaviour of automotive Diesel engines*, ATI/SAE Congress “The sustainable mobility challenge”, pp.115-124, SAE paper n.2006-01-3007, Perugia, 9/2006.

27 Ausiello F.P., De Cesare M., Serra G., Fiorani P., Gambarotta A., Lucchetti G., *A detailed Mean Value Model of the exhaust system of an automotive Diesel engine*, 5th International Mobility Conference on Emerging Automotive Technologies – Global and Indian Perspective, SAE India, New Delhi, 2008.

28 Gambarotta A., Lucchetti G., *A Real-time Model for the Simulation of Steady and Transient Behaviour of Automotive Engines*, Les Rencontres Scientifiques de l'IFP - Advances in Hybrid Powertrains - 25-26 November 2008 – Proceedings, Nov 2008.

29 Guzzella L., H.Onder C., *Introduction to Modeling and Control of Internal Combustion Engine Systems*, Springer-Verlag, ISBN 3-540-22274-X, 2004.

30 L.Guzzella, A.Amstutz, *Control of Diesel engines*, IEEE Trans.on Control Systems Tech., October 1998.

31 Dauron A., *Model-based powertrain control: many uses, no abuse*, E-COSM - Rencontres Scientifiques de l'IFP, Rueil-Malmaison, 2006.

32 Albrecht A., Grondin O., Le Berr F., Le Solliec G., *Towards a stronger simulation support for engine control design: a methodological point of view*, ECOSM - Rencontres Scientifiques de l'IFP, Rueil- Malmaison, 2006.

33 Watson N., Marzouk M., *A non-linear digital simulation of turbocharged Diesel engines under transient conditions*, SAE paper no.770123, SAE Int.Conf. and Exp., Detroit, 1977.

34 Augenti C., Gambarotta A., Pagliarini G., Rainieri S., Vaja I., *Economic feasability analysis of a CCHP system in a tertiary sector application*. ASME-ATI Conference, Milano 2006.

35 Vaja I., Augenti C., Gambarotta A., Pagliarini G., Rainieri S., *Aspetti economici di un impianto trigenerativo applicato al settore terziario*. 61° Congresso Nazionale ATI, Perugia – Italia 12-15 settembre 2006. (in Italin).

36 Hendricks E., Chevalier A., Jensen M., Sorenson S.C. et.al., *Modelling of the Intake Manifold Filling Dynamics*, SAE Technical Paper No. 960037, 1996.

37 Idel'chik I.E., *Handbook of Hydraulic Resistance, coefficients of local resistance and of friction*, 1966

38 Kays W.M., London A.L., *Compact heat exchangers*, 3rd ed., McGraw-Hill, New York, 1984.

39 Acton O., *Turbomacchine*, UTET Torino, 1986. (in Italian)

40 Giannelli R.A., Nam E.K., Helmer K., Younglove T., Scora G., Barth M., *Heavy-Duty diesel vehicle fuel consumption modelling based on road load and power train parameters*, SAE Commercial Vehicle Engineering Conference, 2005, Rosemont, IL, USA

41 Klimstra J., *Optimum Load Step Response of Fuel-Injected Reciprocating Gas Engines*, CIMAC Congress 2004, Kyoto, Japan

42 Macchi E., Campanari S., Silva P., *La microcogenerazione a gas naturale*, Polipress, Milano, 2005. (in Italian)

CHAPTER
FIVE

CASE STUDY:
A COMBINED MCI-ORC POWER UNIT

In this section a practical application of the library of components created and presented in the previous Chapters is proposed. A combined MCI-ORC power unit will be presented and analyzed as a possible solution to enhance the performances of a stationary MCI, in those cases when no heat is usefully recovered. Few applications of such systems exist and the study presented is aimed both at proposing possible solutions for energy optimization and at display the capabilities in system design of the developed libraries of models.

A first and second principle analysis is first presented in Par.5.1 to show how, the application of a properly designed Organic Rankine Cycle, can turn to be a feasible solution to recovery part of the heat discharged by a stationary ICE converting it into useful work that can be easily dispatched as electric power. Different system designs are proposed demonstrating that in some cases, and with some kind of organic fluids, the overall electrical efficiency can be raised of above 10%, meaning a significant energy optimization.

In Par. 5.2 the thermodynamic analysis is extended to more advanced configurations that may be adopted to couple ORCs to ICEs, demonstrating that under certain circumstances the ORC could be employed to reduce the exergy content of the high temperature source of the heat that is released by the ICE (i.e. the hot exhaust gases) still leaving an abundant thermal flux at lower temperature (i.e. the heat discharged by the ORC) that could be employed for cogeneration purposes when the heat is required at medium-low temperatures, as in the cases of building heating applications. The overall effect of the ORC in this case would be that of increasing the second principle efficiency of the thermal unit, the price being the heat to be available at lower temperatures.

A complete dynamic model of the entire combined unit is then presented in Par. 5.3, recurring to the models presented in the previous Chapters, providing a complete tool that can be used to further analyze, also in off design and unsteady operating conditions, the proposed system. The complete model hence can actually constitute a virtual test bench that can represent the behaviour of the designed unit, allowing for analyzing different lay-outs and configurations.

Nomenclature

B	Exergy [kJ]
$\dot{B}$	Exergy Flow [kW]
H	Entalpy [kJ]
$\dot{H}$	Entalpy Flow [kW]
P	Power [kW]
Q	Heat [kJ]
$\dot{Q}$	Heat Flow [kW]
T	Temperature [K]
V	Volume [m^3]
$\dot{V}$	Volume flow rate [m^3/s]
b	Specific Exergy [kJ/kg]
c_p	Specific heat at constant pressure [kJ/kg K]
e	Air excess coefficient [-]
h	Specific Enthalpy [kJ/kg]
m	Mass [kg]
$\dot{m}$	Mass flow rate [kg/s]
p	Pressure [kPa]
s	Specific Entropy [kJ/kg K]
v	Specific volume [m^3/kg]
w	Specific Work [kJ/kg]
Greek symbols	
α	Air fuel ratio [-]
η	Efficiency [-]
η_{ORC}	Organic Rankine Cycle efficiency [-]
η_b	Exergy efficiency [-]
η_g	Global Efficiency [-]
Φ	Heat Availability [-]

ρ	Density
Ψ	Irreversibility factor [-]

Abbreviations and subscripts

C	Condensation
CC	Combined Cycle
EX	Heat Exchanger
ICE	Internal Combustion Engine
ORC	Organic Rankine Cycle
P	Pump
PP	Pinch Point
R	Regenerated
T	Turbine
a	Available
$appr$	Approach
$cond$	Condenser
$crit$	Critical
d	Direct engine gas/organic fluid heat exchange
$dead$	Dead State
e	Engine
ex	Heat Exchanger
f	Fluid
fin	Final
g	Gas
htf	Heat Transfer Fluid
in	Inlet
out	Outlet
tf	Transfer Fluid
w	Water

5.1 Thermodynamic analysis of MCI-ORC combine power unit

Recently many power plants based on internal combustion engines (with net power output ranging from several hundreds kW$_e$ to few MW$_e$) are employed as base components in DES (Distributed Energy System) networks. Internal combustion engines are chosen for their reliability, low specific cost and high conversion efficiency. These engines can be fuelled with biomass, such as vegetal oils or biogas, and the existence of incentives (as Green Certificates in Italy, for systems that use Renewable Energy Sources) makes the operation of these plants viable even if no heat is usefully recovered, therefore with significant energy waste.

Few examples of vapour cycles coupled to internal combustion engines exist and usually only the heat released at medium temperatures such as the exhaust gases of the engine are effectively used. In [1], for example, a setup is proposed where a low speed two stroke marine turbocharged diesel engine with a rated power of over 11MW is the topper of a combined cycle where the exhaust gases are used as input to a bottoming cycle based on a Rankine cycle. A numerical dynamical model is proposed to assess the off-design performances of the combined cycle, showing the tight interactions between the two power units when the Diesel engine is not running at full load.

In [2] the retrofit with a ORC rated about 10kW$_e$ of a small engine with a rated power of 200kWe fuelled with biogas is considered. The bottomer in this case is thermally fed using only the cooling water of the IC engine. The study also proposes the adoption of volumetric machines like scroll expanders in place of turbines for the ORC. These expanders are usually based on modifications of scroll compressors widely used in refrigeration and air conditioning applications and are characterized by good reliability and high efficiency with low specific costs. The use of such systems though is limited to the field of few tens of kW and they are inapplicable when the volumetric flow rates and the net cycle power increases. Moreover they can operate within a limited pressure range [2, 3].

A critical issue in the application of ORCs to industrial ICEs is the availability of waste heat at two different levels of temperature (hot gases at temperatures above 350°C and cooling water at about 80-90°C). In this Paragraph therefore a first and second principle analysis is presented to evaluate the extra power achievable by using an ICE as heat source for a vapour power cycle under the hypothesis of operating the engine at full load and considering different cycle parameters and cycle configurations [4]. The analysis is also aimed to the evaluation of the possibility to efficiently use the low temperature heat source from the engine (i.e. the engine coolant) to power the ORC bottoming cycle.

5.1.1 The system concepts considered in the investigation

In the analysis a commercial cogeneration engine is considered as the topping cycle. The engine is 12 cylinders 4 strokes supercharged natural gas fired medium speed. Main characteristics of the engine are reported in Tab. 4.1.

From the engine data it has been evaluated that about 1700kW$_t$ are available by cooling the exhaust gases down to 393K ($T_{g,min}$), and about 1000kW$_t$ are available from jacket cooling water.

It has been calculated that the air fuel ratio α is 29.2 and the air excess coefficient e is 0.701 at nominal conditions; under the hypothesis of perfect combustion of pure methane the mass composition of the exhaust gases results: CO_2=9.1%, H_2O=7.4%, N_2=74.2%, O_2=9.3%. These values are used to evaluate the properties of the hot gasses.

In the study the engine is assumed to operate at rated conditions since the aim is to determine what organic cycle would better fit the overall heat available.

Organic fluids used for power applications may show different characteristics in the *T-s* diagram and the saturation lines may be bell shaped, nearly isentropic or overhanging depending on the fluid molecule complexity. Usually fluids with simpler molecules (up to 4-5 atoms per mole) are characterized by bell shaped vapour lines and lower critical temperatures while fluids with more complex molecules (over 10 atoms per mole) display a overhanging vapour line and higher critical temperatures. Fluids with intermediate complexity may have a nearly isentropic upper vapour line and vapour remains saturated during expansion [5-7].

In the study three fluids which are commonly used in technical applications are chosen to represent these different behaviours in the *T-s* diagram: benzene (overhanging), R123 (nearly isentropic) and R134a (bell shaped) (Fig. 5.1and Tab. 5.1). They are commonly quoted in Literature as possible fluids for ORCs [5,7-8], even though future works will lead to consider other pure fluids or fluid mixtures [10].

	benzene	R123	R134a
Molar mass [kg/kmol]	78.108	152.93	102.03
Critical temperature [K]	562.05	456.83	374.21
Critical pressure [kPa]	4894	3661	4059
Boiling point at 1atm [K]	353.23	300.97	247.08
Maximum stability temperature [K]	600	600	450

Tab. 5.1. Main thermophysical properties of the selected fluids.

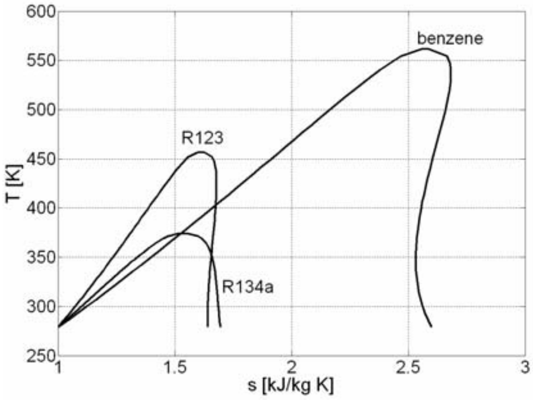

Fig. 5.1. Different shapes of coexistence curves in the *T-s* diagram for the fluids considered.

It should be noted that in the analysis only thermodynamic aspects will be considered. It is important to remark however that fluids for ORC applications must not only be favourable from a thermodynamic point of view, but they also have to satisfy conditions such as [5,11]:

- chemical stability at the operating pressures and temperatures;
- environmental friendliness: low ozone depletion potential (ODP), global warming potential (GWP) and atmospheric lifetime (ALT);
- non toxic, non corrosive and compatible with engine materials;
- low flammability and auto-ignition properties.

In the analysis that follows different cycle configurations will be assumed, in order to compare not only the different fluids but also the cycle setups and to verify the most feasible application of ORCs coupled to ICEs. In all cases the heat released by the engine through the exhaust gases is provided to a heat transfer fluid, namely a diathermic oil, which in turn is used to actually provide heat to the organic fluid used within the power cycle. The diathermic oil maximum temperature is assumed at about 600K.

The configurations of the cycles considered in the analysis are:

- ORC simple cycle thermally powered by engine exhaust gases (Fig. 5.2 (a));
- ORC simple cycle thermally powered by engine exhaust gases and engine jacket water (Fig. 5.2 (b));
- ORC with regeneration thermally powered by engine exhaust gases (Fig. 5.2 (c)).
- For all the cycles considered the following hypothesis will be assumed:
- isentropic turbine efficiency: η_T =0.8 (this value is consistent with data available in literature that attribute turbine efficiencies in the range 0.8 and 0.88 [9,11,12]);

- isentropic pump efficiency: η_P =0.8;
- working fluid temperature at condensation: T_{cond} =308K;
- vaporizing pressure varying between condensation pressure p_{cond} and critical pressure p_{crit};
- negligible pressure losses in the heat exchangers and pipes;
- dry expansion for all fluids.

The last hypothesis has been introduced assuming that a dry expansion would be preferable for the expander, regardless the expander type. This is to eliminate the impingement of liquid droplets on turbine blades. Therefore a slight superheating will be assumed when the isentropic expansion line would cross the vapour line. In other words, it will be considered just the minimum superheating to keep an isentropic expansion totally in the dry zone of the diagram. Introducing high degrees of superheating, however, is not convenient from a thermodynamic point of view, as the cycle efficiency is a weak function of turbine inlet temperature once the evaporating pressure is chosen. In some cases the highest cycle efficiencies are obtained when superheating is avoided and the fluid is expanded directly from dew line, as demonstrated in [7]. In [9] it has been also shown that superheating organic cycles (especially if based on overhanging fluids) increases cycle irreversibility and decreases the second law efficiency.

In the analysis the extra costs of building the ORC when the turbine inlet pressure is raised are also neglected [7]. The turbine pressure therefore has been assumed as an independent variable of the problem, the only limitation being the field of fluid stability.

Fluid properties have been evaluated in all cases using the REFPROP® database [13] that has been utilized in Matlab®. Specific Matlab® functions have been compiled in order to define the cycles and compute the energy balances and exergy analysis in a parameterized way. This makes possible to assess the variation in main cycle data when one or more variables are changed (as, for example, the pressure at the evaporator inlet p_2).

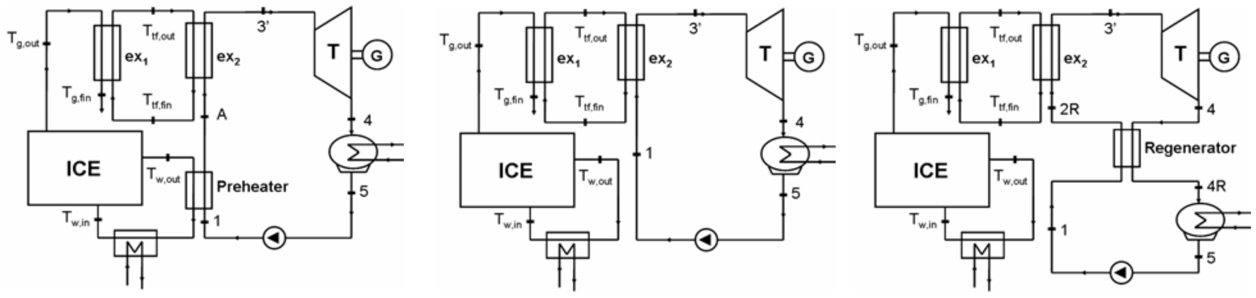

(a) (b) (c)

Fig. 5.2. Scheme of different ORC configurations assumed for ICE bottoming.

5.1.2 The ORC simple cycle

In Fig. 5.3 the heat exchange diagram in the evaporator is proposed for a generic ORC simple cycle with no superheating. Heat needed to vaporize the organic working fluid is provided in this case solely by the transfer fluid which is heated by engine exhaust gases (according to Fig. 5.2 (a)). The temperature of gases at engine exhaust ($T_{g,out}$) is defined and constant, as well as the flow rate ($\dot{m}_g$).

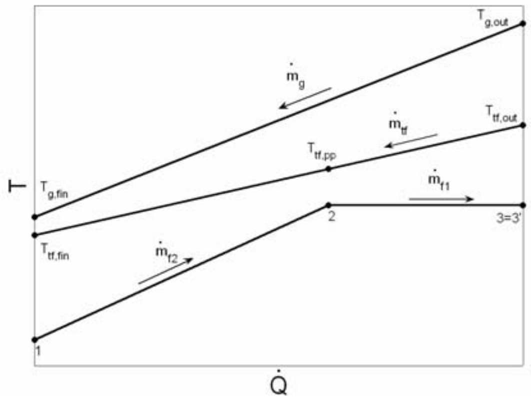

Fig. 5.3. *T*-$\dot{Q}$ diagram in the evaporator for a ORC heated with engine exhaust gases.

If a minimum temperature is defined for the transfer fluid ($T_{tf,min}$), the heat balance at the gas/thermal oil heat exchanger allows to determine the transfer fluid mass flow rate:

$$\dot{m}_{tf,1} = \frac{\dot{m}_g \bar{c}_{p,g} \left(T_{g,out} - T_{g,fin} \right)}{\bar{c}_{p,tf} \left(T_{tf,out} - T_{tf,fin} \right)} \tag{5.1}$$

where $T_{g,fin}=T_{tf,fin}+\Delta T_{app,ex1}$.

The heat balances between transfer fluid and organic fluid can then be evaluated.

A minimum temperature difference at pinch point ($\Delta T_{PP}= T_{tf,PP}-T_2$) to meet the oil/organic fluid heat exchanger performances is imposed and this allows writing a first energy balance referred to the heat required for the phase change of the organic fluid within the evaporator (transformation *2-3'* of Fig. 5.3):

$$\dot{m}_{f,1} = \frac{\dot{m}_{tf} \bar{c}_{p,tf} \left(T_{tf,out} - T_{tf,PP} \right)}{h_{3'} - h_2} \tag{5.2}$$

To be noted that in Eq. (5.2) the organic fluid enthalpies are function of the evaporating pressure chosen for the ORC.

A second energy balance allows to determine the transfer fluid temperature at the evaporator outlet:

$$T_{tf,fin} = T_{tf,PP} - \frac{\dot{m}_{f,1} \left(h_2 - h_1 \right)}{\dot{m}_{tf} \bar{c}_{p,tf}} \tag{5.3}$$

If $T_{tf,fin}$ calculated with Eq.(5.3) is lower than the minimum allowed temperature for the transfer fluid, a procedure decreases the organic fluid mass flow rate; $\dot{m}_{f,2}$ is the fluid mass flow rate that satisfies the imposed condition and represent the new fluid mass flow rate for the cycle. The actual gas pinch point temperature can then be calculated:

$$T_{tf,PP} = T_{tf,out} - \frac{\dot{m}_{f,2}\left(h_3 - h_2\right)}{\dot{m}_{tf}\bar{c}_{p,tf}} \tag{5.4}$$

and Eq. (5.2)÷(5.4) are repeated while $T_{tf,fin}$ is above $T_{tf,min}$.

All the organic fluids considered in the analysis have, especially at relatively high pressures, a specific heat of vaporization that is lower compared to the specific heat required to warm up the fluid between point 1 and 2 therefore $T_{tf,fin}$ calculated with Eq. (5.2) is always smaller than $T_{tf,min,}$. This means that there are not Pinch Point limitations in the heat exchange process and what limits the amount of heat to be introduced to the cycle is the need to avoid overcooling of the transfer fluid employed.

The global efficiency of the system can be defined as the net power produced by the cycle referred to the total available heat [14]:

$$\eta_g = \frac{P_{ORC}}{\dot{Q}_a} = \Phi \cdot \eta_{ORC} \tag{5.5}$$

where Φ is the heat availability:

$$\Phi = \frac{T_{g,out} - T_{g,fin}}{T_{g,out} - T_1} \tag{5.6}$$

Not always the maximum global efficiency is achieved with maximum cycle efficiency. It might happen that with increasing turbine inlet pressure the cycle efficiency increases but the final gas temperature is also increased, thus determining a decrease in the heat availability. Combination of these two terms might provide that the turbine inlet pressure that maximizes η_{ORC} is not the one that maximizes η_g [14,15]. The analysis that follows therefore is due to determining the optimal pressure at turbine inlet that maximizes η_g and that, in turns, provides the maximum ORC power at a given value of $\dot{Q}_a$.

5.1.2.1 The optimal pressure of vaporization

In this section some preliminary evaluations are reported in order to assess the preferable turbine inlet pressure that should be considered for the cycles based on the three fluids under study.

In Fig. 5.4 the cycle efficiency is plotted for the reference fluids in the range of turbine inlet pressures between p_{cond} and p_{crit} (where p_{crit} is the critical pressure of the fluid). As expected benzene displays the highest achievable efficiency. The curves are monotonical for all fluids (solid lines): this is a consequence of the hypothesis of introducing a little degree of superheating when the isentropic expansion is not completely dry. For higher pressures the superheating introduced becomes more significant and this slightly increases the cycle efficiency. The corresponding dotted curves are plotted for the saturated Rankine cycle (with no superheating) and in this case the curves show a maximum for pressures not far from the critical: particularly a maximum value of η_T=0.247 is achieved by benzene at a pressure of 4470kPa.

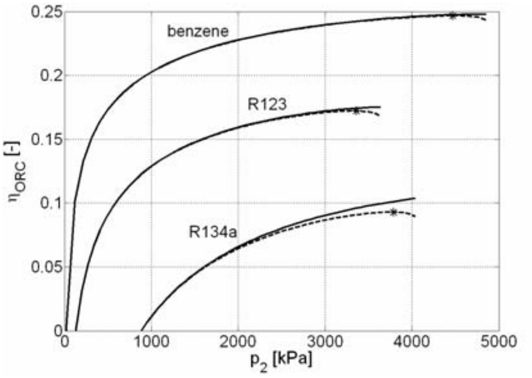

Fig. 5.4. Simple cycle efficiencies for evaporation pressures between p_{cond} and p_{crit}.

The curves in Fig. 5.5 refer to the net power ($P_{ORC}=\dot{m}_f\left(h_{3'}-h_4\right)$, see Fig. 5.2) achievable from the cycles at different pressures of vaporization. The curves again are monotonical as a consequence of pattern of the efficiency curves. In the analysis it will be chosen a optimal value of p_2 as the one that maximizes the efficiency curves referred to saturated Rankine cycles (dotted lines of Fig. 5.4) and the optimal condition is indicated by the symbol * in the figures reported in this section. Therefore the optimum pressure is chosen to be 4470kPa for benzene which gives a net power output of 327kW, 3303kPa for R123 with 231kW, and 3723kPa for R134a with 133kW.

In Fig. 5.6 the cycle power output is plotted in non-dimensional form in the assumed range of pressure with reference to the cycle power output determined at the optimal pressure for each fluid (* of Fig. 5.4). It is possible to note that not only benzene is the fluid that displays the highest value of power output in the range of accepted pressure but also it shows small variations with respect to optimal power over a wide range of pressures. For example at pressures of 1700kPa a Rankine cycle based on benzene still provides about 90% of the optimal power output. This characteristic would allow considering cycles with lower pressure ratios between condenser and evaporator simplifying the compression and expansion phases and still providing good performances from the point of view of the total power provided.

Fluids with bell shaped vapour lines display instead higher variability in the power output with respect to vaporization pressure and a small decrease from the optimal pressure causes a significant reduction in the cycle power output especially for R134a. This means that the Rankine cycles for these fluids must be operated at a pressure as close as possible to the critical pressure.

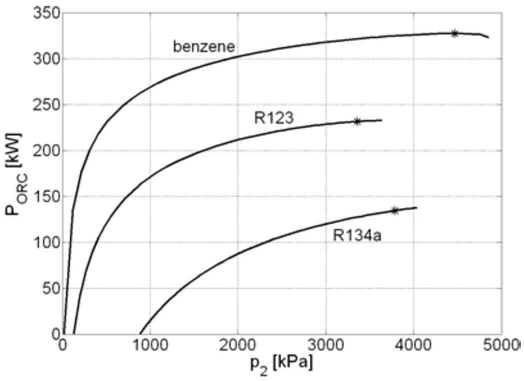

Fig. 5.5. Simple cycle power output at different evaporation pressures.

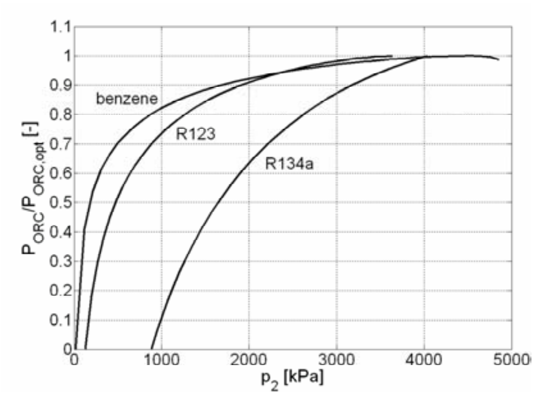

Fig. 5.6. Variation of net cycle power output for simple Rankine cycles at different evaporation pressures.

In Fig. 5.7 the estimated value of working fluid mass flow rate is plotted again with respect to the pressure at turbine inlet. It is possible to observe that benzene requires the lowest fluid mass flow rate as consequence of the highest enthalpy increase between state *3'* and *1* in steady state operation (Tab. 5.2). The energy balance at the evaporator determines higher masses of fluid for R123 and R134a in order to match the total energy of the transfer fluid.

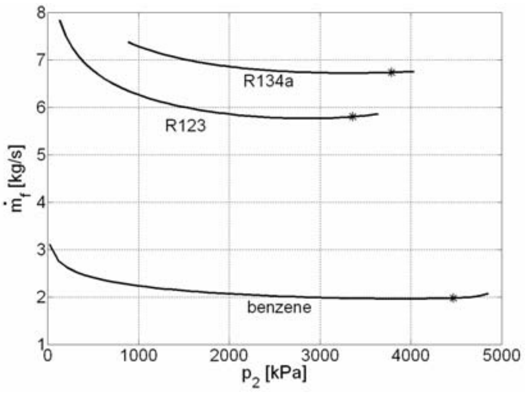

Fig. 5.7. Simple cycle working fluid mass flow rate required at different evaporation pressures.

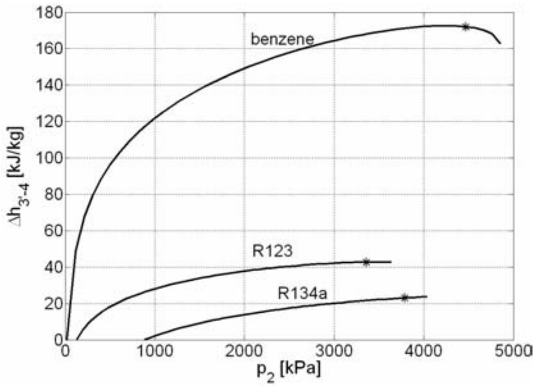

Fig. 5.8. Simple cycle turbine enthalpy drop at different evaporation pressures.

In Fig. 5.8 the enthalpy drop through the turbine ($\Delta h_{3'-4}$) is displayed for the different fluids. A relatively small enthalpy drop for R123 and R134a per unit mass requires relatively high fluid mass flow rates in order to achieve reasonable power at the turbine output, as displayed in Fig. 5.7. Benzene on the other hand shows quite high values of the enthalpy drop over a wide range of evaporating pressures. As a consequence it is reasonable to use a multiple stages turbine while a single stage turbine can be considered for wet fluids. This is further supported by the analysis of Fig. 5.9 where, for each fluid, curves referring to actual volumetric flow rate at the expander inlet ($\dot{V}_3$) and the turbine outlet/inlet volume flow ratio (v_4/v_3) are reported. The ratio v_4/v_3 indicates the increase in fluid volume through the expansion and consequently how much the outlet section of the expander must be wider than the inlet.

From Fig. 5.9 (a) (that refers to benzene) it is possible to note that high turbine outlet/inlet volume flow ratio are reached when the evaporation pressure is chosen to provide maximum power. In these conditions v_4/v_3 =374 and the volume flow rate $\dot{V}_3$ =0.015m^3/s. The turbine outlet/inlet volume flow ratio could be too high for a single stage solution and a more complicated expander would be required, regardless if dynamic or volumetric.

Considerations regarding the power output for benzene (Fig. 5.5 and Fig. 5.6) however suggest that a lower evaporating pressure would allow lower turbine outlet/inlet volume flow ratios still providing net power outputs close to the maximum. Therefore if a lower pressure is chosen probably a simpler expander could be employed. As a reference for this analysis a new optimal value of turbine inlet pressure for benzene is chosen at about 2000kPa (this new condition is indicated by the symbol ■ in Fig. 5.9 (a), even if further and more precise considerations would require the matching with an actual commercial expander. For this value of evaporating pressure the net power output from the cycle becomes 302kW, the ratio v_4/v_3 decreases to 103 and the volumetric flow rate at the expander inlet increases to 0.04 m^3/s (Tab. 5.2).

On the other hand R123 and R134 allow for a lower turbine outlet/inlet volume flow ratio even at the optimal evaporating pressure. A simple single stage expander can be used with these fluids.

As observed the parameter v_4/v_3 changes significantly depending on the working fluid used for the cycle. Some fluids can achieve values up to 550 and usually, when v_4/v_3 is smaller than 50, expansion efficiencies higher than 0.8 can be achieved via a single stage axial turbine [15]. Therefore, according to Fig. 5.9, it can be assumed that cycles based on R123 and R134a can be based on relatively simple expanders with good expansion efficiencies.

Main parameters of the thermodynamic cycles based on the three fluids are reported in Tab. 5.2 where the values for benzene are evaluated at the pressure of 2000kPa. Among the fluids it can be observed that benzene allows for higher efficiencies in converting into work the thermal energy available from the heat source, followed by R123 and R134a. This result is consistent with what found in [7]

	P_{ORC} [kW]	η_{ORC} [-]	$\dot{Q}_{in}'$ [kW]	p_{cond} [kPa]	p_{vap} [kPa]	T_{vap} [K]	$\dot{m}_f$ [kg/s]	$\dot{V}_3$ [m^3/s]	v_4/v_3 [-]	$\Delta h_{3'-4}$ [kJ/kg]	Δh_{0-1} [kJ/kg]
benzene	302.1	0.227	1327	19.6	2000	494.5	2.065	0.039	103	149.2	2.9
R123	231.0	0.174	1327	129.8	3303.1	450.4	5.790	0.021	37	42.6	2.8
R134a	133.5	0.101	1327	883.3	3723.4	369.9	6.729	0.032	5	22.9	3.0

Tab. 5.2.Comparison of ORC cycles for benzene, R123 and R134a. Simple cycle.

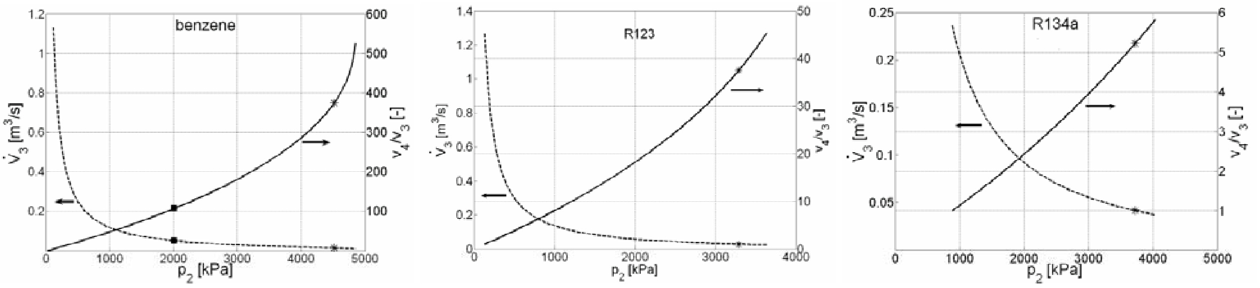

(a) (b) (c)

Fig. 5.9. Volume flow rate at turbine inlet ($\dot{V}_3$) and turbine outlet/inlet volume flow ratio (v_4/v_3) for different fluids at different evaporation pressures.

5.1.2.2 Irreversibility analysis of the cycles

The graphs plotted in Fig. 5.10 show the thermodynamic cycle on the *T-s* diagram for the three organic fluids. The curve referring to the engine exhaust gases is superimposed on the diagrams by properly scaling the specific entropy axes. It is possible to notice that, as expected, the average temperature difference between the gases and the organic fluid is much bigger the lower the critical temperature of the fluid. This temperature difference induces irreversibilities that lead to low thermodynamic efficiencies for R123 and R134a.

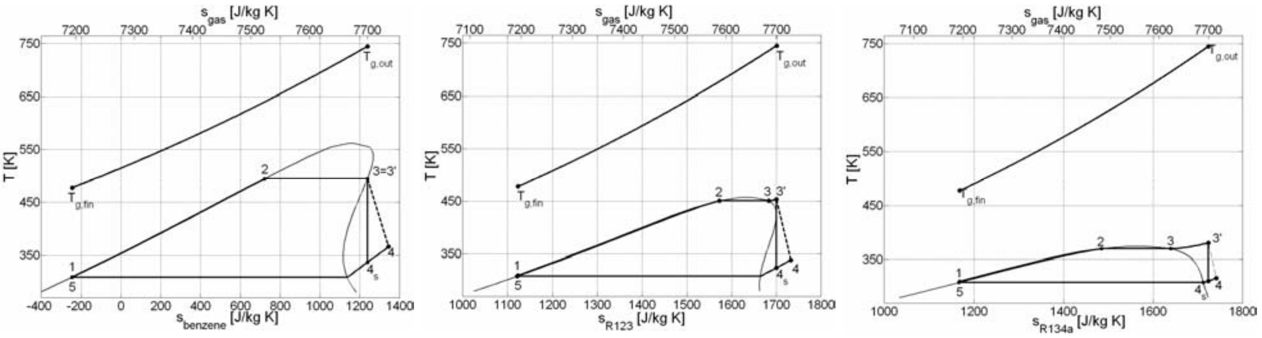

(a) (b) (c)

Fig. 5.10. Optimal organic cycles and engine exhaust gases cooling curve plotted on two superimposed *T-s* diagrams.

An appropriate exergy analysis of the cycles gives a better understanding of the irreversible processes that occur in the cycles. The exergy in fact takes account of the possibility of converting thermal energy it into mechanical energy. In order to evaluate the mechanical energy that can be extracted from a flow at a certain temperature a dead temperature should be defined, which is the temperature of a reservoir where a Carnot cycle can reject heat. For this reason exergy is a pseudo-property as it is not defined solely by the state of the system but also by the dead state that is used [16]. In the following analysis the dead state temperature is assumed to be 298K.

Different exergy efficiency definitions are possible if one selects different system boundaries. Clearly defining the system boundary allows the efficiency to be defined unambiguously. In this case the system is defined by the components that constitute the ORC setup including the heat exchangers necessary for the external heat to be fed to the cycle. The system experiences two inlet streams of energy, i.e. the hot gases and the engine cooling water, and four outlet streams of energy leaving, i.e. the power delivered by the turbine to a user, the heat released to a cold source by the condenser, and the thermal energy still contained in the hot gases and in the engine cooling water.

The total exergy flow of the hot gasses entering the system is:

$$\dot{B}_g = \left[\left(h_{g,out} - h_{g,dead}\right) - T_{dead} \cdot \left(s_{g,out} - s_{g,dead}\right)\right] \cdot \dot{m}_g \qquad (5.7)$$

The exergy flow of the engine coolant can be computed as follow, in the case the water cannot be cooled to the dead state temperature:

$$\dot{B}_w = \left[\left(h_{w,out} - h_{w,in} \right) - T_{dead} \cdot \left(s_{w,out} - s_{w,in} \right) \right] \cdot \dot{m}_w \tag{5.8}$$

The total available exergy flow into the power cycle is then:

$$\dot{B}_a = \dot{B}_g + \dot{B}_w \tag{5.9}$$

Only a fraction of $\dot{B}_a$ will be actually converted into useful work. The amount of exergy wasted from the thermal system can be accounted for as irreversibility of different nature:

- Relative exergy losses due to heat exchange between hot gases and diathermic oil:

$$\Psi_1' = \frac{\left(\dot{B}_g - \dot{B}_{g,fin} \right) - \left(\dot{B}_{tf,out} - \dot{B}_{tf,fin} \right)}{\dot{B}_a} \tag{5.10}$$

where:

$$\left(\dot{B}_g - \dot{B}_{g,fin} \right) = \left[\left(h_{g,out} - h_{g,fin} \right) - T_{dead} \cdot \left(s_{g,out} - s_{g,fin} \right) \right] \cdot \dot{m}_g \tag{5.11}$$

and:

$$\left(\dot{B}_{tf,out} - \dot{B}_{tf,fin} \right) = \left[\left(h_{tf,out} - h_{tf,fin} \right) - T_{dead} \cdot \left(s_{tf,out} - s_{tf,fin} \right) \right] \cdot \dot{m}_{tf} \tag{5.12}$$

- Relative exergy losses due to heat exchange between diathermic oil and organic fluid:

$$\Psi_1 = \frac{\left(\dot{B}_{tf,out} - \dot{B}_{tf,fin} \right) - \left(\dot{B}_{f,3'} - \dot{B}_{f,1} \right)}{\dot{B}_a} \tag{5.13}$$

where:

$$\left(\dot{B}_{f,3'} - \dot{B}_{f,1} \right) = \left[\left(h_{f,3'} - h_{f,1} \right) - T_{dead} \cdot \left(s_{f,3'} - s_{f,1} \right) \right] \cdot \dot{m}_f \tag{5.14}$$

- Relative exergy losses for hot gases downloaded at exchanger 1 exit:

$$\Psi_2 = \frac{\dot{B}_{g,fin}}{\dot{B}_a} \tag{5.15}$$

- If the engine jacket cooling water is not utilised in the power cycle the corresponding exergy loss can be defined as:

$$\Psi_3 = \frac{\dot{B}_w}{\dot{B}_a} \tag{5.16}$$

- If an heat exchanger is introduced to internally regenerate the cycle, exergy loss due to irreversibility in the heat exchange process, with reference to Fig. 5.2c, will be:

$$\Psi_4 = \frac{\left(b_{4-4R} - b_{2R-1}\right) \cdot \dot{m}_f}{\dot{B}_a} \tag{5.17}$$

where $b_{4\text{-}4R}$ is the available specific exergy of the superheated vapour and $b_{2R\text{-}1}$ is the actual specific exergy increase of the liquid in the regenerator, i.e.:

$$b_{4-4R} = h_4 - h_{4R} - T_{dead}\left(s_4 - s_{4R}\right) \tag{5.18}$$

$$b_{2R-1} = h_{2R} - h_1 - T_{dead}\left(s_{2R} - s_1\right) \tag{5.19}$$

Indeed, if an ideal heat exchanger with an ideal fluid is considered, then $T_4 = T_{2R}$ and $T_{4R} = T_1$ and therefore the irreversibility in the internal heat exchange process would be nought and $\Psi_4 = 0$.

- Relative exergy losses due to non-isentropic vapour expansion:

$$\Psi_5 = \frac{\left(b_{3'} - b_4\right) \cdot \dot{m}_f - \left(h_{3'} - h_4\right) \cdot \dot{m}_f}{\dot{B}_a} = \frac{\left[T_{dead} \cdot \left(s_{f,4} - s_{f,3'}\right)\right] \cdot \dot{m}_f}{\dot{B}_a} \tag{5.20}$$

- Relative exergy losses due to irreversibilities in the heat exchange process at the condenser; this term would be nought if temperature of condensation were equal to the dead state temperature:

$$\Psi_6 = \frac{\dot{B}_{f,4} - \dot{B}_{f,5}}{\dot{B}_a} \tag{5.21}$$

where:

$$\left(\dot{B}_{f,4} - \dot{B}_{f,5}\right) = \left[\left(h_{f,4} - h_{f,5}\right) - T_{dead} \cdot \left(s_{f,4} - s_{f,5}\right)\right] \cdot \dot{m}_f \tag{5.22}$$

In the analysis the exergy losses due to non-isentropic liquid compression have been neglected as they are usually small compared to the other causes of irreversibility.

The second-law efficiency of the power cycle, also referred to as exergy efficiency, can be defined as follows:

$$\eta_b = \frac{w_{net,out}}{b_a} = 1 - \frac{b_{destr}}{b_a} \tag{5.23}$$

where b_a is the specific exergy input to the cycle and b_{destr} is the specific total exergy destruction in the cycle [17].

Referring to fluxes instead that specific energy or exergy, the exergy efficiency can be computed as:

$$\eta_b = \frac{\left(h_{3'} - h_4\right) \cdot \dot{m}_f}{\dot{B}_a} = 1 - \sum \Psi_i \tag{5.24}$$

From the previous it follows that:

$$P_{ORC} = \eta_b \cdot \dot{B}_a \tag{5.25}$$

The exergy losses have been calculated for the three cycles plotted in Fig. 5.10, and Tab. 5.3 has been compiled accordingly. Fig. 5.11 shows the exergy losses (and the exergy efficiency, calculated according to Eq.(5.24)) at varying evaporator inlet pressure.

	Ψ_1'	Ψ_1	Ψ_2	Ψ_3	Ψ_4	Ψ_5	Ψ_6
benzene	0.088	0.161	0.180	0.171	0	0.063	0.044
R123	0.088	0.242	0.180	0.171	0	0.054	0.040
R134a	0.088	0.355	0.180	0.171	0	0.035	0.038

Tab. 5.3. Relative exergy losses through the ORC cycles for benzene, R123 and R134a at the optimal evaporating pressure.

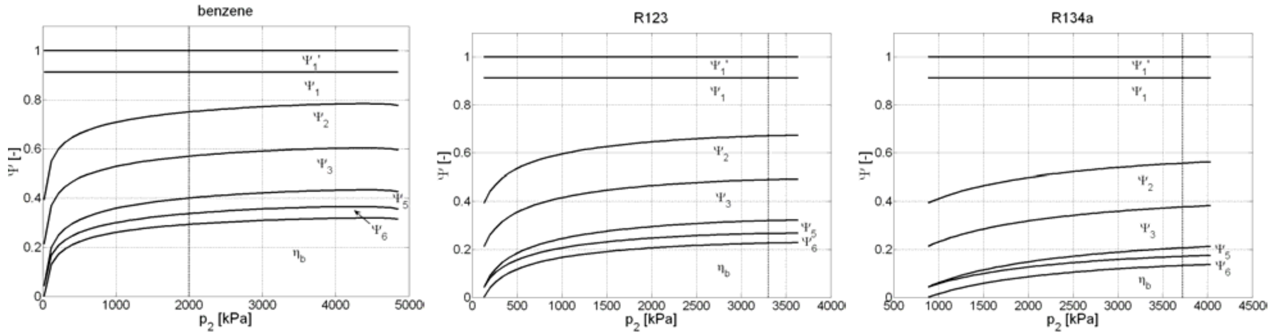

(a) (b) (c)

Fig. 5.11 . Pattern of cycle irreversibility and exergy efficiency at different evaporator inlet pressure for different fluids.

It should be first noted that Ψ_1' is the same for all fluids and does not vary with respect to p_2. This is because, as observed in Par 5.1.2.1, the transfer fluid outlet temperature is always $T_{ft,min}$ therefore the exhaust gases final temperature is always $T_{g,fin}=T_{tf,min}+\Delta T_{app,ex1}$ thus determining the same relative exergy losses due to the gases/oil heat exchange process.

The term Ψ_1 in Tab. 5.3 indicates that a large fraction of the total available exergy is lost in the heat exchange process between hot gases and the working fluid. The overall exergy losses due the heat transfer from the hot source (the exhaust gases) to the organic fluid can be evaluated as the sum of Ψ_1 and Ψ_1'. This fraction is obviously higher with decreasing critical temperature of the organic fluid. It should be noted that the amount of energy effectively transferred from the gasses to the organic fluid is the same in all cases as $T_{g,fin}$, $T_{g,in}$ and $\dot{m}_g$ are the same for all the cycles. This means, in other words, that in these cases the heat availability Φ of Eq.(5.6) does not change with turbine inlet pressure because in all cases it is possible to cool the gases at the heat exchanger outlet down to the minimum allowed temperature and η_g therefore follows the same pattern of η_{ORC} (as already observed from the analysis of Fig. 5.4 and Fig. 5.5). This means that despite the same amount of energy has been introduced in all the cycles, the energy transfer to the fluids has not been equally efficient due to the shape of the thermodynamic cycle, which is a consequence of the organic fluid properties (Fig. 5.10). Providing heat from a high temperature medium to a fluid that cannot achieve high temperatures does not allow to use a large fraction of the potential work. The exergy analysis therefore helps to quantify the irreversibility within power conversion systems and to highlight problems that a purely energetic analysis would not reveal.

From Fig. 5.11 it is possible to see how, obviously, the term $\Psi_1'+\Psi_1$ becomes bigger with decreasing evaporator pressure, as a consequence to the decreasing temperature difference between fluid and gas stream.

The term Ψ_2 is equal for all the fluids (Tab. 5.3) as in all cases gasses are cooled to the same final temperature; the exergy wasted for discharging hot gases to the environment is then the same. Also Ψ_3 is equal for all the cycles because in this case it has been assumed not to use jacket water to provide heat to the organic power cycle. Nevertheless it is possible to see that a certain amount of exergy would be available by exploiting also the jacket water: the theoretical work achievable from using the engine water cooling is about 17% of the total available exergy entering the system. Ψ_2 and Ψ_3 also do not vary with p_2 (Fig. 5.11) because the amount of available exergy wasted with hot gases and engine coolant does not depend on the evaporator inlet pressure.

The term Ψ_4 is zero because these cycles are not regenerated therefore no exergy losses can be accounted in the internal heat exchange process (Tab. 5.3). Ψ_4 therefore is not reported in Fig. 5.11.

Ψ_5 indicates how much potential work is wasted due to expansion irreversibility. This value is a consequence of assuming an adiabatic expansion efficiency of 0.8 in all cases. It is possible to notice that, at the same expansion efficiency, the exergy wasted is higher for benzene and R123 as a consequence of the high enthalpy drop in the turbine for benzene and the high fluid mass flow rate for R123. This suggest that higher expander efficiencies could provide considerable benefits when the overall enthalpy drop and mass flow rate through the turbine is considerable, or, equally, when the cycle power output is higher for the same thermal input. Ψ_5 is the only other term, along with Ψ_1 and Ψ_6 affected by the evaporator pressure (Fig. 5.11). It should be noted that the rate of change of Ψ_5 is opposite to that of Ψ_1, i.e. with decreasing inlet pressure the exergy losses due to non isentropic expansion decreases. However, the importance of Ψ_1 is much bigger and the optimal values of η_b can be found for highest values of p_2.

The term Ψ_6 is related to the exergy that is wasted due to the temperature difference between organic fluids during subcooling/condensation. The amount of theoretical work that could be extracted is negligible as a organic fluid and the dead state, despite the amount of energy discharged through the condenser is considerable.

In Tab. 5.4 the exergy efficiency and system power output are reported for the three ORCs under analysis. The values are also calculated with η_T=0.6 (η_b^* and P_{ORC}^*) and in case of ideal expansion (η_T=1, η_b^{**} and P_{ORC}^{**}). In the latest case the term Ψ_5 becomes equal to 0 and this produces an increase in the cycle exergy efficiency $(\eta_b^{**}-\eta_{(b)}/\ \eta_b$. As consequence to this, not being changed the heat provided to the cycles, the net power output increases accordingly. The biggest relative increase in the cycle performances, under the hypothesis of ideal expansion, is experienced by the R134a, with a net % increase in the exergy efficiency (and consequently of the cycle power output) of about 28%.

As observed a significant cause of exergy destruction is brought by the existence of the diathermic oil circuit. The diathermic oil has been considered in this analysis for safety reasons. Since some of the fluids considered are flammable it avoids the possibility for the hot exhaust gases to get in direct contact with them. The diathermic oil also bring stability to the whole system because its thermal inertia allows to overcome possible variations in the hot gases temperature or mass flow rate. It must however be considered that the diathermic oil circuit reduces the overall power production potential of the organic cycles.

Fig. 5.12 reports the cycle irreversibility under the hypothesis of vaporizing the organic fluids without the interposition of the transfer fluid circuit, and in Tab. 5.5 are reported the exergy losses of the different transformations calculated at the optimal pressures of vaporization. In this case hence the vaporization happens in a gas/organic fluid heat exchanger.

The terms Ψ_1 and Ψ_1', can no longer be defined. Ψ_1'' is introduced to consider the exergy losses due to heat exchange between hot gases and organic fluid:

$$\Psi_1'' = \frac{\left(\dot{B}_g - \dot{B}_{g,fin}\right) - \left(\dot{B}_{f,3'} - \dot{B}_{f,1}\right)}{\dot{B}_a} \tag{5.26}$$

	$\eta_T=0.8$		$\eta_T=0.6$			$\eta_T=1$		
	η_b	P_{ORC}	η_b^{*}	$(\eta_b^{*}-\eta_b)/\eta_b$	P_{ORC}^{*}	η_b^{**}	$(\eta_b^{**}-\eta_b)/\eta_b$	P_{ORC}^{**}
benzene	0.293	302.1	0.219	-0.253	225.1	0.367	0.253	379.1
R123	0.226	231.0	0.166	-0.265	169.1	0.286	0.265	292.7
R134a	0.133	133.5	0.095	-0.286	94.5	0.170	0.278	171.9

Tab. 5.4. Exergy efficiency and cycle power for different expander efficiencies.

	Ψ_1''	Ψ_2	Ψ_3	Ψ_4	Ψ_5	Ψ_6
benzene	0.250	0.057	0.171	0	0.082	0.057
R123	0.355	0.057	0.171	0	0.070	0.052
R134a	0.503	0.057	0.171	0	0.046	0.049

Tab. 5.5. Relative exergy losses through the ORC cycles for benzene, R123 and R134a with direct gas/organic fluid heat exchange.

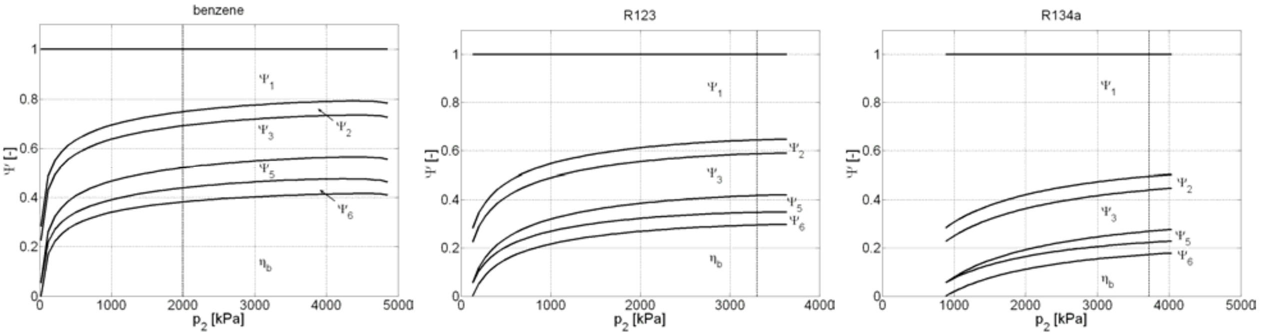

(a) (b) (c)

Fig. 5.12. Pattern of cycle irreversibility and exergy efficiency at different evaporator inlet pressure for different fluids. Case with direct gas/organic fluid heat exchange.

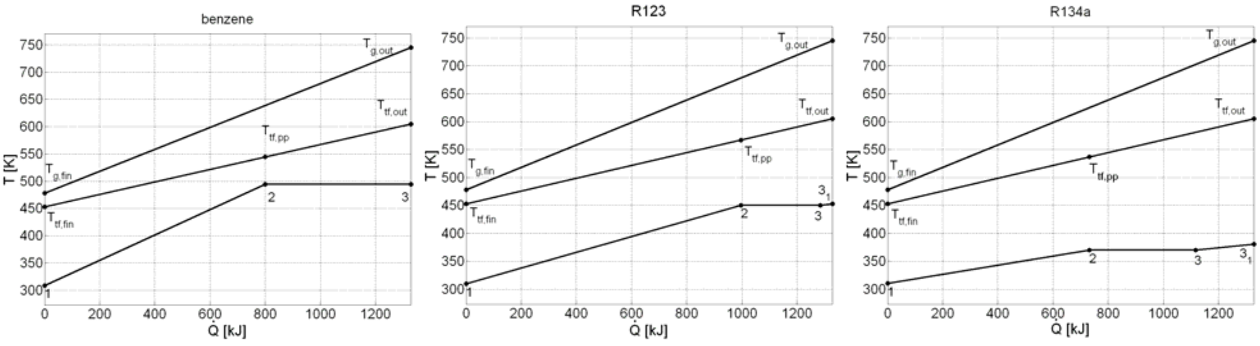

(a) (b) (c)

Fig. 5.13. *T*-$\dot{Q}$ diagrams for benzene, R123 and R134a.

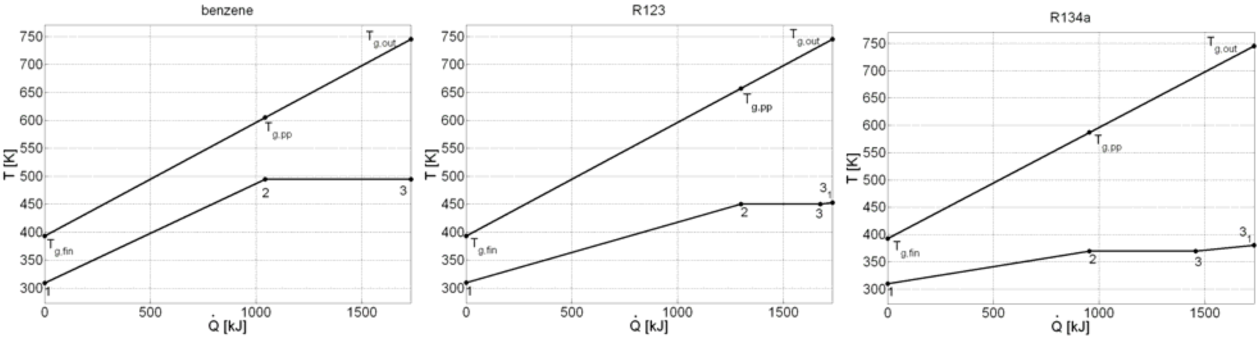

(a) (b) (c)

Fig. 5.14. *T*-$\dot{Q}$ diagrams for benzene, R123 and R134a. Case with direct gas/organic fluid heat exchange.

By Comparing Tab. 5.3 to Tab. 5.5 it is possible to observe that the exergy destruction due to irreversibility in the heat transfer from the hot thermal source to the organic fluid is not changed significantly and $\Psi_1''\sim\Psi_1'+\Psi_1$. The term that experiences the most significant change in the hypothesis of not recurring to an intermediary heat transfer medium is Ψ_2, which measures how much theoretical work is not produced due to the thermal content still available in the exhaust gases.

While the heat content in the gases leaving exchanger 1 of Fig. 5.2 (a) is quite elevate when the diathermic oil circuit is considered ($T_{g,fin}$ is limited by $T_{tf,fin}$), when direct gas/organic fluid heat exchange is considered the hot gases can be cooled to a lower temperature (eventually to the minimum allowed temperature $T_{g,min}$) and hence the reduction in Ψ_2.

The difference of the two cycle configurations can be also appreciated from the data of Tab. 5.6 which report the main figures of the cycle without the diathermic oil circuit. While many parameters have not changed from those reported in Tab. 5.2 (including η_{ORC}, as the same optimal pressures of vaporization have been considered), the actual power of the cycles has increased sensibly; the benzene based cycle now rates 394kW with a net increase in the power output of about 13%, even though the highest relative power increase is experienced by R123 and R134a ($(P_{ORC,d}- P_{ORC})/P_{ORC} \sim 23\%$).

The increased power is a consequence of the increased heat introduced into the cycles ($\dot{Q}_{in,d}$) caused by the lower temperature at which the gases are discharged ($T_{g,fin}$); the actual change in these two parameters can be appreciated comparing the *T*-$\dot{Q}$ diagrams of Fig. 5.13 and Fig. 5.14.

	$P_{ORC,d}$ [kW]	$\eta_{ORC,d}$ [-]	$\dot{Q}_{in,d}$ [kW]	p_{cond} [kPa]	p_{vap} [kPa]	T_{vap} [K]	$\dot{m}_{f,d}$ [kg/s]	$\dot{V}_3$ [m^3/s]	v_4/v_3 [-]	$\Delta h_{3'-4}$ [kJ/kg]	$\frac{P_{ORC,d}-P_{ORC}}{P_{ORC}}$ [-]
benzene	394.1	0.227	1731	19.6	2000	494.5	2.694	0.052	103	149.2	0.135
R123	301.4	0.174	1731	129.8	3303.1	450.4	7.554	0.028	37	42.6	0.234
R134a	174.1	0.101	1731	883.3	3723.4	369.9	8.779	0.042	5	22.9	0.233

Tab. 5.6. Comparison of ORC cycles for benzene, R123 and R134a. Case with direct gas/organic fluid heat exchange

5.1.3 The ORC simple cycle with use of heat available from engine jacket water

A further comparison of the selected cycles has been conducted under the hypothesis of employing the engine jacket cooling water to partially preheat the fluids in the organic cycles. As seen the energy and exergy content of the water out of a typical gas fired engine for stationary applications is not negligible. The available energy flux ($\dot{Q}_w$) is about 1000kW$_t$ for the engine considered, when cooling the water from the 90°C to 80°C (while the available energy in the exhaust gases $\dot{Q}_g$ is about 1700kW$_t$) and the exergy content is about 17% of the total available exergy $\dot{B}_a$, accounting for about 176kW. Therefore the amount of extra power that could be obtained by partially utilizing the heat from water cooling has been analyzed. Conservatively an heat exchanger not too performing has been considered in the water/fluid heat exchange process, with a temperature difference of 20K between water inlet and organic fluid outlet; it should be noted that both fluids are in liquid phase in this case.

In the analysis the same thermodynamic cycles defined in the previous section have been considered with a new heat source to partially power the cycles. A parametric analysis at varying turbine inlet pressure in fact shows that the maximum ORC power output can be achieved for the same pressure at evaporator assumed without water preheating. For this reason, and to compare easily the two plant configurations, the same cycle parameters considered in Par. 5.1.1 are assumed. The cycle efficiency therefore is not changed as well as the main cycle nodes reported in Fig. 5.10.

The heat balance at the water/fluid heat exchanger provides a first value of the organic fluid mass flow rate needed to fully exploit the available energy in the cooling water is therefore:

$$\dot{m}_{f,1} = \frac{\dot{m}_w \overline{c}_{p,w}\left(T_{w,out} - T_{w,in}\right)}{h_A - h_1} \tag{5.27}$$

Another expression of the energy conservation equation should be written to match the available energy from the transfer fluid and the energy required to vaporize completely the fluid and superheat it (if considered):

$$\dot{m}_{f,2} = \frac{\dot{m}_{tf} \overline{c}_{p,tf}\left(T_{tf,out} - T_{tf,PP}\right)}{h_{3'} - h_2} \tag{5.28}$$

For the considered cycles $\dot{m}_{f,1}$ always appears to be greater than $\dot{m}_{f,2}$; this condition actually poses the impossibility to fully exploit the available energy from the cooling water for the considered cycles.

The energy conservation equations allows to define the final temperature of the transfer fluid leaving exchanger 1 of Fig. 5.2b. If $\dot{m}_{f,3} = \min\left(\dot{m}_{f,1}, \dot{m}_{f,2}\right)$ it gives:

$$T_{tf,fin} = T_{tf,PP} - \frac{\dot{m}_{f,3}\left(h_2 - h_A\right)}{\dot{m}_{tf}\overline{c}_{p,tf}} \tag{5.29}$$

Again, whenever $T_{tf,fin}$ is less than the minimum allowed temperature for the oil circuit, the procedure implemented decreases the fluid mass flow rate in order to mach the condition $T_{tf,fin} \geq T_{tf,min}$.

Fig. 5.15 shows the T-$\dot{Q}$ diagrams for the three cycles considered. The heat flow entering the cycle ($\dot{Q}_{in}$') is represented by the sum of the heat flow from the transfer fluid ($\dot{Q}_{tf}$) and the amount of heat extracted from the cooling water effectively used to preheat the working fluid ($\Delta\dot{H}_{1-A}$).

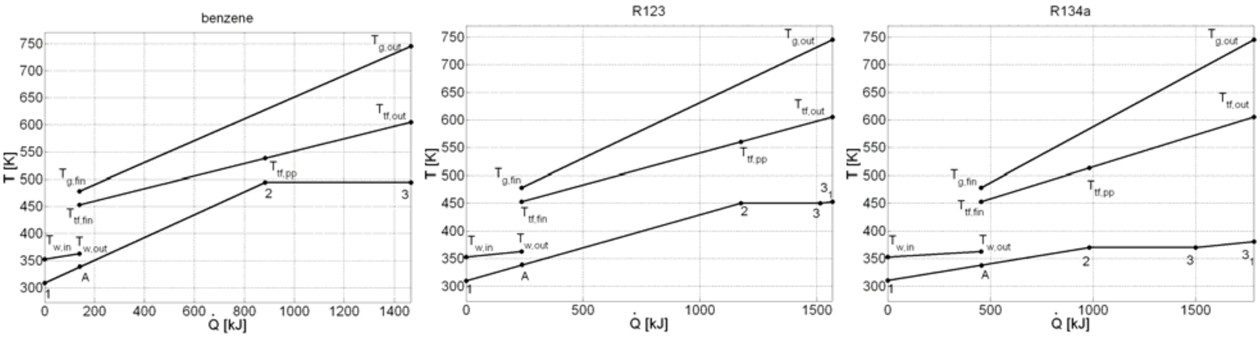

(a) (b) (c)

Fig. 5.15. *T*-$\dot{Q}$ diagrams for benzene, R123 and R134a with preheating using engine refrigerant.

From Tab. 5.7 it is possible to see that the heat introduced into the three cycles is different in this case ($\dot{Q}_{in}$') and increases with decreasing working fluid critical point. R134a for example displays the smallest specific enthalpy increase $\Delta h_{3'\text{-}A}$ from the maximum temperature allowed at the exit of preheater (point *(A)* to the end of evaporation or superheating (point *3'*). Since the value of the fluid mass flow rate through the organic cycle is usually limited by the heat that can be transferred from the thermal fluid, a low value of $\Delta h_{3'\text{-}A}$ determines a higher organic fluid flow rate which, in turn, allows to achieve a higher amount of useful heat from the water. It can be observed from Tab. 5.7 that for R134a the heat introduced into the cycle from the refrigerant is about 25% of the total heat to the cycle ($\Delta\dot{H}_{1-A}/\dot{Q}_{in}$') and the 43% of the total heat contained in the cooling water is effectively used ($\Delta\dot{H}_{1-A}/\dot{Q}_{w}$). The same parameters assume smaller values for R123 (15% and 23%) and benzene (9% and 13%). The increased heat into the cycle, not being changed the cycle net efficiency, determines an increase in the net power delivered by the cycle with respect to the previous case when no preheating was assumed (P_{ORC}'- P_{ORC})/$P_{OR(C)}$. It can be observed from Tab. 5.7 that R134a gives a net increase in the power output of 34% while for a cycle with benzene the increase is only about 10%. R123 displays intermediate characteristics and its relative power increase is 18%. The different amount of heat introduced into the cycle from the cooling water can be graphically observed from Fig. 5.15.

	P_{ORC}' [kW]	$\dot{Q}_{in}'$ [kW]	$\Delta\dot{H}_{1-A}/\dot{Q}_{in}'$ [-]	$\Delta\dot{H}_{1-A}/\dot{Q}_{w}$ [-]	$\dot{m}_f'$ [kg/s]	$\dot{V}_3'$ [m^3/s]	$\frac{P_{ORC}'-P_{ORC}}{P_{ORC}}$ [-]
benzene	333.8	1466	0.095	0.132	2.918	0.044	0.105
R123	272.4	1565	0.152	0.226	6.828	0.025	0.179
R134a	179.3	1782	0.255	0.433	9.037	0.044	0.343

Tab. 5.7. Comparison of ORC cycles for benzene, R123 and R134a with preheating using engine refrigerant.

The new system layout therefore introduces less advantages for cycles designed to utilize fluids with high critical temperatures. Fluid with low critical temperatures and bell shaped vapour lines can significantly increase their capability to produce useful work, but the net power output still remains lower than that achievable by fluids like benzene even with no use of heat from water cooling.

This is confirmed by the exergy analysis. In this case the term Ψ_1' is given by:

$$\Psi_1' = \frac{\left(\dot{B}_{tf} - \dot{B}_{tf,fin}\right) - \left(\dot{B}_{f,3'} - \dot{B}_{f,A}\right)}{\dot{B}_a} \tag{5.30}$$

as the hot gasses are used to evaporate fluid that has already been heated to point A.

Referring to the term Ψ_3 (exergy losses related to the organic fluid preheat with the engine refrigerant), these are both because of irreversibilities in the heat exchanger (Ψ_3') and because of the amount $\dot{m}_w^*$ of refrigerant not used to power the cycle (Ψ_3''):

$$\Psi_3 = \Psi_3' + \Psi_3'' \tag{5.31}$$

where:

$$\Psi_3' = \frac{\left[\left(h_{f,A} - h_{f,1}\right) - T_{dead}\cdot\left(s_{f,A} - s_{f,1}\right)\right]\cdot \dot{m}_f}{\dot{B}_a} \tag{5.32}$$

and:

$$\Psi_3'' = \frac{\dot{m}_w^* \cdot b_w}{\dot{B}_a} \tag{5.33}$$

	Ψ_1'	Ψ_1	Ψ_2	Ψ_3	Ψ_4	Ψ_5	Ψ_6
benzene	0.088	0.131	0.180	0.159	0	0.069	0.048
R123	0.088	0.204	0.180	0.152	0	0.063	0.047
R134a	0.088	0.323	0.180	0.135	0	0.047	0.051

Tab. 5.8. Relative exergy losses through the ORC cycles for benzene, R123 and R134a with preheating using engine refrigerant.

Comparing Tab. 5.8 to Tab. 5.3 and Fig. 5.17 to Fig. 5.11 it is possible to see that exergy losses are reduced in the oil/fluid heat exchange processes when engine coolant is used: Ψ_1 is smaller because with the preheating the organic fluid heated from the hot gasses is on average at higher temperature. Also Ψ_3 is smaller in this case because part of the exergy of the cooling water is effectively transferred to the working fluid; it can be observed that the reduction in Ψ_3 is, as expected, more significant for R134a. As a consequence of the increased fluid mass flow rate the terms Ψ_5 and Ψ_6 appear increased accordingly, that is the exergy losses due to non isentropic expansion and to heat released at the condenser are higher, especially for R123 and R134a. The net effect is however an increase in the exergy efficiency η_b, that is equal to 0.323, 0.266 and 0.175 for benzene, R123 and R134a respectively at the nominal evaporating pressure.

It is possible to evaluate also in this case the actual improvement that would be achieved if the diathermic oil circuit were not employed thus vaporizing the organic fluids via a direct heat exchange with the engine exhaust gases. Again it is considered the possibility to cool the gases down to the minimum allowed temperature and this causes a significant increase in the heat availability to the cycle hence a significant increase in the overall power output.

Main figures of the new system configurations are reported in Tab. 5.9 while the T- $\dot{Q}$ diagrams are in Fig. 5.16.

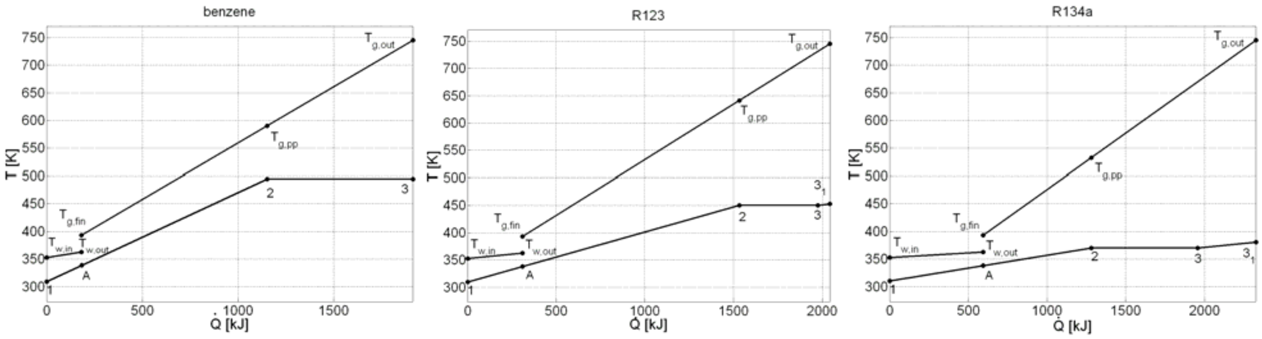

(a) (b) (c)

Fig. 5.16. T-$\dot{Q}$ diagrams for benzene, R123 and R134a with direct gas/organic fluid heat exchange.

From Tab. 5.9 a significant increase in the power generated with direct use of the engine exhaust gases ($P_{ORC,d}'$) with respect to the case when a thermal fluid is considered as medium for the heat transfer (P_{ORC}') can be observed. Particularly the relative power increase $(P_{ORC,d}'-P_{ORC}')/P_{ORC}'$ is 28% for benzene and 30% for R123 and R134a.

This significant increase in the power generated, not being changed the cycle efficiency, is caused not only by the increased heat from the gases, but also by the increased amount of heat from the engine refrigerant that can be recovered (the difference between the two cycle configurations and for each of the fluids is appreciable comparing Fig. 5.16 to Fig. 5.17). The rate of heat actually introduced in to the cycle in the preheating process with respect to the total heat available in the refrigerant ($\Delta\dot{H}_{(1-A),d} / \dot{Q}_{w,d}$) ranges from 17% for benzene to 56% for R134a. This increase is a consequence of the increased mass flow rate of fluid in the cycles ($\dot{m}_{f,d}$'). Again the fluid with lower critical temperature is capable of using a higher fraction of the heat of the engine refrigerant which is available at lower temperature.

In Tab. 5.9 the relative exergy losses are reported for the case under analysis, while the exergy efficiency is, 0.422, 0.347 and 0.228 for benzene, R123 and R134a respectively

	Ψ_1''	Ψ_2	Ψ_3	Ψ_4	Ψ_5	Ψ_6
benzene	0.211	0.057	0.156	0	0.091	0.063
R123	0.306	0.057	0.146	0	0.083	0.061
R134a	0.461	0.057	0.125	0	0.062	0.067

Tab. 5.9. Relative exergy losses through the ORC cycles for benzene, R123 and R134a with direct gas/organic fluid heat exchange.

	$P_{ORC,d}'$ [kW]	$\dot{Q}_{in,d}'$ [kW]	$\Delta\dot{H}_{(1-A),d}/\dot{Q}_{in,d}'$ [-]	$\Delta\dot{H}_{(1-A),d}/\dot{Q}_{w,d}$ [-]	$\dot{m}_{f,d}'$ [kg/s]	$\dot{V}_{3,d}'$ [m^3/s]	$\frac{P_{ORC,d}'-P_{ORC}'}{P_{ORC}'}$ [-]
benzene	435.5	1912	0.095	0.173	2.977	0.057	0.285
R123	355.4	2041	0.152	0.296	8.908	0.033	0.305
R134a	233.9	2325	0.255	0.565	11.790	0.057	0.304

Tab. 5.10. Comparison of ORC cycles for benzene, R123 and R134a with preheating using engine refrigerant with direct gas/organic fluid heat exchange.

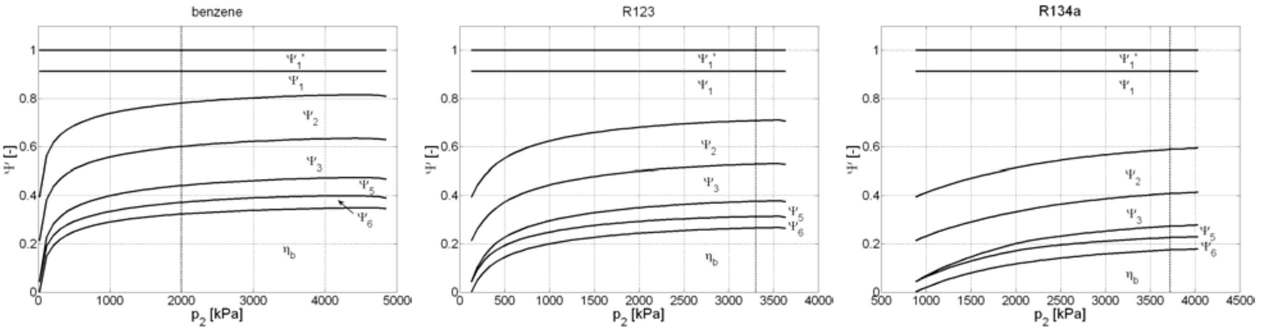

(a) (b) (c)

Fig. 5.17. Pattern of cycle irreversibility and exergy efficiency at different evaporator inlet pressure for different fluids using engine refrigerant.

5.1.4 Organic regenerated cycle

Organic Rankine Cycles modules available in commerce often utilize working fluids with overhanging vapour lines. This condition is not only favourable because it allows to have dry expansions at nearly every operating condition without superheating, but also it makes convenient to regenerate the cycle by sub cooling the vapour at the end of expansion (if the *T-s* diagram is overhanging the fluid is superheated at turbine exit). The regeneration in these cases may be realized without vapour extraction from the turbine, but via a direct regeneration, similarly to what happens in the Brayton-Joule cycles. A scheme of a regenerated ORC is proposed in Fig. 5.2 ©.

For the cycles considered in the present work it is apparent that only benzene is suitable for direct regeneration. It is considered that the regenerative heat exchanger requires a ΔT_{app} of 15K. Under this hypothesis and considering a counterflow heat exchanger, the temperature of the vapour at the heat exchanger outlet can be evaluated, as well as the available energy for the internal heat exchange process ($\dot{Q}_R$):

$$T_{4R} = T_1 + \Delta T_{appr} \tag{5.34}$$

$$\dot{Q}_R = \dot{m}_{f,R}\left(h_4 - h_{4R}\right) \tag{5.35}$$

The state of the liquid at the heat exchanger outlet can be calculated, since:

$$h_{2R} = h_1 + \dot{Q}_R / \dot{m}_{f,R} \tag{5.36}$$

The *T-s* diagram of the regenerated cycle is reported in Fig. 5.18, with superimposed the line referring to the engine exhaust gasses. It is possible to see that, differently to what showed in Fig. 5.10a for the benzene simple cycle, the hot thermal source has to provide heat to vaporize a fluid that is initially at a higher temperature than T_1. Therefore, similarly to what happens when the engine cooling water was used, the fluid mass flow rate through the cycle will be higher than in the case of simple cycle thus providing a higher energy output (the cycle efficiency is also increased in this case). Tab. 5.11 reports the main parameters of the regenerated cycle and it is possible to observe that the circulating mass flow rate is 2.204kg/s (compared to 2.065kg/s of the simple cycle). The net power is thus increased by 6.7% with reference to the simple cycle (P_{ORC}''-$P_{OR(C)}$/$P_{OR(C)}$ and is now rated 322.4kW, with a net cycle efficiency of 24.3%. The power output is lower than that achieved by preheating the fluid with engine cooling water (P_{ORC}'=333.8kW). From Tab. 5.11 it can also be observed that the internal heat exchange provides 89kW$_t$, about 6% of the total heat introduced ($\dot{Q}_R / \dot{Q}_{in}$").

	P_{ORC}'' [kW]	η_{ORC}'' [-]	$\dot{Q}_{in}''$ [kW]	$\dot{Q}_R$ [kW]	$\dot{Q}_R / \dot{Q}_{in}''$ [-]	p_{vap} [kPa]	$\dot{m}_f''$ [kg/s]	$\dot{V}_3''$ [m^3/s]	$\frac{P_{ORC}''-P_{ORC}}{P_{ORC}}$ [-]
benzene	322.4	0.243	1444	89	0.063	2000	2.204	0.042	0.067

Tab. 5.11. Main parameters of benzene regenerated cycle.

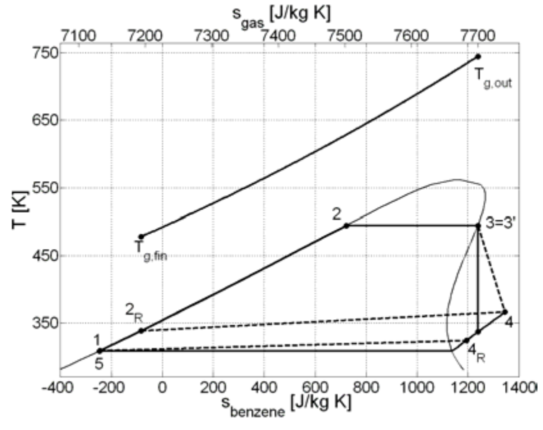

Fig. 5.18. Optimal benzene regenerated cycle and engine exhaust gases cooling curve plotted on two superimposed *T-s* diagrams.

Fig. 5.19 reports the *T*-$\dot{Q}$ diagram for the regenerated cycle, while Fig. 5.20 shows the cycle power versus turbine inlet pressure. It is possible to see that a maximum power of about 360kW could be achieved if the regenerated cycle were operated at a pressure of 4180kPa; the cycle efficiency would be in this case 0.248.

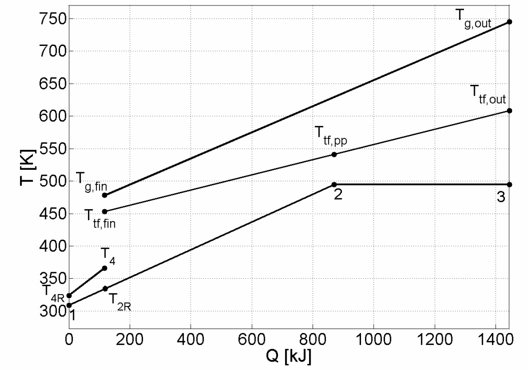

Fig. 5.19. *T*-$\dot{Q}$ diagrams for regenerated benzene cycle.

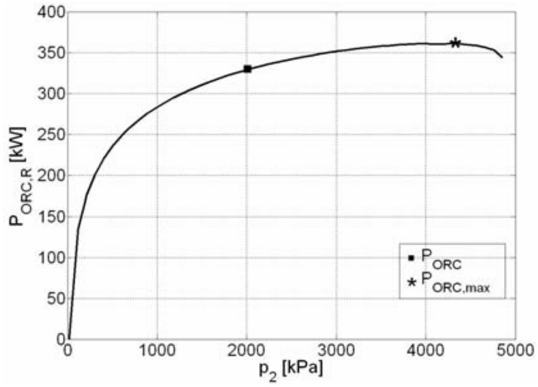

Fig. 5.20. Regenerated benzene cycle power output at different evaporation pressures.

	$\Psi_{1'}$	Ψ_1	Ψ_2	Ψ_3	Ψ_4	Ψ_5	Ψ_6
benzene	0.085	0.143	0.180	0.171	0.007	0.067	0.034

Tab. 5.12. Relative exergy losses for the regenerated benzene cycle.

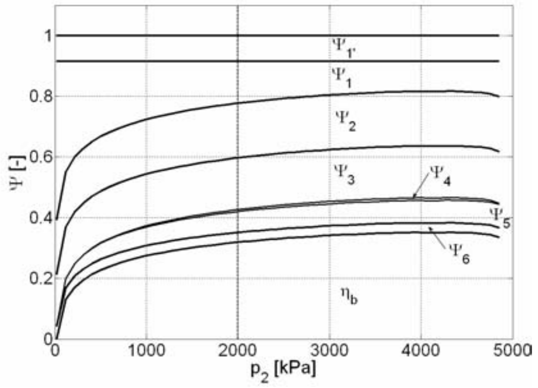

Fig. 5.21. Pattern of cycle irreversibility and exergy efficiency at different evaporator inlet pressure for benzene regenerated cycle.

In the exergy analysis of the cycle it has now to be computed the term Ψ_4 which refers to the irreversibility in the internal heat exchange process due to the temperature difference between the fluids

(Tab. 5.12 and Fig. 5.21). With reference to the simple cycle (Tab. 5.3) the regenerated cycle shows a lower Ψ_1 (the heat exchange with the thermal fluid takes place with a lower average temperature difference) and a higher Ψ_5 (the losses due to non isentropic expansion increase with increasing fluid mass flow rate). The term Ψ_6 is now lower because, despite the increased mass flow rate, a part of the exergy discharged at the turbine outlet is now used in the regenerator and not wasted in the condenser. The overall cycle exergy efficiency η_b is 0.313.

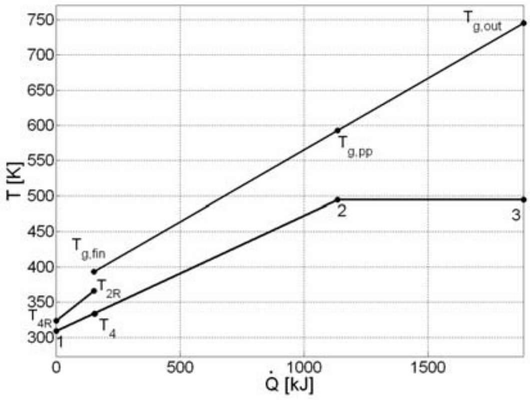

Fig. 5.22. T-$\dot{Q}$ diagrams for regenerated benzene cycle. Case with direct gas/fluid heat exchange.

It is now shown the significant increase in power that could be achieved if a benzene cycle could be operated without the interposition of a diathermic oil circuit. Fig. 5.22 reports the T-$\dot{Q}$ diagram while Tab. 5.12 summarizes the main parameters of the system. A 33% increase in the power produced can be observed ($(P_{ORC,d}''-P_{ORC}'')/P_{ORC}''$) with respect to the regenerated cycle with thermal oil circuit. The overall heat input into the cycle ($\dot{Q}_{in,d}''$) is higher than the overall heat available in the exhaust gases and this is because a fraction of the heat introduced is recovered by the heat that would be otherwise wasted for the subcooling of the vapours at the turbine outlet through the regenerator. The internal heat exchange contributes in this case for about 8% of the total heat input ($\dot{Q}_{R,d}/\dot{Q}_{in,d}''$).

Tab. 5.14 is similar to Tab. 5.4 and shows the increase in exergy efficiency and power output when an ideal expander (η_T=1) or an expander with low isentropic efficiency (η_T=0.6) are considered: in this case the three cycle setups for the benzene are compared and the diathermic oil circuit is considered. It can be noted that the increase in the exergy efficiency $(\eta_b^{**}-\eta_b)/\eta_{(b)}$ with an ideal expander in case of regenerated cycle (0.18) is much smaller than the one observed for the simple cycle (0.25). This shows how the advantages of increasing the efficiency of the expander are less significant when a regenerated cycle is employed. In fact an expander with low efficiency leads to an increase in the superheating temperature of the vapour at the turbine outlet and this energy is partly recovered in the cycle regeneration. It can be observed in fact that when η_T=0.6 the reduction in the cycle efficiency is the smallest for the regenerated cycle.

	$P_{ORC,d}''$ [kW]	$\eta_{ORC,d}''$ [-]	$\dot{Q}_{in,d}''$ [kW]	$\dot{Q}_{R,d}$ [kW]	$\dot{Q}_{R,d}/\dot{Q}_{in,d}''$ [-]	p_{vap} [kPa]	$\dot{m}_{f,d}''$ [kg/s]	$\dot{V}_{3d}''$ [m³/s]	$\frac{P_{ORC,d}''-P_{ORC}''}{P_{ORC}''}$ [-]
benzene	429.0	0.248	1884	153.2	0.081	2000	2.933	0.56	0.330

Tab. 5.13. Main parameters of benzene regenerated cycle with direct gas/organic fluid heat exchange.

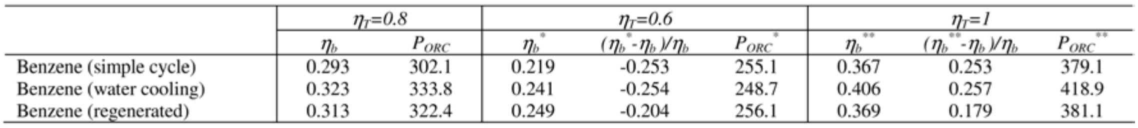

	η_T=0.8		η_T=0.6			η_T=1		
	η_b	P_{ORC}	η_b^*	$(\eta_b^*-\eta_b)/\eta_b$	P_{ORC}^*	η_b^{**}	$(\eta_b^{**}-\eta_b)/\eta_b$	P_{ORC}^{**}
Benzene (simple cycle)	0.293	302.1	0.219	-0.253	255.1	0.367	0.253	379.1
Benzene (water cooling)	0.323	333.8	0.241	-0.254	248.7	0.406	0.257	418.9
Benzene (regenerated)	0.313	322.4	0.249	-0.204	256.1	0.369	0.179	381.1

Tab. 5.14. Exergy efficiency and cycle power for different expander efficiencies and cycle setups. Case with diathermic oil circuit.

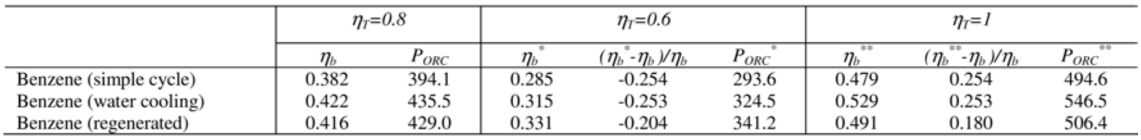

	η_T=0.8		η_T=0.6			η_T=1		
	η_b	P_{ORC}	η_b^*	$(\eta_b^*-\eta_b)/\eta_b$	P_{ORC}^*	η_b^{**}	$(\eta_b^{**}-\eta_b)/\eta_b$	P_{ORC}^{**}
Benzene (simple cycle)	0.382	394.1	0.285	-0.254	293.6	0.479	0.254	494.6
Benzene (water cooling)	0.422	435.5	0.315	-0.253	324.5	0.529	0.253	546.5
Benzene (regenerated)	0.416	429.0	0.331	-0.204	341.2	0.491	0.180	506.4

Tab. 5.15. Exergy efficiency and cycle power for different expander efficiencies and cycle setups. Case with direct gas/fluid heat exchange.

It can also be noted in Tab. 5.14 that if η_T=1 the power output is nearly the same in the regenerated and simple cycle. When isentropic expansion is considered the internal heat transfer is almost zero and regeneration is fruitless. This suggests that when turbines with high isentropic efficiency are available the extra costs for the regenerative heat exchanger can be dropped and a simple cycle configuration can be adopted instead. Tab. 5.14 however displays that the highest increase in the net power output in case of a ideal turbine could be achieved utilizing the preheating with the refrigerant from the engine. The exergy efficiency increase ratio is the highest and the overall power output reaches the theoretical value of about 418kW, which suggest that with highly efficient expander the choice that could optimize the power output would be to preheat the cycle using the engine cooling water. From Tab. 5.14 and Fig. 5.45 it can also be observed that the simple cycle displays values of power output lower than the other two configurations in all the range of expander efficiency considered. This remains true also when a direct gas/organic fluid heat exchange is considered (see Fig. 5.23 and Tab. 5.15). Fig. 5.45 shows also that, as already observed, only at relatively low expander efficiencies the regenerative design of the cycle becomes convenient, also when direct heat exchange is considered, and an expansion efficiency of about 0.7 marks the break even for the water preheated cycle to be more convenient.

Tab. 5.16 and Tab. 5.17 show the terms referring to exergy losses for the three benzene cycle configurations under the hypothesis of ideal expansion. It can in fact be noticed that in both cases Ψ_5 is zero in all cases and exergy is not destroyed through the expander.

Ψ_1 is much smaller for the cycle with water cooling than in the other cases: with regeneration the exergy losses at the evaporator are similar to those in case of simple cycle because the ideal expansion makes the regeneration almost useless. This is the reason why Ψ_6 is not much smaller for the regenerated cycle than in the other cases and Ψ_4 is almost zero.

	Ψ_1	Ψ_1'	Ψ_2	Ψ_3	Ψ_4	Ψ_5	Ψ_6
Benzene (simple cycle)	0.085	0.164	0.180	0.171	0	0	0.032
Benzene (water cooling)	0.085	0.133	0.180	0.159	0	0	0.036
Benzene (regenerated)	0.085	0.162	0.180	0.171	0.001	0	0.032

Tab. 5.16. Relative exergy losses for the benzene based ORC cycles in case of ideal expander (η_T=1). Case with diathermic oil circuit.

	Ψ_1	Ψ_2	Ψ_3	Ψ_4	Ψ_5	Ψ_6
Benzene (simple cycle)	0.250	0.057	0.171	0	0	0.043
Benzene (water cooling)	0.211	0.057	0.156	0	0	0.047
Benzene (regenerated)	0.240	0.057	0.171	0.002	0	0.040

Tab. 5.17. Exergy losses for the benzene based ORC cycles in case of ideal expander (η_T=1). Case with direct gas/organic fluid heat exchange .

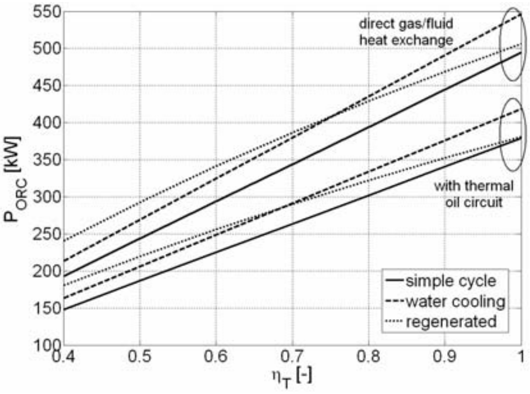

Fig.23: Cycle power versus turbine efficiency for the three cycle configurations assumed for benzene.

5.1.5 Remarks

Tab. 5.18 summarizes the net electrical efficiency estimated for the combined ICE–ORC cycle ($\eta_{C(C)}$ with use of a diathermic oil circuit between hot gases and organic fluid. These values have been calculated assuming a 95% electrical efficiency of the generator coupled to the ORC expander.

A significant increase in the efficiency from the rated electrical efficiency for the engine is apparent (η_e=0.418). Highest values are obtained with benzene, confirming that the highest the critical temperature the better cycle performance. This conclusion has been drawn in other studies, e.g. [16]. With benzene an actual increase in the combined cycle efficiency (η_{CC}-η_e)/ η_e) of about 11% can be achieved, bringing the system efficiency up to 0.464.

From Tab. 5.18 one can also observe that the best cycle configuration appears to be the one that adopts the preheating with engine refrigerant regardless the fluid employed in the organic cycle. This solution is preferable also to the regenerated cycle (considered for benzene only). It has also to be considered that the regenerative preheating requires a liquid-gas heat exchanger and furthermore it has been assumed a quite low temperature difference at the exchanger outlet (ΔT_{appr}). This implies very complex heat exchangers with high exchange surfaces, which leads to components that may need a critical design.

When engine coolant is used for preheating, a liquid-liquid exchange process is performed and the high availability of fluid at high temperatures makes it possible to use simpler components. Therefore when the heat of the engine coolant is wasted it could be preferable to employ the scheme of Fig. 5.2 (b), thus simplifying the design of the required heat exchanger and achieving the highest efficiency increase. This option may become even more interesting in cases when the turbine has a high adiabatic efficiency: it has been shown that with η_T~0.7 the net power delivered by a cycle based on benzene would be greater when engine coolant is used to preheat the cycle, rather than in a regenerated cycle.

While cycles based on R134a give small contributions in both configurations (the increase of engine efficiency may reach 6%), R123 can provide good performances especially when water preheating is adopted. In this case the increase in engine efficiency is 9% and η_{CC} =0.455. R123 or similar fluids may therefore be preferable than overhanging fluids like benzene for the smaller turbine outlet/inlet volume flow ratio. It has been observed that v_4/v_3 is always smaller than 50 for R123, which would allow the use of simple expanders such as single stage turbines.

	η_{CC}		
	Simple cycle	Simple cycle with preheat	Reg. Cycle
benzene	0.459	0.464	0.462
R123	0.449	0.455	-
R134a	0.436	0.443	-
	$(\eta_{CC}-\eta_e)/\ \eta_e$		
benzene	0.099	0.109	0.105
R123	0.075	0.089	-
R134a	0.044	0.059	-

Tab. 5.18. Combined ICE-ORC efficiencies. Case with diathermic oil circuit.

The irreversibility analysis of the cycles helped to identify the major causes of exergy loss through the system. Indeed the biggest exergy destruction takes place in the heat exchange process between organic fluid and engine exhaust gasses. Nevertheless in [18] it has already been pointed out that higher power output is achievable when the working fluid is able to follow better the shape of the heat source fluid to be cooled. All the solutions that help to reduce the average temperature difference between these fluids result in an increase in the exergy efficiency and cycle power. Among these measures the adoption of a fluid with high critical temperature is a straight-forward way to increase system performances. Other ways to reduce the average temperature difference is to introduce preheating of the organic fluid: this may be achieved either by using engine water coolant or by regenerating the cycle. Unfortunately engine coolant is at a temperature level that does not allow great upgrades in the ORC global efficiency: despite its energy and exergy content is not negligible, energy balances have demonstrated that only a fraction of the actual thermal potential of the engine coolant can be effectively used to preheat the cycle.

A significant reduction in the global irreversibility of the system (which would lead to an increase in the exergy efficiency) can be obtained by eliminating the diathermic oil circuit and vaporizing the organic fluid directly with the engine exhaust gases.

This option indeed may not be accepted for safe operation of the system (many of the organic fluids available for ORC applications are flammable) but the work has shown the higher performances that can be achieved with this solution in term of net power generated. Tab. 5.19, analogous to Tab. 5.18, summarizes the results.

A combined cycle efficiency ($\eta_{CC,d}$) of 0.477 ($(\eta_{CC,d}-\eta_e)/\ \eta_e$ =0.14) can be obtained with a benzene cycle (both with regeneration or use of engine refrigerant). R123 shows performances that are higher than those achieved with benzene in the cases when the transfer fluid circuit was considered which suggests that when R123 or other non flammable fluids (usually with bell shaped vapour lines) are utilized, the system design might be simplified eliminating the diathermic oil circuit. R134a again shows unsatisfactory performances.

	Simple cycle	Simple cycle with preheat	Reg. Cycle
	$\eta_{CC,d}$		
benzene	0.472	0.477	0.477
R123	0.459	0.466	-
R134a	0.442	0.450	-
	$(\eta_{CC,d}-\eta_e)/\ \eta_e$		
benzene	0.128	0.142	0.140
R123	0.098	0.116	-
R134a	0.057	0.076	-

Tab. 5.19. Combined ICE-ORC efficiencies. Case with direct gas/fluid heat exchange.

In the next Paragraph therefore the focus will be on more advanced cycles setups in order to assess new ways to couple bottoming power cycles to ICEs and to use a bigger fraction of the power production potential of the engine refrigerant.

5.2 Advanced configurations for ICE bottoming with ORCs

In the previous Paragraph some considerations on the design of an Organic Rankine cycle to be coupled to a stationary internal combustion engine have been proposed. Different cycle configurations as well as different working fluids were assessed in order to determine the preferable solution in term of overall power. An exergy analysis has been also proposed in order to uncover the main causes of irreversibility.

The analysis suggested that fluids with higher molecular complexity are to be preferred because these fluids, characterized by overhanging vapour lines on the *T-s* diagram and higher critical pressures and temperatures, can sensibly reduce the irreversibilities at the heater-evaporator. These fluids however are those that allow the lowest utilization of the heat available from the engine refrigerant as thermal source.

In this Paragraph a more advanced design of the bottom cycle will be proposed, the aim being assessing if it is possible to generate further mechanical power by the thermal power available in the engine coolant. A double cascade organic Rankine cycle, based on the coupling of two different ORC specifically designed to recover heat at different temperature levels, will be analysed to this extent. The top cycle (cycle 1) will be heated by the engine exhaust gases and will have to be as close as possible to a triangular cycle [19] in order to properly follow the curve of cooling of the hot gasses, thus reducing the irreversibility in the heat exchange process. The bottom cycle (cycle 2) will be instead a cycle designed to exploit low grade heat; this second cycle will be partly heated by the engine refrigerant

An analogous concept has been proposed in [20] where a mini-hybrid solar power plant is presented, characterized by a field of solar concentrators and a bio-diesel engine integrated to two superposed organic Rankine cycles. When the system operates in hybrid mode the heat released by the engine, in series with the heat generated by the solar system, is employed to power two simple ORC cycles, the first based on R123 and the second on R134a. Besides the use of solar thermal power the design resembles the one proposed in this Paragraph, with the second ORC powered both by the heat released by the first ORC and by the heat from the engine cooling network, that may be provided either in series as liquid preheater or parallel to the evaporator. Laboratory tests made with the superposed ORCs confirmed adequate operational characteristics with good performances over a broad range of conditions, indicating the feasibility of the design.

In [7] two superposed ORCs are employed to recover heat from a solar system and to power a desalinization plant that can thus be operated, with sunny conditions, entirely on a renewable energy sources. The power unit has been split in to two independent organic Rankine cycle because the top cycle, with a net power of about 100kW, receives heat from the solar collectors in order to drive the high pressure pump of a reverse osmosis unit. The second ORC is used instead to meet the electric consumptions of the auxiliaries of the plant, and this cycle, rating about 40kW, is powered by the thermal power rejected by the top ORC.

In Par. 5.2.1 the double cascade ORC will be specifically analyzed in order to determine the optimal parameters of the cycles and the best fluids to be employed to maximize the power capacity of the energy recovering unit.

In Par. 5.2.2 a different system configuration will be proposed. Starting from the design of the two superimposed ORCs it appears easy to simply by pass cycle 2 and exploit the heat available from the engine refrigerant and the heat released at condenser by cycle 1 to rise the temperature of an heat transfer medium (i.e. water) that can be used for cogeneration purposes (i.e. district heating). In this way a significant flexibility of the system can be achieved since when no cogeneration heat is required both the ORCs could be operated for power generation while, if power is also required in thermal form, the top ORC could still be operated exploiting the high exergy content of the exhaust gases to produce mechanical work delivering heat at its condenser that is less valuable in term of mechanical power generation but could still be employed for thermal purposes. Extra heat could still be extracted by the engine refrigerant placing a proper heat exchanger for the scope, either in series or parallel. Once again optimizations of the system degrees of freedom must be performed and in this case it will be shown that a very important role on the system overall efficiency will be played by the heat transfer fluid input and output temperatures required.

In the analysis the same boundary conditions considered in the previous Paragraph will be assumed to allow an the ORCs will again be coupled to the same 3000kW engine and the same constrains will be applied to the thermal cycles

5.2.1 Double cascade organic Rankine cycles

In Fig. 5.23 it is shown a scheme of the proposed design of the two superposed ORCs used to recover heat from a stationary ICE, while Fig. 5.24 contains the corresponding T-$\dot{Q}$ diagram showing the main heat exchange processes that occur within the system. It can be observed that the lower ORC receives heat by two exchangers placed in series; this design allows rising the temperature of vaporization of cycle 2 ($T_{vap,2}$) by simply increasing the pressure of condensation of the top ORC ($T_{cond,1}$). In this way the heat available by the engine cooling circuit is only due to fluid preheat in ORC2. Note that at decreasing pressure of vaporization for ORC2 point A of Fig. 5.24 might coincide with point *2,2* and in this case the entire heat for fluid preheating would come from the engine coolant.

To be noted that an intermediary diathermic oil circuit has not been considered in this case since the it would reduce too much the temperature of the hot source reducing significantly the possible advantages of the dual cycles configuration.

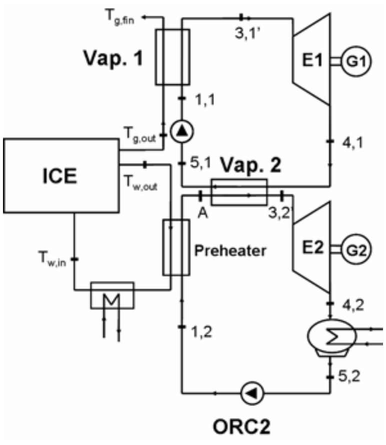

Fig. 5.23: Scheme of the double cascade ORC configurations assumed for ICE bottoming.

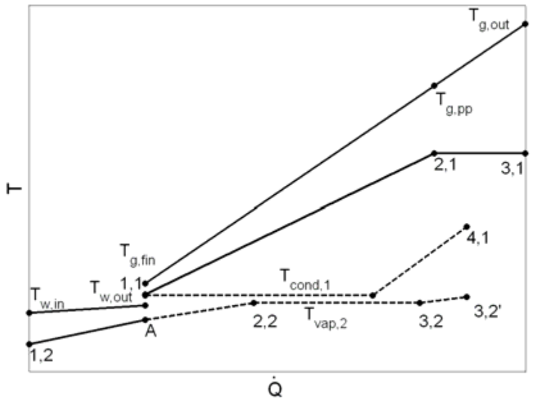

Fig. 5.24: T-$\dot{Q}$ diagram of the double cascade ORC couple to the ICE.

A pair of fluids have to be chosen when a dual ORC configuration is considered. The exergy analysis of the previous Paragraph has demonstrated that fluids with higher critical pressure and temperature are more indicated to recover heat released by a stationary engine and the main advantage lies in the reduced exergy losses that is possible to achieve at the evaporator, due to the smaller temperature difference between heat source and working fluid to be heated. Typically these fluids are of the overhanging type. It should also be noted that further exergy reductions could be achieved by assuming a supercritical Organic Rankine Cycle [19]. The supercritical cycle assumes a shape that is more similar to an ideal triangular cycle than a typical subcritical cycle and this condition is indeed favourable when the heat source is not at constant temperature but is a stream that reduces its temperature while heating the Organic fluid. It will not considered this option in order to keep the system complexity to a reasonable level, since enough complications will be introduced by the coupling of two subcritical Organic Rankine Cycles.

In [20] fluids with low molecular complexity were employed for the double cascade ORC because of the relatively low temperature of the heat supplied (around 165°C) and the significantly low temperature of the heat sink of about 7°C. These very low temperatures allow employing fluids with low critical temperatures which could not be satisfactory when the temperatures of both the heat source and heat sink are raised, as in the case under study; also the power available was very limited compared to that available from the engine considered in this case.

The fluid chosen for the cycle 1 are therefore Toluene and Benzene which are characterized by quite high critical temperatures (benzene: T_{crit}=562K; toluene: T_{crit}=591.7K). In the bottom cycle three fluids with increasing critical temperature are assumed: R134a, Isobutene and Isopentane (R134a: T_{crit}=374.2K; Isobutene: T_{crit}=418.1K; Isopentane: T_{crit}=460.3K).

The procedure implemented to solve and optimize the cycles, described in 5.1.2.1, is realized in a fully parameterized way so that not only the main numerical input data can be changed but also the type of fluid chosen. The results of the analysis, proposed in Par. 5.2.1.2, will display graphs referring to the 2×3 combinations considered of possible fluids to be employed in the top and bottom ORC respectively.

5.2.1.1 Analysis

The first step is defining the main system parameters, including the fluids to be utilized in cycle 1 and 2.

The procedure implements the following energy balance equations:

- Overall thermal power available from the engine cooling water:

$$\dot{Q}_{w,av} = \dot{m}_w \bar{c}_{p,w} \left(T_{w,out} - T_{w,in}\right) \tag{5.37}$$

- Thermal power from engine cooling water effectively used to power ORC2:

$$\dot{Q}_w = \dot{m}_{f,2\_1} \left(h_A - h_{1,2}\right) \tag{5.38}$$

- Thermal power rejected by ORC1 for fluid subcooling and condensation at expander outlet:

$$\dot{Q}_{cond,1} = \dot{m}_{f,1} \left(h_{4,1} - h_{5,1}\right) \tag{5.39}$$

- Thermal power introduced in ORC2 for completing the heating process, vaporizing and, if necessary, superheating the fluid in ORC2; this thermal flow is equal to that released by condensation of ORC1:

$$\dot{Q}_{cond,1} = \dot{m}_{f,2\_2} \left(h_{3',2} - h_A\right) \tag{5.40}$$

- Mechanical power delivered by ORC2:

$$P_{ORC2} = \dot{m}_{f,2} \left(h_{3',2} - h_{4,2}\right) \tag{5.41}$$

A very important parameter to be defined in the analysis is the temperature (or pressure) at condensation for cycle 1 ($T_{cond,1}$). This value, which also defines the pressure and temperature of vaporization for cycle 2 (given ΔT_{1-2}) is a degree of freedom of the problem and has to be determined by a specific optimization procedure.

Once $T_{cond,1}$ is defined in fact cycle 2 is completely defined, being $T_{vap,2}=T_{cond,1}- \Delta T_{1-2}$ and $T_{cond,2}$ fixed by the heat sink temperature. The cardinal nodes and main parameters of the cycle can therefore be determined recurring to the procedure described in the previous chapter in case of simple cycle with no regeneration and thermal power provided only by engine exhaust gases (5.1.2.1). After defining the temperature T_A, through Eq.(5.38), it is possible to determine a first value of the working fluid mass flow rate in cycle 2 ($\dot{m}_{f,2\_1}$) assuming $\dot{Q}_w = \dot{Q}_{w,av}$; the value of the calculated mass flow rate therefore is the one that allows to entirely recovery the heat available in the engine refrigerant water.

For cycle 1 instead the pressure (or temperature at evaporator) must still be defined. $T_{cond,1}$ in fact defines the pressure at condenser ($p_{cond,1}$), but the pressure at evaporator still has to be defined.

An optimization procedure searches for the optimal pressure at evaporator for the top cycle once the condenser temperature is defined (Fig. 5.25). Some constrains are introduced in order to get a value of pressure at evaporator for cycle 1 sufficiently far from the critical pressure of the fluid.

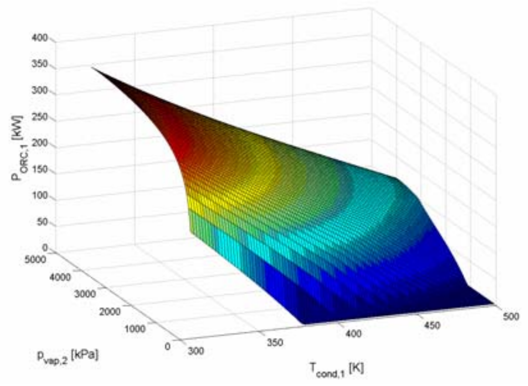

Fig. 5.25: Example of ORC power at varying evaporator pressure and condensation temperature.

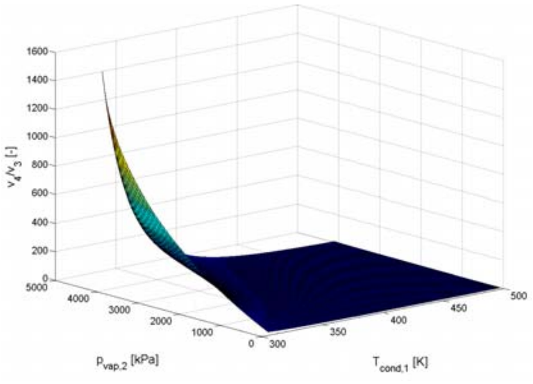

Fig. 5.26: Example of expander inlet/outlet volumetric flow ratio at varying evaporator pressure and condensation temperature.

The value obtained in this way might be too close to the critical pressure (as it can be observed in Fig. 5.25 the curves are basically monotonical with increasing pressure of evaporation) and give values of expander inlet/outlet volumetric flow ratios too high (Fig. 5.26).

The procedure therefore not only determines the pressure at evaporator that gives maximum outlet power once $T_{cond,1}$ is defined but, in cases this pressure is too close to the critical one or gives v_4/v_3 ratios too high, it decreases $p_{vap,1}$ up to reach values that meet the constrains introduced.

Once the parameters of cycle 1 are defined the cycle can be solved and the heat released at the condenser can be used in Eq.(5.40) in order to define what is the required heat transfer fluid mass flow rate in cycle 1 ($\dot{m}_{f,2\_2}$) necessary to recovery $\dot{Q}_{cond,1}$. The actual mass flow rate in cycle 2 ($\dot{m}_{f,2}$) will necessary have to be the smallest between $\dot{m}_{f,2\_1}$ and $\dot{m}_{f,2\_2}$; usually the minimum value is $\dot{m}_{f,2\_2}$ and this means that not all the thermal power of the engine refrigerant can be actually used to preheat the fluid.

In Par. 5.2.1.2, where the main results are shown, some graphs will be dedicated at analyzing what the system characteristics are when $T_{cond,1}$ varies over a range of possible values. Particularly it is assumed that $T_{cond,1}$ may vary in the range between $T_{cond,min}+\Delta T_{12}$ and $T_{crit,2}+\Delta T_{12}$. When $T_{cond,min}<T_{cond,2}+\Delta T_{12}$ indeed cycle 2 degenerates (the condensation temperature of cycle 1 is too low to assume that some heat could be recovered by underposing a new ORC) and only cycle 1 is considered. For increasing $T_{cond,1}$ it becomes reasonable to recovery the heat of condensation of cycle 1. The maximum temperature is fixed for $T_{cond,1}=T_{crit,2}+\Delta T_{12}$; $T_{crit,2}$ is the maximum theoretical temperature allowed for the bottom cycle; any increase of $T_{cond,1}$ above $T_{crit,2}+\Delta T_{12}$ would certainly cause an increase of irreversibillities in the heat exchange process between cycle 1 and 2 (the average temperature difference between the fluids would rise) thus it is not justified considering any higher temperature of condensation for cycle 1.

5.2.1.2 Results and discussion

The main results are presented in graphical form for the 2×3 fluid combinations considered.

In the first set of graphs (Fig. 5.27) the overall double cascade ORC power ($P_{OR(C)}$ is plotted along with the power generated by each of the two Organic cycles, with respect of the condensation temperature for cycle 1 (see also Tab. 5.20). It can be observed that the range of possible condensation temperatures increases with increasing critical temperature of the fluid used at the bottom cycles and this is because, as seen, the range of temperature for condensation of the top cycle is bounded to the critical temperature of the bottom cycle. It can be also seen that at the minimum allowed value of $T_{cond,1}$ the power generated by ORC,2 is zero because the cycle degenerates in these conditions.

From the graphs it can also be observed that when P_{ORC} reaches its maximum, the cycle that mainly contributes to provide power is cycle 1. Fig. 5.23 and Tab. 5.20 also show that once the fluid for the top cycle is defined (either benzene or toluene) the maximum power achievable does not change much with different fluids for the bottom cycle; slightly better results are observed with use of isobutene as fluid in cycle 2 but what makes a more significant difference is the choice of the fluid for the top cycle. Analogously the temperature at which the maximum overall power is achieved is quite insensitive to the choice of fluid for the bottom cycle. Nevertheless it can be observed that the trend of power generated at the bottom cycle follows a nearly continuous pattern irrespective of the fluid utilized. It can also be observed that the optimal value of $T_{cond,1}$ (the one that maximises the overall power output) is quite close to the critical temperature when R134a is utilized as fluid for the bottom cycle wile the other fluids considered for cycle 2 should be preferred as they make it possible to operate the system further away from their critical point.

Average values of double cascade ORC power of about 418-421kW are achieved by system were the top cycle is based on benzene, while the power rises to 428-431kW using toluene as fluid in cycle 1 (Tab. 5.20).

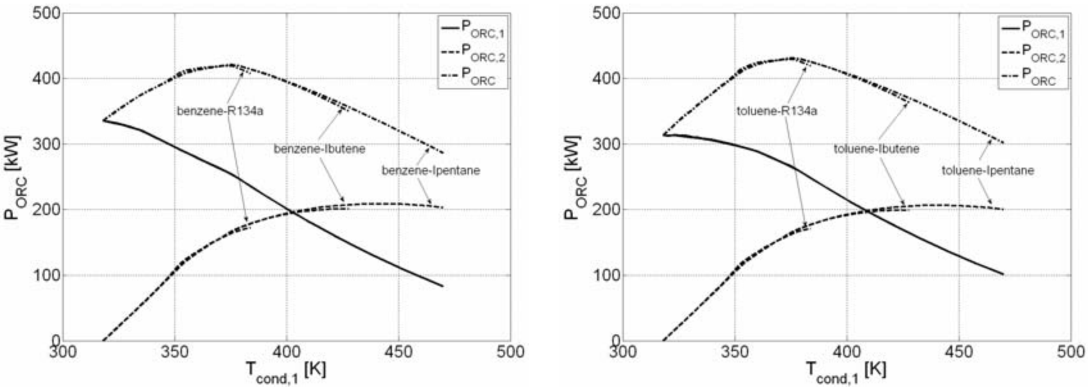

Fig. 5.27. Cycle power at varying condenser temperature of cycle 1.

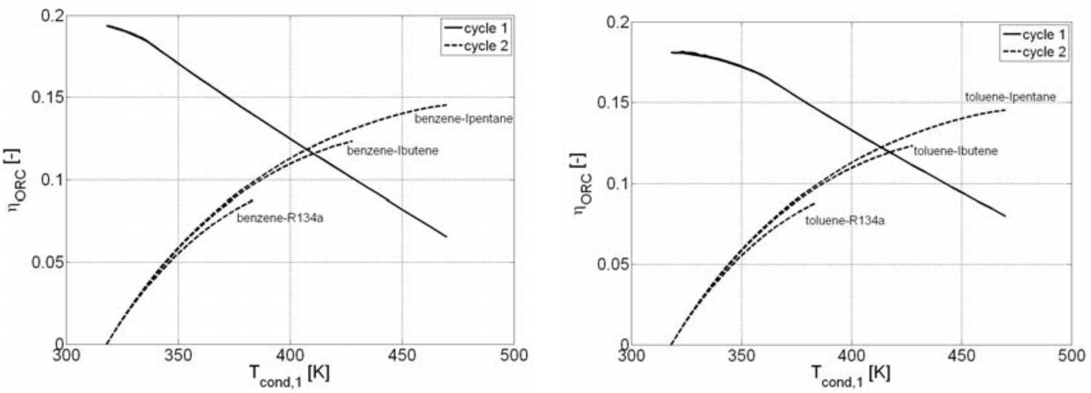

Fig. 5.28. Cycle efficiency at varying condenser temperature of cycle 1.

The plots of Fig. 5.28 report cycle 1 and cycle 2 efficiencies at varying condensation temperatures for the top cycle.

Differences can be observed in the curves referring to the efficiencies of cycle 2, that vary within the range 0.081-0.091 at the optimal value of $T_{cond,1}$ (Tab. 5.20). The efficiency of the top cycle increases notably when passing from benzene (~0.150) to toluene (0.156) determining the observed increase in cycle output power.

In Fig. 5.29 it is reported the working fluid mass flow rate in cycle 1 and cycle 2, again with respect of $T_{cond,1}$. It can first be observed that the fluid R134a used in the bottom cycle requires a much higher mass flow rate due to the lower enthalpy difference that characterize the fluid in the heating-vaporizing process (see Tab. 5.20).

The working fluid mass flow rate is monotonically increasing for cycle 1 with increasing $T_{cond,1}$. This is a consequence of the decreasing difference between $h_{3,1'}$ and $h_{1,1}$ when the temperature at condensation for the cycle increases given the same thermal input to the cycle.

A different pattern of $\dot{m}_f$ is observed for the fluids at the bottom cycle. The working fluid mass flow rate increases for increasing $T_{cond,1}$ while this value reaches $T^* = 353$K. At this point the pressure of vaporization for cycle 2 is such that the temperature of vaporization (point 2_2) becomes equal to the temperature of the engine refrigerant $T_{w,out}$ minus the heat exchanger approach temperature. In symbols:

$$T^{*} = T_{cond,1} - \Delta T_{12} = T_{w,out} - \Delta T_{app,w} = T_{2,2} = T_{A} \tag{5.42}$$

This means that up to values of $T_{cond,1}$ below T^* the heat required for preheating the fluid in cycle 2 (between points *1,1* and *2,2*) is completely provided by the engine refrigerant. Since the heat available from the refrigerant is always bigger than that utilized from the cycle, any increase in $T_{cond,1}$ determines an increase in the fluid mass flow that can be heated (and consequently of the power, since the efficiency increases accordingly). Below T^* in fact, when $T_{cond,1}$ increases, the preheating in cycle 2 is fully covered by the engine refrigerant and the mass flow rate in cycle 2 is only limited by the heat available for vaporization (Eq. 3 and 4), which is the heat rejected by cycle 1 ($\dot{Q}_{cond}$). This thermal power increases for increasing $T_{cond,1}$ while the enthalpy difference $h_{3,2'}-h_{2,2}=h_{3,2'}-h_A$ decreases and hence $\dot{m}_{f2}$ increases.

When $T_{cond,1}$ rises upon T^*, $p_{cond,2}$ is too high for the heat of preheating to be provided entirely from the engine refrigerant and $T_{2,2}>T_A$ and therefore the enthalpy difference $h_{2,2}-h_A$ must be provided by the heat coming from cycle 1. In these conditions the specific enthalpy difference $h_{3,2'}-h_{2,2}$ increases for increasing $T_{cond,1}$ at a higher rate than *pcond,1* and therefore the fluid mass flow rate that can be heated in cycle 2 decreases.

As a consequence to this it can be observed in Fig. 5.30. that the actual thermal power from the engine refrigerant utilized in cycle 2 abruptly decreases once the temperature T^* is reached. The term $\dot{Q}_{A-1,2}/\dot{Q}_w$ expresses in fact the amount of heat provided in the cycle preheating with respect to the overall heat available from the engine refrigerant.

At optimal conditions as much as 51% of the heat rejected through the engine refrigerant is recovered when a bottom cycle based on R134a is employed (Tab. 5.20). Considering the low temperature at which the heat is available the result seems significant and the design of the double cascade cycle turns out to be favourable with respect to a single cycle design, where at maximum 26% of the engine coolant heat could be recovered (see Par. 5.1.3). The extra amount of heat provided by the refrigerant is one of the reasons for the increased power output of the system. When isobutene or isopentane are employed in the bottom cycle the amount of heat recovered from the refrigerant decreases to 37% and 34% respectively.

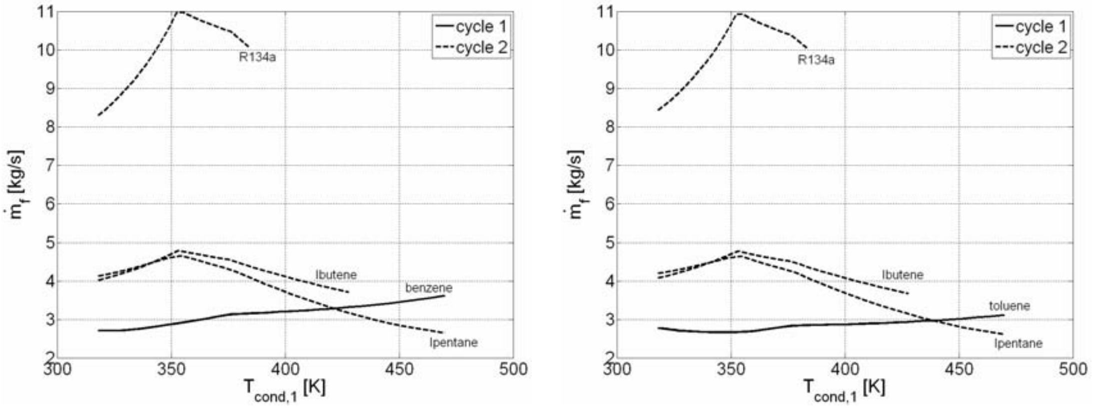

Fig. 5.29. Cycle mass flow rate at varying condenser temperature of cycle 1.

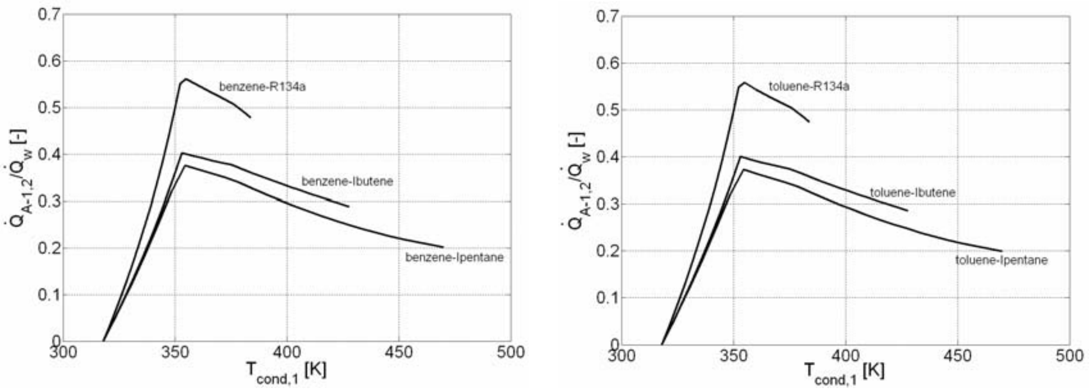

Fig. 5.30. Ratio of thermal power transferred to the bottom cycle from the engine refrigerant with respect of overall power available in the refrigerant at varying condenser temperature of cycle 1.

An important parameter to be considered is the expander outlet/inlet volumetric flow ratio that defines the degree of complexity of the expander to be adopted. From the graphs of Fig. 5.31 it is possible to see that the value of v_4/v_3 is always within a range of acceptable values in the bottom cycle. In the top cycle the ratio v_4/v_3 rises to very high values especially at low condensation temperatures. As already mentioned, in order o limit the system complexity, the value of v_4/v_3 has been limited to 100 for cycle 1 by reducing the value of the pressure at the evaporator (see also Fig. 5.32).

It can also be observed that toluene displays higher values of v_4/v_3 compared to benzene, at the same given $T_{cond,1}$. Particularly, at the optimal value of $T_{cond,1}$ the ratio v_4/v_3 for the top cycle is about 30 for benzene and about 60 for toluene, while for all the fluids employed in the bottom cycles v_4/v_3 is limited to about 5. Indeed benzene appears preferable from the standpoint of expander complexity.

In Fig. 5.32 it is possible to see how the pressure at evaporator in the top cycle decreases when the temperature at condenser is too low; when the expander volumetric flow ratio is below reasonable values the pressure at the evaporator can be raised up to high values in order to give high cycle efficiency. In the bottom cycle the pressure, as expected, rises with increasing $T_{cond,1}$. To be noted that for both benzene and toluene the maximum allowed pressure has been limited to a value that is 1000kPa lower than the critical pressure, in order to guarantee safe operation of the system. If higher pressures were allowed at the top cycle some extra power could be generated by the system.

At the optimal value of $T_{cond,1}$, the pressure at the evaporator in the bottom cycle decreases significantly moving from R134a to isobutene and isopentane; this suggest that for the bottom cycle this latest fluid would be preferable in order to deal with lower maximum pressures. Analogously toluene should be preferred to benzene in the top cycle as the maximum pressures are lower.

From Tab. 5.20 it can also be observed that the pressure at the condenser remains above atmospheric pressure for all the fluids suggested for the bottom cycle. The pressure at the condenser is also above atmospheric pressure when benzene is utilized as fluid for the top cycle and it is slightly below atmospheric pressure when toluene is utilized, even if the degree of vacuum is however very low (the pressure is about 0.8kPa). These conditions are all very favourable because it is not required to deal with components capable of withstanding very low pressures. This is another of the advantages that can be underlined in recurring to double cascade cycles; when simple cycles were employed much lower pressures had to be assumed within the low pressure components of the system (Par. 5.1.2.2).

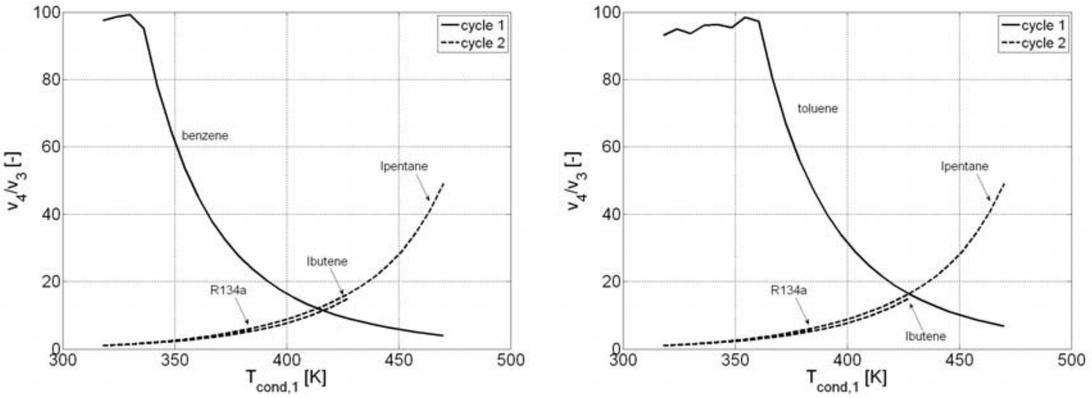

Fig. 5.31. Expander outlet/inlet volumetric flow ratio at varying condenser temperature of cycle1.

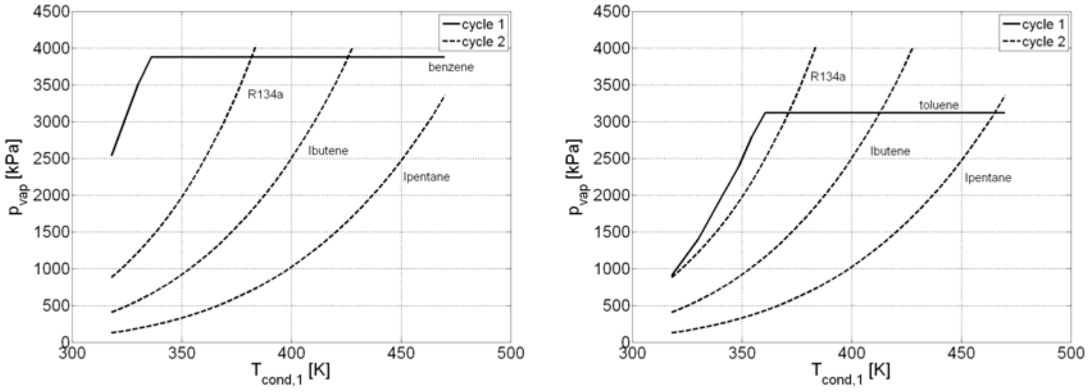

Fig. 5.32. Expander outlet/inlet volumetric flow ratio at varying condenser temperature of cycle 1.

		P_{ORC} [kW]	$T_{cond,1}$ [K]	$\frac{\dot{Q}_{A-1,2}}{\dot{Q}_w}$ [-]	$P_{ORC,1}$ [kW]	$\eta_{ORC,1}$ [-]	$\dot{Q}_{in}$ [kW]	$\dot{m}_{f,1}$ [kg/s]	$v_{4,1}/v_{3,1}$ [-]	$p_{cond,1}$ [kPa]	$P_{vap,1}$ [kPa]
					$P_{ORC,2}$ [kW]	$\eta_{ORC,2}$ [-]		$\dot{m}_{f,2}$ [kg/s]	$v_{4,2}/v_{3,2}$ [-]	$p_{cond,2}$ [kPa]	$P_{vap,2}$ [kPa]
Benzene	R134a	418.7	374.9	0.51	255.1	0.147	2267.3	3.12	30.42	189.2	3877.0
					163.6	0.081		10.49	4.61	883.3	3365.8
	Isobutene	421.5	375.7	0.37	253.9	0.147	2126.8	3.13	29.80	193.2	3877.0
					167.6	0.089		4.55	4.32	406.8	1584.9
	Isopentane	421.2	375.7	0.34	253.9	0.147	2094.3	3.13	29.81	193.1	3877.0
					167.3	0.091		4.31	4.99	128.4	613.3
Toluene	R134a	428.8	376.2	0.50	264.5	0.153	2259.9	2.83	60.34	81.4	3120.0
					164.3	0.082		10.38	4.76	883.3	3454.1
	Isobutene	431.8	376.2	0.37	264.5	0.153	2123.2	2.83	60.35	81.4	3120.0
					167.3	0.090		4.51	4.37	406.7	1600.3
	Isopentane	431.5	376.2	0.34	264.5	0.153	2090.8	2.83	60.34	81.4	3120.0
					166.9	0.091		4.27	5.05	128.3	620.3

Tab. 5.20. Main system parameters for the 2×3 configurations considered.

The set of graphs of Fig. 5.33 reports the T-$\dot{Q}$ diagrams for the combinations of fluids considered. The graphs are plotted at the optimal value of $T_{cond,1}$ reported in Tab. 5.20. It is possible to see the curve referring to the engine exhaust gases, cooling down from the initial temperature $T_{g,out}$ to $T_{g,fin}$, with $T_{g,fin} > T_{g,min}$; the hot gases provide thermal power to heat up and vaporize the fluid of cycle 1. Cycle 2 receives heat first by the engine refrigerant used to rise the working fluid temperature in cycle 2 up to T_A. To be noted that in all cases proposed $T_A<T_2$, hence the optimal cycle configuration is not the one that uses only thermal power from engine refrigerant to preheat the fluid in cycle 2 because this would require a too low pressure of vaporization for cycle 2 which in turns would penalize too much η_2 (see Fig. 5.28).

Part of the heat to warm up the liquid as well as all the heat required to vaporize (and, if necessary, to superheat) the fluid in cycle 2 comes from the heat rejected by the top cycle; reported with dotted lines are the internal heat exchanges between cycle 1 and cycle 2.

If can be observed that the overall heat introduced into the system of the double cascade organic Rankine cycles is different in the many cases considered; the term $\dot{Q}_{A-1,2}$ which, as seen, refers to the actual heat from the engine refrigerant that is usefully employed in cycle 2, differs according to the characteristics of the fluid used in the bottom cycle and increases with the decreasing of its critical temperature; this can be deduced from the term $\dot{Q}_{in} = \dot{Q}_{A-1,2} + \dot{Q}_g$ of Tab. 5.21, where $\dot{Q}_g$ is constant in all cases.

From Fig. 5.33 it is also possible to see that toluene can reach higher temperatures at evaporator and also requires lower heat input to vaporize all the fluid. This condition is such to reduce irreversibilities at the evaporator compared to cycles based on benzene, thus determining the slightly higher cycle efficiency that have already been discussed.

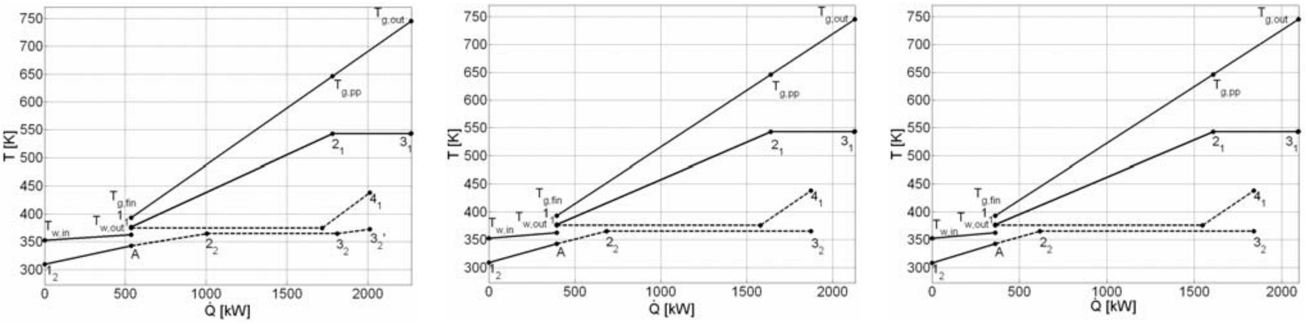

(a) benzene-R134a (b) benzene-isobutene (c) benzene-isopentano

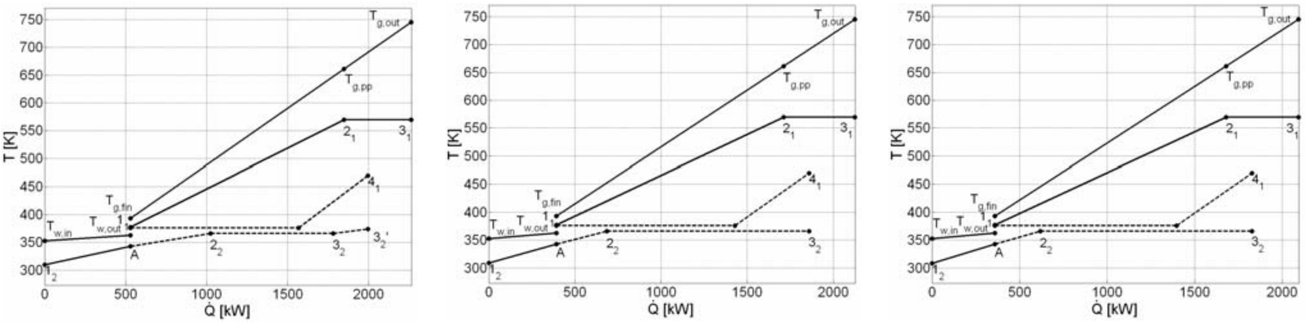

(a) toluene-R134a (a) toluene- isobutene (a) toluene- isopentano

Fig. 5.33. T-$\dot{Q}$ diagrams for the dual cascade cycles under analysis.

In Fig. 5.34 the *T-s* diagrams of the top and bottom organic cycles are reported on superimposed diagrams. It can be seen that, as already observed, when the bottom cycle is based on R134a the temperature of vaporization is quite close to the critical temperature of the fluid. Considering also the higher mass flow rate and the lower power generated by cycles based on R134a, it is possible to state that configurations based on isobutene or isopentane are preferable. Considering the wide application of isopentane in geothermal power plants [20], and the low pressure at evaporator (620kPa) and the relative high pressure at condenser (just above atmospheric pressure, at 128kPa), the fluid can be assumed to be a good choice for the bottom cycle.

As for the top cycle toluene can be preferred to benzene not only because it is less harmful and toxic, but also because it allows operating the top cycle with higher efficiency thus increasing the overall setup power output; nevertheless toluene is already widely used by some ORC manufacturers. In conclusion the pair of fluid toluene-isopentane can be chosen as best option among the many combinations considered even though some other pair of fluids could be considered instead.

A general principle can be drawn however: fluids with high critical temperature and low latent heat of vaporizations should be employed in the top cycle (typically fluid with overhanging vapour lines). Fluids with intermediate critical temperatures (which is usually typical of bell-shaped or nearly-isentropic fluids) must be used for the bottom cycle. If the critical temperature of the fluid used in cycle 2 were raised too much, it would require recurring to overhanging fluids (see Fig. 5.34 (c) and Fig. 5.34 (f)) which are not favourable because the fluid at the turbine exhaust would be in the field or superheated steam. This condition reduces the enthalpy drop through the turbine and increases the heat that must be rejected. This heat could be recovered in a regenerator but this option would further increase the system complexity and therefore is ignored. The best solutions from the point of view of the power generated are in fact those that employ isobutene as fluid in the bottom cycle, both with benzene and toluene as topper.

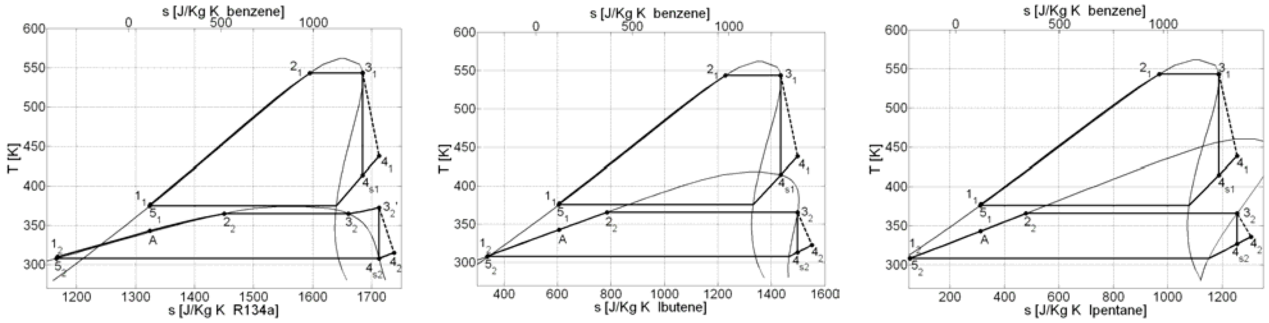

(a) benzene-R134a (b) benzene-isobutene (c) benzene-isopentano

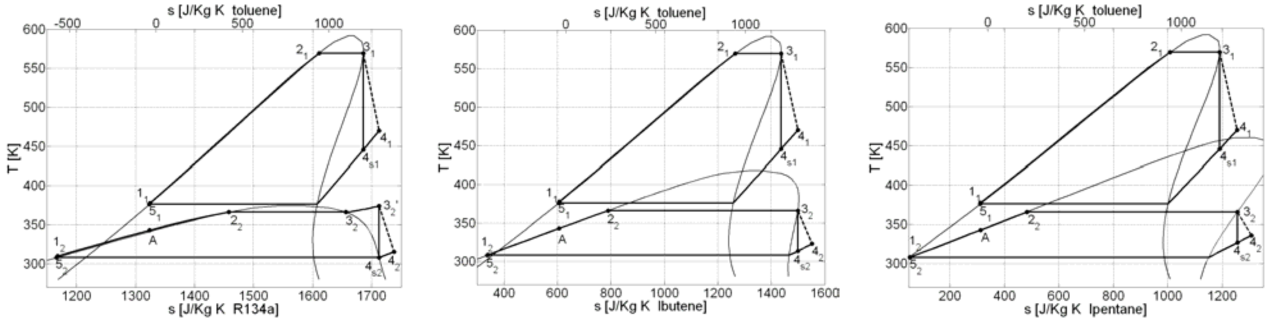

(d) toluene-R134a e) toluene- isobutene f) toluene- isopentano

Fig. 5.34. *T-s* diagrams for the dual cascade cycles under analysis.

To conclude this section is also interesting to show the performances that could be achieved by introducing more efficient expanders both in cycle 1 and 2. The value considered of η_e=0.7 for both the cycles is highly conservative: usually when the volumetric expansion ratio v_4/v_3 is smaller than 50, expansion efficiencies higher than 0.8 can be achieved via a single stage axial turbine [15]. Assuming slightly higher values of the expansion efficiencies seems reasonable and technically acceptable; Tab. 5.21 has therefore been compiled for the couple toluene-isopentane with $\eta_{e,1}$=0.75 and $\eta_{e,2}$=0.8 (in cycle 2 the ratio v_4/v_3 is always well below 50).

The net power increases to 473.3kW ($\Delta P_{ORC}/P_{ORC}$ =0.088, where ΔP_{ORC} expresses the relative increase in power generated with reference to the same couple of fluids but at lower expander efficiency shown in Tab. 5.20), and this is mainly due to the increase in the power generated in the bottom cycle ($\Delta P_{ORC,1}/P_{ORC,1}$=0.069 while $\Delta_{PORC,2}/P_{ORC,2}$ =0.116). The increase in the expander efficiency in cycle 2 is such to compensate also a decreased thermal input to the cycle ($\dot{Q}_{1,2}$ passes from 1826kW to 1801kW), which is caused both by the lower heat rejected by cycle 1 due to the increased expansion efficiency and by the decreased amount of heat that can be obtained by the engine refrigerant (the mass flow rate has decreased now).

		P_{ORC} [kW]	$T_{cond,1}$ [K]	$\frac{\dot{Q}_{A-1,2}}{\dot{Q}_w}$ [-]	$P_{ORC,1}$ [kW]	$\eta_{ORC,1}$ [-]	$\dot{Q}_{in}$ [kW]	$\dot{m}_{f,1}$ [kg/s]	$v_{4,1}/v_{3,1}$ [-]	$p_{cond,1}$ [kPa]	$P_{vap,1}$ [kPa]
					$P_{ORC,2}$ [kW]	$\eta_{ORC,2}$ [-]		$\dot{m}_{f,2}$ [kg/s]	$v_{4,2}/v_{3,2}$ [-]	$p_{cond,2}$ [kPa]	$P_{vap,2}$ [kPa]
Toluene	Isopentane	473.3	376.2	0.34	284.4	0.164	2085.9	2.83	59.81	81.4	3120.0
					188.9	0.105		4.21	4.99	128.3	620.3

Tab. 5.21. Main system parameters for the toluene-isopentane cycle design with expander efficiency of 0.75 and 0.8 for cycle 1 and 2 respectively.

5.2.2 MCI-ORC CHP design

The design of the double cascade ORC as possible system to usefully recover the heat released by a stationary ICE allows a certain flexibility that makes it possible to consider further design without increasing the system complexity. Particularly it has been observed that the cycle 1 can reject heat at temperatures that are quite significant, and the heat might serve not only to power a second organic cycle, but in some cases it could be usefully recovered to warm up a fluid used for cogeneration purposes (CHP, Combined Heat and Power). Indeed this solution is applicable only when the temperature of the heat transfer medium is required not to be too high, roughly in the range 90-130°C which is typical for district heating networks.

The idea in this case is to exploit engine refrigerant to partially heat the heat transfer fluid (as seen the use of engine jacket water in bottoming power cycles is not always of easy application and often is not complete) and to provide the extra heat required to match the temperature and power targets by subcooling and condensing the organic vapour of ORC1. The necessity to raise the temperature at the condenser causes a reduction in the exergy efficiency of the cycle because the heat is rejected at a temperature further from the death state temperature (i.e. some work could still be extracted from the vapour at the condenser inlet) but this causes on the other hand a significant increase in the overall energy efficiency of the system as the heat of condensation is not wasted in the environment but is usefully recovered.

5.2.2.1 Analysis

A scheme of the proposed system is shown in Fig. 5.35 while in Fig. 5.36 it is reported the corresponding T-$\dot{Q}$ diagram where the main heat exchange processes are highlighted.

Differently from Fig. 5.35 and Fig. 5.36 it can be seen how the heat rejected by cycle 1 now serves to rise the heat transfer fluid temperature for cogeneration purposes. It can be observed that, being the fluid employed in the ORC in the state of superheated vapour at the expander outlet, the temperature of the heat transfer fluid may be raised to values higher than the condensation temperature in the ORC.

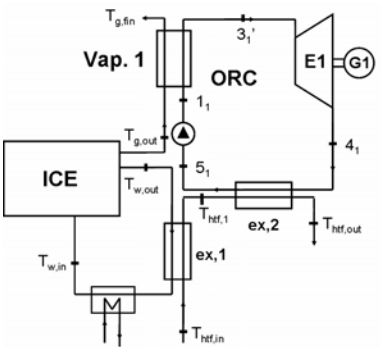

Fig. 5.35: Scheme of MCI-ORC CHP design.

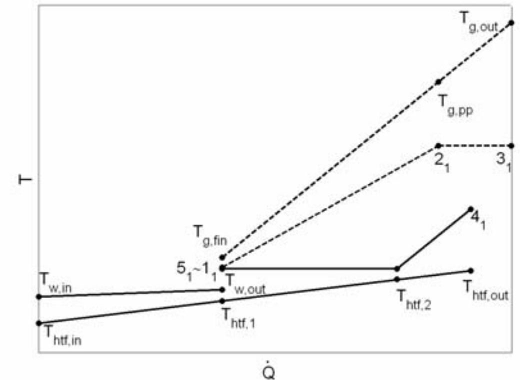

Fig. 5.36: T-$\dot{Q}$ diagram of MCI-ORC CHP design.

The heat available for cogeneration may be, under certain conditions, substantial, being the sum of the heat flux rejected by the engine through the refrigeration circuit and the heat flux of condensation of the ORC. This last term is equal to the heat available in the engine exhaust gases minus the mechanical power recovered through the ORC. Basically the heat available for the cogeneration is not decreased significantly with respect to the case where no ORC bottoming is applied, but now a certain amount of highly valuable energy in mechanical form is produced and subtracted from the overall thermal energy available from the engine. It will be emphasized in the next section how, to make this possible, it is necessary that the temperatures at which the HTF is required are within a certain field of values otherwise neither it is possible to recover the heat of the engine refrigerant nor the ORC would produce a sufficient amount of work to make its introduction into the system feasible.

Particularly, once again a very important parameter (namely the main degree of freedom) to be defined for the ORC is the pressure (and hence the temperature) at condensation.

A specific optimization procedure has been compiled in Matlab® in order to determine the pressure of condensation for the ORC to match the required temperature for cogeneration purposes ($T_{htf,out}$), which is, among with the return temperature of the cogeneration fluid ($T_{htf,in}$) a constrains to the problem.

The procedure also calculates:

- Heat transfer fluid mass flow rate, $\dot{m}_{htf}$;
- Overall thermal power to cogeneration, $\dot{Q}_c$;
- Actual thermal power from engine water transferred to cogeneration heat transfer fluid, $\dot{Q}_{c,w}$;
- Actual thermal power from ORC condensation transferred to cogeneration heat transfer fluid, $\dot{Q}_{c,ORC}$.

The boundary conditions introduced concern the performances of the heat exchangers introduced to power the cogeneration system. Particularly a liquid-liquid heat exchanger (*EX1*) will be required to exchange heat between engine coolant and the heat transfer fluid (usually water) while another exchanger (*EX2*) will be introduced in series to recover the heat of condensation; both exchangers are assumed to be counterflow. The constrains introduced are:

- Minimum approach temperature difference in the liquid-liquid heat exchanger to be observed both at inlet and outlet, $\Delta T_{appr,ex1}$:

$$T_{w,in} - T_{htf,in} > \Delta T_{appr\ ex1} \text{ and } T_{w,out} - T_{htf,1} > \Delta T_{appr,ex1} \tag{5.43}$$

- Minimum Pinch Point temperature between organic fluid during subcooling/condensation and heat transfer fluid to cogeneration, $\Delta T_{pp,ex2}$:

$$T_{cond} - T_{htf,2} > \Delta T_{pp,ex2} \tag{5.44}$$

- Minimum approach temperature difference between heat transfer fluid at cogeneration and organic fluid at the turbine outlet, $\Delta T_{appr,ex2}$:

$$T_{4,1} - T_{htf,in} > \Delta T_{appr,ex2} \tag{5.45}$$

Among the hypothesis introduced it should be mentioned that the procedure is developed in order completely exploit the heat released at the condenser and that the pressure of condensation of the cycle is chosen accordingly. The ORC cycle parameters are then calculated once the condensation pressure is defined with the procedure introduced in the previous section.

Few balance equations can be introduced between the heat transfer fluid in the cogeneration network and the high temperature sources. The main equations are summarized below:

- Heat flux transferred between engine refrigerant and cogeneration heat transfer fluid:

$$\dot{Q}_1 = \dot{m}_w \overline{c}_{p,w} \left(T_{w,out} - T_{w,in} \right) = \dot{m}_{htf,1} \overline{c}_{p,htf} \left(T_{htf,1} - T_{htf,out} \right) \tag{5.46}$$

- Heat flux transferred between ORC fluid during condensation and cogeneration heat transfer fluid:

$$\dot{Q}_2 = \dot{m}_f \left(h_{4,s} - h_{5,1} \right) = \dot{m}_{htf,2} \overline{c}_{p,htf} \left(T_{htf,2} - T_{htf,1} \right) \tag{5.47}$$

- Heat flux transferred between ORC fluid during subcooling and cogeneration heat transfer fluid:

$$\dot{Q}_3 = \dot{m}_f \left(h_{4,1} - h_{4,s} \right) = \dot{m}_{htf,2} \overline{c}_{p,htf} \left(T_{htf,in} - T_{htf,2} \right) \tag{5.48}$$

The procedure implemented is displayed in the flow chart of Annex 2 that summarizes all the operations.

Some parameters must be defined before calculation; these are:

- Type of fluid adopted in the organic Rankine cycle;
- Engine refrigerant inlet and outlet temperature and flow rate ($T_{w,in}$, $T_{w,out}$, $\dot{m}_w$);
- Engine exhaust gas temperature at engine outlet, minimum allowed temperature and flow rate ($T_{g,out}$, $T_{g,min}$, $\dot{m}_g$);
- Cogeneration heat transfer fluid inlet and outlet temperature required by the heat load ($T_{c,in}$, $T_{c,out}$).

At start of calculations a first attempt value of $T_{c,1}$ is defined; after verifying that the temperature matches the requirements of the heat exchanger a first heat flow balance is performed in order to determine the cogeneration fluid mass flow rate that is necessary to completely use the thermal power of the engine refrigerant ($\dot{m}_{htf,1}$). At the same time a procedure performs the calculation of the cogeneration fluid mass flow rate required to exploit the heat released by the organic fluid during subcooling/condensation ($\dot{m}_{htf,2}$). In this case however an iterative procedure is introduced in order to determine the optimal pressure of condensation for the organic cycle that allows achieving the desired temperature of the cogeneration fluid ($T_{c,out}$) and that allows matching the constrains of the heat exchanger introduced in Eq.(5.44)-(5.45). A first attempt value of the condensation temperature equal to $T_{c,1}$ is therefore assumed. The procedure that solves the ORC is recalled and the cycle state points and mass flow rate are calculated accordingly. This allows determining the heat released by the cycle during condensation ($\dot{Q}_2$) and vapour subcooling ($\dot{Q}_3$). Eq.(5.47)-(5.48) allow in fact to determine the mass flow rate $\dot{m}_{htf,2}$ and the temperature of the cogeneration fluid at pinch point ($T_{c,2}$). The mere heat flux balance does not assure that the constrains are verified; indeed the first attempt value of the condensation temperature would be too low; therefore the procedure is reiterated for increasing ORC condensation temperatures while the constrains are fitted.

The actual cogeneration heat transfer fluid mass flow rate is chosen as the smallest between $\dot{m}_{htf,1}$ and $\dot{m}_{htf,2}$. If the smallest mass flow rate is that determined by the thermal power balance with the heat released by the ORC it is apparent that not all the heat rejected with the engine refrigerant can be accepted for cogeneration. The actual value of $\dot{Q}_1$ is then calculated while the values of $\dot{Q}_2$ and $\dot{Q}_3$ are those determined by the iterative procedure.

In cases when the smallest cogeneration heat transfer fluid mass flow rate is that determined by the balance at the first exchanger, a new iterative procedure is introduced in order to further raise $T_{cond,1}$. In this case what limits the heat that can be transferred for cogeneration is the availability of heat from the engine refrigerant. Accepting the value of $\dot{m}_{htf,1}$ calculated in that way would make the temperature of the fluid at the cogeneration network inlet ($T_{htf,out}$) higher than the value required. This is a consequence of the fact that the slope of the heating curves in the T-$\dot{Q}$ diagram is inversely proportional to the fluid mass flow rate times the specific heat at constant pressure.

Assuming a lower mass flow rate of the heat transfer fluid in the second heat exchanger, not being changed the ORC and then the thermal power $\dot{Q}_2$ and $\dot{Q}_3$, would cause ($T_{htf,out}$) to be too high:

$$\frac{1}{\dot{m}_{htf,2}\bar{c}_{p,htf}} < \frac{1}{\dot{m}_{htf,1}\bar{c}_{p,htf}} \tag{5.49}$$

and:

$$T_{htf,out} = T_{htf,1} + \frac{1}{\dot{m}_{htf,2}\bar{c}_{p,htf}}\left(\dot{Q}_1 + \dot{Q}_2\right) \tag{5.50}$$

This condition not only is not favourable because does not allow to match the required cogeneration fluid temperature, but also would break the constrains of Eq.(5.44)-(5.45); it might also happen that $T_{htf,2}>T_{4,1s}$ which is clearly physically not possible.

5.2.2.2 Results and discussion

As described in the previous section, the ORC condensation pressure and temperature are automatically defined by the procedure implemented in order to match the temperature required for cogeneration ($T_{htf,out}$). The temperature of the water returning from the thermal user ($T_{htf,in}$) defines instead the possibility of using the heat of the engine refrigerant and in which amount.

The variables to the problem are hence the temperatures of the fluid used as heat transfer medium for cogeneration purposes, while the procedure uses the energy balances illustrated above to determine some operational parameters of the system as the following:

- Heat transfer fluid mass flow rate: $\dot{m}_{htf}$;
- Thermal power for cogeneration purposes $\dot{Q}_c$ ($\dot{Q}_c = \dot{Q}_{c,ORC} + \dot{Q}_{c,w}$);
- Temperature and pressure of condensation for the ORC: T_{cond}, p_{cond};

- Power of the organic Rankine cycle: P_{ORC};
- Temperature at pinch points of the heating line of the heat transfer fluid: $T_{htf,1}$, $T_{htf,2}$;

The following figures are the parameterized results of the problem at different values of the two variables; particularly $T_{htf,in}$ has been assumed to vary in the range between 313 and 349K, while $T_{htf,out}$ has been assumed in the range 253-403K; higher values of $T_{htf,out}$ are not such to justify the setup.

In Fig. 5.37 it is reported the thermal power employed for cogeneration purposes and recovered by the engine refrigerant at varying inlet and outlet heat transfer fluid temperatures.

It can be observed that for temperatures of the fluid at the inlet of the heat exchangers above 338K the thermal power is zero. In this field of temperatures in fact it is verified the condition $T_{htf,in} > T_{w,in} - \Delta T_{appr\ ex1}$, hence $T_{htf,1}=T_{htf,in}$ and no heat is actually transferred to the cogeneration fluid because its temperature at the inlet is too high to receive heat from the engine refrigerant. In this field of temperatures therefore the cogeneration network can receive heat only from the ORC (see Fig. 5.39a).

As soon as $T_{htf,in}$ decreases below 338K some heat can be recovered by the engine refrigerant, besides the heat that comes from the subcooling and condensation of the organic fluid. In Fig. 5.39(b) it is proposed the T-$\dot{Q}$ diagram with $T_{htf,in}$=335K and $T_{htf,out}$=390K; it can be seen that nearly 440kW come from the refrigerant. A higher thermal power can be recovered by decreasing $T_{htf,out}$; in Fig. 5.39 (c) it is shown how, at $T_{htf,in}$=335K and $T_{htf,out}$=360K, just the entire heat available from the engine refrigerant can be recovered for cogeneration and a thermal power of about 1050kW is transferred to the heat transfer fluid. These are very particular conditions for which the curve referring to the cooling of the engine refrigerant is nearly parallel (in the hypothesis of using the same fluid in both the circuits) to that referring to the htf heating and $T_{w,in} - T_{htf,in} \sim T_{w,out} - T_{htf,1} \sim \Delta T_{appr,ex1}$. Also the mass flow rate of the fluid used for cogeneration is the same as the heat mass flow rate of the fluid used for the engine cooling.

For temperatures of $T_{htf,in}$ further decreasing, $\dot{Q}_{c,w}$ can increase also for high values of $T_{htf,out}$ (Fig. 5.37). When the temperature of the heat transfer fluid at inlet is particularly low there is wide range of temperatures accepted at outlet that allow recovering the maximum amount of thermal power from the engine refrigerant (Fig. 5.39 (d)).

In this case the high temperature difference required for the *htf* makes it necessary to operate with quite low values of $\dot{m}_{htf}$ hence the curve referring to *htf* heating is steeper than that of engine refrigerant cooling.

The heat recovered from the condensation of the organic fluid actually transferred to the *htf* is plotted in Fig. 5.38. It can first of all be observed that the values are less varying if compared to $\dot{Q}_{c,ORC}$. In this case the range of variation is about 80kW for all the couples of $T_{htf,in}$ and $T_{htf,out}$ assumed, and $\dot{Q}_{c,ORC}$ varies from a minimum of nearly 1390 to a maximum of 1470kW.

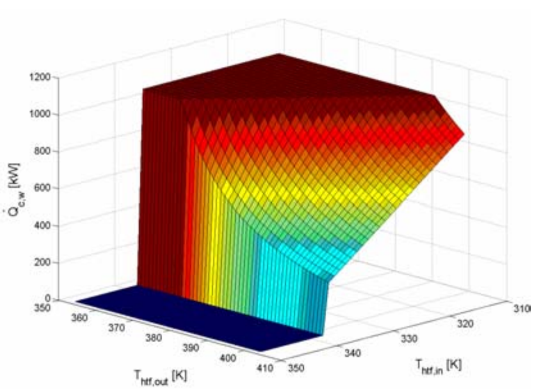

Fig. 5.37: $\dot{Q}_{c,w}$ at varying inlet and outlet heat transfer fluid temperatures.

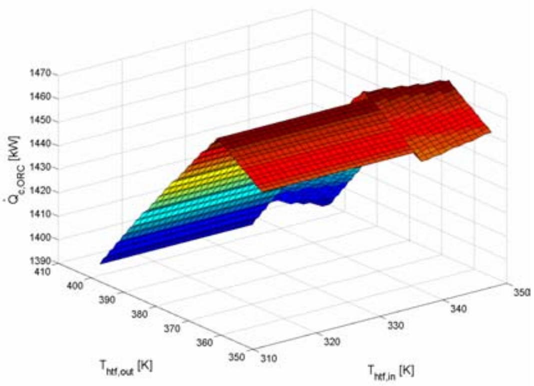

Fig. 5.38: $\dot{Q}_{c,ORC}$ at varying inlet and outlet heat transfer fluid temperatures.

From the figure it can be seen that for increasing $T_{htf,out}$ the power first increases then, when $T_{htf,out}$ reaches the value of about 367K, it starts decreasing. This behaviour is a consequence of the organic fluid mass flow rate (Fig. 5.40 (a)), which increases rapidly while $T_{htf,out}$ is below 367K when the temperature at condenser is low enough for cooling down the engine exhaust gases up to the minimum allowed temperature ($T_{min,g}$). When $T_{htf,out}$ rises above 367K the gas final temperature is limited by the increasing temperature of point 1,1 of the ORC therefore the thermal power available to the cycle decreases hence causing a substantial reduction in the rate of increase of $\dot{m}_f$ for increasing $T_{htf,out}$.

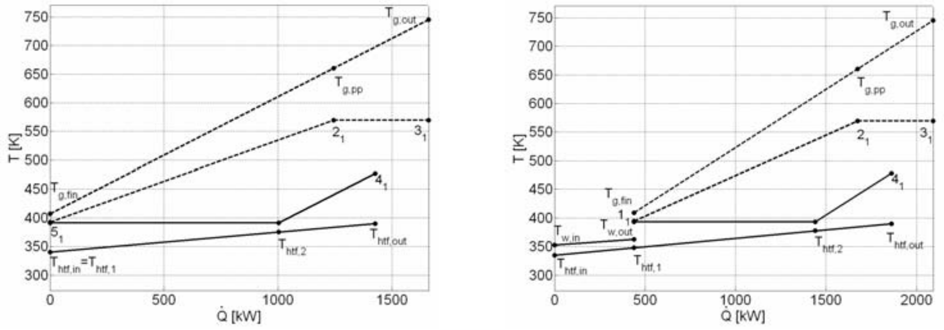

(a) $T_{htf,in}$=340K – $T_{htf,out}$=390K (b) $T_{htf,in}$=335K – $T_{htf,out}$=390K

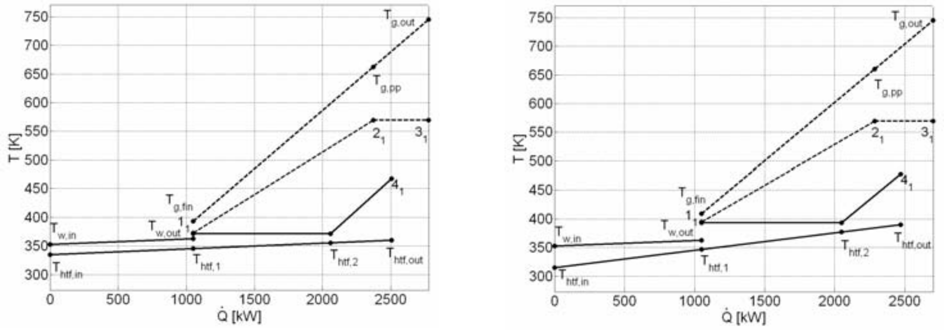

(c) $T_{htf,in}$=335K – $T_{htf,out}$=360K (d) $T_{htf,in}$=315K – $T_{htf,out}$=390K

Fig. 5.39. T-$\dot{Q}$ diagrams for MCI-ORC CHP design.

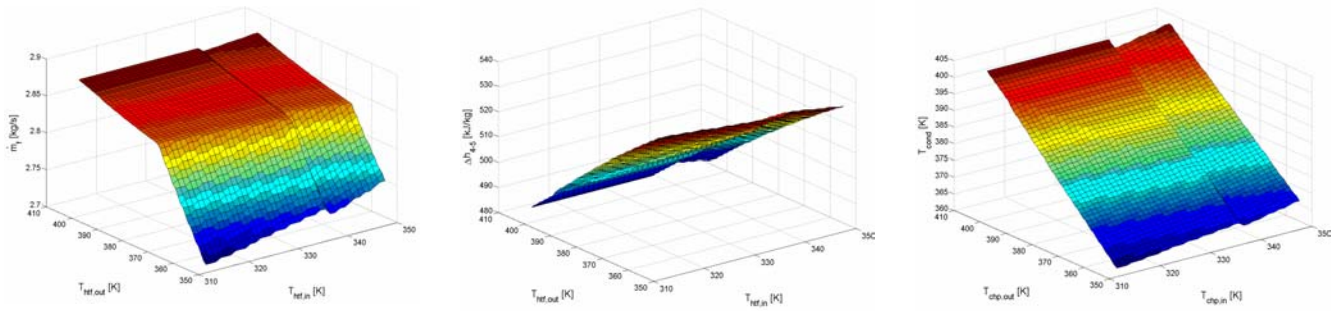

(a) (b) (c)

Fig. 5.40. Some cycle properties at varying inlet and outlet heat transfer fluid temperatures: (a) $\dot{m}_f$, (b) $\Delta h_{4\text{-}5}$ and (c) T_{cond}.

The analysis of Fig. 5.40 (b), where the specific enthalpy difference of the condensing fluid in the ORC ($\Delta h_{4\text{-}5}$) is displayed, shows that for increasing $T_{htf,out}$ the enthalpy difference of the fluid condensing decreases. Since $\dot{Q}_{c,ORC} = \dot{m}_f \times \Delta h_{4\text{-}5}$, the high rate of increase of $\dot{m}_f$ for $T_{htf,out}$<367K makes $\dot{Q}_{c,ORC}$ to increase in this range of temperatures while for $T_{htf,out}$>367K the effect of $\Delta h_{4\text{-}5}$ decreasing becomes predominant and $\dot{Q}_{c,ORC}$ change behaviour.

From Fig. 5.38 it can also be observed a slight decrease in the power available as soon as the heat transfer fluid inlet temperature rises above 338K, the value that limits the possibility to employ engine refrigerant to preheat the htf. When that threshold is passed the temperature at condenser undergoes a sudden drop (Fig. 5.40 (c)) because the temperature of the heat transfer fluid approaching the heat exchanger with the condensing organic fluid is no longer at $T_{htf,1}>T_{htf,in}$ but is at the lower temperature $T_{htf,in}$.

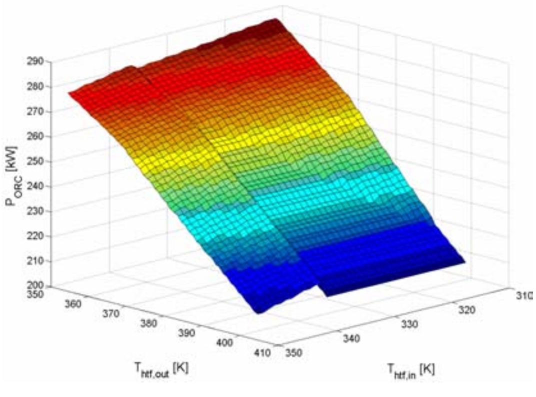

Fig. 5.41: P_{ORC} at varying inlet and outlet heat transfer fluid temperatures.

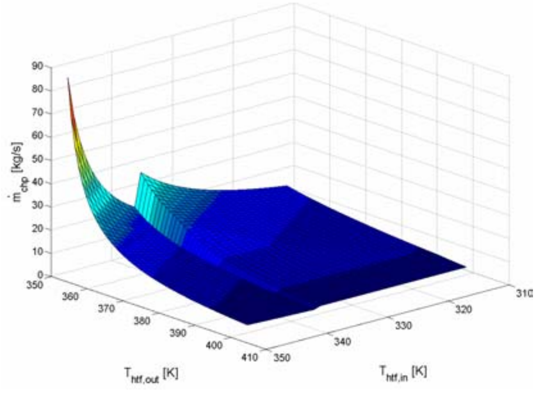

Fig. 5.42: $\dot{m}_{htf}$ at varying inlet and outlet heat transfer fluid temperatures.

The actual mechanical power generated by the organic Rankine cycle is plotted in Fig. 5.41. As expected P_{ORC} is nearly insensible to $T_{htf,in}$ while it is subject to serious variation depending on the temperature required for the heat transfer fluid at the outlet of the heat exchangers. The highest $T_{htf,out}$, the lowest is the power that can be recovered in mechanical form by the system.

The power produced in the range of temperatures assumed for $T_{hftf,out}$ spam between 209-287kW; it can be seen that even in the worst conditions, when a heat transfer fluid at 403K is required, the power produced is significant and such to justify the introduction of the ORC to use the exergy of the engine exhaust gases recovering their potential mechanical power and releasing the heat at lower temperature in order to warm up the fluid required for cogeneration.

In Fig. 5.42 it is displayed the heat transfer fluid mass flow rate calculated for the different temperatures considered. It can be observed that in most of the field of temperatures the value of the heat transfer fluid flow rate is limited within values of the order of magnitude of 10kg/s. Should the temperature difference of the heat transfer fluid be too small from inlet to outlet, a peak in $\dot{m}_{htf}$ could be observed, in order to make the fluid capable to deliver all the thermal power available. Another smaller peak can be seen when $T_{htf,in}$ decreases below the value of 338K and the thermal power available arises suddenly due to the availability of the heat from the engine refrigerant (Fig. 5.37).

In Fig. 5.43 it is finally proposed the overall thermal power recovered for cogeneration purposes, $\dot{Q}_c = \dot{Q}_{c,ORC} + \dot{Q}_{c,w}$. Since, as already observed, $\dot{Q}_{c,ORC}$ does not vary significantly, the pattern of $\dot{Q}_c$ follows the one defined by $\dot{Q}_{c,w}$, with the difference that $\dot{Q}_c$ is never zero but in the range of temperatures where it was observed that the engine refrigerant could not contribute to power the htf, the actual thermal power is equal to $\dot{Q}_{c,ORC}$. For all the other values of $T_{htf,in}$ and $T_{htf,out}$, $\dot{Q}_c$ rises by the amount of power recovered by the refrigerant which might be quite significant in some areas of the plot, where a nearly-triangular plateau with the highest values of $\dot{Q}_c$ is drawn.

It can be observed therefore that the combined MCI-ORC CHP plant should be operated just in this area, where the maximum thermal power of about 2500kW is usefully recovered. The possibility to operate the system at these high levels of energy utilization depends only on the temperatures imposed at the heat transfer fluid at inlet/outlet of the heat exchangers and, of course, by the existence of a thermal user that effectively employs the thermal power recovered.

As already observed, $T_{htf,in}$ should be below 338K to exploit the engine refrigerant. This value is quite low even though some district heating networks may have such return temperatures. To gather an adequate exploitment of the heat available $T_{htf,out}$ must instead be the lowest possible, even though values of 370K are sufficient to get good results in terms of recovered thermal power, and the temperature is compatible with heating requirements of buildings.

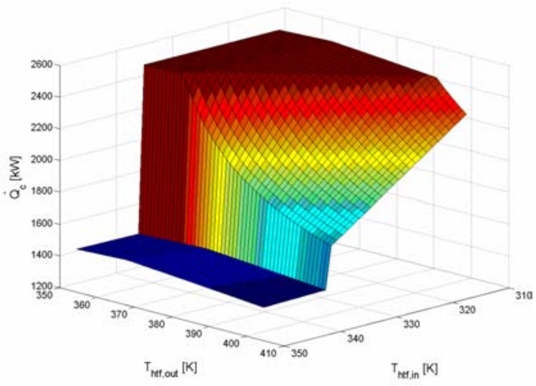

Fig. 5.43: $\dot{Q}_c$ at varying inlet and outlet heat transfer fluid temperatures.

As a reference case the following couple of temperatures will be therefore considered: $T_{htf,in}$=333K (60°C), $T_{htf,out}$=368K (95°C). The T-$\dot{Q}$ diagram of the system is reported in Fig. 5.44 while the main operational data are reported in Tab. 5.22.

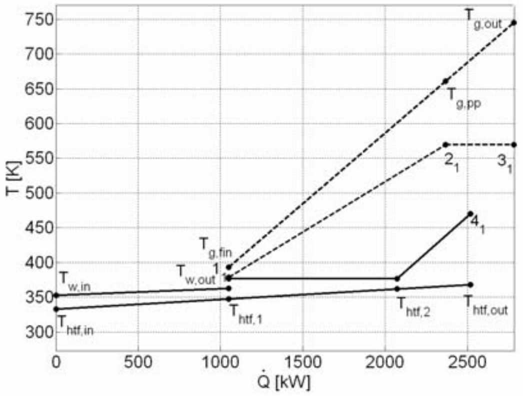

Fig. 5.44: T-$\dot{Q}$ diagram at the reference inlet and outlet heat transfer fluid temperatures.

P_{ORC} [kW]	η_{ORC} [-]	T_{cond} [K]	$\dot{Q}_{c,w}$ [kW]	$\dot{Q}_{c,ORC}$ [kW]	$\dot{Q}_c$ [kW]	$\dot{m}_{htf}$ [kg/s]	$T_{htf,1}$ [K]	$T_{htf,2}$ [K]
263.1	0.152	377	1050	1464	2517	17.12	347.6	362.0

Tab. 5.22. Main system parameters at the reference inlet and outlet heat transfer fluid temperatures.

In this scenario the engine produces 2928kW$_e$, while the Organic cycle used as bottomer recovers 263kW of mechanical power that, with a generator efficiency of 0.95 turn to be 250kW$_e$ (to be remembered that a particularly low expander efficiency of 0.7 is considered in this analysis) giving a total of 3178kW$_e$.

Besides the electrical power the system generates also a total of 2517kWt, even if at relatively low temperature.

The primary energy of the fuel fed to the system is 7002kW, therefore the electrical efficiency is 0.454 (the value for the engine alone is 0.418) and the thermal efficiency is 0.359 (the initial value was 0.441), with a EUF of 0.813 (the original value was 0.859).

The introduction of the ORC therefore has contributed to increase the electrical production of the system, that notoriously is more valuable and dispatchable than thermal energy, still leaving the possibility to recover heat at a reasonable temperature for heating purposes.

To be noted that the temperature imposed at the condenser of the ORC for the cogeneration necessity (Tab. 5.1) is close to the optimal value designed for the coupling of a further ORC in dual cascade design. This suggests that the system could be operated in cogeneration mode when thermal load is present and that the second ORC could be used to recover heat by the system when the need of thermal power ceases to exist.

If the top cycle based on toluene were coupled with a bottom cycle based on isopentane, at the value of $T_{cond,1}$ =377K required by the cogeneration needs, a total mechanical power of 431.4kW could be generated (263.1kW by ORC1 and 168.3kW by ORC2). The electrical power would be 409.8kWe and the total electrical power generated by the MCI-ORCs system would pass to 3338kW$_e$, with an overall electrical efficiency of 0.477.

Tab. 5.23 can hence be compiled, where the two configuration, based on the same toluene ORC top cycle, can be compared in terms of actual energy outputs and efficiencies

	MCI-ORC CHP design	**MCI-double cascade ORC design**
Top cycle	Toluene ORC	Toluene ORC
Heat released by top cycle	cogeneration	Isopentane ORC
System electrical power [kW]	3178	3338
System electrical efficiency [-]	0.454	0.477
System thermal power [kW]	2517	-
System thermal efficiency [-]	0.359	-
EUF [-]	0.813	0.477

Tab. 5.23. Comparison of two system configurations: CHP and double cascade ORC design.

5.2.3 Remarks

Even though not all the thermal power rejected by the engine can be used to power the cycles (particularly only about 30-50% of the engine refrigerant heat flux can be successfully utilized at optimal operating conditions), the proposed double cascade ORC design allows reaching mechanical power of about 430kW, higher than nearly 380kW recovered when a cycle based on just one ORC is utilized, given the same engine as source of heat.

Besides the increase in power, the design of the double cascade ORC allows a certain flexibility of operation and by simply by-passing the lower ORC, heat can be recovered in thermal form for cogeneration purposes. The amount of heat recoverable depends strongly on the temperatures required for the heat transfer fluid at inlet and outlet of the network, and only a limited field of these temperatures allows full heat recovery. Within this field however the possibility exists for the heat transfer fluid to be utilized within some heating processes.

Ideal applications for the double cascade ORC system seem therefore those where alternative engines are being operated without heat recovery.

Examples to this are biogas fired engines coupled to digestors. In these cases the MCI-ORC CHP design could be assumed and the heat transfer fluid could be employed to heat the digestor or for greenhouses: the temperatures required by both processes seem compatible to those available from the MCI-ORC cogenerator.

Another interesting application might be marine diesel engines: a double cascade ORC system could recover the heat rejected to produce electrical power (that can be used for onboard applications) thus reliving the main generator from some power absorption and reducing the engine fuel consumptions. If thermal power were required for sanitary water production, kitchens or room heating the bottom ORC could be by-passed and hot water generated with the heat released by the top ORC.

Concerns may exist on the feasibility and transient response to quick turning up or down of the bottom ORC. Dynamic models of the ORCs will therefore be presented in order to have a better understanding of the response of the system to external disturbances before further proceeding with experimental analyses.

5.3 Dynamic models of MCI-ORC combined power units

From the first and second principle analysis presented in the previous paragraphs emerges that the combined ICE-ORC power unit may represent an interesting solution to valorise and recovery thermal power available from ICEs that is often wasted. The proposed designs need testing in order to effectively analyse the mutual interactions that may exist between the engine and the Rankine cycle and to evaluate the off design performance of the unit and the response to change in the overall system inputs. Prior to dispose of an actual physical unit suitable for testing, some considerations and design optimizations can be performed recurring to complete dynamic models that can be built up by properly bounding together the single components available from the presented libraries.

5.3.1 ORC simple cycle thermally powered by engine exhaust gases with intermediary diathermic oil circuit

The first configuration proposed features an R123 based organic Rankine cycle coupled to a stationary ICE to recover the waste heat released through the exhaust gases by means of an intermediary diathermic oil circuit, according to the scheme of Fig. 5.2 (a).

The proposed plant lay-out can be built up in a Simulink® workspace by dropping the ICE and ORC blocks from the 'Energy Systems' sub-library. The complete model also needs an heat exchanger to be introduced that represent the component where the heat content of the engine exhaust gases is transferred to the thermal oil. A dynamic heat exchanger model with no phase change, is chosen from the 'state determined' library for the scope. The hot thermal oil constitutes the fluid stream that enters the ORC system and is provided to the evaporator in order to heat and vaporize the organic fluid. The whole plant is represented as from Fig. 5.45 that shows the Simulink® lay out of the proposed ICE-ORC combined unit design.

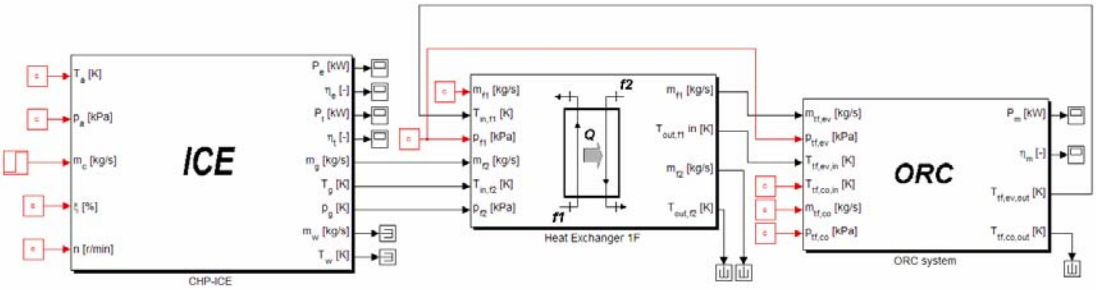

Fig. 5.45. Simulink® lay-out of the ICE-ORC combined unit with heat recovery from engine exhaust gases and intermediary diathermic oil circuit.

The cogenerative ICE, as well as the ORC unit chosen for the dynamic analysis, are the same considered in the previous Chapter where details on the main parameters of the two models have also been provided. The model should represent the systems discussed in the thermodynamic analysis of Par. 5.1.2.

As it can be evinced from Fig. 5.45 the ambient air temperature an pressure to the ICE are kept constant during the simulation as well as its rotational speed, that is constantly 1000r/min for generator synchronization. As for the ORC overall inputs it can be observed that the conditions of the condenser refrigerator (water in this case) are maintained constant during the simulation.

A significant overall system output that, as already observed, has strong effect on the performances of the ICE unit, is the fuel mass flow rate. Now the effects of changing this input signal want to be analyzed also for the diathermic oil heat exchanger and the whole ORC system linked to it, and the presented dynamic model is suitable for the scope.

Particularly the results of a 1200s simulation are proposed in the following set of plots and the ICE fuel mass flow rate is assumed to experience a step change 0.10-0.14kg/s at simulation time *t*=600s.

The results regarding the ICE are very similar to those shown in the previous chapter since the ICE is unaffected by the presence of the heat exchanger and the ORC. For reference the ICE output power and overall efficiencies are reported in Fig. 5.46.

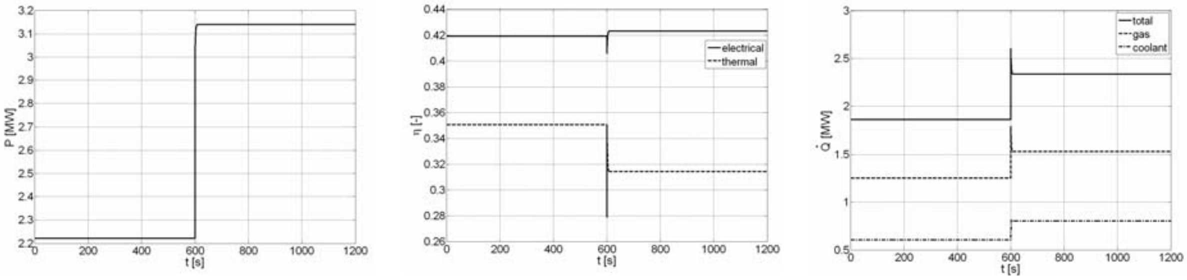

(a) (b) (c)

Fig. 5.46. ICE output mechanical power (a), efficiencies (b) and thermal power (c).

To be noted that, according to the arrangement of Fig. 5.45, the thermal oil stream leaving the evaporator, whose mass flow rate is kept constant during the simulation assuming that its flow is guaranteed by a simple constant speed circulator, is directly sent to the diathermic oil heat exchanger with no external action aimed at controlling its temperature. This lay out turned out to be not favourable from the stand point of system stability, and the ORC plant responded without finding any equilibrium operating condition, as witnesses by the few sample figures reported in Fig. 5.47 to Fig. 5.51 that refer to the described configuration.

Fig. 5.47 particularly shows that the overall ORC output power oscillates significantly and this is due to oscillations in the evaporator pressure (Fig. 5.49 (c)) that determines variation in the fluid specific enthalpy at turbine inlet and in the turbine mass flow rate (Fig. 5.48 (b)).

What generates the difficulty for the system to reach a stable operating condition is the fact that the diathermic oil input temperature to the ORC evaporator depends on the temperature of the diathermic oil that the gas heat exchanger sees at its inlet, which in turn depends on how consistent was the heat exchange of the thermal oil with the organic fluid, due to the open loop design of the diathermic oil circuit. From Fig. 5.51 it can be observed in fact that the temperature profile of the diathermic oil leaving the evaporator (at L=0, since the evaporator is counterflow) and entering the evaporator (at $L=L_{ev}$) are just corresponding to the temperature profiles recorded at the gas heat exchanger inlet (L=0) and outlet ($L=L_{ex,1}$). The temperature distribution is indeed different within the exchangers due to the smaller convection coefficient of the gases compared to the evaporating fluid, and this is why the gas heat exchanger is longer than the evaporator, given the same thermal power to be exchanged.

When diathermic oil enters the evaporator at relatively high temperature (Fig. 5.51 (b)) the organic fluid enthalpy leaving the evaporator (Fig. 5.50 (b)) and mass flow rate (Fig. 5.48 (a)) tend to increase, the latter due to increasing number of nodes where phase change occurs. These two combined effects lead to an increase the pressure in the evaporator (Fig. 5.49 (c)) and this causes the vapour mass flow rate to the turbine to increase, determining an increase in the power output. The vapour mass flow to the turbine causes the liquid fraction stored in the hot drum to decrease (Fig. 5.49 (a)) and the pump control loop responds to this phenomena with increasing the rotational speed (Fig. 5.49 (b)) which causes less organic fluid mass flow rate to the evaporator to be increased determining an improvement in the heat exchanging capabilities of the organic fluid reducing the diathermic oil temperature at the evaporator outlet. The lowered temperature of the diathermic oil entering the gas heat exchanger cause its temperature, when returned to the evaporator, to be lower and this causes a series of analogous, but opposite, concatenate effects to originate

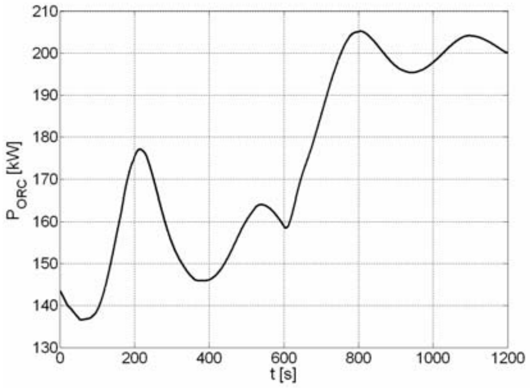

Fig. 5.47. ORC overall net output power.

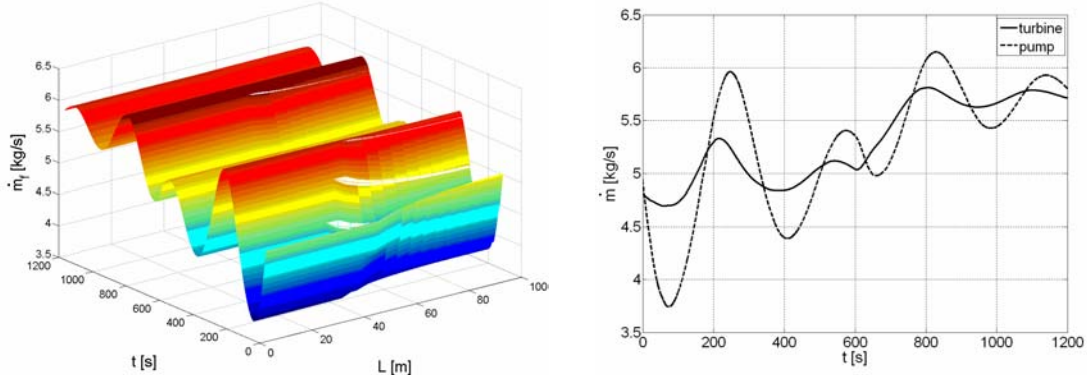

(a) (b)

Fig. 5.48. (a) Organic fluid mass flow rate through evaporator, (b) organic fluid mass flow rate through pump and turbine.

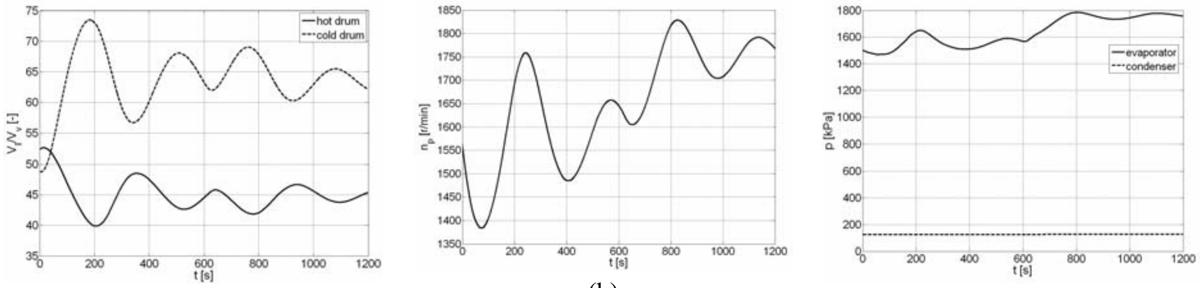

(a) (b) (c)

Fig. 5.49 Main ORC operational parameters: (a)liquid to vapour fractions in the hot and cold drums, (b) pump rotational speed and (c) condenser and evaporator pressures.

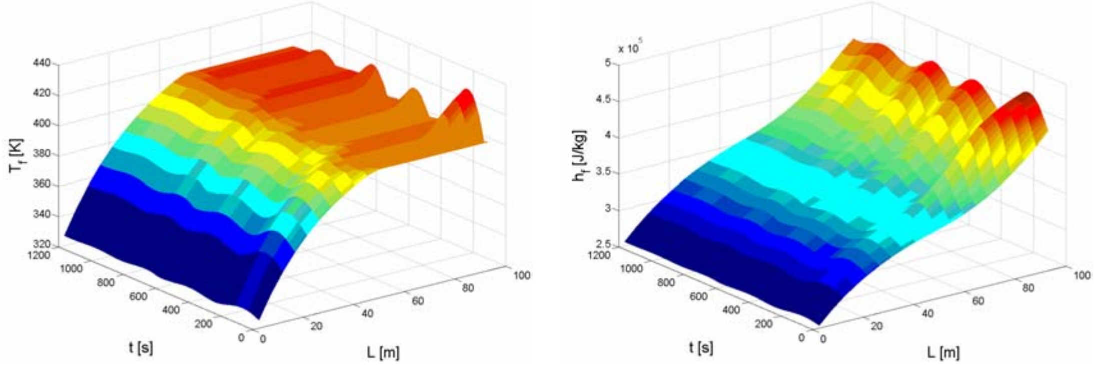

(a) (b)

Fig. 5.50. Organic fluid temperature (a) and specific enthalpy (b) distribution within the evaporator.

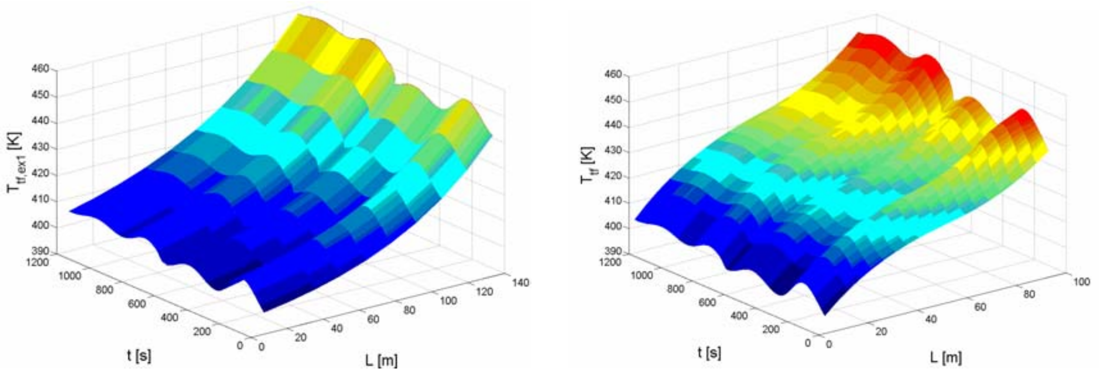

(a) (b)

Fig. 5.51. Diathermic oil temperature distribution in: (a) exhaust gases heat exchanger, (b) ORC evaporator.

Better results can be obtained when a controller is inserted that makes the diathermic oil temperature returning to the gas heat exchanger to be nearly constant.

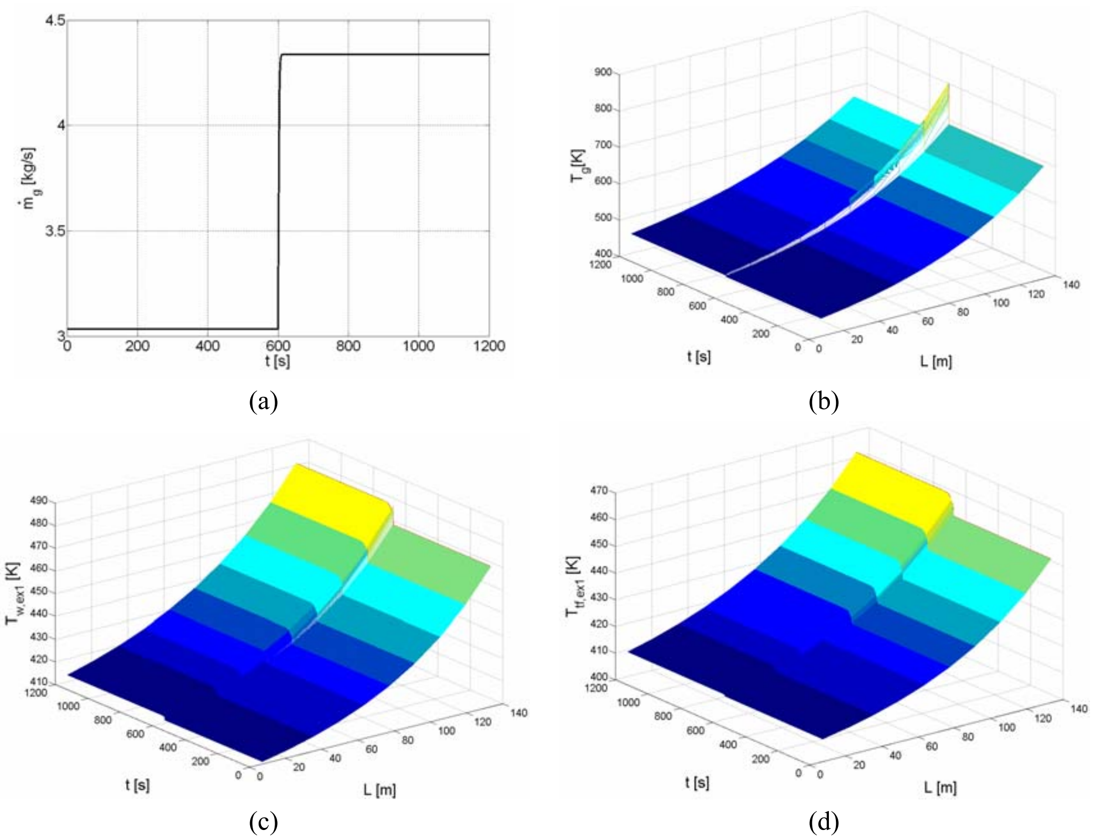

(a) (b)

(c) (d)

Fig. 5.52. Main figures of the gas-diathermic oil heat exchanger: (a) engine exhaust gas mass flow rate, (b) Engine exhaust gas temperature distribution within the exchanger, (c) exchanger wall temperature distribution, (c) diathermic oil temperature distribution within the exchanger.

It is possible to see from Fig. 5.52 (d) how regular is the temperature distribution of the heat transfer fluid within the gas heat exchanger when a constant temperature at inlet (L=0) is guaranteed. The profile highlights the increased available power from the engine exhaust gases when the step change in the fuel mass flow rate to the ICE is imposed at *t*=600s. From Fig. 5.52 (b) it can be observed that, as already observed, the engine exhaust gas temperature actually decreases in that instant but the available thermal power increases due to the significant increase in the exhaust gases mass flow rate (Fig. 5.52 (a)).

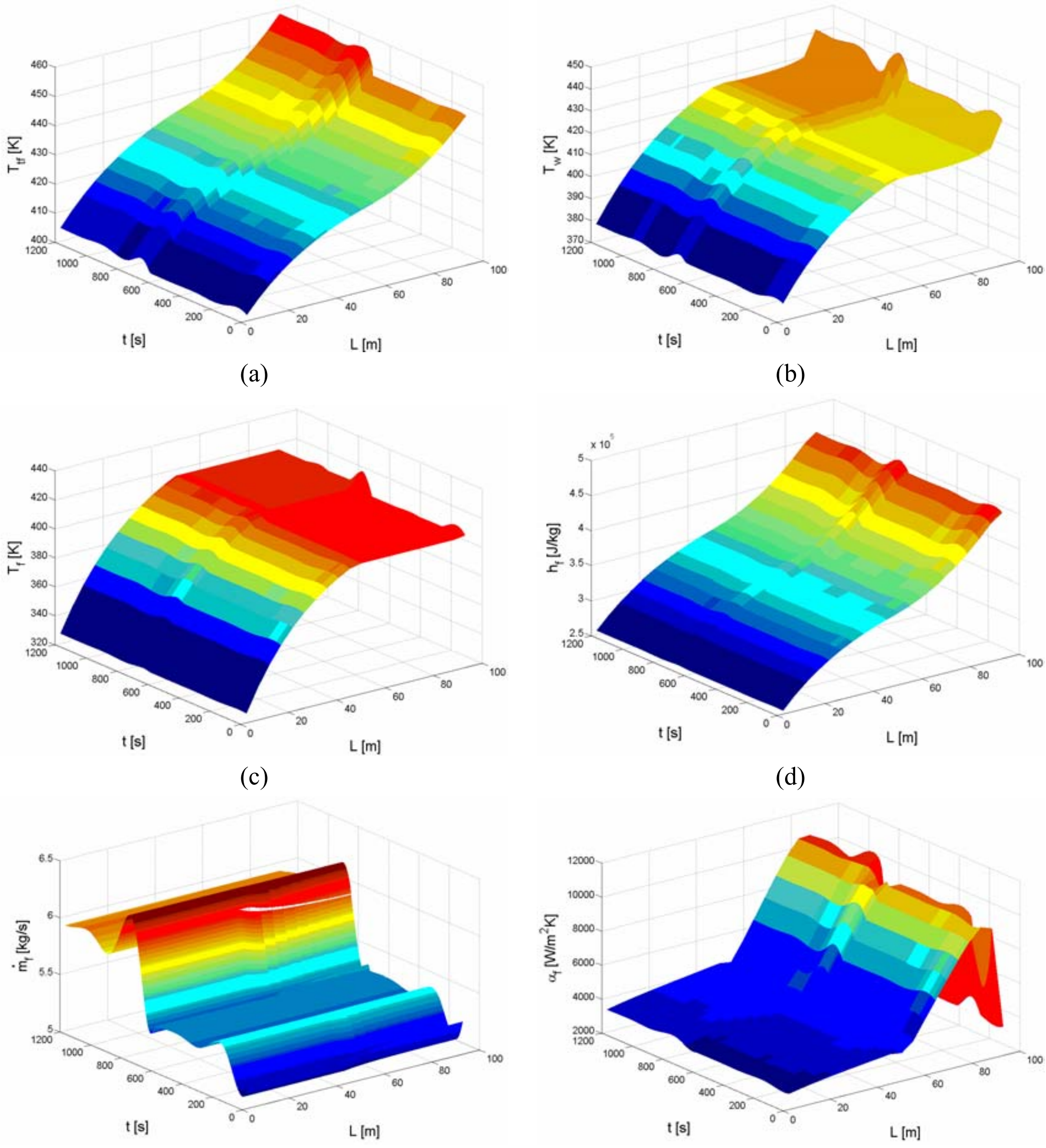

(a) (b)

(c) (d)

(e) (f)

Fig. 5.53. Main figures of the evaporator: (a) diathermic oil temperature distribution, (b) exchanger wall temperature distribution, (c), organic fluid temperature distribution, (d) organic fluid specific enthalpy distribution, (e) organic fluid mass flow rate, (f) heat exchange coefficient distribution in the organic fluid side of the evaporator.

The set of plots of Fig. 5.53 refer to the conditions in the ORC evaporator. It can be seen how again the profiles are much better developed and plainer than those reported in Fig. 5.50. The diathermic oil temperature profile at evaporator inlet is much smoother (Fig. 5.53 (a)). The evaporator wall temperature (Fig. 5.53 (b)) has a distribution within the exchanger that follows close the temperature distribution of the organic fluid (Fig. 5.53 (c)) due to the higher heat exchange convection coefficient in the organic fluid side. It is possible to recognize the heating region (where the organic fluid passes from subcooled liquid to saturated liquid) and the phase change region (where the fluid passes from saturated liquid to saturated vapour) characterized by the plateau of constant temperature distribution with respect to evaporator length. The evaporator is exactly designed and the fluid in the last node is nearly in the condition of saturated vapour (it can be seen that sometimes some slight superheating is achieved, confirming that the thermodynamic state of the last node is close to the upper saturation line). This is further confirmed by analysis of the pipe wall temperature profile (Fig. 5.53 (b)) where the last nodes experience a sharp temperature increase, which happens because, when the organic fluid vapour fraction within the pipe reaches high values (0.9 or above) or is superheated, as seen in Par. 3.2.3 the convection coefficient between pipe and organic fluid experience a sudden drop, hence the heat exchange process with the diathermic oil prevail and the wall temperature tends in these nodes to become closer to the diathermic oil entering the exchanger. The described drop in the organic fluid convective heat exchange coefficient in this region can in fact be appreciated from Fig. 5.53 (f).

To be observed that the ORC responds to the increased available thermal power from the heat transfer fluid mainly with an increase in the circulation mass flow rate than with increased evaporating pressure and temperature. The organic fluid temperature of evaporation experiences just a slight increase at *t*=600s as consequence to the slightly increased pressure in the hot drum (Fig. 5.53 (c) and Fig. 5.55 (b)) while the mass flow rate circulating in the evaporator increases significantly (Fig. 5.53 (e)). Fig. 5.54, that shows a detail of the temperatures of transfer fluid, wall and organic fluid around the moment when the transient occurs, highlights that the fluid temperature experiences a smaller increase compared to the wall and transfer fluid. The figure also reveals how longer is the transient phenomena that regards the organic fluid compared to the profile of the transfer fluid for example.

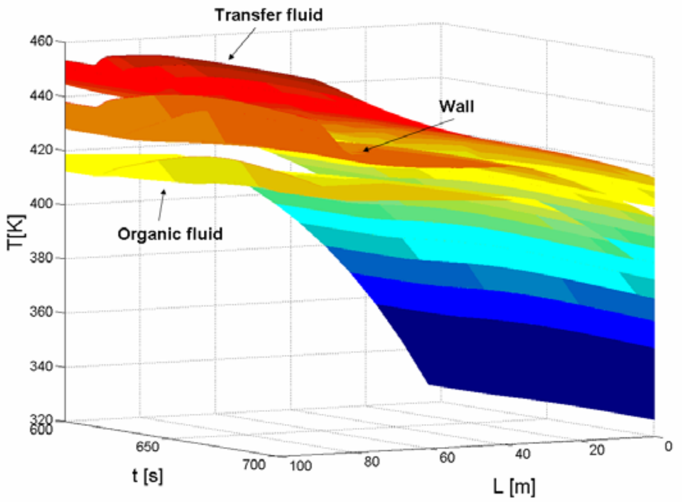

Fig. 5.54. Detail of the temperature distribution of transfer fluid, wall and organic fluid in the evaporator.

The transfer fluid temperature, as well as specific enthalpy (Fig. 5.55 (d)) have a slight increase following the temperature increase of the transfer fluid that cause the pressure in the evaporator to raise. As soon as the liquid fraction in the hot drum starts to decrease (Fig. 5.55 (c)) due to the increased mass flow rate to the turbine generated by the increased pressure in the evaporator system, the controller responds promptly increasing the pump rotational speed and therefore the mass flow rate to the evaporator. Observing in detail Fig. 5.55 (a) just after the disturbance occurs, it can be seen that the turbine mass flow rate first increases, generating an unbalanced net mass flow rate to the hot drum that makes its level to decrease, and hence the pump regulating loop to respond, with some characteristic time delay, bringing the liquid level back to the set point value after a while but setting the operating mass flow rate circulating to a new value. Fig. 5.55 (a) also highlights how the designed system is capable of reaching stable operating conditions, witnessed by the equal value of the mass flow rate reached in the main flow control devices of the system, turbine and pump. In fact, besides some instability after the initial transient and right after the disturbance, the two mass flow rate, with an overall characteristic time response of about 400s, reach a stable operating point that was not observed in the case of Fig. 5.48 (b).

The ORC net output power also displays a stable profile with this system configuration, as shown by Fig. 5.56. The overall output power is prompter in responding to the disturbance than the circulating mass flow rate and after about 200s the new value is reached. It is interesting to appreciate the increased output power when the engine provides more thermal power to the gas heat exchanger, and that the global organic cycle efficiency slightly increase since the system is brought to operate closer to the rated operating condition (Fig. 5.56 (b)).

However, while the engine response to the increased mass flow rate in terms of output power is nearly instantaneous, the ORC cannot follow it as promptly and it takes some time to stabilize to the higher value due to all the inertias encountered by the thermal power to be converted in mechanical power.

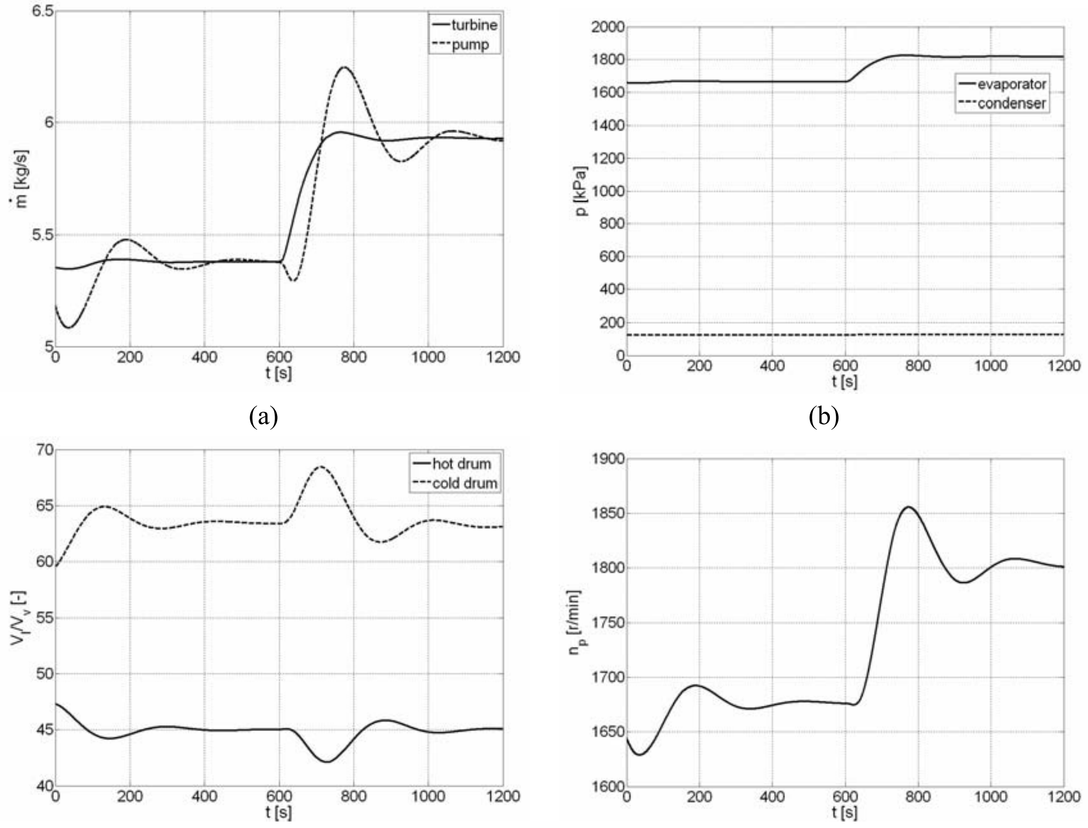

(a) (b)

(c) (d)

Fig. 5.55. Main parameters of the organic cycle: (a) turbine and pump mass flow rates, (b) evaporator and condenser pressures, (c) liquid to vapour fraction in the separators, (d) pump rotational speed.

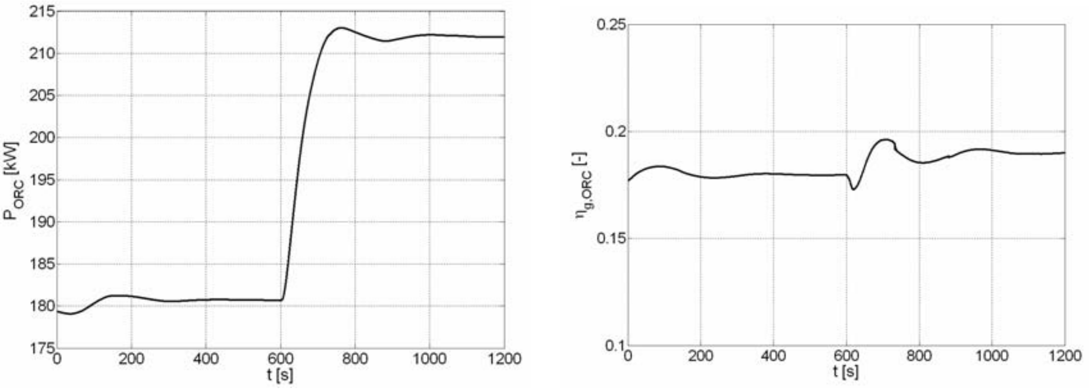

(a) (b)

Fig. 5.56. ORC overall net output power (a) and ORC global cycle efficiency (b).

Interesting is also Fig. 5.57 that displays the overall output power generated by the combine ICE-ORC power unit. It shows how the contribution of the ORC is consistent and that globally the combined cycle system (CC) responds in term of mechanical power analogously to the way the ICE alone would respond, and the transient response of the ORC is nearly unperceivable, causing the overall power to just take few hundreds seconds to adjust to the steady state value, as shown by the detail of Fig. 5.57 (b).

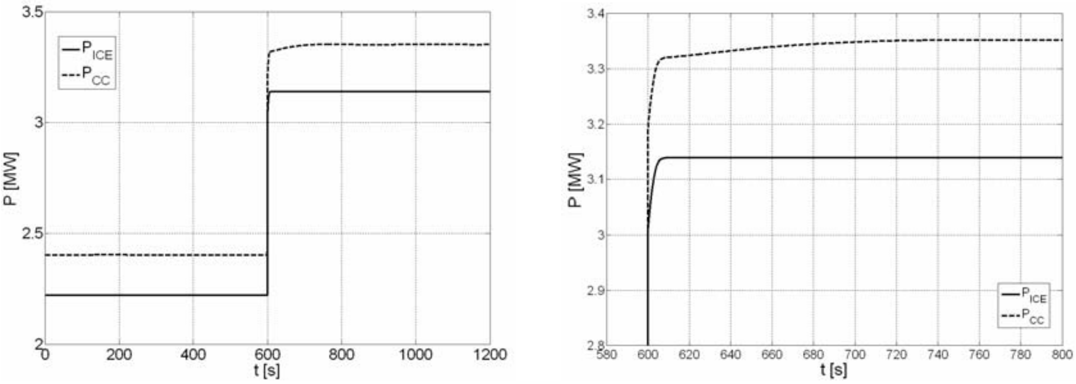

(a) (b)

Fig. 5.57. (a) Overall power output of the MCI-ORC Combined Cycle (CC), (b) detail.

It is finally interesting to see how the main operational parameters of the combine ICE-ORC system, while not identical to those calculated in the thermodynamic analysis of Par. 5.1, are though very similar confirming that the dynamic model proposed can properly represent the systems, The model can then be employed for comprehensive simulations useful to reveal characteristics behaviour under unsteady operations in order to understand how the system would respond to variation on some of the overall inputs. It is also suitable to provide some important information for system design and control. In the example of the system here presented the dynamic model realized helped to reveal how a control loop on the diathermic oil transfer fluid temperature is essential for system stability, helping also to quantify and qualify the effects of the missing control in comparison to the analogous system where control was inserted.

5.3.2 The ORC simple cycle with direct use of engine exhaust gases

By properly rearranging the components that constitute the lay-out, a new configuration of the ICE-ORC setup can be created. In this case the ORC is thermally powered by the engine exhaust gases without recurring to the intermediary diathermic oil circuit. The system configuration can be created by simply connecting the ICE and the ORC models from the ‘Complete Power Systems’ library, and setting the ORC evaporator to utilize hot exhaust gases as heat transfer medium (Fig. 5.58).

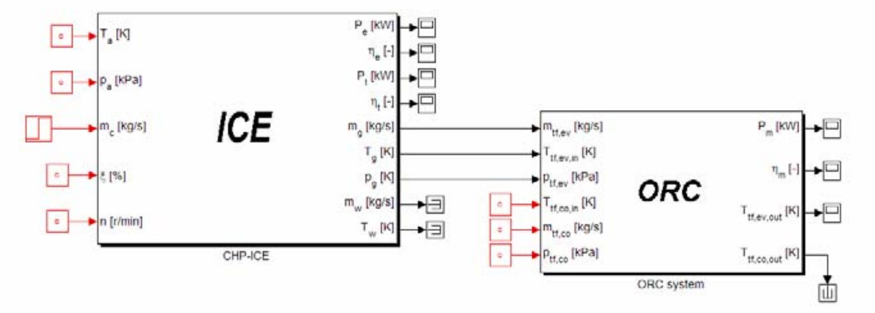

Fig. 5.58. Simulink® lay-out of the ICE-ORC combined unit with heat recovery from engine exhaust gases and intermediary diathermic oil circuit.

Some simulations have been executed and the results here presented refer to a transient generated by a step change in the fuel mass flow rate fed to the engine identical to that described in the previous paragraph, to facilitate the comparison of the results.

From the figures it can first of all be observed that, differently from the case when the intermediary diathermic oil circuit is inserted, the system displays slightly lower stability. This is due to the lower thermal inertia of the heat transfer medium. This analysis therefore displays the importance of an intermediary fluid to transfer the heat from the engine exhaust gases to the ORC not only for safety reasons but also to stabilize the operation of the ORC and make the system less sensible to the changes in the fluid mass flow rate that may occur in transient operational conditions. The ORC pump controller had be redesigned to guarantee a smoother operation of the cycle, if direct use of the exhaust gases had to be employed.

It is however possible to observe the average significant increase in the overall useful power generated by the organic Rankine cycle, with respect to the case when diathermic oil circuit was employed, which is capable of enhancing notably the combined ICE-ORC power output (Fig. 5.61). The evaporator equivalent length is now longer than that of the cycle with intermediary oil circuit for the reduced overall heat transfer coefficient (Fig. 5.59). The evaporator is designed in such way to cool down the gases to the minimum considered temperature of about 120°C. It can also be observed how, as expected, the average fluid mass flow rate circulating is higher due to the increased thermal power available from the heat source (Fig. 5.60).

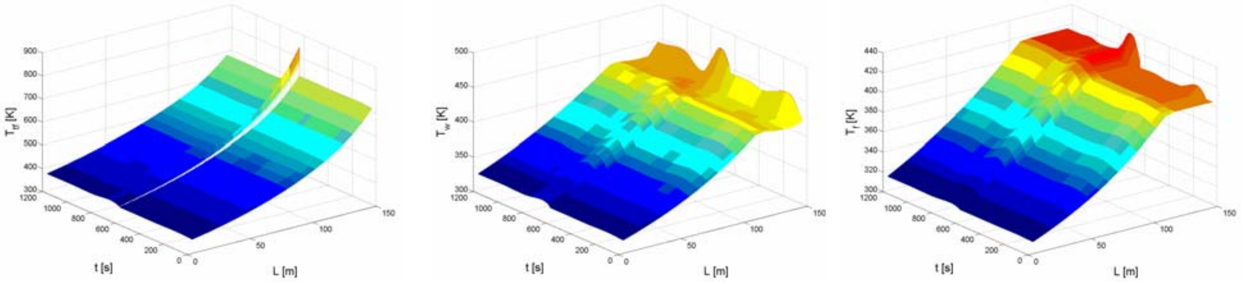

(a) (b) (c)

Fig. 5.59. Main figures of the evaporator: (a) transfer fluid temperature distribution, (b) exchanger wall temperature distribution, (c) organic fluid temperature distribution.

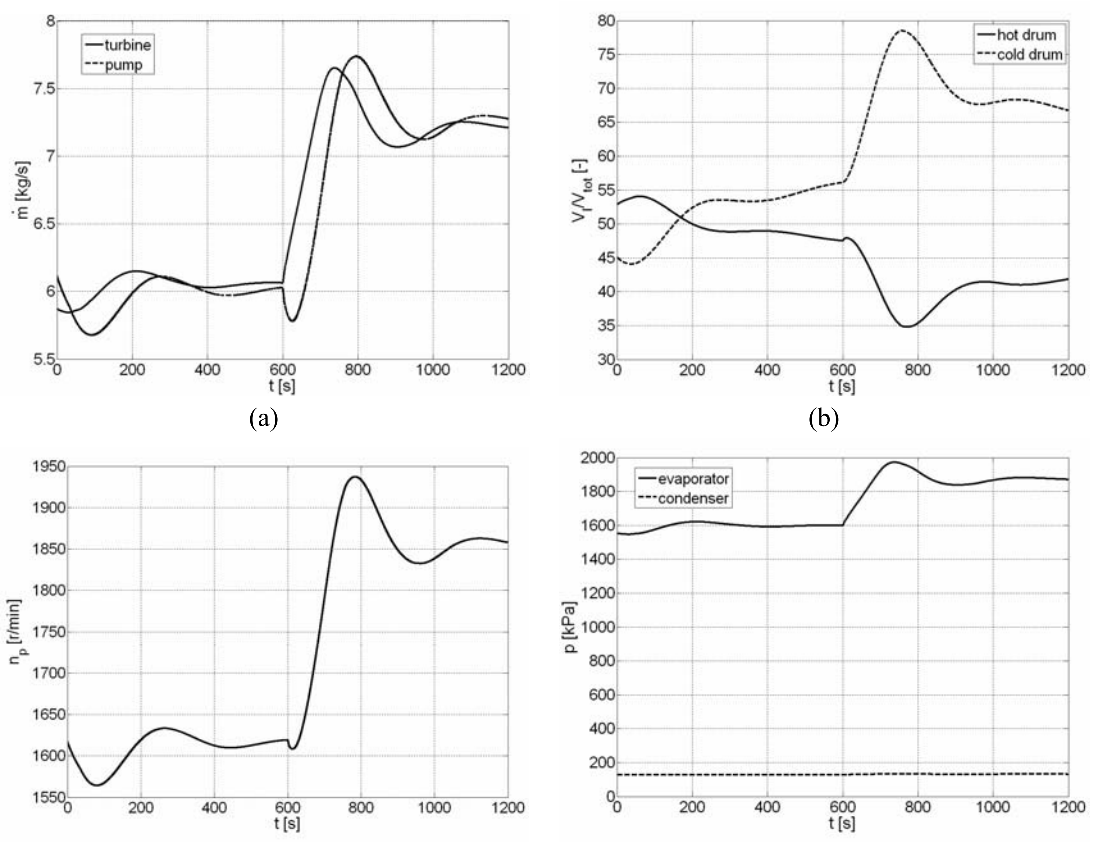

(a) (b)

(c) (d)

Fig. 5.60. Main ORC operational parameters: (a) turbine and pump fluid mass flow rate, (b)liquid to vapour fractions in the hot and cold drums, (c) pump rotational speed and (d) condenser and evaporator pressures.

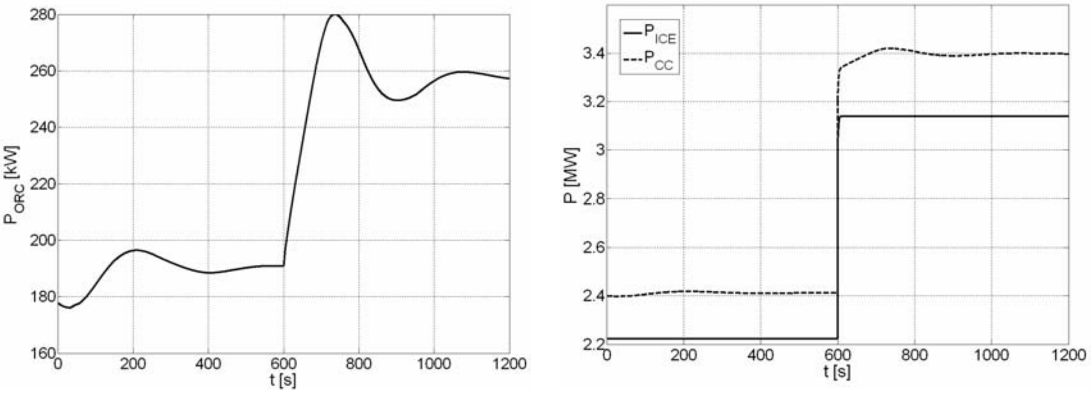

(a) (b)

Fig. 5.61. (a) Net ORC output power and (b) Overall power output of the MCI-ORC Combined Cycle

5.3.3 The ORC thermally powered by engine exhaust gases and engine refrigerant water

The last configuration proposed features a thermal powering of the ORC through a direct use of the engine exhaust gases and a preheating of the organic fluid through the engine refrigerant water.

The lay-out of the ORC system must in this case be slightly modified with respect to the configuration previously assumed, since two evaporators disposed in series are now required to utilized the two different transfer media. A first evaporator model, called Preheater (PH), recovers part of the heat from the engine refrigerant rising the organic fluid temperature coming from the condenser. The second exchanger is the actual evaporator and the hot stream is in this case constituted by the engine exhaust gases.

The lay out of the proposed ORC is displayed in Fig. 5.62 where the main components are easily recognizable.

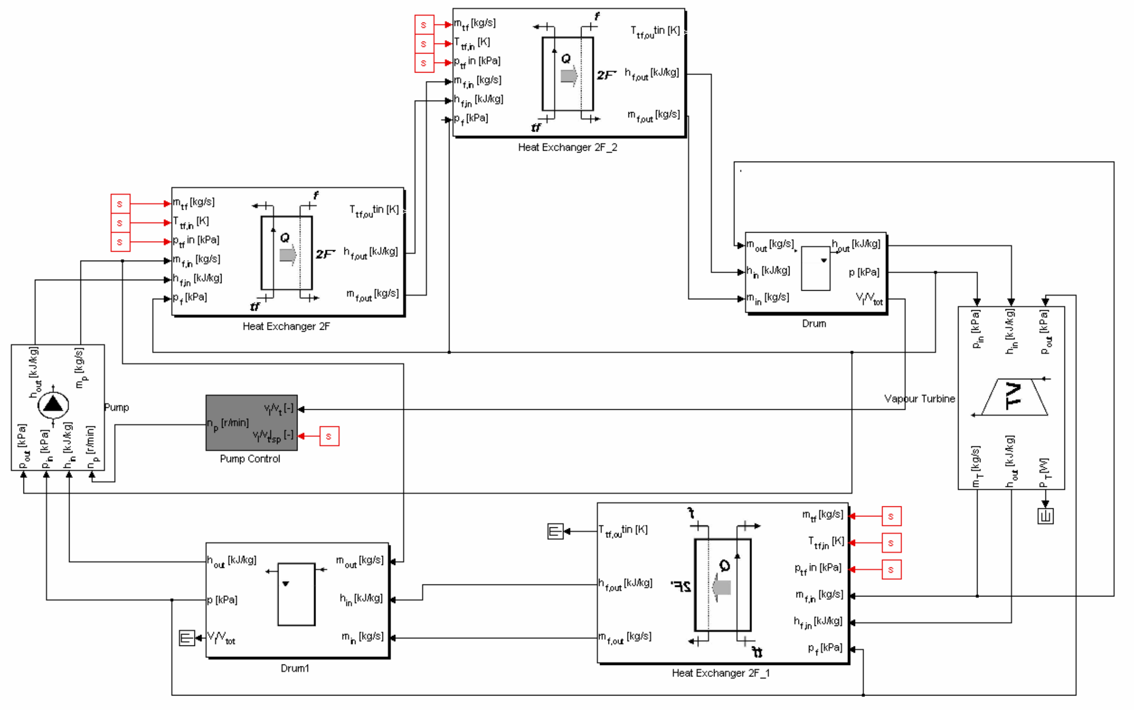

Fig. 5.62. Simulink lay-out of the ORC system with two evaporators placed in series.

The ORC complete block will therefore feature more inputs in this case, to comprise the low temperature thermal stream constituted by the engine refrigerant, as from Fig. 5.63.

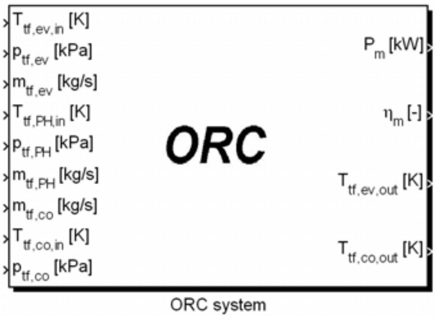

Fig. 5.63. Simulink® block of the ORC system with two evaporators placed in series. Upper level.

The dynamic model of the proposed combined unite is then displayed in Fig. 5.64.

As observed in the previous Chapter, the ICE model does not perform an actual calculation of the refrigerant instantaneous mass flow rate and temperature. However, since the availability of thermal power from the refrigerant is bigger than the thermal power that can be exploited by the ORC preheater, it has been assumed that the a fraction of the nominal engine refrigerant mass flow rate, at its nominal temperature, is provided to the ORC.

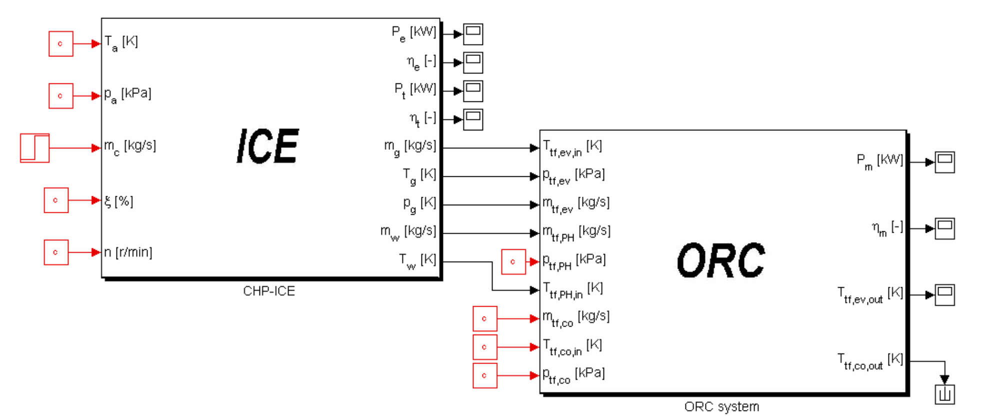

Fig. 5.64. Simulink® lay-out of the ICE-ORC combined unit with heat recovery from engine exhaust gases and refrigerant.

Some results are displayed in the figures reported below.

Fig. 5.65 refers to the preheater where the engine refrigerant is employed. It can be observed that the engine water enters at the rated temperature of 90°C and leaves the exchanger at 80°C. The wall temperature is close to the organic fluid temperature, since the low engine refrigerant mass flow rate imposed, determines low values of the Reynolds number and hence low values of the convection coefficient in the water pipe heat exchange.

The organic fluid raises its temperature in the preheater by about 20K; after the preheating it enters the actual evaporator and it is possible to observe, from Fig. 5.65 (c), that its temperature at the evaporator inlet equals the temperature at which it leaves the preheater. Again the engine gases are cooled down to a temperature of about 120°C (Fig. 5.65 (a)).

Fig. 5.67 displays the main parameters of the organic cycle. It is possible to observe that the pump speed (and hence the fluid mass flow rate) and evaporator pressure reach values on average higher than in the case of Par. 5.3.2. To be noted that the same parameters of the PID pump controller have been here employed. This is a consequence of the higher thermal available, that forces the ORC system to stabilize in different operating points.

The raising in the mentioned cycle parameters determines an increase in the cycle power (Fig. 5.68) and, as expected, this configuration is the one that delivers the highest value of ORC power among the three analyzed, also resulting in the highest combined ICE-ORC power.

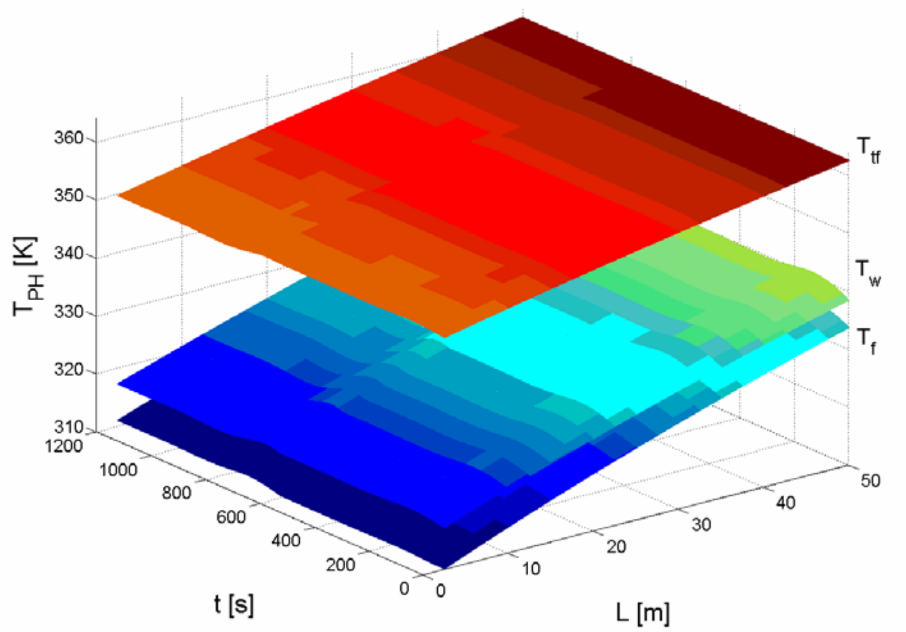

Fig. 5.65. Temperature distribution of engine refrigerant (*tf*), heat exchanger wall (*w*) and organic fluid (*t*) in the preheater.

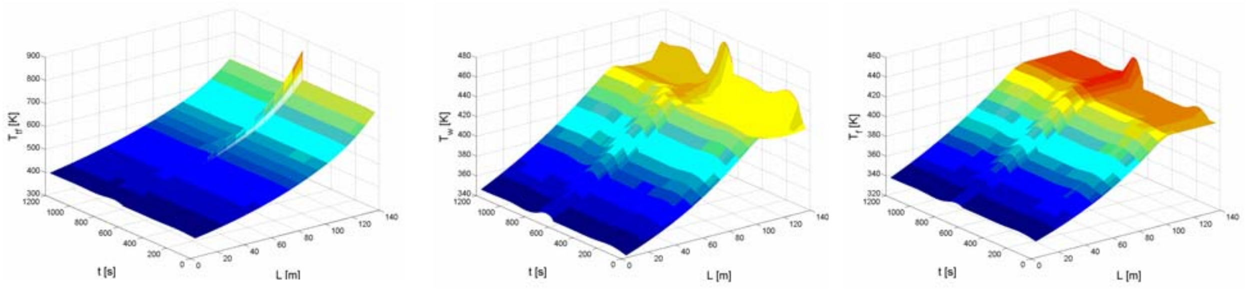

(a) (b) (c)

Fig. 5.66. Main figures of the evaporator: (a) transfer fluid temperature distribution, (b) exchanger wall temperature distribution, (c) organic fluid temperature distribution.

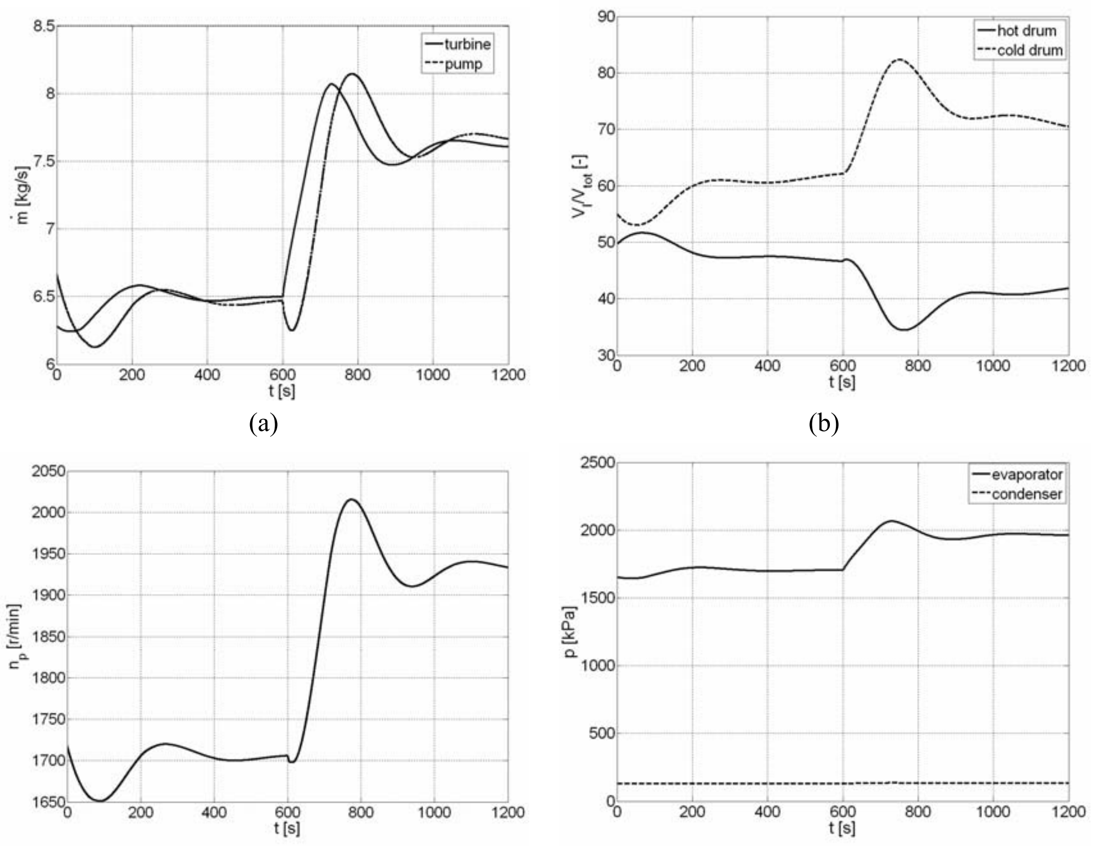

(a) (b)

(c) (d)

Fig. 5.67. Main ORC operational parameters: (a) turbine and pump fluid mass flow rate, (b)liquid to vapour fractions in the hot and cold drums, (c) pump rotational speed and (d) condenser and evaporator pressures.

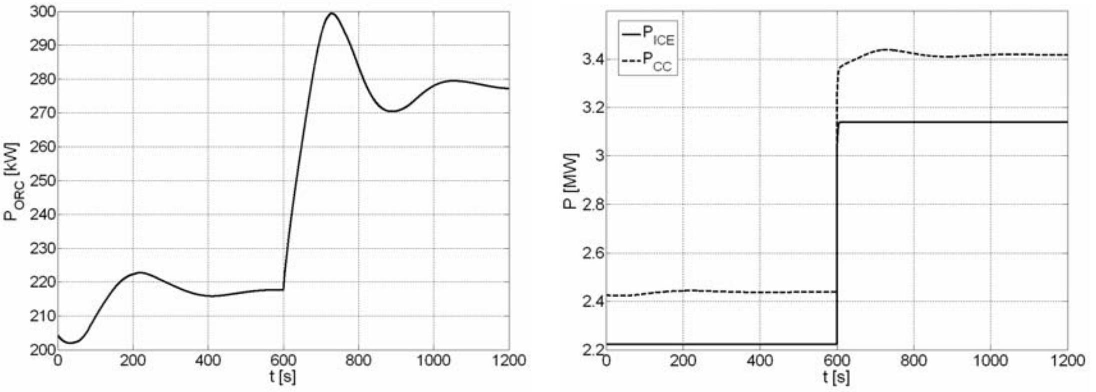

(a) (b)

Fig. 5.68. (a) Net ORC output power and (b) Overall power output of the MCI-ORC Combined Cycle.

5.4 Summary

In the Chapter the combination of organic Rankine cycles with stationary alternative internal combustion engines is presented as possible solution to increase the second principle efficiency of engines.

A comprehensive thermodynamic analysis has been conducted in order to illustrate the different system configuration proposed and to quantify the advantages of the solution, demonstrating that under certain circumstances the employment of ORCs can provide a significant contribution to the overall mechanical energy flux generated by the ICE. Some very advanced lay-outs, that employ two ORCs in a superimposed configuration, are also discussed demonstrating that in some cases, the solution of employing ORCs to enhance the engine second principle efficiency, can apply also if heat is required for cogeneration purposes. This is of course when the heat is required at temperatures not too elevated, and in these cases the ORC can still be placed on the ICE exhaust gas circuit, employing their significant exergy content to generate mechanical power and releasing heat at temperatures that can still be compatible with the heating needs of some thermal users.

The proposed system have been further analyzed recurring to the libraries of components illustrated in the previous Chapters and dynamic models of some of the configurations identified have been presented. The scope was to highlight the contribution of comprehensive dynamic models in developing new system designs and the models realized helped to uncover some interactions between the engine and the ORC that generates unstable operation conditions, that would have been hard to quantify without a similar tool.

Even if the system control design have not been optimized, the dynamic model proposed can be used to develop the controllers to be applied to the system to stabilize its behaviour, which is another of the uses of the created library of components.

The proper development of the controllers will be object of future works; the examples presented here had the main scope to display the easy way provided by the presented library of models to create different system configurations and to analyze systems of which no experimental execution still exists.

Refernces

1 Danov S.N., Gupta A. K., *Modeling the Performance Characteristics of Diesel Engine Based Combined-Cycle Power Plants – Part I: Numerical Model*, ASME Journal of Engineering for Gas Turbines and Power, 126, pp.28-34, 2004.

2 Kane M., Favrat D., Gay B., Andrei O., *Scroll Expander Organic Rankine Cycle (OR(C) Efficiency Boost of Biogas Engines*, Proc. of ECOS 2007, A. Mirandola et al., eds., Padua, Italy, vol.2, pp.1017-1024, 2007.

3 Kane M., Larrain D., Favrat D., Allani Y., *Small hybrid solar power systems*, Energy 28, pp.1427-1443, 2003.

4 Gambarotta A, Vaja I., *Internal combustion engine bottoming with organic Rankine cycles. A thermodynamic analysis*, Proc. of ECOS 2008 A. Ziebik et al., eds., Cracow, Poland, vol.2, pp.715-723, 2008.

5 Saleh B., Koglbauer G., Wendland M., Fischer J., *Working fluids for low-temperature organic Rankine cycles*, Energy; 32, pp.1210-1221, 2007.

6 Macchi E. *Cicli di potenza per impianti solari*, La Termotecnica, 23, pp.309-327, 1979 (in Italian).

7 Hung T.C., Shai T.Y., Wang S.K., *A review of organic Rankine cycles (ORCs) for the recovery of low-grade waste heat*, Energy, 22, pp.661-667, 1997.

8 Chen Y., Lundqvist P., Johansson A., Platell P., *A comparative study of the carbon dioxide transcritical power cycle compared with an organic Rankine cycle with R123 as working fluid in waste heat recovery*, Applied Thermal Engineering 26, pp.2142-2147, 2006.

9 Mago P.J., Charma L.M. Srinivasan K., Somayaji C., *An examination of regenerative organic Rankine cycles using dry fluids*, Applied Thermal Engineering 28, pp.998-1007, 2008.

10 Angelino G., Colonna P., *Multicomponent Working Fluids for Organic Rankine Cycles (ORCs)*, Energy, 23, pp.449-463, 1997.

11 Maizza V., Maizza A., *Unconventional working fluids in organic Rankine cycles for waste heat recovery systems*, Appl. Thermal Engineering 21, pp.381-390, 2001.

12 Drescher U., Bruggermann D., *Fluid selection for the Organic Rankine Cycle (OR(C) in biomass power and heat plants*, Applied Thermal Engineering 27, pp.223-228, 2007.

13 REFPROP Version 6.01, NIST Standard Reference Database 23, the US Secretary of Commerce, America; 1998.

14 Liu B.-T., Chien K.-H., Wang C.-C., *Effect of working fluids on organic Rankine cycle for waste heat recovery*, Energy 29, pp.1207-1217, 2004.

15 Invernizzi C., Iora P., Silva P., *Bottoming micro-Rankine cycles for micro-gas turbines*, Applied Thermal Engineering, 27, pp.100-110, 2007.

16 Winterbone D. E., *Advanced Thermodynamics for Engineers*, John Wiley and Sons Inc., New York, 1997.

17 Kanoglu M., Dincer I., Rosen M.A., *Understanding energy and exergy efficiencies for improved energy management in power plants*, Energy Policy 35, pp.3967-3978, 2007.

18 Larjola J., *Electricity from industrial waste heat using high-speed organic Rankine cycle (ORC)*, Int. J. of Production Economics, 41, pp.227-235, 1995.

19 Schuster A., Sotiros K., Aumann R., *Efficiency optimization potential in supercritical Organic Rankine Cycles*, In Proceedings of ECOS 2008, Krakow, Poland, June 24-27, 2008, Vol.2: 725-732.

20 Kane M., Larrain D., Favrat D., Allani Y., *Small hybrid power system*, Energy 2003;28: 1427-1443.

CHAPTER
SIX

CONCLUSIONS

In the present Work a full library of models of the most common macro-components that may constitute advanced energy systems have been presented. Different modeling methodologies have been applied depending on the characteristics of the physical component that had to be mathematically modelled. In some cases the component has been assumed capable of storing mass, energy or momentum (or moment of momentum) and differential equations have been cast to represent the time evolution of the 'level variables' of the components, also known as states. In these cases therefore the methodology applied has led to realizing 'state determined' components that have been introduce into the corresponding library set. In some other cases it has been assumed that the storing capabilities of the component are negligible. This is the case for example of the so called 'flow control devices' and their time behaviour can be represented via a sequence of steady state values, according to a quasi-steady approach. Quite often these components are represented through empirical correlations leading to *black-box* models. Since no state variables have been defined they have been grouped in the 'not state determined' component library.

These two libraries, that have been inserted in the standard Simulink® library browser for ease of access and to exploit the advantages of the dynamic library link, cover quite a wide range of the physical components that can be found in standard energy conversion systems and power systems. It should however be noted that the library can easily be extended or improved. Among the improvements the full validation of the described components is one of the goals sought in future works. In fact, the unavailability of test facilities and proper data on the behaviour of real components did not allow to validate all the presented models, even though validation has been proposed in all the cases when it have been possible.

Though not all the models underwent a proper validation, hence the library cannot at right be considered a 'validated library', the models of different components have been properly coupled together, according to the right cause-effect, that has been at the base of the modeling approach, providing functional models of complete energy systems.

Examples have been presented with reference to 'standard' power systems as Micro Gas Turbines, Organic Rankine Power cycles and stationary CHP alternative Internal Combustion Engines. The realized models, whose basic constituents are the physical components inserted in the 'state determined' and 'not state determined' libraries, have been grouped together constituting the 'complete energy systems' library.

In all the cases the models proved to operate reliably providing reasonable results. To be noted that while not always the results obtained can be considered 'valid', since the validation procedure as remembered was not complete, scope of the work was to demonstrate how the single model components could be coupled together to represent advanced energy systems of known design. Whenever some of the components that were not validated should be improved through a rigorous validation procedure, it could be easily replace the homologous non-validated component in the library, contributing to the accuracy of the overall results. Therefore, while the models of full energy systems provided results that cannot considered to be rigorous in terms of physical values, their scope was mainly to demonstrate the methodology and theory to properly use the library of models in order to produce sophisticate virtual machines that allow to reproduce the behaviour of real physical system.

The ultimate goal of the realized library of models however is to provide a useful tool to design and try different solutions to enhance the overall efficiency of the system, solutions that may be too complex to test on physical test benches on the first place, hence a virtual test bench, the simulation environment, can be used to predict the behaviour and performances of the system under development.

On example of this is presented through the ICE-ORC combined power unit intended for stationary applications. The idea is here proposed as a possible solution to increase the second principle efficiency of internal combustion engines in all the cases when they are operated without heat recovery. A comprehensive thermodynamic analysis is first presented demonstrating the advantages of the solution and the different ways to couple the ICE to one or more ORCs. The availability of heat at different temperature levels from the engine and the desire to still consider the possibility of obtain heat at a suitable temperature level for cogeneration purposes has brought to design and discuss many configurations.

After proving the sustainability of the solution from a thermodynamic standpoint, the library of models has usefully been employed to design full dynamic computer models of some of the proposed configurations of the ICE-ORC combined unit. The models allowed to investigate and analyze the actual response to changing inputs besides the mutual interactions between the two power units, revealing information of the operating behaviour of the plant even though the physical system is actually not available. The full model can also be employed to properly design the control unit, since the dynamic model has revealed that stable operation can be reached only with robust controllers, even though the issue has not been covered within this Thesis. Scope of the examples was mainly to demonstrate the capability of the proposed libraries of models to built up any desired configuration of the energy system that is being developed and optimized.

The work has at the end lead to building a full working and robust dynamic model of a combined ICE-ORC power unit that allows a deep and punctual analysis of all the heat exchangers and the thermodynamic parameters within any component of both ICE and the ORC. It seems that at present such model can hardly be found in the open literature.